Development of multi-messenger real-time analyses for the KM3NeT neutrino telescope

Massimiliano Lincetto

Aix-Marseille Université

École doctorale 352 : Physique et sciences de la matière

KM3NeT

Centre de Physique des Particules de Marseille - UMR7346

Thèse présentée pour obtenir le grade universitaire de docteur

Physique et Sciences de la Matière
Physique des Particules et Astroparticules

Massimiliano LINCETTO

Development of multi-messenger real-time analyses for the KM3NeT neutrino telescope

Développement d'analyses multi-messager en temps réels pour le télescope à neutrino KM3NeT

Soutenue le 01/12/2020 devant le jury composé de :

Marie-Anne BIZOUARD	OCA, Université Côte d'Azur	Rapporteure
Ronald BRUIJN	NIKHEF, University of Amsterdam	Rapporteur
Inés GIL-BOTELLA	CIEMAT, Madrid	Examinatrice
Eric KAJFASZ	CPPM, Aix-Marseille Université	Examinateur
Erin O'SULLIVAN	Uppsala University	Examinatrice
Jose BUSTO	CPPM, Aix-Marseille Université	Directeur de thèse
Damien DORNIC	CPPM, Aix-Marseille Université	Encadrant

Numéro national de thèse/suffixe local : 2020AIXM0396/044ED352

Résumé

Depuis la découverte des rayons cosmiques au début du XXe siècle, leur origine est incertaine. Exploitant différentes techniques de détection, de nombreuses études expérimentales ont été menées à bord de ballons, de satellites et au sol. À ce jour, le spectre des rayons cosmiques est mesuré sur plus de douze ordres de grandeur en énergie (de 10^8 à 10^{20} eV). Ce spectre suit au premier ordre une loi de puissance, $E^{-\gamma}$, avec $\gamma \simeq 2,7$. Néanmoins, on observe trois structures dans ce spectre : un raidissement entre 10^{15} eV et 10^{17} eV (*genoux*), un durcissement vers $10^{18,5}$ eV (*cheville*) et une coupure possible autour de $10^{19,5}$ eV. L'interprétation de ces caractéristiques implique des changements de compositions, les mécanismes d'accélération et de propagation des rayons cosmiques dans l'Univers. La recherche de l'origine des rayons cosmiques a conduit à l'étude des phénomènes les plus violents et les plus énergétiques de l'Univers. Les restes de supernovae ont été proposés comme la principale source de rayons cosmiques galactiques, mais ce paradigme présente quelques problèmes ouverts. La production des rayons cosmiques extra-galactiques est attribuée à des accélérateurs cosmiques (noyaux actifs de galaxies, sursauts gamma) et/ou à des réservoirs de rayons cosmiques (galaxie à sursaut de formation d'étoiles, amas de galaxies). Depuis le milieu du XXe siècle, l'astronomie *multi-longueurs d'onde*, avec la radio, les rayons X et les rayons γ, s'est développée pour compléter les observations optiques traditionnelles. Les émissions non thermiques des objets astrophysiques sur l'ensemble du spectre électromagnétique sont une signature de l'accélération des particules. Ces émissions électromagnétiques peuvent avoir comme origine une population d'électrons par processus *leptonique* (rayonnement synchrotron ou diffusion Compton inverse) et/ou une population de hadrons par processus *hadronique* (collision $p-p$ ou $p-\gamma$). Cette derniere hypothese lie les rayons cosmiques avec l'émission électromagnétique à haute énergie (astronomie *multi-messenger*). Les neutrinos ne sont produits que dans les processus hadroniques, ce qui fait que leur détection est une signature unique d'une source de rayons cosmiques. Les connexions entre les rayons γ, les neutrinos astrophysiques et les rayons cosmiques de très haute énergie représentent l'une des énigmes les plus intrigantes de l'astrophysique actuelle.

L'astronomie des neutrinos extrasolaires a débuté en 1987 avec la première détection de neutrinos de faible énergie provenant d'une supernova à effondrement de cœur dans le grand nuage de Magellan. La récente découverte du flux de neutrinos astrophysiques à haute énergie par IceCube marque une nouvelle étape dans cette astronomie multi-messager. Mais aucune source n'a pu être formellement identifiée. Cette difficulté à établir l'origine des sources de neutrinos astrophysiques plaide en faveur de la conception et de la construction de la prochaine génération de téles-

copes à neutrinos. Ces instruments sont basés sur l'installation de réseaux de modules optiques dans de grands volumes de glace ou d'eau situés à grande profondeur. L'interaction des neutrinos par le biais de processus à courant chargé ou à courant neutre entraîne la production de particules chargées, qui en se propageant produisent de la production de lumière de Cherenkov dans le milieu. La détection de cette lumière par les modules optiques permet de reconstruire indirectement la direction et l'énergie des neutrinos de haute énergie (> quelques GeV). Plus haute est l'énergie, meilleures seront les performances de la reconstruction.

L'expérience KM3NeT, successeur d'ANTARES, est actuellement en construction dans la mer Méditerranée. Il sera composé de deux détecteurs. ORCA, construit au large de Toulon, en France, vise à déterminer la hiérarchie de masse des neutrinos par la mesure des oscillations des neutrinos atmosphériques, avec une masse instrumentée de 8 Mton. ARCA, construit au large de Capo Passero, en Italie, sera un télescope à neutrinos à l'échelle d'un km^3 optimisé vers la découverte et l'observation de sources de neutrinos astrophysiques. Tout en adoptant des densités d'instrumentation différentes, ARCA et ORCA partagent la même technologie, en particulier, le même élément de détection de base : le module optique (DOM). Les DOM contiennent chacun 31 tubes photomultiplicateurs (PMT) de 80 mm de diamètre installés dans une sphère en verre résistante à la pression. Les lignes de détection verticales (DU), ancrées au fond de la mer à une profondeur de 2,5 3,5 km, sont équipées de 18 DOMs régulièrement répartis sur toute la hauteur. Les premières lignes de ARCA et ORCA ont été déployées en 2016 et 2017. Le détecteur ORCA comportera 115 lignes (2070 DOM), tandis que 230 lignes équiperont le détecteur ARCA.

Les analyses présentées dans cette thèse exploitent les DOM comme des détecteurs autonomes contrairement aux analyses communes qui identifient les événements en corrélant les signaux de photons détectés sur plusieurs modules optiques. Les émissions de photons Cherenkov sont fortement corrélés dans le temps et peuvent être détectés sur plusieurs PMT sous la forme de coïncidences à l'échelle de 10 ns. L'étude de ces taux de coïncidences (*multiplicité*, ie nombre de PMTs en coïncidence) permet de discriminer les différentes origines des signaux optiques de manière statistique. Le taux de comptage individuel des PMTs KM3NeT dans l'eau de mer est d'environ 7 kHz, principalement dominé par les désintégrations radioactives dans l'eau provenant majoritairement du ^{40}K. La bioluminescence de certains organismes marins peut entraîner une émission de lumière diffuse ou localisée avec un taux pouvant atteindre plusieurs (dizaines) MHz sur une échelle de temps d'une centaine de millisecondes à plusieurs heures. Au dessus d'une multiplicité de 6-7, les taux de coïncidences commencent à être dominés par les muons atmosphériques.

Comme le niveau de radioactivité dans la mer est très stable, les mesures des taux de coïncidence sont utilisés pour l'étalonnage in-situ du détecteur. Ceci permet de déduire l'éventuel décalage en temps entre une paire de PMTs avec une précision inférieure à 1 ns et de mesurer les efficacités de détection de chaque PMT.

Les muons et les neutrinos atmosphériques sont originaires de la désintégration des mésons π, K et charmés produits dans l'interaction des rayons cosmiques dans

la haute atmosphère. La demi-vie relativement longue des muons relativistes dans le référentiel terrestre, combinée à leur pouvoir de pénétration élevé, en fait une source omniprésente de bruit de fond pour la plupart des expériences de physique des particules. Les télescopes à neutrinos ne font pas exception à la règle. Bien que le taux de muons détectés dans le volume instrumenté soit fortement réduit en construisant les détecteurs en profondeur, ils représentent toujours une source principale de bruit de fond qui dépasse largement le nombre d'événements de neutrinos. Les différentes stratégies d'identification des neutrinos reposent sur une connaissance détaillée des propriétés (taux, énergie et distribution angulaire) du flux de muons arrivant dans le détecteur. Ce flux de muons atmosphériques a été étudié dans cette thèse en analysant les données de coïncidence des DOM. A partir d'une multiplicité 8, les coïncidences représentent un échantillon de muons atmosphériques de haute pureté détectés par chaque DOM à sa profondeur. Leur taux correspond au flux total intégré sur l'angle solide à une profondeur donnée. L'étude de ces taux de coïncidence ont permis de mesurer le taux de muons en fonction de la profondeur de la mer entre 2200 et 3400 m. Les données des trois premières unités de détection KM3NeT déployées (deux dans l'ARCA et une dans l'ORCA) ont été utilisées dans cette étude. À l'aide de simulations de Monte Carlo calibrées, les taux de coïncidence ont été corrigés pour tenir compte des variations d'efficacité de détection de chaque PMT. La mesure de cette relation intensité du flux en fonction de la profondeur est parfaitement compatible avec la prédiction d'un modèle du flux de muons avec une incertitude inférieure à 2 %, ce qui reflète la grande précision obtenue avec cette mesure. A partir de simulations détaillés, la *surface effective* d'un DOM par rapport au flux de muons atmosphériques sous l'eau a été calculée, ce qui a permis de calculer le flux de muons intégré sur tout l'angle solide (Figure 0.1).

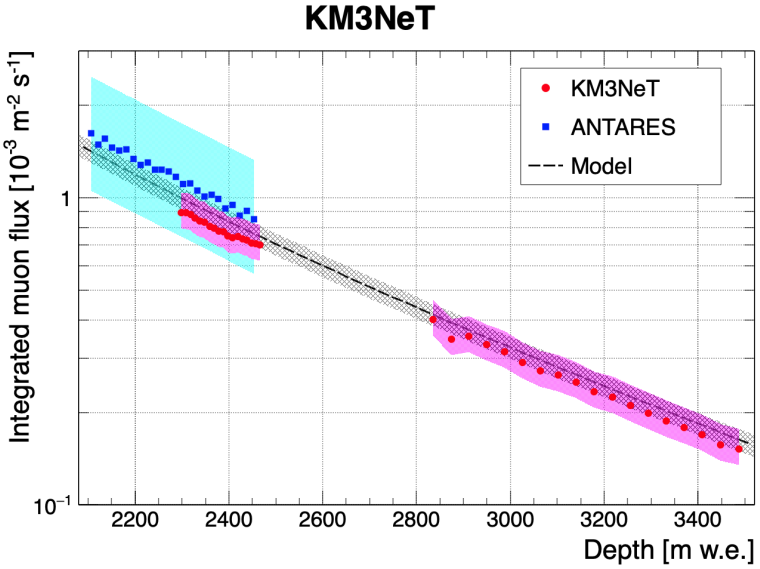

FIGURE 0.1 – Dépendance en profondeur du flux de muons mesuré avec les premières lignes de détection KM3NeT.

La partie principale de cette thèse est l'étude de la détection des neutrinos de supernova (galactique) à effondrement du cœur (CCSN) avec les détecteurs KM3NeT. Dans une CCSN, 99 % de l'énergie gravitationnelle est libérée sous la forme de neutrinos quasi-thermiques avec une énergie moyenne comprise entre 10 et 20 MeV. À ces énergies, les neutrinos interagissent par désintégration bêta inverse (plus de 90-95 %), par diffusion élastique sur les électrons (quelques pourcents) et par interactions quasi-élastiques avec les noyaux d'oxygène (moins d'un pourcent). Les leptons issus de ces interactions ne produisent que de petites traces d'une longueur moyenne de l'ordre de quelques centimètres, qui ne peuvent pas être reconstruites individuellement (souvent un seul DOM est touché). L'analyse repose donc sur la recherche d'une augmentation globale du taux de coïncidences sur l'ensemble du détecteur. Afin de s'affranchir des bruits de fond optiques induits par la bioluminescence et les désintégrations radioactives, une coupure avec une multiplicité élevée est utilisée. La contamination par les muons atmosphériques est au contraire réduite en exploitant la détection des coïncidences corrélées entre plusieurs modules optiques. Après le filtrage des bruits de fond, la sensibilité de détection est optimisée en comparant la distribution des taux de coïncidences en fonction de la multiplicité à une simulation de signal de la CCSN (Figure 0.2). Les flux de neutrinos des CCSN sont tirés de modèles 3D fournis par le groupe MPA Garching, avec des progéniteurs de 11, 27 et 40 masses solaires. La sélection optimale concerne la plage 7-11 en multiplicité. La sensibilité de détection, basée sur la recherche d'un signal pendant les 500 ms suivant le début de l'événement du CCSN, est indiquée sur la Figure 0.3.

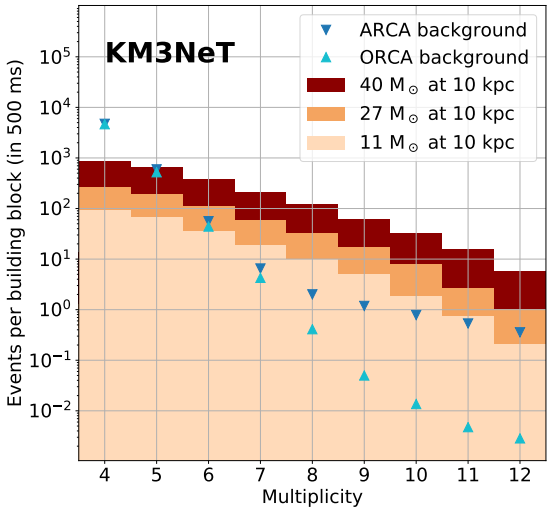

FIGURE 0.2 – Nombre attendu d'événements de fond pour un détecteur ARCA et ORCA de 115 lignes, comparé à la prédiction du signal CCSN pour les trois modèles de progéniteurs.

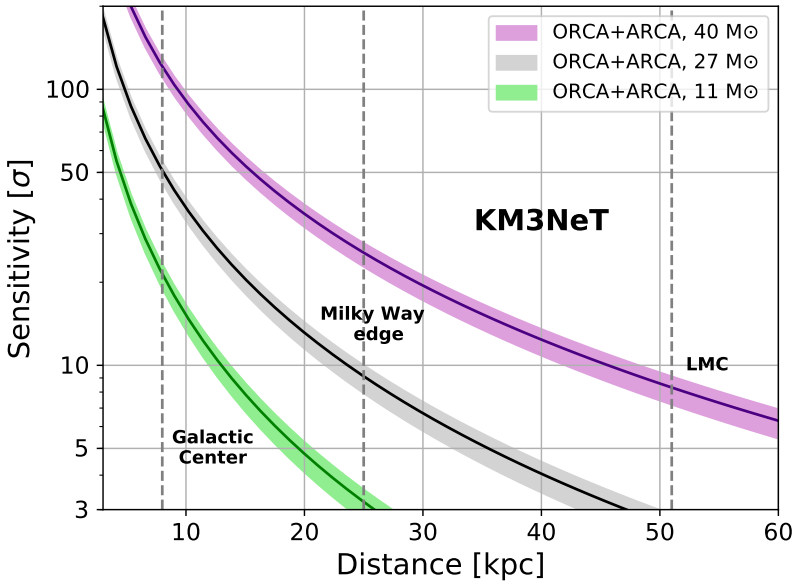

FIGURE 0.3 – Sensibilité de détection du KM3NeT CCSN en fonction de la distance de la source pour les trois modèles de progéniteurs.

Cette analyse basé sur l'algorithme de filtrage du fond et de sélection des événements a été implémentée dans la chaîne d'analyse en temps réel des deux détecteurs. Depuis début 2019, cette analyse de recherche de supernovae est opérationnelle sur les flux de données en ligne des détecteurs ORCA et ARCA. Une évaluation du nombre

d'événements dans la sélection est faite toutes les 100 ms avec une fenêtre de temps glissante sur les 500 ms précédentes. Ces résultats sont transmis à une application dédiée où les données des deux détecteurs sont combinées pour produire un trigger commun. Ce système est capable de traiter tous les scénarios possibles dans lesquels le flux de données d'un détecteur est légèrement retardé ou interrompu. Un dernier module est chargé de l'analyse des données de trigger et de la génération de messages d'alerte dès que le trigger surpasse un seuil prédéfini. Cette analyse est intégrée dans le système mondial d'alerte rapide pour la détection de supernovae avec des neutrinos *Supernova Neutrino Early Warning System* (SNEWS). SNEWS est un réseau auquel contribuent plusieurs détecteurs de neutrinos dans le but de diffuser des alertes supernovae à la communauté astronomique, permettant d'anticiper leur suivi optique. Fonctionnant actuellement comme un simple système d'alerte basé sur les coïncidences, le système SNEWS est en train d'être updaté, *SNEWS 2.0*, dans un cadre multi-messagers beaucoup plus riche avec la transmission d'alerte sous le seuil, un échange enrichi de données entre les expériences et un programme optimisé de suivi électromagnétique.

Durant le run O3 entre février 2019 et mars 2020, les collaborations LIGO-Virgo ont produit deux alertes pour la détection d'ondes gravitationnelles (OG) non modélisées (dont la première a ensuite été rétractée après une analyse plus poussée). Ces alertes pourraient être liées à une supernova de effondrement de cœur à proximité. Dans une fenêtre de quelques secondes autour du temps des OG, l'analyse supernova a été faite pour rechercher une éventuelle contrepartie. Comme aucun excès significatif de neutrino n'a été observé, des limites supérieures sur l'absence de signal ont pu être calculées. En comparant avec le signal prédit, celles-ci ont été traduites en limites sur la distance et l'énergie de la CCSN. Les résultats ont été rendus publics avec les deux premières circulaires publiées sur le GCN par la Collaboration KM3NeT.

Pour faire de l'astronomie avec des neutrinos de haute énergie, la précision de pointage du détecteur est un élément clef. Le pointage absolu d'un télescope à neutrinos sous-marin n'est pas trivial, car les positions absolues des éléments du détecteur sur le fond marin ne peuvent être déterminées qu'avec une précision limitée. Cela se traduit par une erreur sur l'orientation globale du réseau de lignes, et donc sur le pointage absolu des événements reconstruits. Un hydrophone installé sur chaque ancre permet de déterminer la position du pied des lignes de détection avec une méthode de *multi-latération* en exploitant un ensemble de balises autonomes placées à grande distance. La position absolue des lignes est donc évaluée indirectement, en se basant sur les positions des balises telles que mesurées avec un balise acoustique au moment du déploiement. L'excellente résolution angulaire (<0.1 degré) de la reconstruction des traces dans ARCA pose un défi pour atteindre une contrainte sur l'erreur systématique du pointage absolu inférieure à la résolution de la reconstruction. Dans cette thèse, une stratégie complémentaire d'étalonnage des détecteurs KM3NeT est proposée, avec deux objectifs. Le premier est de calibrer directement la position absolue de toutes les ancres avec une étude indépendante, en utilisant une balise à la surface de la mer dont la position est connue. Le second est de vérifier la calibration de la

position des ancres avec une technique de *beamforming*, où les signaux de tous les hydrophones sont combinés pour maximiser le gain dans la direction de la source, comme dans un réseau en phase. Ainsi, la position de la balise à la surface de la mer reconstruite est comparée à ses coordonnées mesurées avec un GPS différentiel de haute précision, pour estimer l'incertitude sur le pointage absolu du détecteur.

Mots clés : rayons cosmiques, astronomie multi-messager, astrophysique, neutrino, telescope a neutrino

Abstract

Since the discovery of the cosmic-ray radiation at the beginning of the 20th century, the hunt for their sources has been driving the research into the most energetic phenomena in the Universe. Astronomy has developed consequently, first with the exploration of the non-visible portion of the electromagnetic spectrum known as multi-wavelength astronomy. The perspective has been widened further by multi-messenger astronomy, with the notable discoveries of gravitational waves and of the astrophysical neutrino flux. Neutrinos, in particular, emerge as a formidable cosmic messenger. Being light, neutral and weakly-interacting particles, they can travel unperturbed over cosmic distances, overcoming the limits of electromagnetic radiation (absorption) and charged particles (deflection by magnetic fields). Their emission is also especially revealing of the astrophysical properties of the source. For cosmic-ray source candidates, high-energy neutrinos would be an unequivocal signature of occurring hadronic acceleration processes. Whereas IceCube and ANTARES have observed the astrophysical neutrino flux, its origin is not yet established. In the special case of core-collapse supernovae, low-energy neutrinos carry more than 99% of the star gravitational energy and are believed to drive the explosion mechanism. These are observable only for galactic or near-galactic events, and only one event, SN 1987A, has been recorded since the beginning of the neutrino era. This scenario calls for the design and construction of a new generation of neutrino telescopes. By instrumenting two deep-sea sites with digital optical modules, for a total of ~ 200 000 photomultiplier tubes, the KM3NeT ORCA and ARCA detectors will address the open questions on the neutrino mass ordering and the sources of astrophysical neutrinos, respectively. The analyses presented in this thesis exploit the KM3NeT design by analysing the coincidences detected by the 31 PMTs of each optical module. The first part of this work consists of a measurement of the atmospheric muon rate as a function of the sea depth in the depth range between 2200 and 3500 m, performed with the first three detection units across the two sites. The result is compatible with a state-of-the-art model of the underwater muon flux within the systematic uncertainties. The analysis has been instrumental to the validation of the detector time and efficiency calibration, and the development of the simulation procedures. The main subject of this thesis is the determination of the KM3NeT capability of detecting a galactic core-collapse supernova event resulting in a neutrino burst on the 10 MeV energy scale. The development of the background filtering and event selection strategy is described in detail. The discovery sensitivity is evaluated by comparison with a simulation of the signal expected from the neutrino flux, as predicted by advanced three-dimensional models of a supernova explosion. The implementation of the analysis algorithm in

an online trigger application is described, together with the first implementation of the real-time multi-messenger infrastructure for KM3NeT. The alert generation mechanism and its integration in the global SNEWS alert network are introduced. The first follow-up analyses of gravitational-wave alerts are reported. The last part of this work addresses the absolute pointing of the detector, which accuracy is important to the full exploitation of the sub-tenth of degree resolution of KM3NeT at high-energy. With the ORCA detector as a test-bed, a procedure exploiting acoustic multilateration and beamforming techniques is proposed to determine the absolute position of the detection units on the seafloor and subsequently verify the pointing accuracy of the telescope.

Keywords: multi-messenger astronomy, astroparticle physics, astrophysical neutrinos, core-collapse supernova neutrinos

Contents

Résumé 3

Abstract 10

Contents 12

List of Figures 16

List of Tables 19

1 Multi-messenger astronomy and astrophysical neutrinos 20
1.1 Cosmic rays . . . 21
1.1.1 Discovery and early history . . . 21
1.1.2 Modern era . . . 23
1.1.3 Direct detection . . . 26
1.1.4 Extensive air showers and the high-energy spectrum . . . 28
1.2 Origin and propagation of cosmic rays . . . 32
1.2.1 Acceleration of cosmic rays . . . 32
1.2.2 Hillas criterion . . . 35
1.2.3 Energy budget . . . 37
1.2.4 UHECR propagation . . . 37
1.3 The multi-messenger view . . . 38
1.3.1 The gamma-ray sky and the CR connection . . . 40
1.4 Galactic source candidates . . . 46
1.4.1 Supernova remnants . . . 46
1.4.2 Other galactic candidates . . . 47
1.5 Extragalactic source candidates . . . 48
1.5.1 Active Galactic Nuclei . . . 48
1.5.2 Gamma-ray Bursts . . . 53
1.5.3 Cosmic-ray reservoirs . . . 55
1.5.4 Other extragalactic candidates . . . 55
1.6 Neutrinos . . . 56
1.6.1 Neutrino interactions . . . 57
1.6.2 Neutrino oscillation . . . 58
1.6.3 Atmospheric neutrinos . . . 60
1.6.4 Astrophysical neutrinos . . . 61
1.7 Astrophysical neutrino detection and observation . . . 61

1.7.1 Cherenkov signatures of high-energy neutrinos . . . 62
1.7.2 Introduction to neutrino telescopes . . . 64
1.7.3 Background in the search for astrophysical neutrinos . . . 67
1.7.4 Astrophysical diffuse neutrino flux . . . 70
1.7.5 Point source searches . . . 75

2 The KM3NeT detector 77
2.1 General overview . . . 77
2.1.1 PMT signal digitisation and data transmission . . . 82
2.1.2 On-shore data acquisition system . . . 84
2.1.3 Optical data filtering and triggering . . . 86
2.2 Detector calibration . . . 89
2.2.1 Detection Unit and inter-DOM time calibration . . . 89
2.2.2 Intra-DOM PMT time and efficiency calibration . . . 90
2.2.3 Position calibration . . . 90
2.2.4 Atmospheric muons as calibration source . . . 93
2.3 Monte Carlo simulation . . . 94
2.3.1 Event generation . . . 95
2.3.2 Cherenkov light simulators . . . 97
2.3.3 Detector response simulation . . . 99
2.4 Event reconstruction . . . 100
2.4.1 Track reconstruction . . . 100
2.4.2 Shower reconstruction . . . 101
2.4.3 Reconstruction performance . . . 101
2.5 KM3NeT deployment history and current status . . . 104

3 Dependence of the atmospheric muon flux on seawater depth 105
3.1 Atmospheric muon flux underwater . . . 106
3.2 Characterisation of DOM coincidence rates . . . 109
3.3 KM3NeT ARCA2 and ORCA1 data sample . . . 111
3.4 Coincidence rates in ARCA2 and ORCA1 . . . 113
3.5 Depth dependence of the atmospheric muon flux . . . 117
3.6 Estimation of the DOM effective area . . . 120
3.7 Absolute measurement of the atmospheric muon flux . . . 123
3.8 Evaluation of systematic uncertainties . . . 124

4 Core-collapse supernova neutrino detection 126
4.1 Core-collapse supernovæ . . . 127
4.1.1 Introduction . . . 127
4.1.2 Core-collapse mechanism . . . 130
4.1.3 CCSN neutrino phenomenology . . . 132
4.1.4 SN 1987A . . . 133
4.1.5 Galactic and near-galactic CCSN rate and progenitors . . . 134
4.2 CCSN neutrino detection with KM3NeT . . . 136

4.2.1 Flux model . . . 137
4.2.2 Low energy neutrino interactions in water . . . 139
4.2.3 Simulation of CCSN neutrinos . . . 141
4.2.4 Effect of the photon detection efficiency . . . 142
4.3 Study of the background . . . 144
4.3.1 Data sample and Monte Carlo simulation . . . 145
4.3.2 Background coincidence rates . . . 146
4.3.3 Background filtering . . . 147
4.4 Sensitivity estimation . . . 154
4.4.1 Statistical definitions . . . 154
4.4.2 Multiplicity selection . . . 155
4.4.3 Systematic uncertainties . . . 158
4.4.4 Detector combination . . . 158
4.4.5 Sensitivity as a function of the distance . . . 160
4.4.6 KM3NeT model in SNOwGLoBES . . . 161
4.4.7 Comparison with other experiments . . . 163
4.5 Benchmarks of the analysis algorithm . . . 163
4.5.1 Filter robustness . . . 163
4.5.2 Bioluminescence impact on detector efficiency . . . 166
4.5.3 Implications and perspective . . . 168
4.6 Online supernova trigger . . . 168
4.6.1 Multi-messenger context . . . 168
4.6.2 Statistical treatment . . . 169
4.6.3 Technical implementation . . . 172
4.6.4 Low-level data buffering . . . 176
4.6.5 Graphical monitoring . . . 176
4.7 Follow up of gravitational wave alerts . . . 178
4.7.1 Analysis outline . . . 178
4.7.2 S191110af (retracted) . . . 179
4.7.3 S200114f . . . 181
4.7.4 Perspective for future follow-ups . . . 183
4.8 Supernova astronomy and astrophysics . . . 184
4.8.1 Flux spectral properties . . . 184
4.8.2 Standing accretion shock instability . . . 187
4.8.3 Timing and triangulation . . . 189
4.9 Conclusions and perspective . . . 191

5 Absolute pointing of the detector **194**
5.1 Beamforming principle . . . 195
5.2 Proof of concept . . . 196
5.2.1 Signal template . . . 196
5.2.2 Noise and signal simulation . . . 197
5.2.3 Footprint calibration . . . 198

5.2.4 Beamforming 199
5.2.5 Operational environment 199
5.2.6 Simulated measurement 200
5.3 Sea survey 202
5.3.1 Transmitter data 203
5.3.2 Hydrophone data 204
5.3.3 Transmitter - hydrophones correlation 208
5.4 Preliminary conclusions 209

Conclusion **211**

Bibliography **212**

List of Figures

1.1 V. Hess final balloon survey . . . 23
1.2 Spectrum of cosmic rays at the Earth . . . 24
1.3 Relative chemical abundance in cosmic rays . . . 25
1.4 Direct measurement of the flux of cosmic ray nuclei . . . 27
1.5 All-particle spectrum from air shower measurements . . . 30
1.6 2nd order Fermi accelertion . . . 33
1.7 1st order Fermi acceleration . . . 34
1.8 Particle flow in 1st order Fermi acceleration . . . 34
1.9 Hillas plot for cosmic ray source candidates . . . 36
1.10 Interaction length and energy loss distance for cosmic rays . . . 38
1.11 Astrophysical messengers in an artist's impression . . . 39
1.12 Astrophysical horizon for different messengers . . . 40
1.13 *Fermi*-LAT sky-map . . . 42
1.14 Gamma-ray image of SNR RX J1713.7-3946 . . . 44
1.15 SNR RX J1713.7-3946 multi-wavelength spectral energy distribution . . . 45
1.16 Schematic classification of AGN . . . 49
1.17 Illustration of an AGN jet structure . . . 50
1.18 Multi-wavelength SED for Markarian 501 . . . 51
1.19 SSC model fit to Mrk501 SED . . . 52
1.20 Markarian 421 multi-wavelength lightcurve . . . 53
1.21 Measured and predicted fluxes for natural and reactor neutrinos. . . . 56
1.22 Feynman diagrams for common neutrino interactions . . . 58
1.23 Neutrino and antineutrino cross sections . . . 58
1.24 Prompt and conventional atmospheric neutrino fluxes . . . 60
1.25 High-energy neutrino interactions . . . 62
1.26 Track-like and shower-like Cherenkov emission in water . . . 63
1.27 Event topologies . . . 64
1.28 Field of view of neutrino telescopes . . . 66
1.29 ANTARES measurement of the vertical muon flux . . . 68
1.30 ANTARES measurement of the atmospheric muons angular distributon 68
1.31 Angular distribution of atmospheric muon and neutrino fluxes . . . 69
1.32 IceCube measurement of the astrophysical neutrino flux . . . 71
1.33 IceCube diffuse flux: intensity and spectral index . . . 72
1.34 ANTARES measurement of the astrophysical neutrino flux . . . 73
1.35 IceCube diffuse flux flavour fit . . . 74
1.36 Multimessenger spectral energy distribution . . . 75

1.37 IceCube neutrino point-source search 76
1.38 ANTARES neutrino point-source search 76

2.1 Exploded view of a KM3NeT digital optical module 78
2.2 ARCA seafloor layout 81
2.3 ORCA seafloor layout 82
2.4 KM3NeT PMT wavelength-dependent quantum efficiency 83
2.5 KM3NeT PMT response 83
2.6 KM3NeT Trigger and Data Acquisition System 85
2.7 Processing of optical data 86
2.8 Logic of data manipulation in the data filter 88
2.9 Coincidence rate as a function of the PMT opening angle 91
2.10 Calibration principle with K40 92
2.11 Time of arrivals of beacon acoustic signals for a DOM 93
2.12 Calibration of detection unit time offsets with atmospheric muons . . 94
2.13 Overview of the KM3NeT Monte Carlo chain 95
2.14 Instrumented volume, can and interaction volume 96
2.15 Cherenkov PDF of the photon times of arrival 98
2.16 ARCA ν_μ reconstruction performance 102
2.17 ARCA ν_e reconstruction performance 102
2.18 ORCA reconstruction: angular resolution 103
2.19 ORCA reconstruction, energy resolution 103

3.1 Ground angular distribution of atmospheric muons 106
3.2 Muon energy loss in water as a function of the energy 107
3.3 Muon intensity as a function of depth in water 108
3.4 Side and bottom views of a KM3NeT DOM. 109
3.5 KM3NeT PPM-DU coincidence rate as a function of multiplicity 111
3.6 ARCA2 and ORCA1 deviation of photon detection efficiency vs time . . 113
3.7 Time difference distribution for all PMT pairs in a DOM 114
3.8 ARCA2 and ORCA1 coincidence rates as a function of the multiplicity . 115
3.9 Probability of the PMT contribution to coincidence rates vs multiplicity 116
3.10 ARCA2 and ORCA1 multiplicity ≥ 8 coincidence rates vs time 117
3.11 Multiplicity ≥ 8 coincidence rate of all DOMs as function of depth . . . 118
3.12 ARCA2 and ORCA1 efficiency-corrected ≥ 8 multiplicity coincidence rates 120
3.13 Simulated muon flux at the boundary of the generation volume 122
3.14 DOM effective area with respect to atmospheric muons 123
3.15 Measurement of the integrated atmospheric muon flux as a function of depth 124

4.1 Spectral classification of supernovæ 128
4.2 Supernova type vs initial mass and metallicity 130
4.3 Neutrino observation from SN 1987A 134
4.4 Distribution of expected galactic supernovæ 136

4.5 Neutrino fluence in the CCSN accretion phase . . . 138
4.6 Cross sections for CCSN neutrino interactions in water . . . 140
4.7 Energy and time-dependent CCSN neutrino interaction rates . . . 141
4.8 Efficiency scaling of the CCSN neutrino signal . . . 144
4.9 Background coincidence rate for the CCSN search . . . 146
4.10 CCSN signal and background events as a function of the multiplicity . . . 147
4.11 Coincidence correlation filter statistics . . . 149
4.12 Multiplicity versus distance of closest approach from muon events . . . 150
4.13 Distributions of the time range of triggered hits . . . 152
4.14 Rejection efficiency of the *triggered events veto* . . . 153
4.15 Rejection efficiency for sea data and simulations . . . 154
4.16 Signal and background events for the supernova search . . . 156
4.17 Horizon for CCSN 5σ discovery . . . 157
4.18 Significance combination with Stouffer and Fisher methods . . . 160
4.19 KM3NeT combined CCSN sensitivity . . . 162
4.20 Background distribution for the coincidence correlation filter . . . 165
4.21 Background distribution for the triggered events filter . . . 166
4.22 Instrumentation efficiency vs fraction of active PMTs . . . 167
4.23 CCSN online trigger horizon . . . 170
4.24 Overview of the online framework . . . 173
4.25 Supernova online monitoring . . . 177
4.26 S191110af follow up . . . 180
4.27 `S200114f` localisation by LIGO-Virgo . . . 181
4.28 S200114f follow up . . . 182
4.29 CCSN exclusion region for a typical follow-up . . . 184
4.30 Average energy and signal scale contours . . . 186
4.31 CCSN fitted mean energy error distribution . . . 186
4.32 Neutrino light-curve and power spectrum . . . 187
4.33 Background CDF for the SASI search . . . 188
4.34 Fit of the arrival time of the CCSN neutrino burst . . . 190
4.35 Light-curve triangulation performance . . . 192

5.1 Grating lobes in a beamforming pattern . . . 197
5.2 Reference and simulated signals with cross-correlation . . . 201
5.3 Result of beamforming procedure . . . 202
5.4 GG9 and transducer . . . 203
5.5 Sea survey: GG9 vessel navigation . . . 204
5.6 Sea survey: transducer position vs time . . . 204
5.7 Raw acoustic data processing . . . 206
5.8 Quality distribution of detected chirps . . . 207
5.9 Acoustic event progression . . . 208
5.10 Verification of speed of sound . . . 209

List of Tables

2.1 KM3NeT ARCA and ORCA geometrical properties 79

4.1 CCSN signal events vs multiplicity 143
4.2 CCSN effective mass vs multiplicity 143
4.3 Rejection efficiency for the coincidence correlation filter 149
4.4 Rejection efficiency for triggered events filter 153
4.5 Systematic uncertainties on the CCSN sensitivity 159
4.6 Expectation values for the number of CCSN signal and background events 161
4.7 SNOwGLoBES estimate of the number of detected events in different detectors 164
4.8 S191110af follow up 180
4.9 S200114f follow up 182
4.10 Sensitivity results with ORCA + ARCA for the three different stellar progenitors considered. 189

1 Multi-messenger astronomy and astrophysical neutrinos

Multi-messenger astronomy encompasses the study of different classes of astronomical objects and astrophysical phenomena through the detection of different *messengers*. In human history, the observation and the study of the Sky are as ancient as the first forms of written language. The work of Nicolaus Copernicus on the heliocentric model (1543) is considered as the birth of modern astronomy. Originally focused on observation of visible light, the discipline has significantly evolved through the 19th and 20th centuries to include other parts of the electromagnetic spectrum. Observations spanning across radio waves, infrared, ultraviolet, X and γ radiations contribute to what has taken the name of *multi-wavelength* astronomy. The 20th century has witnessed as well the birth of non-electromagnetic observations. Cosmic rays were discovered in the 1910s, sparking fundamental and still partially unsolved questions about their origin. Neutrinos from an extraterrestrial source have been first observed from a supernova explosion in 1987. In the early 2010s, the discovery of the diffuse high-energy astrophysical neutrino flux by the IceCube experiment opened the quest for the identification of high-energy neutrino sources in the Sky. Finally, in 2015, the first of a series of gravitational wave events were observed by the LIGO and Virgo observatories, providing strong confirmation for General Relativity and opening an entirely new scenario in modern astronomy.

Sommaire

1.1 Cosmic rays . . . 21
1.1.1 Discovery and early history . . . 21
1.1.2 Modern era . . . 23
1.1.3 Direct detection . . . 26
1.1.4 Extensive air showers and the high-energy spectrum . . . 28
1.2 Origin and propagation of cosmic rays . . . 32
1.2.1 Acceleration of cosmic rays . . . 32
1.2.1.1 Fermi 2nd order acceleration . . . 32
1.2.1.2 Stochastic diffuse shock acceleration, Fermi 1st order . . . 33
1.2.1.3 Magnetic reconnection . . . 35
1.2.1.4 Characteristic times . . . 35
1.2.2 Hillas criterion . . . 35

1.2.3 Energy budget . . . 37
1.2.4 UHECR propagation . . . 37
1.3 The multi-messenger view . . . 38
1.3.1 The gamma-ray sky and the CR connection . . . 40
1.3.1.1 Modeling a γ-ray source: RX J1713.7-3946 . . . 43
1.4 Galactic source candidates . . . 46
1.4.1 Supernova remnants . . . 46
1.4.2 Other galactic candidates . . . 47
1.5 Extragalactic source candidates . . . 48
1.5.1 Active Galactic Nuclei . . . 48
1.5.1.1 AGN classification . . . 49
1.5.1.2 Jet structure and models . . . 49
1.5.1.3 SED and time variability . . . 50
1.5.1.4 Non-blazar AGN sources . . . 53
1.5.2 Gamma-ray Bursts . . . 53
1.5.3 Cosmic-ray reservoirs . . . 55
1.5.4 Other extragalactic candidates . . . 55
1.6 Neutrinos . . . 56
1.6.1 Neutrino interactions . . . 57
1.6.2 Neutrino oscillation . . . 58
1.6.3 Atmospheric neutrinos . . . 60
1.6.4 Astrophysical neutrinos . . . 61
1.7 Astrophysical neutrino detection and observation . . . 61
1.7.1 Cherenkov signatures of high-energy neutrinos . . . 62
1.7.2 Introduction to neutrino telescopes . . . 64
1.7.3 Background in the search for astrophysical neutrinos . . . 67
1.7.4 Astrophysical diffuse neutrino flux . . . 70
1.7.5 Point source searches . . . 75

1.1 Cosmic rays

1.1.1 Discovery and early history

The first attempts to identify the origin of natural radioactivity were conducted at the beginning of the 20th century. Electroscopes were used to probe ionisation rates in a variety of experimental surveys. Among a few suggestive anomalies, the first results obtained near to the ground level seemed consistent with the hypothesis that radiation originated in the Earth crust. This idea was favoured by strong *a priori* considerations at the time, and indications of the opposite were not very well received by the community. Italian physicist Domenico Pacini first challenged this view, finding compatible rates of radiation across sites on the ground and the sea surface. He was also the first to perform an underwater survey. Measurements conducted at few

metres of depth in the Gulf of Genova and the lake of Bracciano proved evidence for attenuation of the radioactive rates compared to the sea surface. Disfavouring the sea bed and the water as the main sources of the detected radioactivity, there was the first hint for its extraterrestrial origin. Alfred Gockel followed with high-altitude balloon-based measurements, disproving the previously assumed decrease of ionisation levels with height over the ground. It took an extensive series of accurate surveys by Victor Hess starting from the year 1911 to finally characterise the profile of radiation levels as a function of altitude (see Figure 1.1). Hess found that ionisation first decreased to a minimum, and then started to increase with height [1]. This finding marked the discovery of an extraterrestrial source of radiation, today universally known as *cosmic rays* (CR). Hess excluded the Sun as the primary source and measured a different absorption coefficient for CRs than for γ-rays. In the 1920s, the identification of the flux dependence on the geomagnetic latitude and the development of the Geiger-Muller counter allowed to confirm that cosmic rays are charged particles. Far before the rise of the accelerator era, cosmic rays opened the door to particle physics. Cloud chambers allowed the discovery of positrons, muons, and charged pions. In 1936, Prof. V. Hess and Dr C. D. Anderson were awarded the Nobel Prize in Physics for the discovery of cosmic rays and the positron, respectively. A brief historical review can be found in Reference [2].

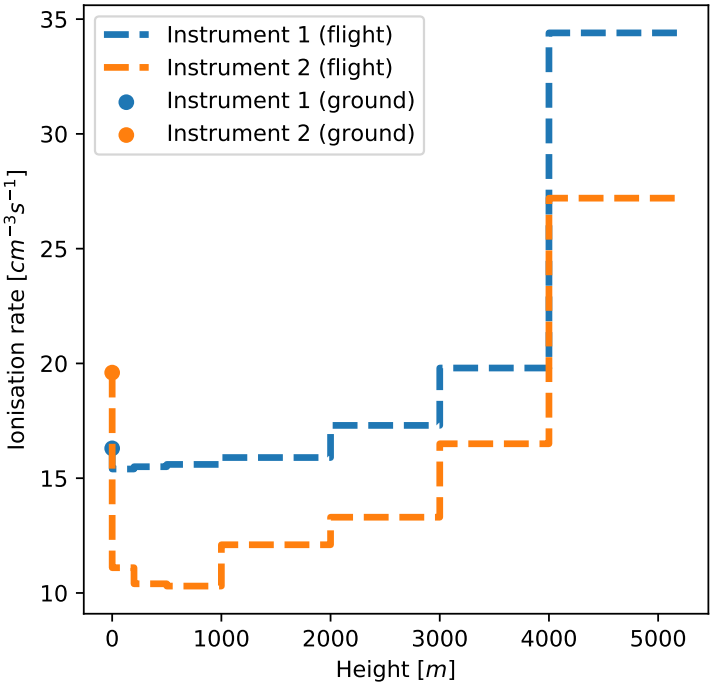

Figure 1.1 – Ionisation rate as a function of height above ground measured in the final balloon survey conducted by Victor Hess on 5 August 1912 [1].

1.1.2 Modern era

Today, the cosmic ray (CR) flux is known to consist of different particles, with a composition dominated by protons and helium nuclei. The origin of cosmic rays is attributed to galactic and extragalactic astrophysical sources, where charged particles are confined and accelerated by their inner magnetic fields. After escaping their source, CRs propagate in the intergalactic and interstellar media where they are deflected by large scale magnetic fields. A synthetic overview of experimental data on cosmic ray physics can be found in Chapter 29 of the "Review of Particle Physics" [3]. Their interpretation is discussed in several sources, among which Reference [4] and [5]. A general view of the CR energy spectrum, highlighting its main components, is given in Figure 1.2. With the first determinations of the flux composition, it was observed that the relative abundance of chemical elements in cosmic rays is slightly different from the one of the solar system and meteoritic matter. This is shown in Figure 1.3, reporting a historical plot by Shapiro and Silberberg [6]. This observation is explained by the production of *secondary* cosmic rays in the interactions of the *primaries*, produced at the source, with the particles of the interstellar gas. The primary CR composition include electrons, protons and the common stable products of stellar nucleosynthesis

(He, C, O, Fe). Light secondary nuclei (Li, Be, B), that are thought to be normally destroyed in stellar interiors, can be produced by spallation of protons and light nuclei with particles of the interstellar medium (C, N and O) [7]. Radiative pair-production is responsible for the antimatter component, mainly consisting of positrons and antiprotons.

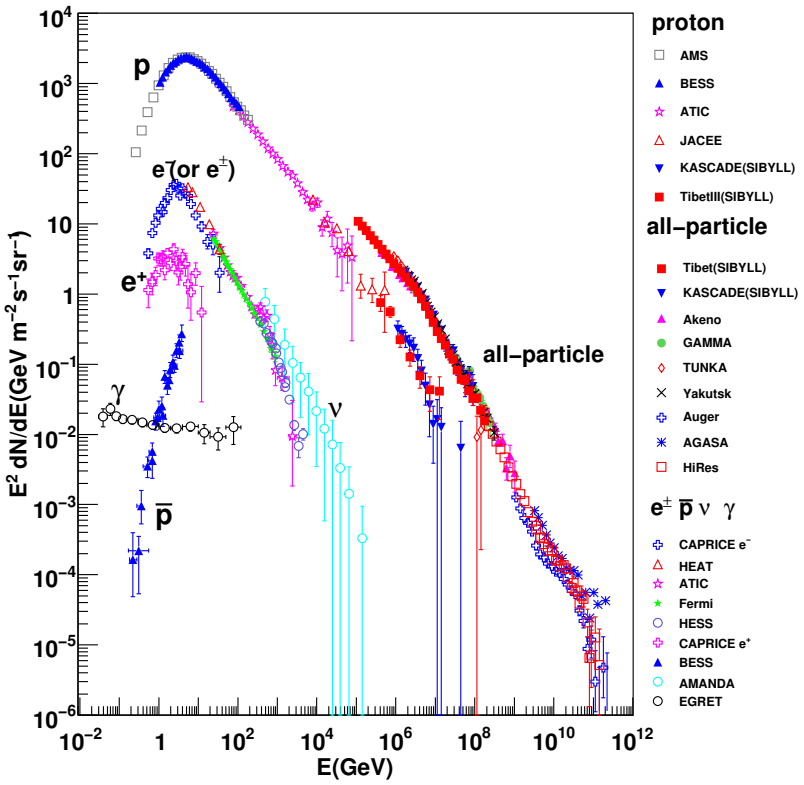

Figure 1.2 – Spectrum of cosmic rays at the Earth. Proton spectrum and all-particle spectrum as measured by different experiments. The subdominant contributions from electrons, positrons and antiprotons are shown as measured by the PAMELA experiment. The atmospheric neutrino and diffuse gamma-ray background are also reported. Source: [8].

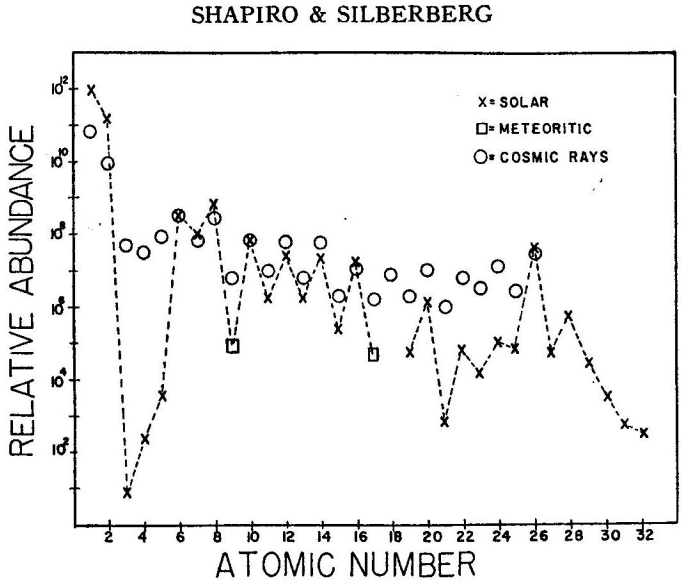

Figure 1.3 – Comparison of the relative abundances of the elements in the cosmic radiation at the top of the Earth's atmosphere, and in the solar photosphere (except for the meteoritic values for F and Cl). Solar data are normalized to hydrogen (10^{12}); cosmic ray data are normalized so that the abundances of carbon coincides with that of Solar carbon. Source: [6].

The CR energy spectrum spans from $\sim 10\,\mathrm{MeV}$ to $100\,\mathrm{EeV}$, with a flux intensity decaying as a power law ($E^{-\gamma}$, $\gamma \approx 2.7$). The measured intensity goes from $\sim 10^4\,\mathrm{m^{-1}s^{-2}}$ at 1 GeV to few particles per $\mathrm{m^2}$ per year at $10^{15}\,\mathrm{eV}$. At the Earth, the low energy part of the spectrum is absorbed in the atmosphere. It can be probed with *direct detection* in high-altitude balloon-borne or satellite-based experiments. Around 100 TeV the potential for direct observation ends as the flux becomes too small compared to the typical size of the detectors. Contextually, *indirect detection* becomes possible as the CR interaction in the upper atmosphere produces particle cascades known as *air showers* that can be detected at the ground level.

It is useful to remind that the gyroradius (or *Larmor radius*), r_g, for a particle with charge Ze moving in a magnetic field B is given by:

$$r_g = \frac{p}{ZeB}\,. \tag{1.1}$$

More in general, the dynamics of an ultra-relativistic charged particle in a magnetic field depends on its *rigidity*, R, defined as the ratio between its velocity and charge:

$$R = r_g B\,c = \frac{pc}{Ze}\,. \tag{1.2}$$

As covered in Reference [5], the relative abundance of secondary cosmic rays with respect to primaries can be exploited to estimate the (energy-dependent) characteris-

tic time scale of diffusion, t_{esc}, (or *escape time*) from the Galaxy. The estimation of a $t_{esc} \sim 10^7$ yr much larger than the size of the Galaxy expressed in light-years ($\sim 10^3$ ly) suggests that charged particles are confined by magnetic fields in the interstellar medium, and diffuse at a slow rate to the extragalactic space. For light and abundant primary elements, the number of accelerated nuclei per unit of volume and time, $Q(E)$, can be expressed as:

$$Q(E) = \frac{4\pi}{c} \frac{\phi(E)}{t_{esc}} \tag{1.3}$$

where $\phi(E) \propto E^{-\alpha}$ is the spectrum of the CR flux as measured at the Earth. Given the observed energy-dependence for the diffusion time scale, $t_{esc} \propto E^{-\delta}$, the spectrum of the cosmic ray sources can be inferred as $Q(E) \propto E^{-(\alpha-\delta)}$. The value of δ predicts the energy scale at which flux anisotropies should arise as ct_{esc} decreases to approach the galactic size.

1.1.3 Direct detection

Direct measurements of the cosmic-ray spectrum and composition have been carried out with high-altitude balloon and satellite instruments in the Earth orbit. Important contributions in this field came from the ACE [9], PAMELA [10], AMS [11] and CREAM [12] experiments. The measured fluxes of primary nuclei at the Earth are reported in Figure 1.4. The galactic CR spectrum in the local interstellar medium outside of the heliosphere was probed by the *Cosmic Ray Subsystem* of the Voyager 1 and Voyager 2 spacecraft [13, 14].

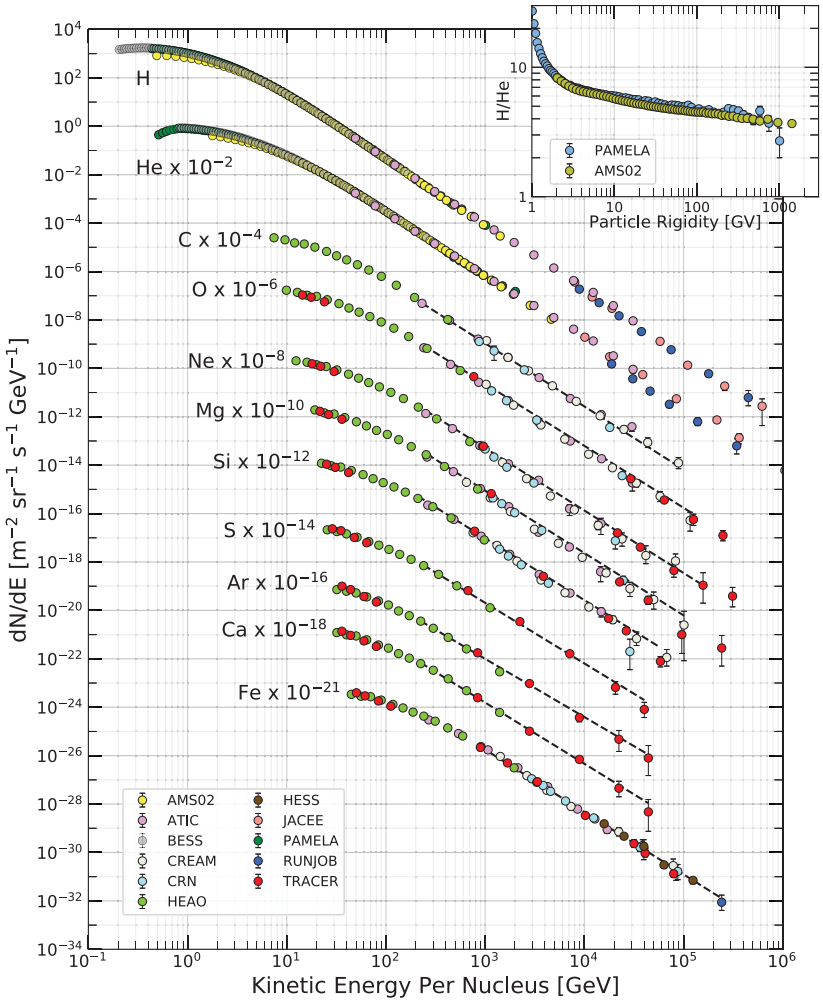

Figure 1.4 – Fluxes of nuclei of the primary cosmic radiation in *particles per energy-per-nucleus* as a function of *energy-per-nucleus*. The inset shows the H/He ratio as a function of the particle rigidity. Source: [3].

In the 1 GeV – 100 TeV energy range, the spectrum of nucleons as a function of the energy-per-nucleon (E) can be described by the formula:

$$I_N(E) \approx 1{,}8 \cdot 10^4 \left(\frac{E}{\mathrm{GeV}}\right)^{-\alpha} \mathrm{m^{-2}\,s^{-1}\,sr^{-1}\,GeV^{-1}} \tag{1.4}$$

where $\alpha \approx 2.7$ is the differential spectral index. The t_{esc} energy-dependence estimated by the ratio between secondaries and primaries gives a value of $\delta \approx 0.6$, suggesting a source spectrum $\propto E^{-2.1}$, compatible with existing acceleration models (see further Section 1.2.1). For galactic cosmic rays, this would imply anisotropies growing from $\sim$ 1% to 10% between 20 TeV and 1 PeV, a much higher magnitude with respect to experimental observations by IceCube and TIBET [15] (for a more detailed discussion, refer to Section 9.3.7 of Reference [4]). This makes an cogent case for probing the t_{esc}

behaviour in the energy region beyond the domain of direct detection, where however detailed composition measurements are not easily achievable.

Weak magnetic fields can significantly deviate low energy cosmic rays on local scales. Down at the GeV scale, time and position-dependent modulations are produced by the geomagnetic field. Up to 10 GeV, cosmic rays are deflected by the magnetic fields in solar winds. An eleven-year modulation is observed in the flux intensity in anticorrelation with the solar cycle. This can be further verified by comparing the spectra measured by ACE and AMS with the Voyager measurements in the local interstellar medium [16].

1.1.4 Extensive air showers and the high-energy spectrum

As cosmic rays above 100 TeV enter the atmosphere, they interact with air molecules to produce large particle cascades named *extensive air showers* (EAS). In this context, the original interacting particle and the cascade products are referred to as *primary* and *secondaries* respectively. The study of air showers started at the end of the 1930s with the work of P. Auger and B. Rossi [17]. In an air shower, the collision of a CR primary particle with an air nucleon produces charged and neutral mesons (π and K) by hadronic interaction. Charged mesons undergo further interactions with nuclei, developing a hadronic cascade at the core of the air shower. The prompt decay of neutral mesons in pairs of gamma photons gives origin to electromagnetic sub-showers. In turn, charged mesons decay producing atmospheric muons and neutrinos.

The following description of the air shower physics is based on Reference [18]. The development of each cascade (hadronic or electromagnetic) in the air shower can be described as a sequence of steps in which a population of *parent* particles interact to produce a new *generation*, with a higher number of particles and lower mean energy. At each step of the hadronic cascade, 1/3 of the energy goes to neutral pions and is transferred to the electromagnetic component of the EAS. The scale of cascades is conveniently represented in terms of *interaction depth*, namely the integral of the atmospheric density over a given path length expressed in $\mathrm{g\,cm^{-2}}$. The longitudinal development of an individual cascade in terms of the number of particles can be parameterised by the Gaisser-Hillas formula [19]:

$$N(x) = N_{max}\left(\frac{x}{w}\right)^{w} e^{w-x};\; w \equiv \frac{X_{max}-X_0}{\lambda},\; x \equiv \frac{X-X_0}{\lambda} \tag{1.5}$$

where X_0 is the depth of the primary interaction, X_{max} the depth of the maximum development of the shower, N_{max} the number of particles at the maximum and λ the interaction scale length in units of depth. In this, N_{max} scales roughly with the energy of the primary as $E/(1{,}5\,\mathrm{GeV})$. The number of muons (N_μ) is related to the total energy left in the air shower when the average energy of the charged pions falls below their *critical energy*, namely the point at which the decay probability equals the interaction probability. In a good approximation, an air shower induced by the interaction of a nucleus with mass number and energy (A, E) can be described as a *superposition* of

A air showers where the primary is a proton with energy EA^{-1}. The distributions of X_{max} and N_μ can therefore be used to infer the chemical composition of the primary particle flux. As an example, with respect to protons, ^{56}Fe-induced showers reach the maximum development at a depth $\sim 100\,\mathrm{g\,cm^{-2}}$ shallower, while producing $\sim 30\%$ more muons [18]. This provides a mean to probe the composition at EAS detectors, although with a much larger uncertainty compared to direct measurement. At best, the only the relative fractions of protons and nuclei can be determined.

By observation of the electromagnetic and hadronic components of extensive air showers, ground-based experiments are measuring the high-energy part of the CR spectrum ($E > 100\,\mathrm{TeV}$). The most common design for an EAS observatory is a large scale array combining atmospheric *fluorescence detectors* and *surface detectors* for particles. The instrumentation of a wide area is necessary to probe the tiny flux intensity at the highest energies. Fluorescence detectors consist of focusing mirrors and photomultiplier-based cameras. They detect the air fluorescence induced by the ionising action of electromagnetic cascades. In parallel, surface detectors measure the flux of charged particles reaching the ground in coincidence, employing scintillation or water Cherenkov techniques. Notable experiments in this field are Tibet-ASγ [20] and KASCADE [21] covering up to the PeV scale; Fly's Eye [22] (upgraded to HiRes [23]), Telescope Array [24] and the Pierre Auger Observatory [25] reaching the EeV scale and beyond. The all-particle energy spectrum measured through air showers is shown in Figure 1.5. The measured energies of cosmic-ray induced air showers extend far beyond the maximum energy produced in particle accelerators. The precise energy estimation of the primary therefore relies on the extrapolation of hadronic models calibrated at lower energies. For comparison, the maximum centre-of-mass energy reached at the Large Hadron Collider (LHC) [26], 14 TeV, is equivalent to the case of a 10^{17} eV proton colliding with a nucleon at rest.

The cosmic-ray spectrum exhibits two steepening regions (*knee* and *second knee*) at $10^{15} - 10^{16}$ eV and 10^{17} eV and a hardening plateau around $10^{18{,}5}$ eV (*ankle*). The integrated flux intensity is $\sim 1\,\mathrm{yr^{-1}\,m^{-2}}$ at the first knee and $\sim 1\,\mathrm{yr^{-1}\,km^{-2}}$ at the ankle. Cosmic rays beyond 1 EeV are referred to as *Ultra high-energy Cosmic Rays* (UHECR). The isotropy of the flux above 10^{19} eV suggests a dominant extragalactic origin since at these energies the gyroradius for charged particles exceeds the galactic size. The interpretation of the spectral region between the (first) knee and the ankle is related to the transition from galactic to extragalactic sources.

As discussed in Reference [5], one explanation for a knee-like steepening of the spectrum is the *Peters cycle* [27]. As a consequence of the rigidity-dependent kinematics of charged particles (see Equation (1.2) and (1.1)), nuclei with higher electric charge are accelerated to higher energies. At the accelerating limit of galactic sources, the progressive energy cutoff as a function of the nucleus atomic number would appear as a steepening combined with a stepped change in the flux composition. A transition over the most common nuclei, from hydrogen to iron, allows for a factor 26 in energy. However, the spectrum beyond the first knee extends smoothly over two orders of magnitude, requiring more complicate models (injection of heavier elements, the

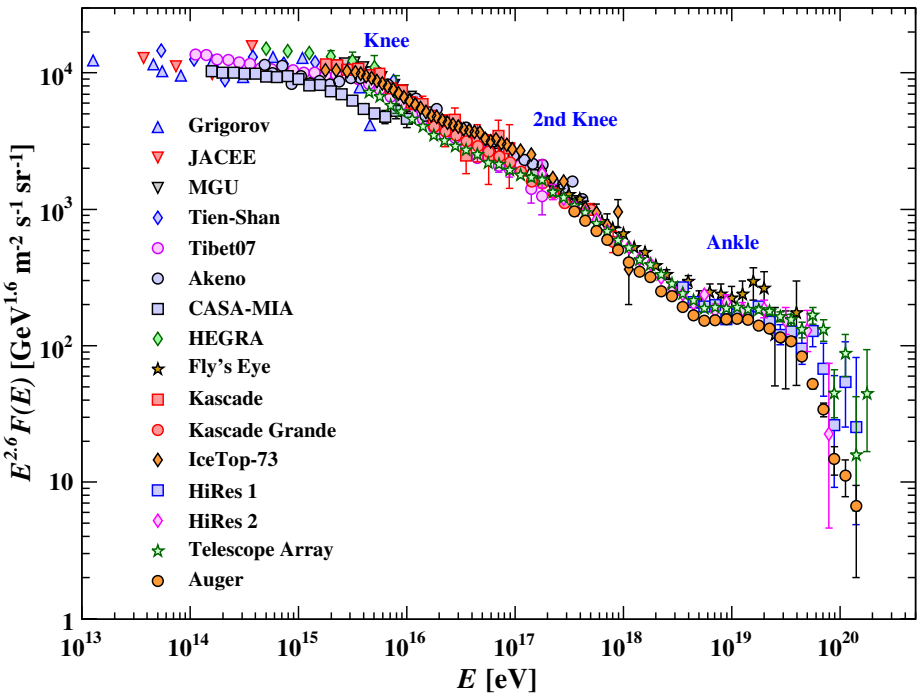

Figure 1.5 – All-particle spectrum as a function of *energy-per-nucleus* from air shower measurements. Source: [3].

existence of different populations of sources, etc.). An alternative explanation for the knee would be a sharper decay with the energy of the escape time t_{esc} occurring above a certain critical rigidity. If this was the case, a smooth transition to heavier elements in the flux composition would be expected.

In the traditional interpretation, the transition to extragalactic cosmic rays occurs at the ankle, where the hardening can be intuitively explained as a different population of sources blending with the galactic component. More recently, it has been proposed that the galactic to extragalactic transition could occur at energies as low as $5 \cdot 10^{17}$ eV, in correspondence with the second knee. This is suggested by HiRes measurements that indicate a change in composition from heavy to light elements at this scale. The hypothesis is especially attractive as it naturally explains the ankle as part of a spectral *dip* due to pair-production radiative processes of protons interacting with the Cosmic Microwave Background (CMB). This interpretation is exhaustively covered in Reference [28] and [29]. It implies a quite softer $E^{-\beta}$, $\beta = 2.7$ source spectrum for extragalactic protons, requiring a different acceleration model compared to galactic cosmic rays. It has been argued [30, 31], however, that this model is viable only assuming a pure proton spectrum for extragalactic sources or at least a fairly large proton fraction (85%) in the case of mixed composition. For a higher fraction of nuclei, the interpretation of the transition at the ankle is recovered and both galactic and extragalactic components are best fitted with a source spectral index $\beta = 2.2 - 2.3$.

The suppression of the spectrum beyond the 10^{19} eV point is debated [32]. Its interpretation depends, again, on the determination of the flux composition. The propagation of protons above this energy scale is suppressed by the *Greisen-Zatsepin-Kuz'min (GZK) effect* [33, 34]. As a consequence of the relativistic Doppler effect, resonant production of Δ barions is expected from scattering with the photons of the Cosmic Microwave Background (CMB). In the rest frame of a particle travelling with a Lorentz factor Γ, photons with a mean energy ϵ_γ will appear as having an energy $E_\gamma = \epsilon\Gamma(1+\cos\theta)$, with θ being the angle between the particle and the photon. For the measured temperature of the CMB $T = 2{,}725\,\mathrm{K}$, $\epsilon_\gamma = 6{,}4 \cdot 10^{-4}$ eV. The $E_\gamma = 150\,\mathrm{MeV}$ resonance threshold then corresponds to a Lorentz factor $\Gamma = 1{,}17 \cdot 10^{11}$, reached by protons at $5 \cdot 10^{19}$ eV. The production and decay chain of the Δ^+ barion can be visualised as follows:

$$\gamma + p \rightarrow \Delta^+ \rightarrow \begin{cases} p + \pi^0\,;\, \pi^0 \rightarrow \gamma\gamma \\ n + \pi^+\,; \quad \begin{array}{l} n \rightarrow p + e + \nu_e \\ \pi^+ \rightarrow \mu^+ + \nu_\mu\,;\, \mu^+\overline{\nu}_\mu + \rightarrow e^+ + \nu_e \end{array} \end{cases} . \tag{1.6}$$

The extremely energetic outgoing neutrinos are referred to as *cosmogenic* and their search constitute a specific field of study. As the proton loses on average $\sim 20\%$ of his energy in such a collision, the characteristic scattering length of the process limits the maximum travelling distance to $\sim 70 - 200\,\mathrm{Mpc}$ depending on the energy of the primary. This defines the so-called *GZK volume*. If extragalactic cosmic rays are protons, sources above $\sim 5 \cdot 10^{19}$ eV would have to be within this radius. This would

have strong implications on the source abundance (as a limited volume needs to satisfy the power budget requirement) and result in observable anisotropies. The most recent data from the Pierre Auger Observatory suggest, on the other hand, a mixed composition scenario at UHE, with an important contribution from heavy nuclei. In analogy with the knee interpretation, the UHE suppression would be due to *source exhaustion*, as the highest accelerating limit is reached.

The determination of the flux composition, anisotropy and possibly the observation of sources in UHE region and beyond will be crucial to disentangle the galactic and extragalactic contributions in the highest energy region. This will b the goal of the new generation of EAS experiments as the upgrade of the Pierre Auger Observatory, *AugerPrime* [35], and the spacecraft-based atmospheric fluorescence detector JEM-EUSO [36].

1.2 Origin and propagation of cosmic rays

Despite the prominence of the cosmic-ray flux, its origin is a central mystery unsolved in astrophysics. Intra- and extra-galactic magnetic fields deviate the trajectory of charged particles, preventing direct localisation of the sources by their incoming directions. To reach the observed energies, a CR source must be able to accelerate charged particles through non-thermal processes.

1.2.1 Acceleration of cosmic rays

In this section, an overview of the cosmic rays acceleration mechanism is given. In particular, the Fermi 2nd and 1st order acceleration mechanisms are summarised following Reference [37]. Magnetic reconnection is briefly introduced after.

1.2.1.1 Fermi 2nd order acceleration

Fermi originally proposed a model [38, 39] where particles gain momentum by repeated scattering with moving plasma clouds powered by supernova explosions. These propagate in the interstellar medium with random velocities in the order of $\sim 15\,\mathrm{km\,s^{-1}}$. In this model and its further development illustrated in the next section, cosmic rays are treated in the *test particle* approximation, where the bulk motion of the cloud is not perturbed by the accelerated particle(s).

The Fermi model is illustrated in Figure 1.6.

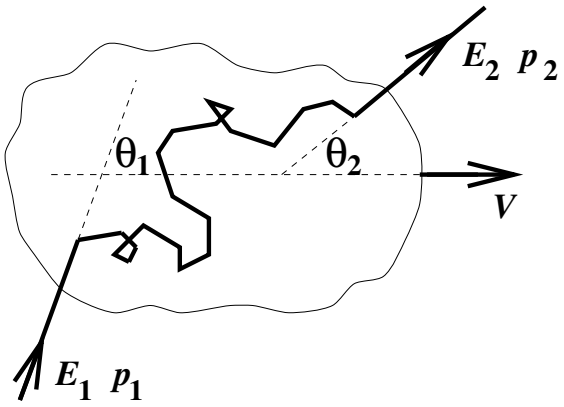

Figure 1.6 – Fermi acceleration as in the original proposed mechamism (today known as 2nd order). Source: [37].

The energy gain $\langle E_2 - E_1 \rangle$ can be derived by intuitive kinematic considerations. In the reference frame of the cloud (for which the *primed* notation is here adopted) the particle energy is conserved as it undergoes collisionless scattering off magnetic fields ($E'_1 = E'_2$). The outgoing direction is randomised in the repeated scatterings ($\langle \cos\theta'_2 \rangle$). In the reference frame of the observer, head-on collisions are slighly privileged due to the motion of the cloud ($\langle \cos\theta_1 \rangle = -\beta/3$). By equating the (Lorentz transformed) boundary conditions in the reference frame of the observer, the energy gain is shown to have a second-order dependence on the cloud velocity $\beta = V/c$:

$$\frac{\langle \Delta E \rangle}{E} \simeq \frac{4}{3}\beta^2 . \tag{1.7}$$

While very intuitive, this mechanism is not ideal as for the typical values of $\beta \lesssim 10^{-4}$ results in a very inefficient acceleration. In fact, due to the random distribution of the cloud velocities, the frequency of *surpassing* collisions slowing down the particle is almost as high as the frequency of *head-on* collisions in which the particle is accelerated.

1.2.1.2 Stochastic diffuse shock acceleration, Fermi 1st order

To solve the problem of the inefficient acceleration, Fermi's original idea was further developed in the 1970s into the *stochastic diffuse shock acceleration* or *Fermi 1st order acceleration*. The principle is illustrated in Figure 1.7. The case is here exemplified for a supernova explosion, but the model applies to different kinds of strong astrophysical shocks. In the shock acceleration scenario, ejecta of matter are moving at a speed, $V_p \sim 10^4\,\mathrm{km\,s^{-1}}$, much higher than the speed of sound in the ISM ($\sim 10\,\mathrm{km\,s^{-1}}$). In correspondence, a strong shock wave is produced and propagates radially from the source at a speed $V_s \simeq 4/3 V_p$.

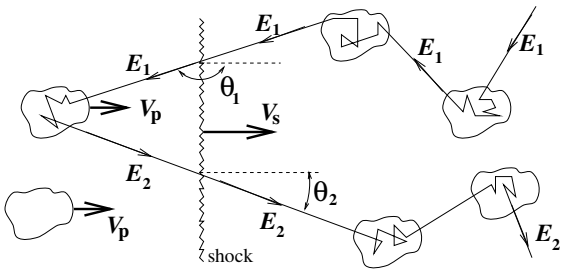

Figure 1.7 – 1st order Fermi acceleration. Source: [37].

The ISM and its associated magnetic fields accumulate on the wavefront. The magnetic irregularities on the two sides of the shock can be seen as clouds of the original Fermi model. For a particle entering the shock $\langle \cos\theta_1 \rangle = -2/3$ and for the opposite, in the reference frame of the shock, $\langle \cos\theta_2' \rangle = 2/3$. Developing the kinematics, it can be shown that this results in a net energy gain:

$$\frac{\langle \Delta E \rangle}{E} \simeq \frac{4}{3}\beta_p \simeq \beta_s \,. \tag{1.8}$$

The more efficient first-order dependence can be intuitively explained by considering that a particle moving with the plasma will see the plasma on the other side of the shock as approaching at V_p, with a strong preference for head-on collisions.

Once defined the acceleration model, it should be verified that the resulting energy spectrum is compatible with experimental observations. The probability of repeated crossing of the shock is evaluated by comparing the net flow of particles crossing the shock upstream (R_{cross}) with the downstream loss rate from the shock (R_{loss}) as seen in Figure 1.8.

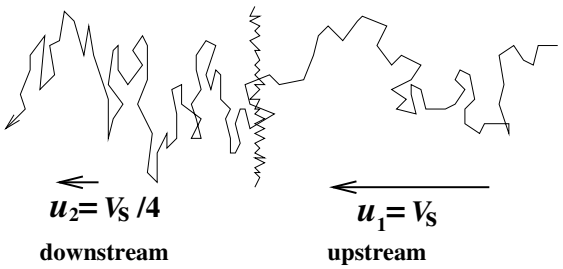

Figure 1.8 – Flow of particles across the propagating shock. Source: [37].

The probability of crossing the shock once and escaping $P_e = R_{loss}/R_{cross}$ is shown to be equal to V_S/v, with v the particle velocity. The corresponding probability of crossing the shock at least k times is $P_r^k = (1-P_e)^k$. Considering an initial number of particles N_0 there will be $N_k = N_0 P_r^k$ particles that went through k shock crossings, reaching an energy of $E = E_0\left(1+E^{-1}\Delta E\right)^k$. At last a power law energy spectrum is

obtained as:

$$\frac{N}{N_0} = \left(\frac{E}{E_0}\right)^{\frac{\ln P_r}{\ln\left(1+\frac{\Delta E}{E}\right)}} \approx \left(\frac{E}{E_0}\right)^{-1} \rightarrow \frac{dN}{dE} \approx E^{-2}. \tag{1.9}$$

1.2.1.3 Magnetic reconnection

Magnetic reconnection occurs when different sections of a magnetised plasma collide releasing large amounts of energy from the recombination of their magnetic fields. While usually associated with the dynamics of the solar corona, magnetic reconnection has been recently proposed [40] as production mechanism for high-energy multi-messenger emissions (microquasars and more in general black-hole powered sources). The principle is especially intriguing to explain flaring sources that exhibit fast time variations and require the acceleration to occur within compact regions. An up-to-date review of the role of magnetic reconnection in astrophysical sources is given in Reference [41].

1.2.1.4 Characteristic times

For a stochastic acceleration process, it is useful to define some characteristic time scales [42]. The *acceleration time*:

$$t_{acc} : \frac{dE}{dt} = \frac{E}{t_{acc}} \tag{1.10}$$

defines the rate at which the particle gains energy. Comparing t_{acc} with the escape time t_{esc} as introduced in Section 1.1.2, the spectral index of a source with spectrum proportional to $E^{-\gamma}$ can be expressed as $\gamma = 1 + t_{acc}/t_{esc}$, where $t_{acc} \sim t_{esc}$ is required to observe a value of $\gamma \simeq 2$. The picture is complicated by the fact that in general both t_{acc} and t_{esc} depend on the energy. A characteristic time, t_{loss}, exist for the each energy loss process affecting cosmic-ray particles in the source (synchrotron radiation, propagation losses). In some cases, the age of the source, t_{age}, can also be used to constrain its energy spectrum, that will naturally have an upper limit for $t_{acc} \sim t_{age}$.

1.2.2 Hillas criterion

A cosmic ray source must be able to confine the charged particles as they are accelerated to the observed energies. In this regard, the *Hillas criterion* [42, 43] can be used to estimate the maximum energy reachable by a cosmic acceleration process. Given R_S the characteristic size of the source, the confining requirement for the gyroradius, $r_g \leq R_S$, allows to define the maximum energy reachable in the acceleration process, E_{max}:

$$E_{max} = \Gamma Z e B R_S \tag{1.11}$$

where the Lorentz factor Γ accounts for the relativistic bulk motion of the accelerating region. As already introduced in Section 1.1.4, E_{max} is proportional to the atomic

number Z of the accelerated nucleus, with a factor of 26 between iron and protons. It is interesting to observe that for a fixed E_{max} a variety of sources can exist with different reciprocal values of B and R_S. An up-do-date classification of sources in the (B, R_S) plane is illustrated by the *Hillas plot* shown in Figure 1.9.

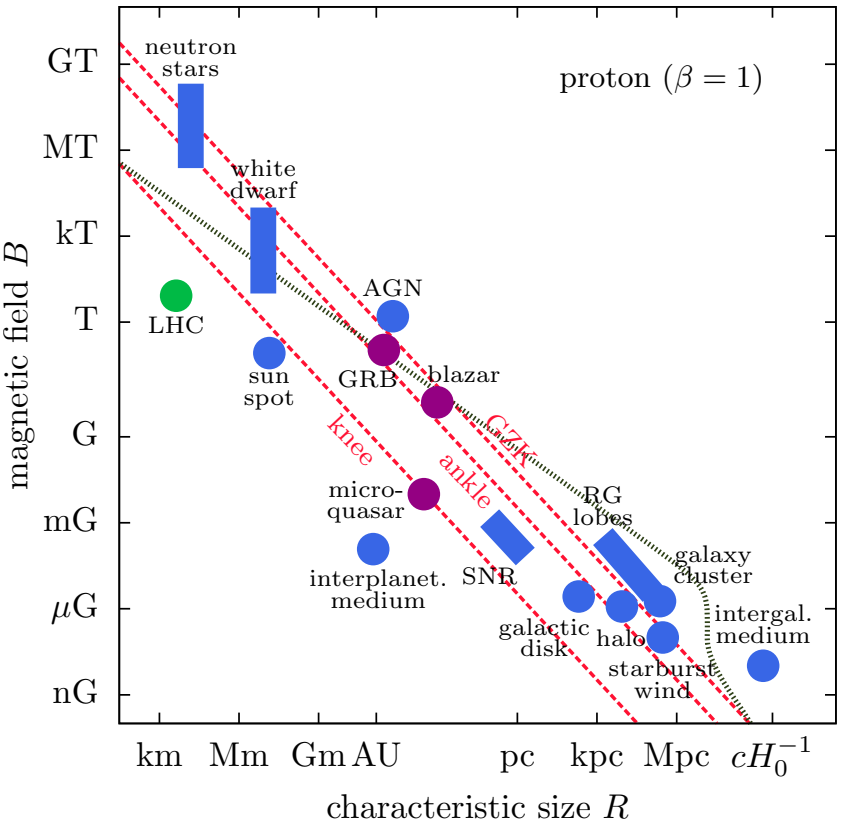

Figure 1.9 – *Hillas plot* with upper limits on the reachable CR proton energy dependent on the size of the accelerating region and magnetic field strength. Steady and variable source are shown in blue and violet respectively. For comparison, the LHC machine is indicated in green. Red lines indicate the upper limits due to the loss of confinement in the acceleration region for CRs at the *knee*, *ankle*, and the *GZK cutoff* regions. The dotted grey line corresponds to a second upper limit that arises from synchrotron losses in the sources and interactions in the cosmic photon background. Source: [44].

The plot allows for a first skimming of cosmic ray source candidates. As noted in the original Reference [42], other constraints on energy come from energy losses in the source (e.g. synchrotron radiation) and during the CR propagation. In general, a source model needs to ensure the compatibility between the characteristic times t_{acc}, t_{esc} and t_{loss} with the observed spectrum and composition of the CR flux. Supernova remnants (SNR) and microquasars are among the best candidates for galactic sources.

Diffuse CR production in the galactic disk and halo are also possible. Extragalactic candidates include active galactic nuclei (AGN), γ-ray bursts (GRB), galaxy clusters and starburst galaxies.

1.2.3 Energy budget

The density of the sources needs to provide the energy budget necessary to power the observed cosmic ray flux at the galactic and extragalactic scale [45]. The energy density of Galactic cosmic rays is $\rho_g^{CR} = 10^{-12}\,\mathrm{erg\,cm^{-3}}$. Given the Galactic volume $V \approx 10^{67}\,\mathrm{cm}^3$ and the diffusion time for galactic cosmic rays $t_{esc} \approx 10^7\,\mathrm{yr}$ the equivalent power is $L = \rho_{CR}\,V\,t_{esc}^{-1} \approx 10^{41}\,\mathrm{erg\,s^{-1}}$. This equals to $\sim 10\%$ of the energy released by supernovae when assuming 10^{51} erg per event at a frequency of one every $20-50$ years. Similarly, the density of cosmic rays for extragalactic sources $\rho_{eg}^{CR} = 3\cdot 10^{-19}\,\mathrm{erg\,cm^{-3}}$ indicates a required power budget of $2\cdot 10^{44}\,\mathrm{erg\,s^{-1}}$ for active galaxies and $3\cdot 10^{52}\,\mathrm{erg\,s^{-1}}$ for gamma-ray bursts, after normalisation to their relative abundance. While the orders of magnitude are compatible with the electromagnetic emission by these sources, the attribution is still uncertain.

1.2.4 UHECR propagation

The propagation of cosmic rays is affected by different processes. This is especially crucial to tying the observed experimental features with the source population(s). The effect of magnetic fields on the CR propagation has been introduced in the Chapter for different phenomena (confinement, acceleration, diffusion). For UHECR, it is interesting to note that deflection from galactic and extragalactic magnetic fields plays a role in determining potential anisotropies in the observed flux. UHECRs are also subject to energy losses in propagation in the extragalactic space. Below the GZK threshold, scattering with the CMB radiation results in pion photoproduction and Bethe-Heitler e^+/e^- pair production [46, 37]. For protons and nuclei, the mean interaction distance for the two photoproduction processes $x_{p\gamma}$ can be calculated considering the photon number density and the respective cross sections. The characteristic energy loss distance is then defined as:

$$\frac{E}{dE/dX} = \frac{x_{p\gamma}(E)}{\kappa(E)} \tag{1.12}$$

where $\kappa(E)$ is the inelasticity of the interaction. Nuclei can be also fragmented either by *photodisintegration* against the CMB photons or in pion photoproduction. For iron, the latter dominates above $3\cdot 10^{12}\,\mathrm{GeV}$. The characteristic distance for the photodisintegration process is defined in analogy as $A/(dA/dx)$ for a given atomic mass number A. In Figure 1.10 the mean interaction distance and the energy loss distance are shown as a function of the energy for protons and iron nuclei, together with the characteristic photodisintegration distance for iron.

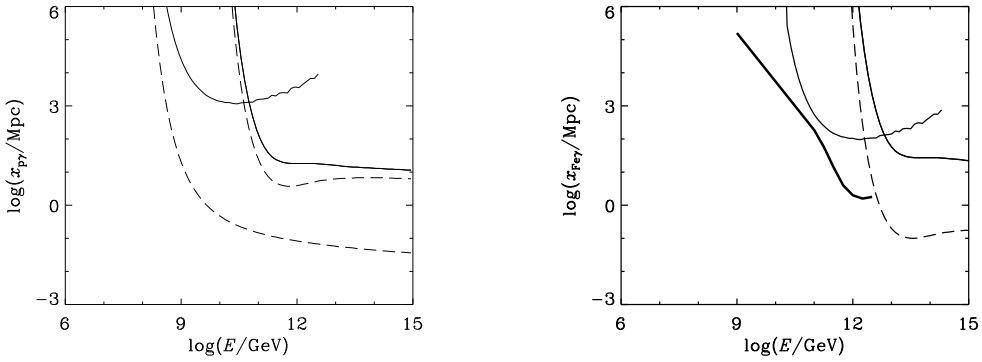

Figure 1.10 – Mean interaction length (dashed lines) and energy-loss distance (solid lines), E/(dE/dx), for processes involving protons (left panel) and iron nuclei (right panel). When both present, lower and higher energy curves represent pair production and pion production respectively. On the right, only the energy loss distance is shown for pair production and the thick solid curve represents the photodisintegration distance. Source: [37].

1.3 The multi-messenger view

In the last two decades, *multi-messenger astronomy* has made dramatic steps forward thanks to the contribution of γ-ray, gravitational wave and neutrino detectors. As cosmic rays are the product of hadronic acceleration, the identification of their sources can rely on other signatures of hadronic interaction.

Deep inelastic hadronic collisions in a cosmic-ray source should result in abundant production of neutral and charged pions, which in turn decay producing two important messengers: γ-rays and neutrinos respectively. The candidate processes connecting cosmic-ray acceleration with neutrino and γ emission are *proto-hadronic* / *hadro-nuclear* collisions:

$$p + p/N \rightarrow \begin{cases} X + \pi^0 \,;\, \pi^0 \rightarrow \gamma\gamma \\ X + \pi^+ \,;\, \pi^+ \rightarrow \mu^+ + \nu_\mu \,;\, \mu^+ \rightarrow \overline{\nu}_\mu + e^+ + \nu_e \\ X + \pi^- \,;\, \pi^- \rightarrow \mu^- + \nu_\mu \,;\, \mu^- \rightarrow \nu_\mu + e^- + \overline{\nu}_e \end{cases} \quad ; \tag{1.13}$$

where X is a generic baryonic state, and *photo-hadronic* resonant production of baryons, dominated by the process:

$$p + \gamma \rightarrow \Delta^+(1232) \rightarrow \begin{cases} p + \pi^0 \,;\, \pi^0 \rightarrow \gamma\gamma \\ n + \pi^+ \,;\, \pi^+ \rightarrow \mu^+ + \nu_\mu \,;\, \mu^+ \rightarrow \overline{\nu}_\mu + e^+ + \nu_e \end{cases} \quad ; \tag{1.14}$$

although higher resonances with nucleon/Δ intermediate states are possible [47].

In 2015, the LIGO and Virgo interferometers have opened the era of gravitational-

wave astronomy with the first detections of compact binary mergers. The coalescence of two compact astrophysical objects, as in the case of two black holes, two neutron stars, or a black hole and a neutron star, is an established generation mechanism for gravitational waves as predicted by General Relativity. When at least a neutron star is involved, the coalescence process can produce relativistic jets of matter where efficient particle acceleration occurs.

The privilege of a multi-messenger approach derives from the different properties of each cosmic messenger [48], as illustrated in Figure 1.11.

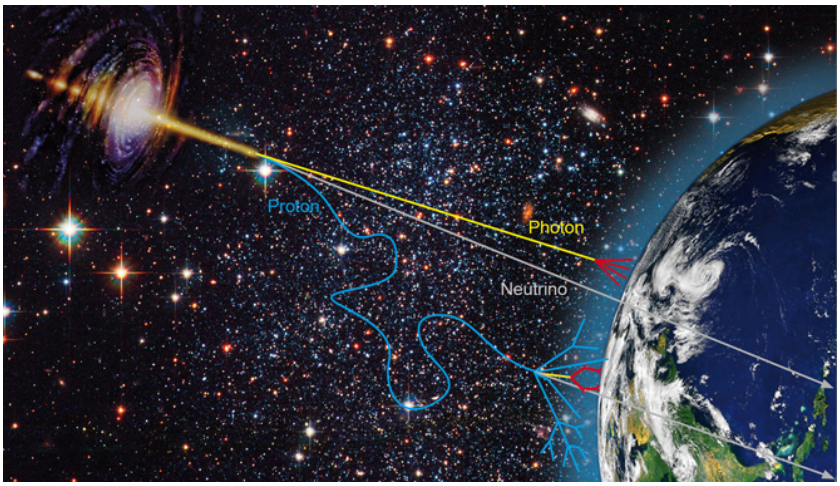

Figure 1.11 – Artist's impression of different astrophysical messengers reaching the Earth from a cosmic-ray source. Credit: DESY, astro.desy.de/theory/multi_messenger_astrophysics/index_eng.html

Cosmic-ray particles are largely deflected by magnetic fields, making it hard to pinpoint their source. Anisotropies reflecting the source distribution can arise only at the highest energies, where the observation potential is reduced by the tiny flux and a horizon limited by the interactions with the CMB. High-energy photons as γ-rays are also probes for non-thermal processes and they travel undeflected, but they are also subject to absorption as they travel over large distances. On the other hand, the Universe is transparent to gravitational waves and neutrinos. The observational horizons for the different astrophysical messengers are compared in Figure 1.12.

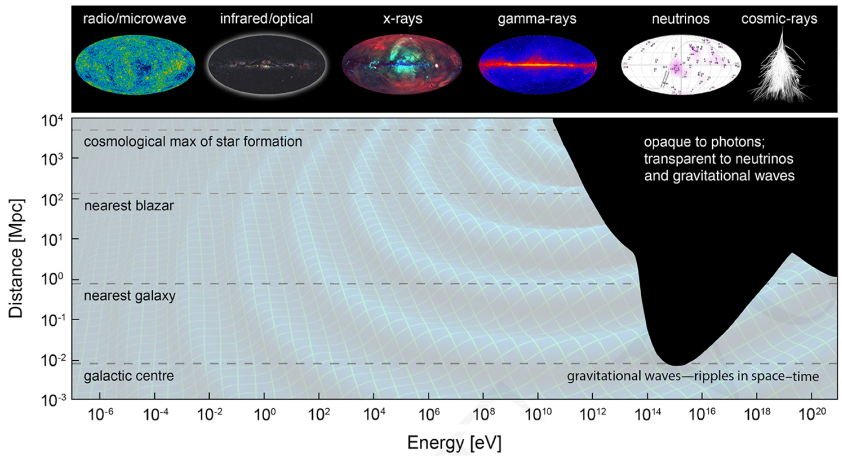

Figure 1.12 – Distance horizon at which the Universe becomes optically thick to electromagnetic radiation. Lower energy photons can reach the Earth from very far sources, while the highest energy photons and cosmic rays are attenuated. The Universe is transparent to gravitational waves and neutrinos at all energies. Source: [48].

The discovery of the diffuse astrophysical neutrino flux by the *IceCube Neutrino Observatory* [44] (see Section 1.6.4) is a landmark for multi-messenger astronomy. Despite some suggestive associations with transient events, the magnitude of the observed flux cannot yet be explained in terms of the known populations of candidate sources.

1.3.1 The gamma-ray sky and the CR connection

Compared to neutrinos, γ-rays are easier to detect, and γ-ray astronomy is nowadays a well-developed field of study. Low-energy γ-rays (up to some hundreds of GeV) are observed with satellite-based experiments, the most prolific to date being the *Fermi Gamma-ray Space Telescope* (often referenced as *Fermi*, formerly GLAST) [49]. The high-energy part of the spectrum is explored with ground-based *imaging atmospheric Cherenkov telescopes* (IACT), that reconstruct the Cherenkov emission from the electromagnetic showers induced by the interaction of the γ photons in the atmosphere. Notable IACTs are the VERITAS [50], MAGIC [51] and H.E.S.S. [52] experiments. As of today, the community effort is focused on building the next-generation *Cherenkov Telescope Array* (CTA) [53] that will consist of two sites on the opposite Earth hemispheres. They will be instrumented with differently-sized telescopes, providing a wide sky coverage, high sensitivity over an extended energy range, and fast transient follow-up capabilities. The study of high-energy γ-rays is also performed with surface Cherenkov detectors similar but denser compared to the ones employed in EAS arrays. In practice, there are overlaps between the two categories. Notable experiments that adopt this design are *Milagro* [54], HAWC [55] and LHAASO [56].

Compared to atmospheric Cherenkov telescopes, ground-based detectors can profit from the continuous coverage of a wide field-of-view (> 1,5 sr).

Contrary to neutrinos, γ-rays are not unequivocal signatures of hadronic interactions. High-energy photons can also be produced in purely leptonic processes. Multi-wavelength astronomy allows studying the electromagnetic (EM) emission of astrophysical objects from the radio to the high-energy γ-ray portion of the spectrum. The typical characterisation of an astrophysical source is given by its electromagnetic *spectral energy distribution* (SED), representing the energy density as a function of the photon energy. Typical SEDs for different classes of astrophysical objects follow a common *double bump* shape with a first peak located between the optical and X-ray domain and a second peak in the high-energy γ-ray section of the spectrum. In the common interpretation, the first bump is attributed to synchrotron radiation emitted by accelerated electrons in the source. The high-energy emission of the second bump can be explained as having an either leptonic or hadronic origin. For hadronic models, high-energy photons come from the usual $\pi^0 \rightarrow \gamma\gamma$ described in Equation (1.13) and (1.14). In the leptonic scenario, the photons of the radiation field of the source are boosted to higher energies in *inverse Compton scattering* (IC) with a population of relativistic electrons having Lorentz factors $\Gamma \sim 100 - 1000$. Different spectral features can result, depending on the properties of the radiation fields at the source (CMB, infrared, optical photons) and the spectral index of the injected relativistic electrons.

Cosmic rays interacting with the particle and radiation fields of the interstellar medium (ISM) are at the origin of the *Diffuse Galactic γ-ray Emission* (DGE). The *Fermi*-LAT instrument has conducted the most sensitive survey of the DGE to date, in the energy range going from 30 MeV to several hundreds of GeV [57]. Figure 1.13 shows an image of the γ-ray sky based on 60 months of *Fermi*-LAT data.

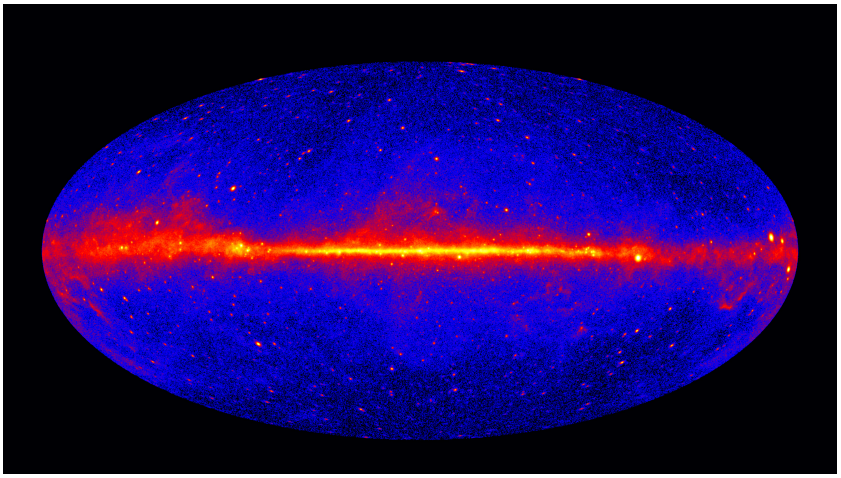

Figure 1.13 – *Fermi*-LAT 60-month image, constructed from front-converting γ-rays with energies above 1 GeV. The most prominent feature is the bright band of diffuse glow along the map's center, in correspondence of the Galactic Plane. Credits: NASA / DOE / *Fermi*-LAT, svs.gsfc.nasa.gov/11342.

The diffuse production of γ-rays is attributed to pion photoproduction followed by $\pi^0 \to \gamma\gamma$ decay, as discussed in Section 1.2.4. Experimental observations by *Milagro* [58] have revealed a TeV excess in the diffuse emission from the Galactic Plane, that could be the signature of a population of undiscovered point sources [59]. Diffuse TeV emission has been also observed at the ridge of Galactic Centre by *H.E.S.S.* [60]. The detection of $\mathcal{O}(10\,\text{TeV})$ γ-rays is considered an indication of the presence of PeV-accelerated protons [61, 62], that would be instrumental to explain the observation of galactic cosmic-rays at such energies. The observation of the diffuse astrophysical neutrino flux allowed to further constrain the CR diffusion in the galaxy and the global γ-ray picture. From this, alternative models as the KRA-γ [63] have been proposed to fit the diffuse γ-ray and neutrino observations assuming a radial dependence of the CR transport properties in the Galaxy.

One of the most interesting discoveries of *Fermi*-LAT is the observation of the *Fermi bubbles* [64], two large (40°-wide) γ-ray structures extending 50 degrees above and below the Galactic Center. The bubbles are spatially correlated with a hard-spectrum microwave excess known as *WMAP haze* [65]. Different explanations have been proposed for the origin of the Fermi bubbles, such as past accretion events into the central massive black hole or a nuclear starburst. A multi-year observational study of the bubbles has been performed by *Fermi*-LAT [66]. The γ-ray spectrum of the data can be fitted both by leptonic inverse Compton (IC) and hadronic models. The IC scenario could also explain the observed microwave signature, as a synchrotron product of the same population of electrons. The debate on the origin of the Fermi bubbles is still open and demands new multi-messenger surveys [67].

Different γ-ray catalogues have been compiled from observational data of γ-ray

point sources. The 4FGL [68] catalog of *Fermi*-LAT comprises the results of eight years of data in the 50 MeV – 1 TeV range, for a total of 5064 sources above a significance of 4σ. Seventy-five sources have been modelled as spatially extended. The majority of identified sources consists of 3130 blazars, followed by 234 pulsars, whereas 1336 sources do not have a plausible identification. The sources in the very-high-energy (VHE) part of the spectrum, mostly observed by ground-based IACTs, are collected in the TeVCat [1] online catalog [69]. TeVCat. At the time of writing, the catalogue aggregates data from about 230 sources, dominated by blazars, pulsar wind nebulae and supernova remnants, whereas 59 sources remain unidentified. A subset of 39 sources in TeVCat comes from the HAWC 2HWC catalog [70]. Of these, 19 are unassociated to previous observations in the TeV γ region, the remaining associated consist of 2 blazars (Markarian 421 and 501), 10 between PWNe and SNR, and 8 unidentified. The detection of VHE γ-rays without counterpart in the lower-energy electromagnetic bands is intriguing as it challenges common models for cosmic particle acceleration [71].

1.3.1.1 Modeling a γ-ray source: RX J1713.7-3946

As an exemplary case for the modelling of a γ-ray source, SNR RX J1713.7−3946 has been the subject of a multi-wavelength campaign across the radio, keV X-ray and TeV γ-ray spectra. A combined X/γ-ray image of the object is shown in Figure 1.14. Its multi-wavelength spectral energy distribution is illustrated in Figure 1.15 where leptonic and hadronic emission models are compared, as discussed in Reference [72].

1. http://tevcat.uchicago.edu/

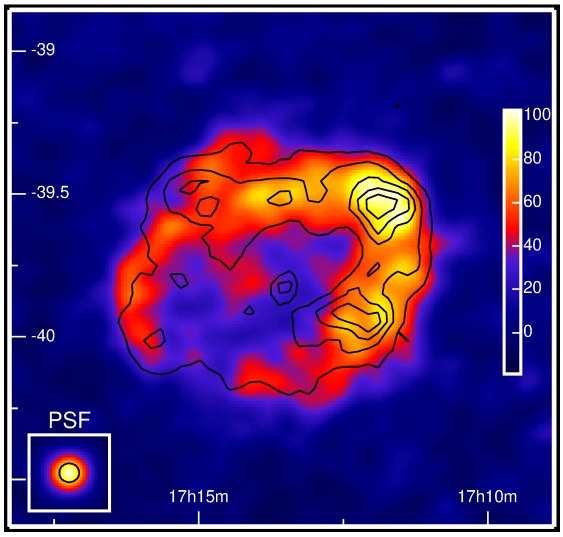

Figure 1.14 – Image of SNR RX J1713.7-3946 composed with high 2004-2005 energy gamma-ray data from the H.E.S.S. telescope. The linear colour scale is in units of excess counts per smoothing radius (0,1′). Contours from 1 – 3 keV X-ray observation from the ASCA satellite are drawn as black lines. Source: [73].

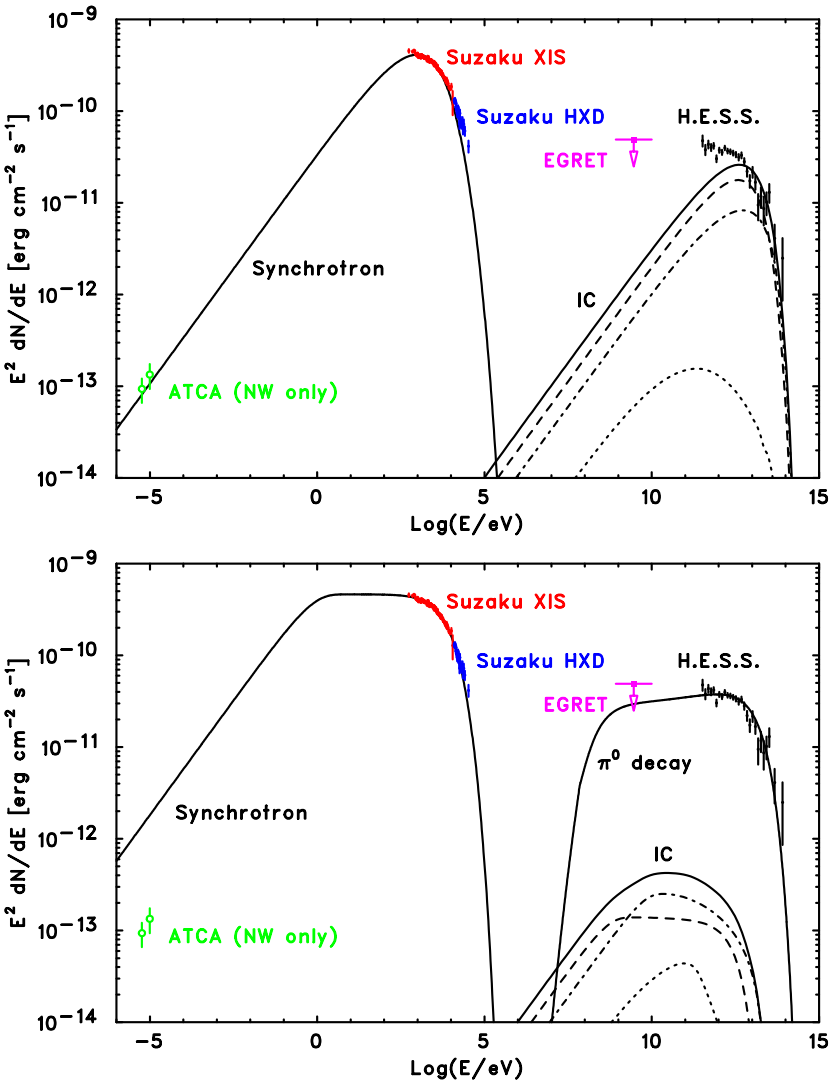

Figure 1.15 – Multi-wavelength spectral energy distribution (SED) measured for SNR RX J1713.7−3946 from the radio to TeV γ-rays. Top: purely leptonic model including synchrotron radiation and inverse compton (IC) scattering with electron injection index of 2.0 and a magnetic field of 14 µG. Bottom: hadronic model with 200 µG magnetic field, injection index of electrons and protons 2.0, constant injection during 1000 yr. In both panels, dashed, dash-dotted and dotted lines are for IC of CMB, infrared and optical photons respectively. Source: [72].

The disagreement between the leptonic model prediction and the low-end of the H.E.S.S. data can be interpreted as a hadronic pion-decay contribution coupled to a stronger magnetic field. However, different leptonic models could still fit the data provided the inclusion of an additional population of either optical photons or relativistic electrons. The most recent and detailed study of SNR RX J1713.7−3946 by

H.E.S.S. Reference [74] points to a two-component γ-ray spectrum that cannot be easily explained by standard diffusive shock acceleration models. The final interpretation of multi-wavelength data is not yet conclusive on the leptonic or hadronic origin. Settling the case will require γ observations with higher energy coverage and angular resolution (as enabled by CTA) or neutrino detectors achieving high sensitivity in the very-high-energy part of the spectrum.

1.4 Galactic source candidates

As introduced in Section 1.1.4, cosmic rays up to around the second knee of the spectrum (Figure 1.5) are believed to be of Galactic origin. Supernova remnants are the most prominent candidate sources for galactic cosmic rays, although the paradigm is challenged by some phenomenological and observational constraints. This Section gives an overview of supernova remnants as cosmic-ray sources and briefly covers other proposed candidates.

1.4.1 Supernova remnants

A supernova explosion leaves behind a shock wave that propagates in the interstellar medium carrying significant energy for hundreds to thousands of years. This object is referred to as *supernova remnant* (SNR). Remarkably [75], the link between supernovae and cosmic rays had been suggested by Baade and Zwicky in 1934 [76] at the very early stage of supernova astronomy and even before the nature of the cosmic radiation was established. As introduced in Section 1.2.1, the Fermi acceleration model applies naturally to the context of the SNR shock propagation. The classification of SNRs in the *Hillas plot* (Section 1.9) makes them good candidates for the production of CRs at least up to the knee, and possibly to the ankle, but the actual modelling of acceleration up to these energies is problematic. While the *SNR paradigm* holds as the most successful theory for the genesis of galactic cosmic rays, many issues are still open. In this section, a brief overview is given starting from Reference [77].

A primary consideration in favour of the SNR paradigm is that supernovae seem to be the only source powerful enough to account for the energy budget of galactic CRs. For this, supernovae are required to transfer energy to the CR population with a typical efficiency of $\sim 10-20\%$. This is satisfied in a diffusive shock acceleration scenario, but the corresponding energy balance is not compatible with a model adopting the *test particle* approximation. The influence of the accelerated particles on the source cannot be neglected and should produce observable effects. Besides, the typical diffusion time from the remnant to the interstellar medium would suggest a maximum cosmic-ray energy in the GeV range, orders of magnitude below the $\sim 10^{15}$ eV of the knee. To solve this inconsistency, CR particles need to have an active role in producing the very same magnetic field on which they scatter, so that the characteristic acceleration time is reduced and higher energies can be attained. This scenario can

be accommodated in *non-linear diffusive shock acceleration* (NLDSA) models and is further sustained by the observation of narrow X-ray rims, attributed to synchrotron radiation by high-energy electrons accelerated in intense magnetic fields on the shock surface.

The observation of γ-rays above 100 MeV from supernova remnants has traditionally been proposed as a test for the cosmic-ray origin [78]. While leptonic emission in a SNR can naturally occur by inverse Compton scattering of CMB photons, a hadronic process requires a sufficiently high density of target particles to produce a detectable γ-ray signal. A natural association between supernova remnants and dense environments comes from the fact that dense molecular clouds in the Galaxy can host star-forming regions, where the birth of massive stars making good SN progenitors is more likely. The signature of a SNR shock propagating in a dense molecular is the 1720 MHz O-H maser line in the microwave spectrum, which observed for over 10% of supernova remnants, all of which are γ emitters [79]. Multi-wavelength campaigns have pointed to the likely hadronic nature of the γ emission for supernova remnants `IC443` [80] and `W28` [81]. It is a long-standing question whether or not supernova remnants can be *pevatrons*, sources accelerating protons to the PeV scale of the knee (and beyond). The hadronic fit of γ-ray data for `RX J1713−3946` points to a proton population at the source with a 150 TeV cutoff, standing one order of magnitude below. The intensity of magnetic fields required to produce PeV energies cannot easily be explained by the shock compression in the ISM within current NLSDA models [82]. Also, several γ-ray SEDs determined by Fermi-LAT, where `RX J1713−3946` seems to be the exception, hint to a steep injection spectrum ($\gamma \simeq 2.4-3$) that is in contrast with the flat ($\gamma \lesssim 2$) prediction by for the DSA process.

1.4.2 Other galactic candidates

Novae are transient luminous emissions sometimes observed in binary systems, attributed to nuclear explosions occurring in a dense surface region of an accreting white dwarf. High-energy γ-rays have been detected by *Fermi*-LAT from a nova in the binary system `V407 Cygni`. The emission could be explained as the result of proton-proton interaction, that would also produce sub-GeV neutrinos [83]. If the GeV γ emission is, on the other hand, the product of inverse Compton by electrons in the few tens of GeV range, hadronic γ and neutrino emission could occur at higher energies, possibly up to TeV energies [84]. Enhanced observation capabilities by CTA and neutrino telescopes could open a new window on novae as cosmic tevatrons [85]. The ∼ 10% ratio between γ-emitting novae and the total of the optically-discovered suggests that most of the γ sources are nearby [86].

Pulsar wind nebulae (PWN) or **plerions** are nebulae contained in the envelopes of supernova remnants and fueled by the pulsar winds. These are produced by the extremely intense magnetic fields generated by the spinning neutron star. A special class of pulsars with strong surface magnetic fields (*magnetars*) could

even produce CRs beyond the ankle [87].

Binary systems have been extensively observed in the X-ray domain (XRB). Radio observations have confirmed that they present variable relativistic jets [88]. A subset of XRBs has been observed to have γ-ray emission in the GeV to the TeV scale that indicates efficient particle acceleration, although it could have leptonic nature [89].

Microquasars are a sub-class of X-ray binaries that typically produce relativistic jets with $\Gamma \sim 3-10$. They have been proposed as the possible origin of narrow spectral features in the cosmic-ray spectrum as well as power-law decaying flux components [90].

1.5 Extragalactic source candidates

Around $10^{17} - 10^{18,5}$ eV (start of the UHECR region) the contribution from extragalactic sources to the CR flux becomes important. Above 10^{19} eV the main source candidates are Gamma-Ray Bursts, active galaxies and starburst galaxies. Following Equation (1.11), energies up to $10^{20} - 10^{21}$ eV can be expected from these objects.

1.5.1 Active Galactic Nuclei

Active galaxies represent a few per cent fraction of all galaxies. Their central nucleus is brighter than the rest of the galaxy and is referred to as an *active galactic nucleus (AGN)*. Active galactic nuclei emit across the entire electromagnetic spectrum from radio waves to the TeV scale. This non-thermal characteristic makes them important candidate sources for extragalactic cosmic rays. Observable features of AGN exhibit strong time variability. In particular, they can be radio-loud and produce relativistic jets. Of special interest are those AGN for which the jets point in the Earth direction, known as *blazars*. Among AGN, from 5 to 15% are radio-loud and less than 5% are blazars.

On September 22, 2017, a 290 TeV neutrino was detected by the IceCube Neutrino Observatory from the direction of the known TXS 0506+056 γ-ray blazar, which at the time was in a flaring state. The observation sparked a vast multi-messenger survey [91]. The post-trial significance of the association is around $\sim 3\sigma$ and its implications are still highly debated. Aside from the low energy burst from a galactic supernova SN1987A, this would be the first time neutrinos are detected in coincidence with an electromagnetic source. Consequential searches in IceCube archival data have highlighted a mildly significant neutrino flare from the same direction, however without a corresponding increase in the γ-ray activity [92]. Multi-wavelength electromagnetic data for the corresponding time interval are sparse, but the relatively high number (13 ± 5) of detected neutrinos can be hardly accommodated by theoretical model [93].

1.5.1.1 AGN classification

A general classification of AGN as a function of the viewing angle is given in Figure 1.16. Blazars can, in turn, be classified in two main subclasses: *flat spectrum radio quasars (FSRQ)* with strong and broad optical emission lines, and *BL Lacertae (BL Lac)* objects with a weak feature-less optical spectrum. Depending on their synchrotron peak frequency, they can be divided in *low*, *intermediate* and *high synchrotron peaked* (LSP, ISP, HSP). HSP *BL Lacs* are rare powerful gamma-ray emitters.

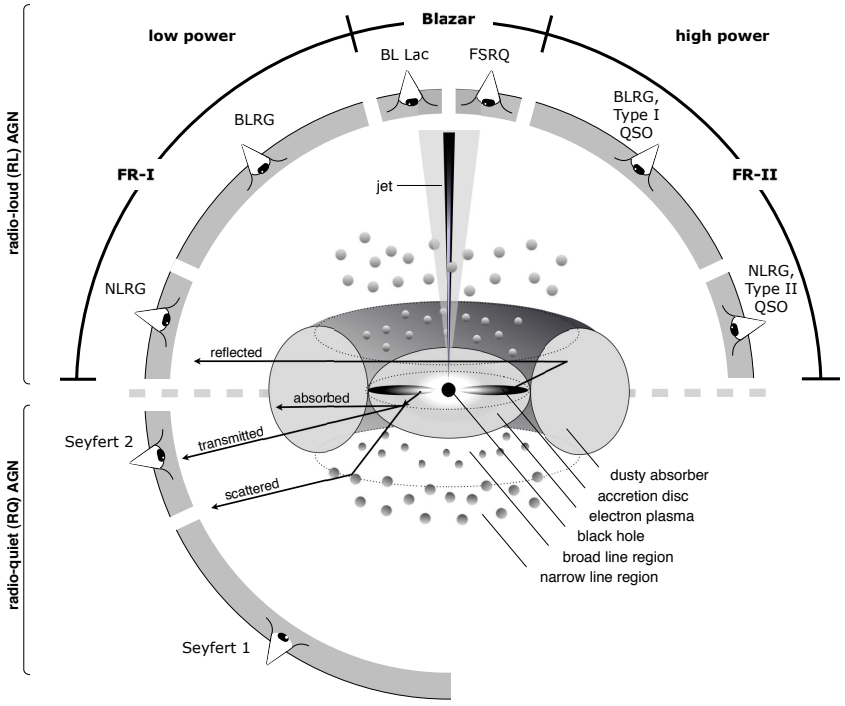

Figure 1.16 – Schematic representation of AGN classification [94]. The type of visible object depends on the viewing angle, on the jet and the power of the central engine. Radio loud object are thought to have symmetric jets. Author: Marie-Luise Menzel (MPE). Source: [95].

1.5.1.2 Jet structure and models

In general, the dynamics of AGN jets are still debated and different models can be used to fit the experimental observations. In particular, blazars can be modelled as *multi-zone* objects to explain some of the observed features. As an example, Figure 1.17 illustrates the models from Koers and Tinyakov [96] (on the left) and Becker and Biermann [97] (on the right) as compared in Reference [98]. In the first, protons are accelerated by shocks at the base of the jet and subsequently scatter with X-ray photons (in turn produced by inverse Compton in the corona). Neutrons and neutrinos escape the confining regions, with neutrons decaying before leaving the jet, producing CR protons. In the second, protons are accelerated by stable shocks at a

few thousands gravitational radii. They interact with the synchrotron photon field generated by relativistic electrons in the magnetic field of the jet, being accelerated along its axis. Neutrinos are here produced as a collimated beam. This model yields specifically a larger emission of CR protons compared to neutrinos.

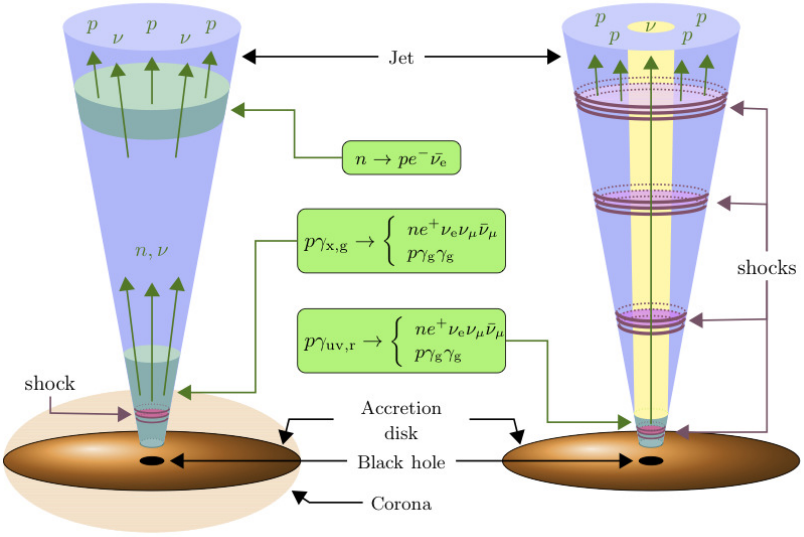

Figure 1.17 – Schematic illustration of AGN jet structure according to the models of Koers and Tinyakov [96] (left) and Becker and Biermann [97] (right) Source: [98].

1.5.1.3 SED and time variability

A class of AGN that has drawn special interest in multiwavelength astronomy are *Markarian Galaxies*, identified with a UV-bright nucleus. Observational data from *BL Lacs* Markarian 421 and Markarian 501 are examined here as examples of the typical multi-wavelength features of this class of objects. Markarian 501 has been the target of an extensive multi-wavelength campaign [99] between August 2008 and November 2009. The spectral energy distribution from microwaves to high-energy γ-rays is given in Figure 1.18. Four regions of data points can be identified from the left to the right: radio, optical, X-ray and γ.

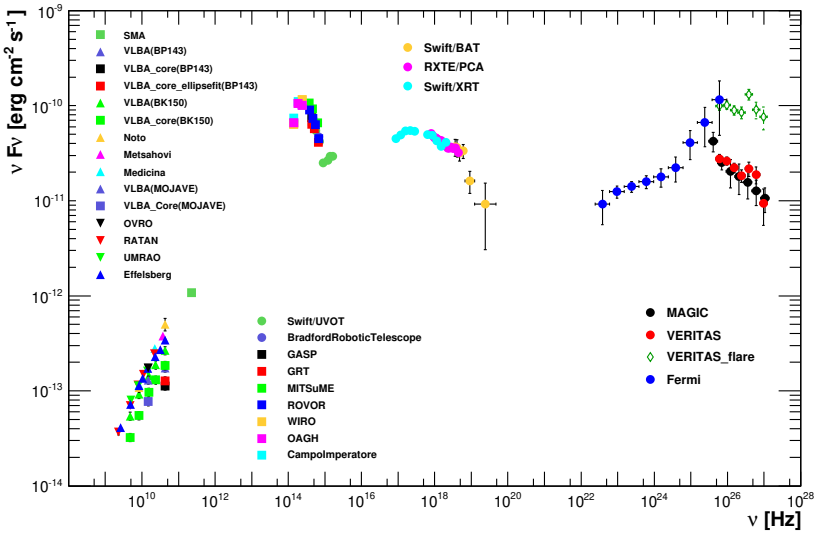

Figure 1.18 – Spectral energy distribution for Mrk 501 averaged over all observations of the multi-wavelength campaign performed between 2009 March 15 (MJD 54905) and 2009 August 1 (MJD 55044). The legend reports the correspondence between the instruments and the measured fluxes. The VERITAS data from the flare observed in the interval MJD 54952.9–54955.9 were removed from the data set used to compute the average spectrum, and are depicted separately as green diamonds. Source: [99].

The typical *double bump* pattern is again observed. It is attributed to a combination of synchrotron and inverse Compton radiation. In particular, in the purely leptonic *synchrotron self-Compton* (SSC) scenario, the blazar is modelled after a single acceleration zone in which electrons and positrons scatter on their own emitted synchrotron radiation [100]. In Figure 1.19 the Markarian 501 spectral energy distribution is fitted with a SSC model.

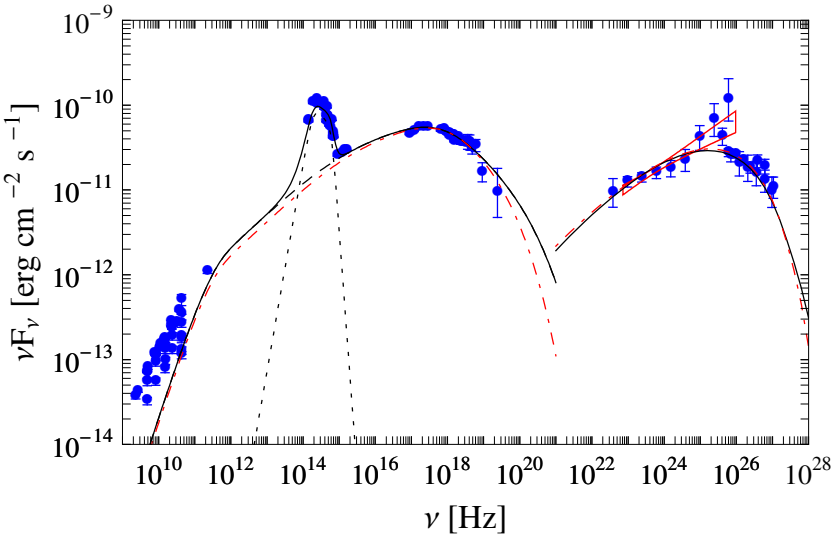

Figure 1.19 – Fit of SSC model fits to the broadband emission spectrum of Mrk 501. The red bow-tie in the figure corresponds to the 68% containment of the power-law fit to the average Fermi-LAT spectrum (index 1.74 ± 0.05). The dotted black curve denotes the fit to the starlight emission of the host galaxy assuming a template of a luminous elliptical. The black and red-dot dashed curves correspond to the main set of the model parameters considered (variability timescale $t_{var} \simeq 4$ days), while the red dot-dashed curves to the alternative set of the model parameters with the emission region size decreased by an order of magnitude ($t_{var} \simeq 0.35$ days). Source: [99].

As an example of the time variability of the blazar emission, a multi-wavelength campaign conducted on Markarian 421 between February 2007 and July 2009 [101] is here reported. The light-curve of the source as observed by different instruments is reported in Figure 1.20. In particular, MAGIC and Swift cover the γ-ray spectrum, RXTE/ASM the X-ray, GASP-WEBT the optical and Metsähovi / OVRO the radio. In the *Period 2* of the observation, multiple series of flares were identified in the blazar emission. The X-ray and VHE γ bands show a direct correlation during both high- and low-activity periods over many months. High-variability in these bands is associated with low-variability in the optical and radio emissions. The X-ray/γ correlation can be interpreted in a leptonic synchrotron-self-Compton scenario, with a single population of electrons at the origin of both emissions. A hadronic interpretation would likely require a proton-synchrotron radiation to produce a high-energy γ emission, cascading down to fuel correlated electron and photon fields, which in turn could be the origin of the X-ray emission.

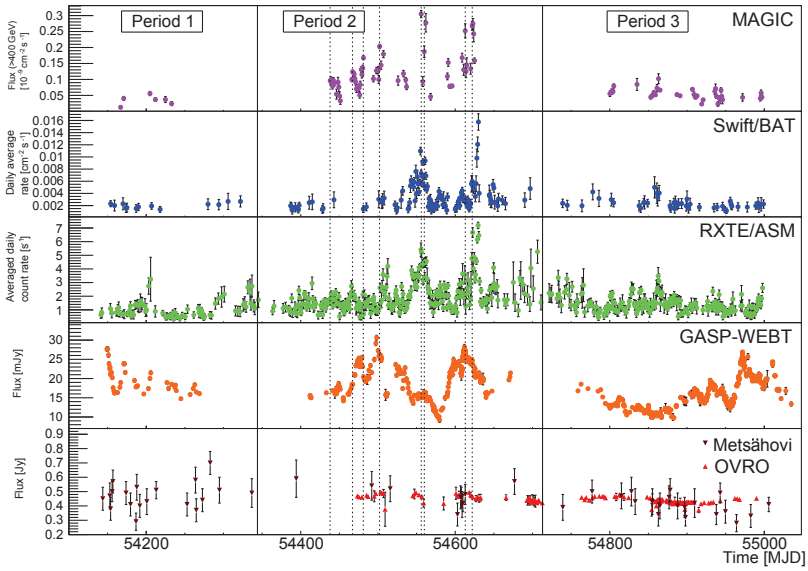

Figure 1.20 – Markarian 421 light curves as measured by MAGIC, *Swift*/BAT, *RXTE*/ASM, GASP-WEBT, Metsähovi and OVRO from top to bottom in the time range from February 2007 to July 2009. The vertical dotted black lines denote the position of the TeV γ-ray flares. Source: [101].

1.5.1.4 Non-blazar AGN sources

While blazars are of special interest due to their powerful γ-ray emission, their assessed contribution to the astrophysical neutrinos observed by IceCube is small. The comparison between the extragalactic neutrino and γ-ray backgrounds in the 10 – 100 TeV range suggests that a contribution to the astrophysical neutrino flux should come by sources without a very-high-energy γ counterpart. *Low-luminosity AGN (LLAGN)* [102] (*BL Lac* objects for an off-axis observer) and coronae of AGN cores [103] have been proposed as candidates.

1.5.2 Gamma-ray Bursts

In 1967, the *Vela Project* military satellites operated by the United States Air Force detected flashes of gamma radiation of unknown origin. Researchers from the Los Alamos National Laboratory discovered the anomalies in the data in 1969. In 1973 they published the discovery of gamma-ray bursts of cosmic origin [104]. GRBs are characterised by highly relativistic outflows with $\Gamma \geq 100$, allowing the acceleration of UHECR according to Equation (1.11).

The emission of a γ-ray burst is usually articulated in two phases: the *prompt* phase, attributed to the inner region of the expanding shock, and a broadband *afterglow* that originates from the shockwave interaction with the circumburst medium. The time, T_{90}, over which 90% of the prompt emission energy occurs is used to classify GRBs in

short ($T_{90} < 2$ s) and long ($T_{90} > 2$ s). Long GRBs are more energetic and likely originate from the core collapse of a massive star into a black hole (the same process that can produce a core-collapse supernova). LGRBs are observed up to a redshift value $z = 9.2$ and can be extremely bright with luminosities between 10^{51} and $3 \cdot 10^{54}$ erg/s. Short GRBs are in general weaker and attributed to compact binary mergers (neutron star - neutron star or neutron star - black hole). The primary instruments for GRBs detection are today the *Burst Alert Monitor* of the *Swift* satellite (*Swift*-BAT) [105] and *Gamma-ray Burst Monitor* of the *Fermi* spacecraft (*Fermi*-GBM) [106]. GBM provides an all-sky coverage in the 10 keV – 25 MeV, up to the lower limit of the *Fermi*-LAT instrument.

On August 17, 2017, the LIGO and Virgo interferometers detected the signature of a binary neutron star merger (GW170817) in coincidence with the observation of GRB 170817A by the *Fermi*-GBM and INTEGRAL instruments [107]. It was followed by the most extensive multi-messenger campaign to date, involving tens of observatories across the electromagnetic and particle spectra [108].

Swift-BAT and *Fermi*-GBM produce low-latency GRB alerts that can be followed up by a network of ground-based observatories, especially Cherenkov telescopes. The H.E.S.S. and MAGIC γ-ray Cherenkov telescopes have finally achieved the long-awaited observation of LGRBs in the *very-high-energy* (VHE) part of the spectrum, above 100 GeV. The first three events have been detected between 2018 and 2019 (180720B [109], 190114C [110], 190829A [111]). These observations allow to significantly constrain the nature of the GRB afterglow radiation. The production of VHE gamma-rays is indicative of efficient particle acceleration, that could be leptonic or hadronic. As observed for GRBs 180720B and 190114C, the VHE emission is similar in radiated power and temporal decay compared to the synchrotron-generated X-ray peak, suggesting a common source. As of today, the best fitting scenario for the spectrum of the observed VHE γ photons is the purely-leptonic synchrotron self Compton (SSC) mechanism [112]. The question of whether there is room for a sub-dominant hadronic contribution is still open and out of the reach with the available data.

The origin of the prompt GRB emission, originating in the inner regions of the expanding shock, is still highly debated. The observation of this phase by ground-based telescopes is difficult as their pointing latency is usually in the order of tens-of-seconds. GRB 190114C has been promptly followed up by MAGIC (~ 1 min), but the time profiles of keV-MeV spectra from *Swift*-BAT and *Fermi*-GBM indicate that the prompt phase had terminated well before. As of today, there is no probe of the prompt VHE γ emission.

The upper energy limit of the GRB photon spectrum is still unconstrained, as the MAGIC observation of GRB 190114C shows no hint of a cutoff at TeV energies. At the same time, the scattering of γ photons with the extragalactic background light results in severe suppression of the spectrum, making the detection more challenging. Future observations could provide insights on the spectral index at the highest energies and the eventual presence of cutoff mechanisms. In particular, it is to be determined if the maximum photon energy achieved by GRBs is determined by the population of accelerated particles, the loss of efficiency of radiative processes or by the intrinsic

$\gamma - \gamma$ opacity of the source. The determination of the highest achievable γ energy is fundamental to constrain the bulk Lorentz factor of the jet and characterise the acceleration mechanisms.

1.5.3 Cosmic-ray reservoirs

In contrast with the paradigm of *cosmic accelerators* as AGN or GRBs, large-scale structures have been proposed as possible extragalactic *cosmic ray reservoirs*. In a reservoir, cosmic rays originate in a large number of accelerators and are further scattered and accelerated by large-scale magnetic fields. As the highest energy particles can escape the confinement, reservoirs are a good candidate for UHECR production. *Starburst galaxies* present very high rates of star formation and supernova explosions. Their size is $\mathcal{O}(100\,\mathrm{kpc})$ with interstellar magnetic fields at the $0.1 - 1\,\mathrm{mG}$ scale. Efficient cosmic-ray confinement and acceleration may occur, although energy losses are expected in their turbulent interstellar medium [113]. *Galaxy clusters* are Mpc-sized objects that are known to exhibit non-thermal synchrotron emission showing as radio halos. Observational data suggest the presence of relativistic particles and $0.1 - 1\,\mu\mathrm{G}$. magnetic fields in the inter-cluster medium, where cosmic rays could be accelerated [114].

1.5.4 Other extragalactic candidates

Core-collapse supernovae have been recently advocated as cosmic-ray production sites in the immediate aftermath of the explosion, well in advance of the development of the remnant [115]. In the *choked-jet* scenario associated to a subset of type Ib,c supernovae, the jet interacting with the star envelope could produce high energy neutrinos, that escape a region opaque to γ radiation [116]. In the *interacting* scenario concerning type IIn SNe, high-energy neutrinos and γ-rays are attributed to the interaction of the star ejecta with a dense circumstellar medium [117].

Tidal disruption events (TDE) occur when tidal forces end up in the disintegration of a star as it approaches a black hole. The star-composing nuclei can be accelerated to ultra-high-energy by the jets produced in the tidal dynamics [118]. TDEs have been proposed as the possible source for as much as 10% of the observed astrophysical neutrino flux [119]. On October 1, 2019, IceCube observed a 0,2 PeV neutrino found to be in coincidence with the tidal disruption event (TDE) `AT2019dsg` identified by the *Zwicky Transient Facility* optical telescope [120] with a 0.2% probability of a random association. Despite the mild significance, the detection has sparked significant interpretative efforts and renewed the interest in TDEs as sources of astrophysical neutrinos.

1.6 Neutrinos

Since their discovery in 1956, neutrinos have been probably the most intriguing particles in the Standard Model. Neutrinos are elementary particles existing in three flavours correspondent to the three charged leptons: ν_e, ν_μ, ν_τ. Neutrinos are stable and neutral, subject only to the weak and gravitational forces. The observation of neutrino oscillations has proven neutrinos as massive, a feature not predicted by the Standard Model. The question of whether neutrinos are Majorana or Dirac particles, namely if they are their own antiparticle, is still open. Thanks to their very small cross section for weak interactions, neutrinos can travel unperturbed intergalactic distances, making them formidable astrophysical messengers.

Neutrinos are produced in a variety of natural and artificial sources, and have been observed from the keV to the few PeV energies. The main natural sources are the Sun, radioactivity in the Earth (*geoneutrinos*) and atmospheric neutrinos produced by the interaction of cosmic rays in the atmosphere. Artificial sources include nuclear reactors (for electron antineutrinos) at the MeV scale [121] and dedicated beam facilities at particle accelerators that cover from tens to hundreds of GeV [122]. Figure 1.21 illustrates the known (measured) and predicted neutrino fluxes from natural sources and nuclear reactors.

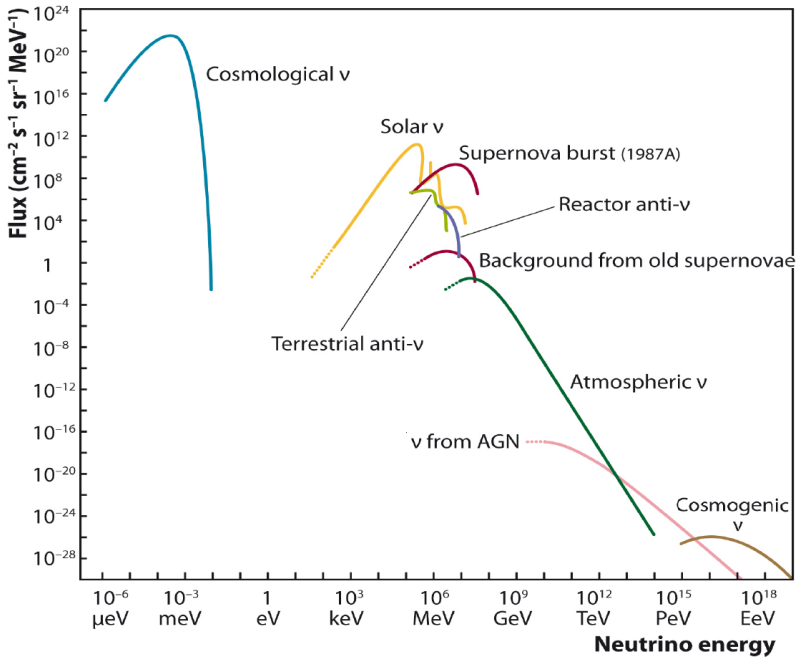

Figure 1.21 – Measured and predicted fluxes for natural and reactor neutrinos.

A brief overview of extraterrestrial neutrino fluxes follows:

Cosmological neutrinos around 10^{-4} eV are part of the Universe background particle radiation. Thermal decoupling of neutrinos occurred ~ 1 s after the Big

Bang at a temperature of 1 MeV ~ 10^6 K. As a consequence of redshift, their expected temperature is at 1,95 K. Although there is indirect evidence for the cosmic neutrino background, direct observation is beyond the reach of existing experiments.

Core-collapse supernova neutrinos have been detected so far in the single observation of the SN1987A explosion in the Large Magellanic Cloud. This type of supernovae releases 99% of the gravitational energy of the progenitor as an all-flavour low-energy neutrino emission. The subject is covered in depth in Chapter 4.

Astrophysical neutrinos above 50 TeV are expected from the decay of charged pions produced in hadronic interactions inside CR sources (see Section 1.6.4).

Cosmogenic neutrinos are expected at ultra high energy as a byproduct of the GZK process (discussed in Section 1.1.4).

1.6.1 Neutrino interactions

An extensive overview of neutrino interactions can be found in Reference [123]. Neutrino weak interactions occur by the exchange of a W (charged-current) or Z (neutral current) boson. At very low energy (below 1 MeV), neutrinos can undergo coherent interaction with nuclei, either in scattering or capture reactions (stimulated beta emission). Between 1 and 100 MeV, quasi-elastic neutrino-nucleon interaction takes place. In a typical charged-current interaction, the neutrino exchanges a W with a nucleon, producing a charged lepton of the same flavour as the incoming neutrino, and converting the nucleon from proton into neutron, or vice-versa. The process can occur either on free particles (e.g. protons in hydrogen) or in atomic nuclei, resulting in a shift of the atomic number. In a neutral-current interaction, the neutrino scatters off another particle exchanging momentum through a Z boson. Elastic scattering on electrons is a peculiar case of superposition between a charged-current and neutral-current process. Feynman diagrams for quasi-elastic neutrino interactions are given in Figure 1.22. At higher energies, the interaction becomes increasingly inelastic as the exchanged boson starts to resolve the inner structure of the nucleus. Between 1 and 5 GeV, the cross section is dominated by resonant production of barions as the $\Delta(1232)$. As the energy approaches the 100 GeV scale, the *deep inelastic scattering* sets in, as the neutrino scatters off individual nuclear components and breaks the nucleus. In the final state, an emission of hadronic particles can be observed (*hadronisation*). Charged-current neutrino cross sections as a function of energy are reported in Figure 1.23.

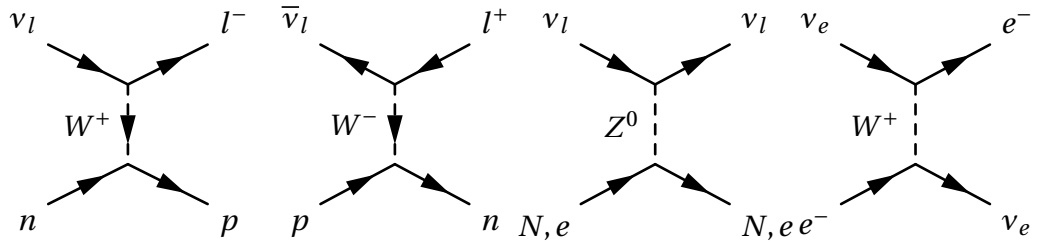

Figure 1.22 – Feynman diagrams for typical quasi-elastic charged-current and neutral-current neutrino interactions.

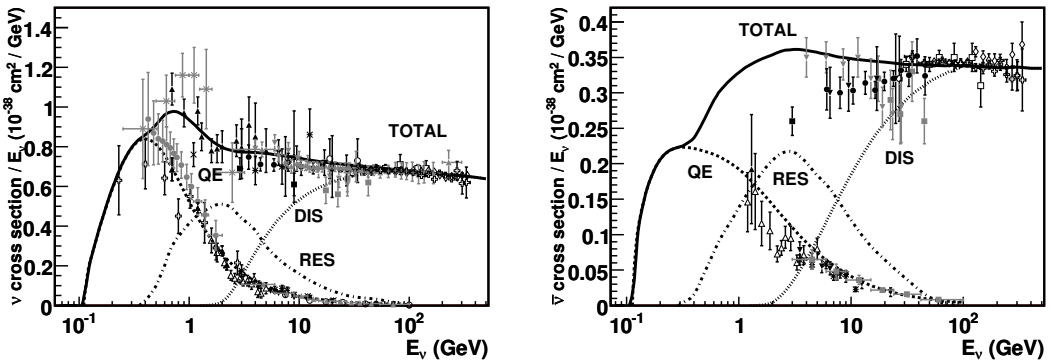

Figure 1.23 – Total neutrino and antineutrino per nucleon charged-current cross sections for an isoscalar target (same number of protons and neutrons) divided by neutrino energy and plotted as a function of energy. Contributions include quasi-elastic scattering (dashed), resonance production (dot-dash), and deep inelastic scattering (dotted). Source: [123].

1.6.2 Neutrino oscillation

When a neutrino is produced or interacts in a charged-current process, it does so as a given flavour e, μ, τ. Flavour eigenstates are not coincident with mass eigenstates, but they can be expressed as a superposition of states (ν_e, ν_μ, ν_τ). This is known as *neutrino mixing*:

$$|\nu_\alpha\rangle = \sum_i U^*_{\alpha i} |\nu_i\rangle \longleftrightarrow |\nu_i\rangle = \sum_\alpha U_{\alpha i} |\nu_\alpha\rangle \ . \tag{1.15}$$

The $U_{\alpha i}$ eigenvalues are elements of a unitary transformation represented in the *Pontecorvo-Maki-Nakagawa-Sakata* matrix, as in the following:

$$\begin{bmatrix} \nu_e \\ \nu_\mu \\ \nu_\tau \end{bmatrix} = \begin{bmatrix} U_{e1} & U_{e2} & U_{e3} \\ U_{\mu 1} & U_{\mu 2} & U_{\mu 3} \\ U_{\tau 1} & U_{\tau 2} & U_{\tau 3} \end{bmatrix} \begin{bmatrix} \nu_1 \\ \nu_2 \\ \nu_3 \end{bmatrix} \tag{1.16}$$

The $U_{\alpha i}$ elements are often more intuitively represented by trigonometric functions of *mixing angles* (θ_{ij}) and an imaginary phase factor ($e^{i\delta}$) that introduces the possibility

of charge-parity (CP) symmetry violation in the leptonic sector:

$$\begin{bmatrix} \nu_e \\ \nu_\mu \\ \nu_\tau \end{bmatrix} = \begin{bmatrix} 1 & 0 & 0 \\ 0 & c_{23} & s_{23} \\ 0 & -s_{23} & c_{23} \end{bmatrix} \begin{bmatrix} c_{13} & 0 & s_{13}e^{-i\delta_{CP}} \\ 0 & 1 & 0 \\ -s_{13}e^{i\delta_{CP}} & 0 & c_{13} \end{bmatrix} \begin{bmatrix} c_{12} & s_{12} & 0 \\ -s_{12} & c_{12} & 0 \\ 0 & 0 & 1 \end{bmatrix} \begin{bmatrix} \nu_1 \\ \nu_2 \\ \nu_3 \end{bmatrix} \tag{1.17}$$

where s_{ij} and c_{ij} indicate $\sin\theta_{ij}$ and $\cos\theta_{ij}$ respectively. In case neutrino are Majorana particles, two more phases are introduced [124]. Neutrinos evolve in time as mass eigenstates.

Given that the PMNS matrix is not diagonal, after a determined amount of time the neutrino will be in a different superposition of flavour eigenstates, with a non-zero probability of interacting as a different flavour. This phenomenon is called *neutrino oscillation* and is experimentally observed as naturally ultra-relativistic neutrinos propagate in space. In vacuum, the probability of oscillating from one flavour α to another flavour β can be derived as:

$$P_{\alpha\to\beta} = \delta_{\alpha\beta} - 4\sum_{i>j} \mathrm{Re}\left(U^*_{\alpha i}U_{\beta i}U_{\alpha j}U^*_{\beta j}\right)\sin^2\left(\frac{\Delta m^2_{ij}L}{4E}\right) + 2\sum_{i>j} \mathrm{Im}\left(U^*_{\alpha i}U_{\beta i}U_{\alpha j}U^*_{\beta j}\right)\sin\left(\frac{\Delta m^2_{ij}L}{2E}\right) \tag{1.18}$$

where L is the traveled distance (baseline) and E is the neutrino energy. Notably, the mixing angles determine the amplitude of the oscillations while the mass squared differences affect its period. The observation of neutrino oscillation in nature is a proof that neutrino are massive particles. Different ranges of Δm^2_{ij} can be investigated by experiments probing different energy scales and baselines, accessing different parameters of the mixing matrix. In particular, the three factors composing the matrix in Equation (1.17) are respectively probed by atmospheric, reactor and solar neutrino experiments.

As neutrino propagates through a medium with a given (varying) density, adiabatic or partially adiabatic flavour conversion can occur. This is known as *Mikheyev-Smirnov-Wolfenstein* (MSW) effect [125]. Due to charged-current scattering by electrons, ν_e are subject to a potential V_e which is different from the one seen by other flavours V_a. This results in a time evolution dependent on an effective potential that can be written as a function of the electron density n_e:

$$V \equiv V_e - V_a = \sqrt{2}G_F n_e \tag{1.19}$$

where G_F is the Fermi weak coupling constant. Flavour conversion in dense media is especially relevant for the phenomenology of solar and core-collapse supernova neutrinos, where due to the extremely dense medium neutrinos leave the source as mass eigenstates. Flavour conversion in the Earth of atmospheric neutrinos can be exploited at the GeV to determine the neutrino mass ordering, as foreseen by the

KM3NeT experiment [126].

1.6.3 Atmospheric neutrinos

Atmospheric neutrinos produced in air showers are of particular interest in multi-messenger astronomy. As they originate in the decay of secondary charged mesons, they are tied to the flux of primary cosmic-ray particles entering the atmosphere. At the same time, they are a background to astrophysical neutrino searches. A review of atmospheric neutrinos oriented to the physics with neutrino telescopes is given in Reference [127].

The accurate modelling of the atmospheric muon flux is crucial to the reliability of the related discoveries. Both atmospheric neutrinos and atmospheric muons originate in the same meson decay processes. The decay of π and K mesons gives birth to the *conventional* flux [128], which is dominant in overall intensity. The mean lifetime for charged pions allows them to travel several meters, losing energy in collisions before decaying. The production cross section for heavier charmed mesons is much smaller but, being extremely short-lived, they decay before any significant energy loss taking place. This gives origin to the *prompt* neutrino flux [129] that features a harder spectrum and dominates the background at higher energy. In general, the neutrino flux is coupled to the parent particle spectrum up to the particle own *critical energy*, above which re-interaction dominates over decay. The critical energies for π, K are 115 and 850 GeV respectively. In the region of interest for astrophysical neutrinos, the spectrum of atmospheric neutrinos is one unit steeper than the one for primary CR particles, $\phi_\nu(E) \propto E^{-\gamma_\nu}$ with $\gamma_\nu \sim 3.7$.

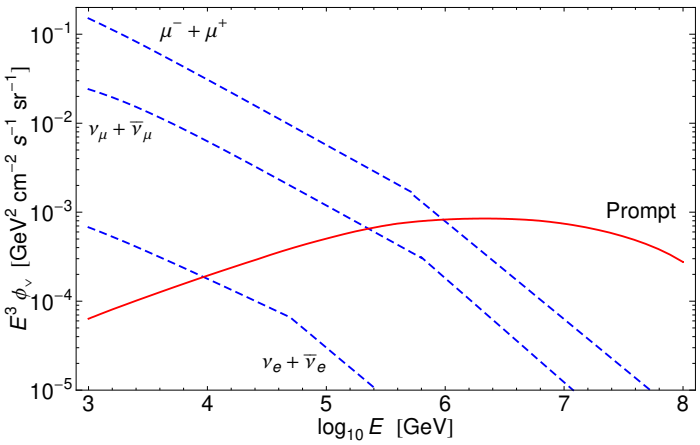

Figure 1.24 – Prompt (solid line) and conventional (dashed lines) fluxes of $\nu_\mu + \bar{\nu}_\mu$, $\nu_e + \bar{\nu}_e$, and $\mu^+ + \mu^-$. The three prompt fluxes, approximately equal, are here represented by the $\nu_\mu + \bar{\nu}_\mu$ flux. Source: [129].

The same distinction between conventional and prompt flux applies to atmospheric

muons, as further discussed in Chapter 3. While the flux of cosmic rays originating air showers is anisotropic, the flux of high-energy atmospheric neutrinos hardens at higher zenith angles. This comes from the competition between re-interaction and decay: mesons at higher zenith angles have a higher probability to decay before losing energy.

1.6.4 Astrophysical neutrinos

As introduced in Section 1.2, sources of cosmic rays are also candidates for neutrino production. Neutrinos from GeV to PeV energies can be observed with large Cherenkov neutrino detectors (*neutrino telescopes*) installed deep underwater or under ice. As introduced in Section 1.3 with *proto-hadronic*/*hadro-nuclear* (p-p, Equation (1.13)) and *photo-hadronic* (p-γ, Equation (1.14)) interactions can be responsible for the joint production of high-energy neutrinos and γ-rays in a cosmic-ray source.

Since γ-rays can also originate in purely electromagnetic processes, the neutrino is the only messenger that provides unequivocal proof of hadronic acceleration in the source. A good candidate source for high-energy neutrinos should be able to accelerate CR particles to the TeV energy and be sufficiently dense to allow efficient production in the aforementioned processes. If the accelerated particles could flow away from the source without significant interaction, then the hadronic production of high-energy γ-rays and neutrinos would be suppressed. The p-p channel is the privileged channel in galactic sources and extragalactic cosmic-ray reservoirs, while the p-γ process is privileged in the scenario of cosmic accelerators. In p-p production, neutrinos are expected to follow the primary cosmic-ray spectrum (E^{-2}), as accelerated protons collide with hadronic matter at rest. In particular, the neutrino typically carries 1/20 of the energy of the parent pion. In the p-γ channel, the energy spectrum will be a convolution of the source cosmic-ray and X-ray radiation spectra [130]. This results in a harder $\propto E^{-1}$ distribution at low energy transitioning to a E^{-2} shape at high energy.

Waxman and Bahcall [131, 132] set an upper bound on the flux of astrophysical neutrinos based on the observation of UHECR and bare constraints on the acceleration process. For a CR production rate $\dot{\epsilon}_{CR} \sim 5 \cdot 10^{44}\,\mathrm{erg\,Mpc^{-3}\,yr^{-1}}$ the derived limit on each neutrino flavour is $E_\nu^2 \phi_l(E_\nu) \simeq 10^{-8}\,\mathrm{GeV\,cm^{-2}\,s^{-1}\,sr^{-1}}$. Sensitivity below this threshold is reached by neutrino telescopes at the $\sim 100\,\mathrm{Mton}$ scale [133]. While being an important benchmark in the historical perspective, all predictions of state-of-the-art astrophysical models for the neutrino production in UHECR sources are today well below the *Waxman-Bahcall bound*.

1.7 Astrophysical neutrino detection and observation

The small cross section of neutrino interactions combined with the magnitude of the fluxes of interest dictates the need for very large instrumented volumes. Long string Cherenkov detectors are designed to efficiently exploit natural ice or water reserves as

particle detectors. The interaction and detection of neutrinos in Cherenkov detectors are briefly introduced, followed by the first result on the astrophysical neutrino flux by the IceCube [134] and ANTARES [135] experiments. The KM3NeT detector will be introduced in Chapter 2.

1.7.1 Cherenkov signatures of high-energy neutrinos

At the energy of atmospheric and astrophysical neutrinos, interactions are dominated by resonant hadron production and *deep inelastic scattering* respectively. A review of high-energy neutrino interactions and propagation in the Earth can be found in Reference [136]. Under these conditions, the signature of a charged-current neutrino interaction is represented in Figure 1.25. The interaction of the neutrino with a nucleon at rest results in the production of (i) a charged lepton of the same flavour (ii) a hadronic shower either by the produced barion or by the fragmentation of the recoiling nucleon. In case of a neutral-current scattering, the neutrino escapes and only (ii) takes place.

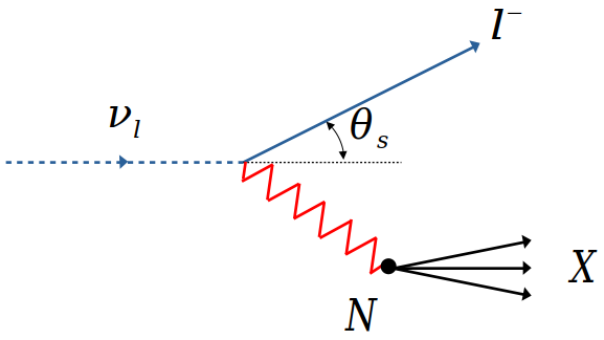

Figure 1.25 – Schematic representation of a high-energy neutrino interaction. Adapted from Source: [137].

As the charged particles in the final state surpass the phase velocity of light in the medium, they stimulate the production of light through *Cherenkov effect*. This occurs as the medium gets polarised along the shockwave induced by the superluminal charge. Cherenkov photons are emitted along the particle trajectory at a characteristic *Cherenkov angle* $\cos\theta_c = (n\beta)^{-1}$ dependent on the refractive index of the medium n ($= 1.33$ for water) and $\beta = v\,c^{-1}$ where v is the particle velocity. The spectral density of Cherenkov photons for a particle of electric charge q is described by the *Frank-Tamm* formula:

$$\frac{d^2E}{dx\,d\omega} = \frac{q^2}{4\pi}\mu(\omega)\,\omega\left(1 - \frac{1}{\beta^2 n^2(\omega)}\right) \tag{1.20}$$

where $\omega = 2\pi\lambda^{-1}$ with λ the light wavelength, $\mu(\omega)$ the wavelength-dependent magnetic permeability of the medium, and dx the differential path segment. According to this, the Cherenkov spectra is peaked at blue wavelengths. Besides inducing Cherenkov light, the interaction products undergo energy loss in the medium. Muons propagate in a straight line (*track*) losing energy by ionisation and radiative processes (as Brehmmstralung and pair-production). In the *minimum ionising particle* regime (below 100 GeV) their average energy loss is $\sim 5\,\mathrm{GeV\,m^{-1}}$. At relativistic energies, electrons produce Brehmmstralung radiation giving birth to a typical *electromagnetic shower*. Hadrons, in analogy, undergo further hadronic interactions generating an *hadronic shower*. Finally, ν_τ interactions produce a hadronic shower and a muon from the τ particle decay. If the latter has sufficiently high energy, the neutrino interaction vertex and the τ decay vertex can be distinguished in the so-called *double bang* topology. For the Cherenkov signature, electromagnetic and hadronic showers result in a similar topology where most of the light is released within a few meters. In the context of water or ice-based neutrino telescopes, events are usually classified in two categories: *muon tracks* and *showers* (or *cascades*). A schematic representation of the two is given in Figure 1.26.

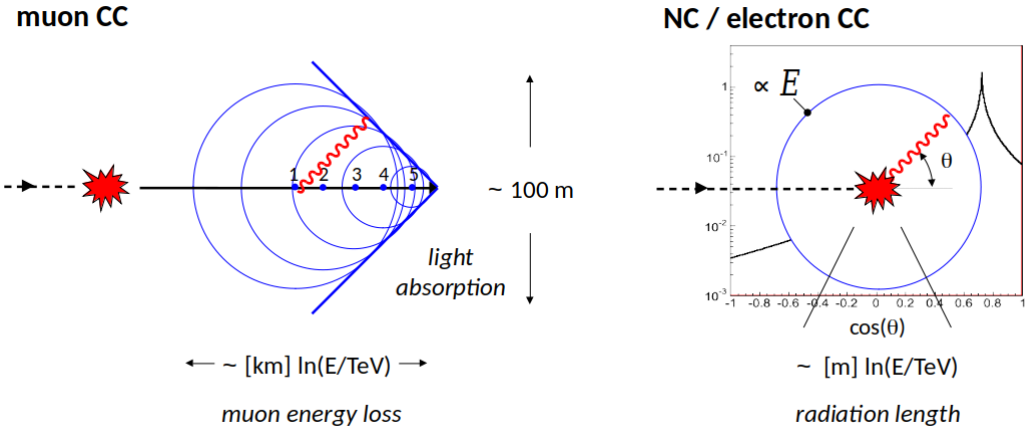

Figure 1.26 – Development of a track-like (left) and shower-like (right) event in water. Adapted from Source: [137].

As seen here, the addition of the light induced along the muon track produces in a conical wavefront with an intensity that decays as r^{-1} (instead of r^{-2} for a point-like spherical emission), where r is the distance in the θ_c direction. For the shower, the superposition of the Cherenkov cones of a large number of particles with a given lateral spread will smear the angular profile of the light emission. At this point, the properties of the medium affect the propagation of photons. For water and ice the most relevant are *chromatic dispersion*, light *absorption* and light *scattering*. Chromatic dispersion occurs as shorter wavelength travel faster than longer ones, effectively smearing the time of arrival of the photons. Absorption results in loss of light over a typical scale, the *absorption length*, in the order of ~ 100 m for water and ice. This implies that

photons can be detected from Cherenkov emissions occurring up to a few hundreds of metres away. In analogy, scattering causes random changes of the photon trajectory over a typical scale that takes the name of *scattering length*. The latter exhibit a striking difference between ice and water, being in the order of ~ 50 cm and ~ 260 m as respectively measured in the IceCube [138] and ANTARES [139] sites.

1.7.2 Introduction to neutrino telescopes

Neutrino telescopes are designed to efficiently collect the Cherenkov photons emitted by neutrino interactions. To this purpose, arrays of photomultiplier tubes (PMT) are used to instrument a large volume of water or ice. These detectors are called *neutrino telescopes* since they are specifically designed to reconstruct the direction of high-energy neutrinos as precisely as possible. This is a fundamental requirement for neutrino astronomy. Graphical examples of track-like and shower-like events as detected in a deep-sea neutrino telescope are given in Figure 1.27.

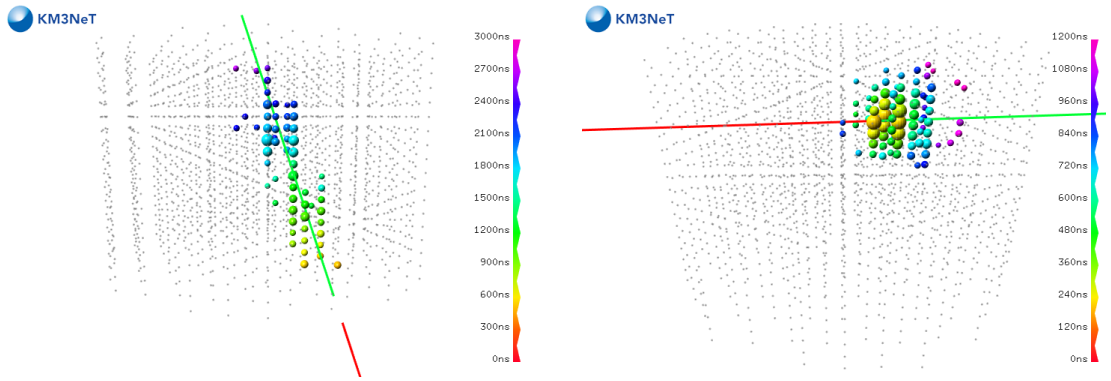

Figure 1.27 – Graphical representation of a simulated track-like event (left) and an electromagnetic shower event (right) from a neutrino interaction in the KM3NeT ARCA detector. The neutrino and the outgoing lepton trajectories are shown in red and green, respectively. The detected photons are highlighted on a grid of optical sensors with a color representing the hit time relative to the interaction. Source: [126].

.

Technologies for deep underwater neutrino detectors have been researched starting with the DUMAND project in 1976 [140]. A prototype detection string was first operated suspended from a ship. The first off-shore deployment in the designated Hawaii site occurred in 1993. Early instrument failures brought to the cancellation of the project. In the 1990s, the *Baikal Deep Underwater Neutrino Telescope* [141] was built under the homonym lake in Russia and evolved in the early 2000s to host more than 200 optical modules arranged in vertical strings. In 1995-1996 the AMANDA neutrino detector started the operations in the Antarctica [142] with 19 strings for a total of 677 optical modules. In the same decade, deep-sea technologies were further

developed with the NEMO [143] and NESTOR [144] projects in Italy and Greece respectively. NEMO and NESTOR tested a different design, in which horizontal lattice towers support the optical modules in a semi-rigid structure. Between 2006 and 2008, the 12 lines of the ANTARES [135] neutrino telescope were deployed in the French Mediterranean. ANTARES consists of vertical strings with 25 floors, each featuring 3 10-inch PMTs sustained by a titanium structure. Following the path of *AMANDA*, the IceCube experiment was built between 2005 and 2010, with 86 detection strings deployed in the ice in the South Pole [134]. Since 2015, the GVD project for the construction of a cubic kilometre telescope has been undergoing at the Baikal site, as an evolution of the existing detector [145]. The construction of next-generation KM3NeT [126] started in 2016 with the first element of the ARCA detector in the Italian Mediterranean Sea, followed in 2017 by the first element of the ORCA detector in the French site, near to the ANTARES location.

Geographical and environmental factors play a role in the design choices adopted to attain the required detector performances. The total absorption of sunlight is achieved already at moderate depths (a few hundreds of meters). Deeper sites can be preferred for improved shielding from the atmospheric muon flux, in a tradeoff with the cost of technology and infrastructure. In neutrino telescopes, the atmospheric muon background dominates the rate of events originating above the horizon. As a result, these detectors have better sensitivity to neutrinos coming from the opposite side of the Earth, thanks to the complete muon rejection. As the Galactic Centre is located in the Southern Sky, detectors on the Northern hemisphere are favoured in the search for Galactic sources. In Figure 1.28 the 2π downward field-of-view for a detector in the Mediterranean Sea is highlighted. Adopting muon vetoes and event containment criteria, neutrino telescopes can still recover the 4π sky coverage at the cost of a decreased sensitivity.

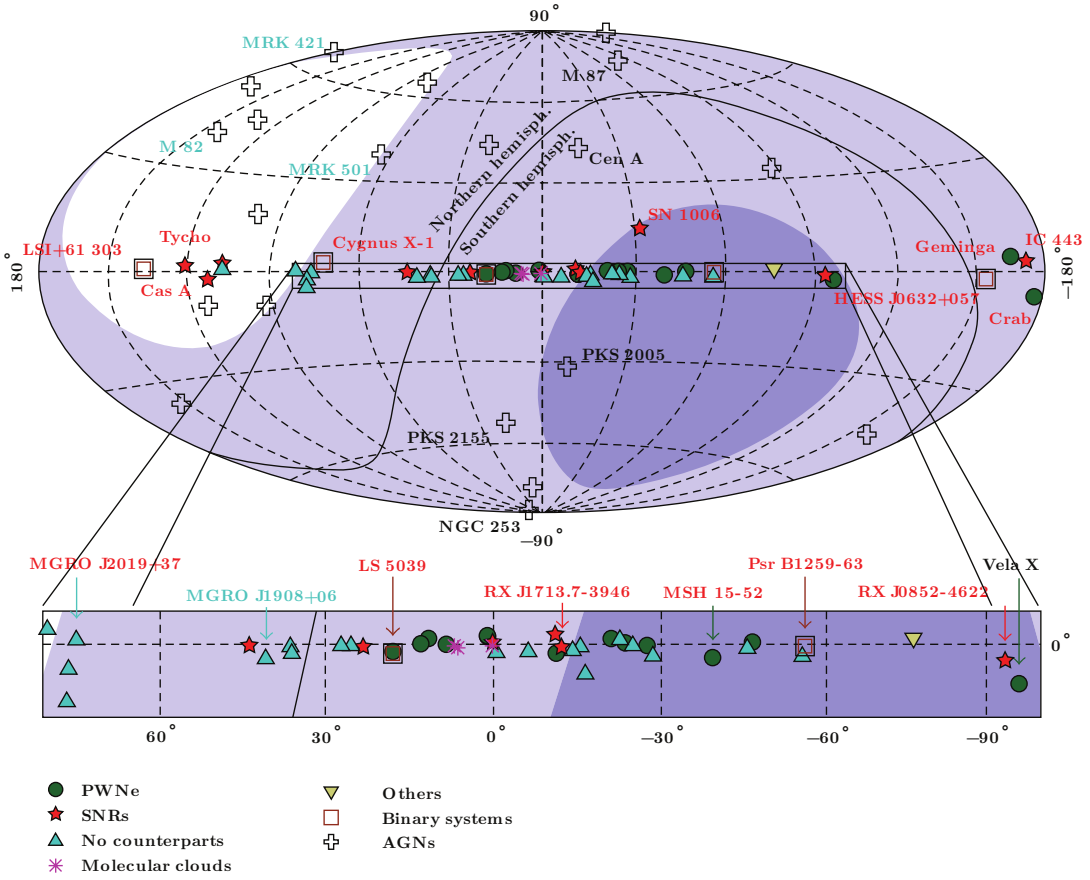

Figure 1.28 – Field of view of a Mediterranean-based neutrino telescope in Galactic coordinates. Shades of blue indicate the fraction of time for which the area is visible (light blue: >25%; dark blue: >75%). The field of view of IceCube is the whole Northern Hemisphere. 2π downward sensitivity is assumed. High-energy γ-rays sources are indicated. Figure by A. Kappes published in [146].

The aforementioned differences in the optical properties of the medium also affect the final performance figures of a neutrino telescope. Compared to ice, water has a higher absorption coefficient but a significantly lower scattering probability, resulting in a better angular resolution and much easier event reconstruction. This is especially beneficial for shower-like events, that have a higher probability of being fully contained in the instrumented volume, providing sensitivity to the full Sky.

On the other hand, water-based detectors require complex underwater infrastructure and continuous position calibration as the detector elements can move under the effect of sea currents. Seawater, in particular, has some additional drawbacks. The salinity is responsible for the optical background of radioactive origin (mostly ^{40}K), not a concern for freshwater or antarctic ice. This increase the background hit rate of PMTs of an order of magnitude compared with typical *dark noise* figures. Due to its

excellent stability in time and space, the ^{40}K background can be used as an *in-situ* calibration source for sea-based detectors. In natural waters, bioluminescent organisms can also be prominent sources of background light that can create diffuse or localised increases of the PMT hit rate. Bioluminescence can vary in time on relatively fast time scales ($0.1 - 1$ s) and show trends over longer periods associated, for example, with sea currents.

1.7.3 Background in the search for astrophysical neutrinos

The fundamental principle at the base of the detection of neutrino events in a neutrino telescope is based on the identification of correlated photon signals compatible with a track-like or shower-like event topology across the instrumented volume.

The first step in the process is the identification and rejection of the *optical background*. This consists of spurious uncorrelated hits recorded at the level of the individual PMT. For 3-inches PMTs, typical optical background rates go from ~ 500 Hz for the unavoidable PMT dark noise to ~ 7000 Hz for radioactive decays in seawater. Bioluminescence on its own can cause variable counting rates even up to several (tens of) MHz. By requiring tight space and time correlation between the detected photons, the optical background is suppressed at the so-called *trigger level*. The events identified by the trigger are processed by reconstruction algorithms and further classified according to their topology. The remaining optical background contamination, mostly from random coincidences, is filtered at this stage.

After the *trigger* the *event rate* at a neutrino telescope is dominated by the muon tracks produced by downgoing *atmospheric muons*. The typical vertical intensity and angular as measured in ANTARES is shown in Figure 1.29, where it is compared with previous measurements by different experiments. In Figure 1.30 the ANTARES measurement of the zenith angle distribution at a depth of 2000 m underwater is shown.

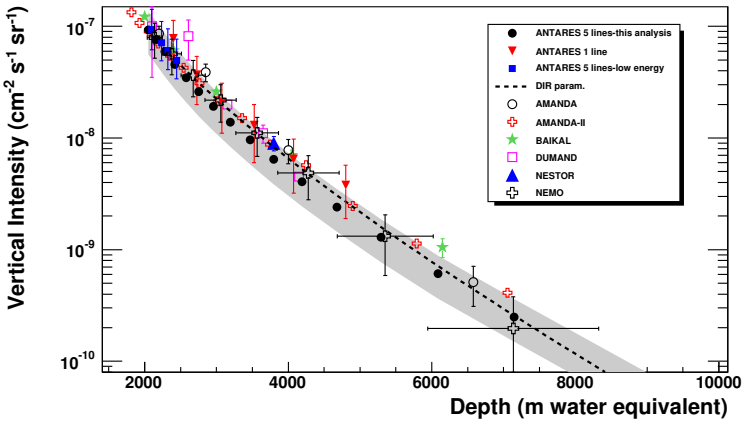

Figure 1.29 – Vertical muon flux of atmospheric muons for the 5 line ANTARES data (black points) as a function of the slant depth. Downward triangles show the results from line 1 data. Full squares show the results obtained with a new method and a low muon energy event selection [147]. Expectation from Bugaev parametrization (dotted line) is superimposed [148]. A compilation of results obtained with other underwater detectors is shown: AMANDA, AMANDA-II, Baikal, DUMAND, NESTOR, NEMO.

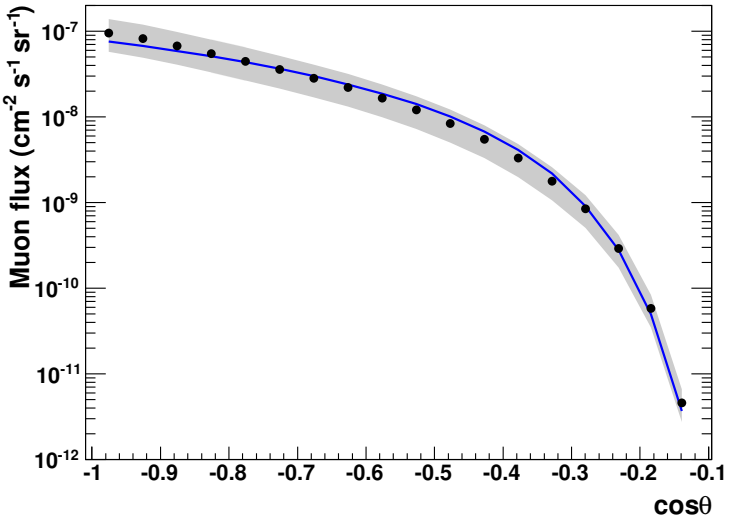

Figure 1.30 – ANTARES 5 lines measurement of the angular distribution of the atmospheric muon flux at 2000 m depth (black points) as a function of the cosine of the zenith angle. The solid line is the expectation from the MUPAGE [149] simulation. The grey band represents the systematic uncertainties on the measured flux.

For the ANTARES detector, the typical ratio between the rate of atmospheric neutri-

nos and atmospheric muons is $\sim 10^{-6}$. Different strategies can be adopted to select a neutrino sample:

upgoing events the Earth provides natural shielding from atmospheric muons coming from the lower hemisphere. A common strategy is to select track-like *upgoing events* to build a muon neutrino sample;

shower events due to their limited spatial extension, most of NC or electron CC induced showers are well contained inside the detector volume. Fully contained showers can provide a high-purity neutrino sample, however with little control on the flavour composition.

starting events by selecting events with the vertex originating inside the instrumented volume the contamination from penetrating atmospheric muons can be significantly reduced. This strategy allows building an all flavour neutrino sample.

Finally, it is required to identify *astrophysical neutrinos* over the *atmospheric neutrino background*. In Figure 1.31 the contributions to the event background in neutrino telescopes from atmospheric muons and neutrinos is compared as a function of the zenith angle.

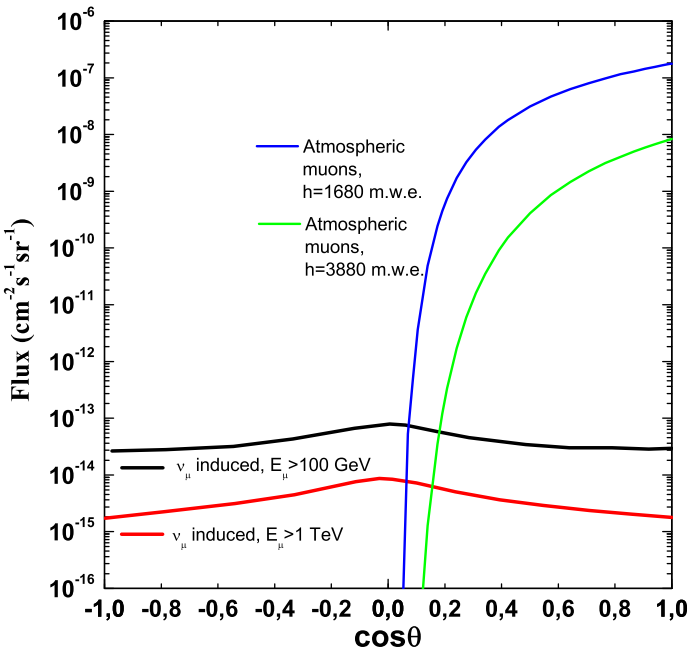

Figure 1.31 – Different contributions (as a function of the cosine of the zenith angle) of the: i) atmospheric muons for two different depths; ii) atmospheric neutrino induced muons, for two different muon energy thresholds. Source: [150].

The astrophysical and atmospheric neutrino fluxes are tied in different ways to the CR spectrum. As introduced in Section 1.6.4, astrophysical neutrinos follow the spectrum of protons at the source (p-p), or a convolution of the proton and photon spectra (p-γ). The corresponding spectral index, γ, is relatively hard, and can be expected at $1 \lesssim \gamma \lesssim 2$. Conversely, atmospheric neutrinos (see Section 3.1) are tied to the primary CR particle spectrum as measured at the Earth ($\gamma \sim 2.7$), with a spectral index even one unit steeper for the *conventional* flux. For an isotropic astrophysical flux, the difference in the spectral indices is the main distinctive feature between the two fluxes.

1.7.4 Astrophysical diffuse neutrino flux

High-energy neutrinos in the range from 30 TeV to few of PeV have been observed by the IceCube Neutrino Observatory [44]. The detected flux is isotropic in the arrival direction and compatible with the hypotheses of flavour and $\nu/\overline{\nu}$ equipartition. The measurement is consistent with the Waxman-Bahcall bound above $\sim$ 100 TeV with a $E_\nu^2 \Phi_{\nu_l} \simeq 10^{-8}\,\mathrm{GeV\,cm^{-2}\,s^{-1}\,sr^{-1}}$. The observation of non-atmospheric neutrinos above 100 TeV is considered as the discovery of the *astrophysical diffuse neutrino flux*, here shown in Figure 1.32.

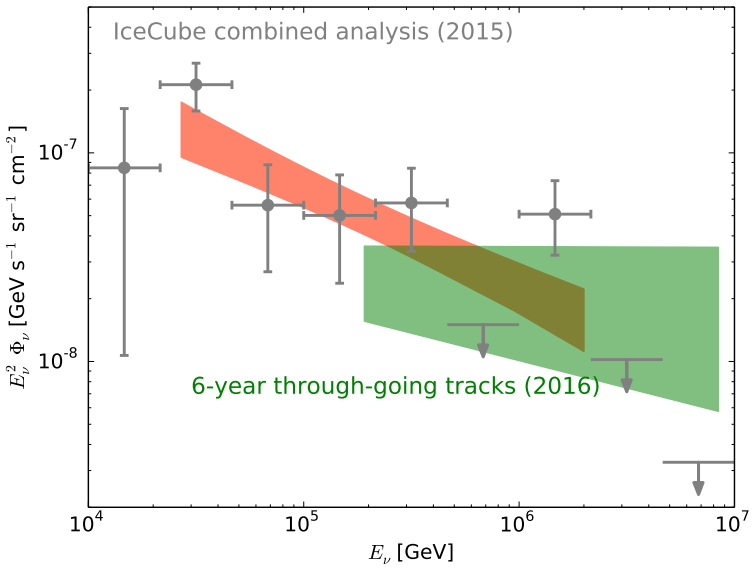

Figure 1.32 – IceCube measurement of the diffuse astrophysical neutrino flux. Spectrum of cosmic neutrinos measured in a combined analysis of all detection channels. The red bar indicates the best fit with a power-law spectral hypothesis. The grey points display the result for a fit of the neutrino flux in individual energy bands. A measurement based on 6 years of through-going muons (green bar) sensitive at higher energies indicates a harder spectrum above a few hundred TeV. Source: [44].

The all-flavour energy spectrum is fitted as a first approximation by a simple power-law:

$$\Phi_\nu = \phi \left(\frac{E}{100\,\mathrm{Tev}} \right)^{-\gamma} \tag{1.21}$$

where ϕ is the normalisation of the flux at 100 TeV. The IceCube measurements are performed using different event samples. The first is represented by muon neutrino tracks selected in the upgoing direction, to reject the prominent background of atmospheric muons. The second is using all-sky high-energy starting events (HESE), namely events of any topology for which the vertex can be confidently identified to be inside the instrumented volume. The third considers only electromagnetic cascades. In Figure 1.33 the best-fit flux parameters by the different analyses of IceCube are shown. The existing tensions in the spectral indices fitted to the different samples could hint at energy-dependent anisotropies in the flux, or be the product of intrinsic systematic biases, however, they still lack satisfactory statistical significance.

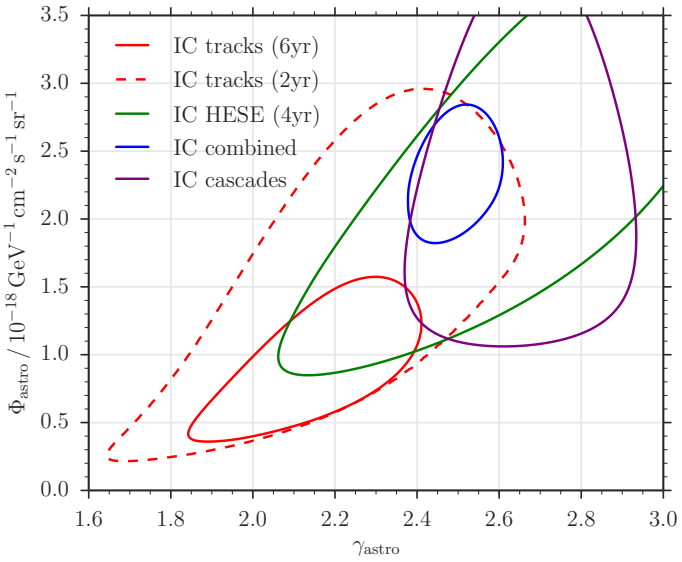

Figure 1.33 – Astrophysical flux Φ_{astro} and spectral index γ_{astro} as measured by different IceCube analyses: through-going tracks, high-energy starting events (HESE), electromagnetic cascades and a combined sample. Contour lines show the 90% CL. Source: [151].

The ANTARES neutrino telescope observed of a mild excess over the atmospheric flux in the same energy range [152], with flux normalisation and spectral index compatible with the IceCube measurements within one standard deviation. The ANTARES measurement is shown in Figure 1.34.

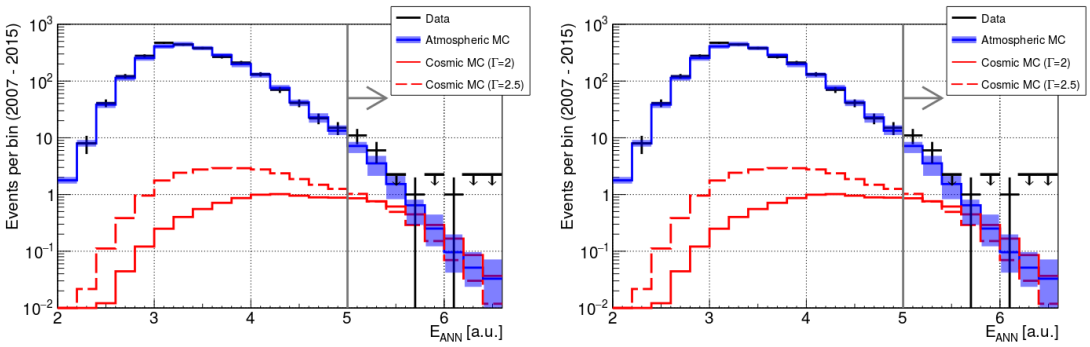

Figure 1.34 – ANTARES measurement of the diffuse astrophysical neutrino flux: econstructed energy for track-like (top) and shower-like (bottom) events. The solid (dashed) red histogram shows the cosmic neutrino expectation for a flux $\propto E^{-2}$ ($E^{-2.5}$) with normalisation $\phi(100\,\mathrm{TeV}) = 10^{-18}$ ($1{,}5 \cdot 10^{-18}\,\mathrm{GeV}^{-1}\,\mathrm{cm}^{-2}\,\mathrm{s}^{-1}\,\mathrm{sr}^{-1}$). The blue line represents the sum of all atmospheric events, scaled up to match the fitted atmospheric contribution. The uncertainties are depicted as a shaded area. The grey line represents the energy-related cut. Data after unblinding are shown as black crosses. For empty bins, upper limits are indicated by a horizontal bar with an arrow beneath. Source: [152].

From Equations (1.13) and (1.14), the production of astrophysical neutrinos in pion decays yields a 2:1 ratio between muon neutrinos and electron neutrinos at the source. Considering Equation (1.18) neutrino oscillations over an extremely long baseline L can be observed only as the average of the sine terms. The oscillation probability reduces in this case to $P_{\alpha\to\beta} \simeq \sum |U_{\alpha i}|^2 \left|U_{\beta i}\right|^2$. An original ratio $\nu_e : \nu_\mu : \nu_\tau \leftrightarrow 1:2:0$ would be detected at the Earth as $1:1:1$. In general, the flavour ratio measured at the Earth can be used to constrain the original production model [153]. In presence of strong magnetic fields, muons can significantly lose energy through synchrotron radiation before decaying (*muon damped* scenario). Only the direct ν_μ from the pion decay would be observed at high energy, resulting in a $0:1:0$ flavour production ratio. In the *neutron beam* scenario, extremely high magnetic fields could suppress both the muon and the pion decay neutrinos, so that only lower energy ν_e from the decay of energetic neutrons would be visible ($1:0:0$ ratio). In Figure 1.35 the flavour ratio measured by IceCube for the diffuse flux is shown.

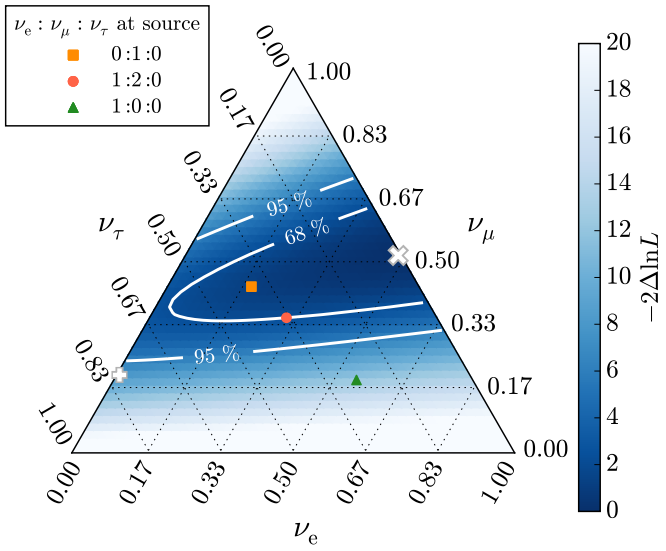

Figure 1.35 – Profile likelihood scan of the flavour composition of the astrophysical neutrino flux as measured at Earth by the IceCube experiment. Individual contributions are read off the three sides of the triangle. The best-fit composition is marked with ×, accompanied by indications of 68% and 95% confidence regions. Each colored marker indicates a ratio $\nu_e : \nu_\mu : \nu_\tau$ at the source (see legend) as it would be measured on Earth. The best-fit composition obtained in an earlier IceCube analysis is marked with a +. Source: [44].

Notably, the order of magnitude of the astrophysical neutrino energy density, $E^2\Phi(E)$, overlaps with the diffuse gamma-ray background (at lower energy) and with UHECR measurements (at higher energy). This hints that the same class of sources is responsible for the production of these three messengers. As the diffuse γ-ray emission observed by *Fermi*-LAT is known to be largely dominated by AGN, important efforts have gone into models able to connect these three observations. A comparison of experimental data with a unification model by Murase and Waxman [154] is reported in Figure 1.36. The stacking point-source search of IceCube against the *Fermi*-LAT catalogue allows constraining the contribution of AGN to the diffuse flux in the 10 TeV – 2 PeV to a maximum of 27% (50%) when assuming a spectral index of 2.5 (2.2) [155].

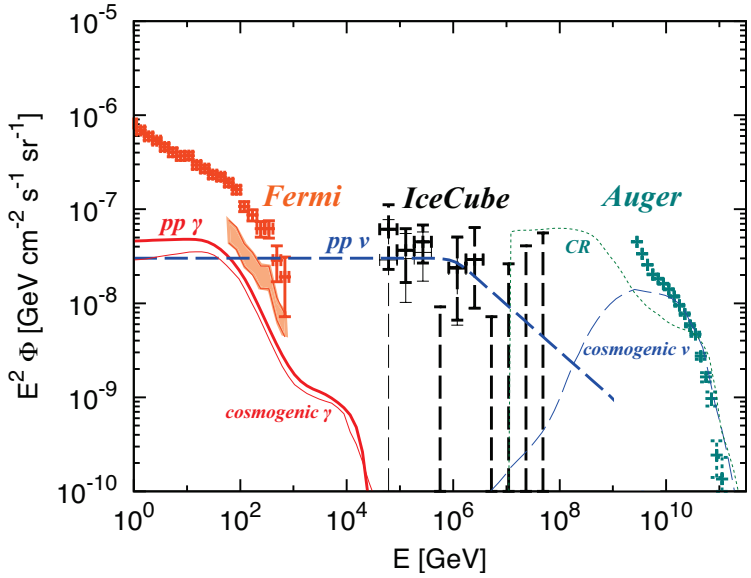

Figure 1.36 – Diffuse CR (thin dotted line), gamma-ray, and all-flavor neutrino (thick dashed line) predicted by the grand-unified cosmic particle model by Murase and Waxman compared with experimental observations. Data are: Fermi-LAT measurement of the total extragalactic gamma-ray background (orange markers) with the non blazar-originating contribution (shaded orange band); IceCube measurement of the astrophysical neutrino flux (black markers); Pierre Auger Telescope measurement of UHECR (green markers). Source: [154].

1.7.5 Point source searches

The observation of the diffuse flux opens the quest for identification of neutrino point sources. Point sources searches are based on the identification of clusters of events in a given direction in excess over the atmospheric neutrino flux. The results of the point search from IceCube [156] are shown in Figure 1.37. Due to the large number of tested locations in the sky, the significance of apparent clustering is heavily suppressed by the trial factor (*look-elsewhere effect*). The most significant clusters for the northern and southern sky have post-trial p-values of 29% and 17% respectively. The most recent update of the point source search of ANTARES is reported in Figure 1.38. Circled in red is the most significant cluster, with a post-trial p-value of 23%.

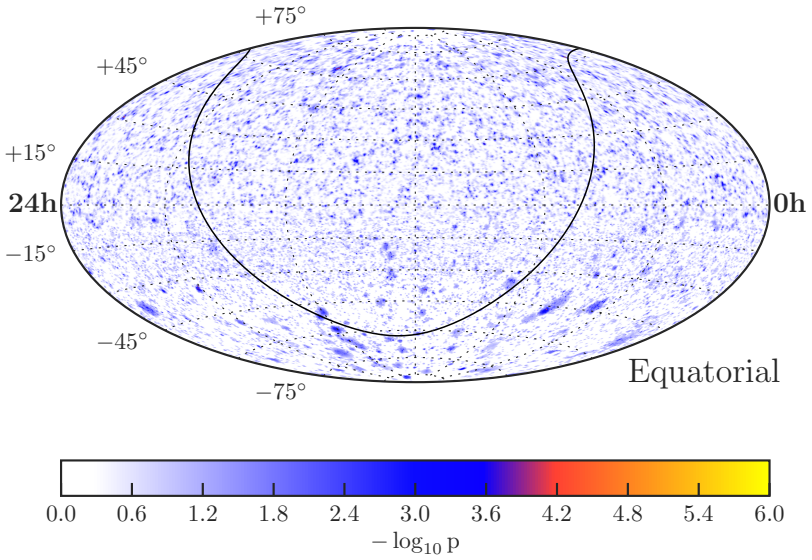

Figure 1.37 – IceCube search for neutrino point sources: map of p-values representing the local probability that an excess of events at a given position in the sky is due to a fluctuation of the expected background. Source: [156].

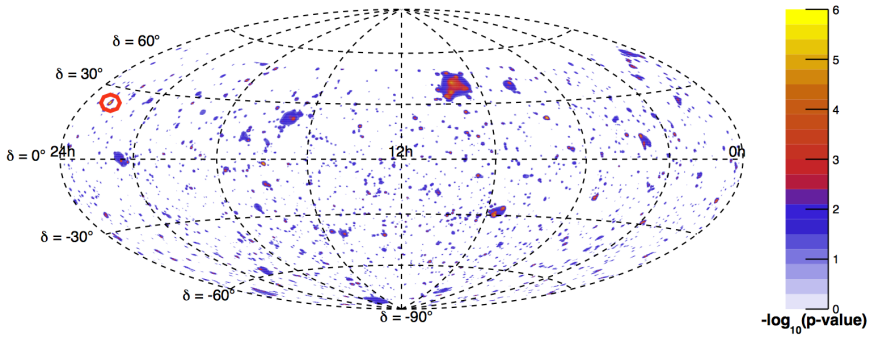

Figure 1.38 – Sky map in equatorial coordinates of pre-trial p-values for a point-like source of the ANTARES visible sky. The red contour indicates the location of the most significant cluster of the full-sky search.

An increase in the discovery potential can be achieved using space and time correlation with multi-wavelength data to significantly reduce the atmospheric background for a given observation. Correlation with source catalogues or with multi-messenger observations is a common strategy in this regard.

2 The KM3NeT detector

Sommaire

2.1 General overview . . . 77
2.1.1 PMT signal digitisation and data transmission . . . 82
2.1.2 On-shore data acquisition system . . . 84
2.1.3 Optical data filtering and triggering . . . 86
2.2 Detector calibration . . . 89
2.2.1 Detection Unit and inter-DOM time calibration . . . 89
2.2.2 Intra-DOM PMT time and efficiency calibration . . . 90
2.2.3 Position calibration . . . 90
2.2.4 Atmospheric muons as calibration source . . . 93
2.3 Monte Carlo simulation . . . 94
2.3.1 Event generation . . . 95
2.3.2 Cherenkov light simulators . . . 97
2.3.3 Detector response simulation . . . 99
2.4 Event reconstruction . . . 100
2.4.1 Track reconstruction . . . 100
2.4.2 Shower reconstruction . . . 101
2.4.3 Reconstruction performance . . . 101
2.5 KM3NeT deployment history and current status . . . 104

2.1 General overview

KM3NeT (Kilometre Cube Neutrino Telescope) is a network of neutrino detectors under construction in the Mediterranean Sea. The detectors achieve sensitivity to neutrino interactions from the MeV to the multi-PeV energy scale, covering an ample variety of science cases. The general reference for KM3NeT design and physics goals is [126].

KM3NeT consists of two detectors. ORCA (*Oscillation Research with Cosmics in the Abyss*), built 40 km off the coast of Toulon (France), is an 8 Mton densely instrumented detector aimed at the (tens of) GeV scale. It is mainly designed for the neutrino mass ordering determination through the measurement of atmospheric neutrino oscillations. ARCA (*Astroparticle Research with Cosmics in the Abyss*), located 80 km from Portopalo di Capo Passero (Italy), is aimed at the discovery of astrophysical neutrino sources in the TeV to PeV range.

Beyond its main physics goals, KM3NeT has a wide range of capabilities. In particular, the main subject of this thesis is the search for supernova neutrino bursts in the 1 – 100 MeV range with ORCA and ARCA. Complementary fields of study for ORCA include the search for sterile neutrinos, CP-violation and signatures of non-standard interactions through the study of neutrino oscillations. Its low energy threshold provides also sensitivity to low energy (GeV-scale) astrophysical neutrinos (e.g. solar flares). At high energy, ARCA can be sensitive to neutrino signatures of the annihilation or decay of dark matter particles in the Sun and Galactic structures. Other studies cover signatures of exotic physics (e.g. magnetic monopoles) and violation of Lorentz invariance.

In total, the KM3NeT detectors will employ as much as ~ 200 000 photomultipliers reaching an instrumented volume at the km^3 scale. Thanks to the high absorption length and low scattering probability of light in water, the directional and timing information carried by Cherenkov photons can be exploited by recording the hit times with nanosecond accuracy.

The KM3NeT design is based on the Digital Optical Module (DOM), a pressure-resistant glass sphere featuring thirty-one 80 mm PMTs with three-dimensional coverage. An illustration of the DOM is given in Figure 2.1 (left). The PMTs are equipped with reflector rings to increase their sensitive area and encased in a 3D-printed supporting structure. A transmissive gel filling ensures the optical coupling between the PMTs and the inner surface of the glass sphere. Each DOM is provided with a custom electronic board responsible for the digitisation, readout and transmission of the PMT signals. Since the detector elements can move under the effect of sea currents, the DOM is equipped with orientation sensors (compass, accelerometer) and acoustic transducers used for real-time positioning.

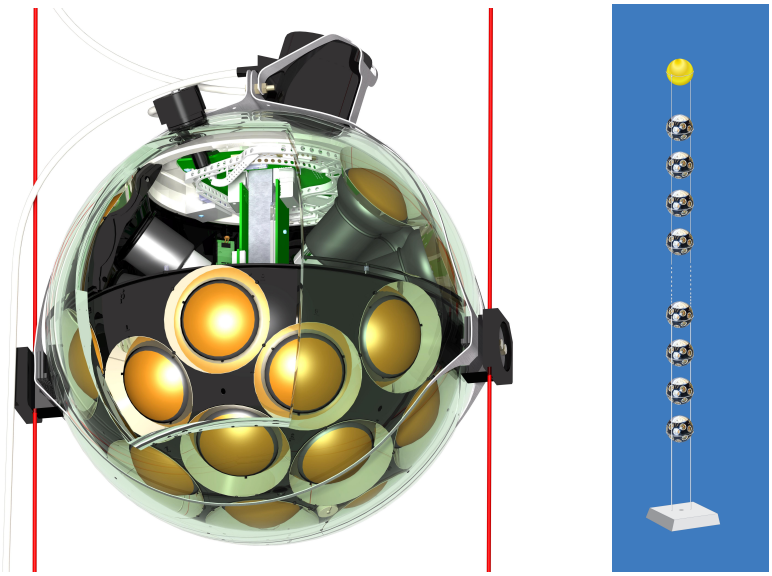

Figure 2.1 – Left: exploded 3D illustration of a KM3NeT digital optical module. Right: illustration of a KM3NeT detection unit.

	ARCA	ORCA
Building blocks	2	1
Detection units	230	115
DOM vertical spacing	36 m	9 m
DU horizontal spacing	90 m	20 m

Table 2.1 – Summary of the geometrical properties of the KM3NeT ARCA and ORCA detectors.

A group of eighteen DOMs is vertically arranged to form a detection unit (DU), as illustrated in Figure 2.1 (right). Each DOM is encircled with a titanium collar connected at opposite sides to two polymer ropes using plastic support structures. The detection unit is anchored to the seabed. A buoy connected to the top contributes to keeping the vertical orientation of the line. The *vertical electro-optical cable* (VEOC) runs along the DU and is connected to each DOM with a pressure-resistant penetrator. The VEOC is an oil-filled plastic tube carrying, for each DOM, an optical fibre for data transfer, a fibre pair for bidirectional exchange of slow control data and two copper wires for the power supply distribution. At the anchor, the VEOC is connected to the *DU base*, a titanium sphere housing the power supply system, the control electronics and the optical network hardware. The DU base interfaces the detection unit to the seafloor network.

A group of 115 detection units is arranged in a quasi-cylindrical array to form a *building block*. ARCA and ORCA share the same DOM design, differing in the instrumentation density and the overall size of the detector array. The average vertical spacing between the DOMs in a detection unit and the mean horizontal distance between the positions of the DUs are optimised for the different energy scales of interest in the two detectors. The ARCA and ORCA detector geometries are summarised in Table 2.1.

Each KM3NeT detector is connected to shore through one or more *main electro-optical cables* (MEOC) consisting of a conductor for power and a bundle of optical fibres for data. The KM3NeT-It (ARCA) seafloor layout is illustrated in Figure 2.2. The ARCA Phase-1 deployment stage consists of 24 DUs connected to the shore by the first MEOC. The MEOC arrives at a *cable termination frame* (CTF) which is connected to the (secondary) junction boxes. DUs are connected to a junction box in a star topology. A second MEOC is foreseen to support the completion of the two building blocks (Phase-2). It will be split at a *branching unit* to serve two CTFs. The ARCA MEOC carries power at 10 kV DC, converted at 375 V DC at the CTF. In a similar hierarchical star topology, each Phase-2 junction box will support seven DUs. The KM3NeT-Fr (ORCA) seafloor layout is shown in Figure 2.3. It employs two MEOCs, where the second will be repurposed from ANTARES. In this, each MEOC is directly connected to a junction box where it is branched out to the next in the chain. Each junction box supports six-to-eight groups of four daisy-chained DUs. The ORCA MEOC supplies

the detector with a single conductor at 3.5 kV AC (the return path being through the sea). The Phase-1 of ORCA consists of six detection units and has been completed in early 2020.

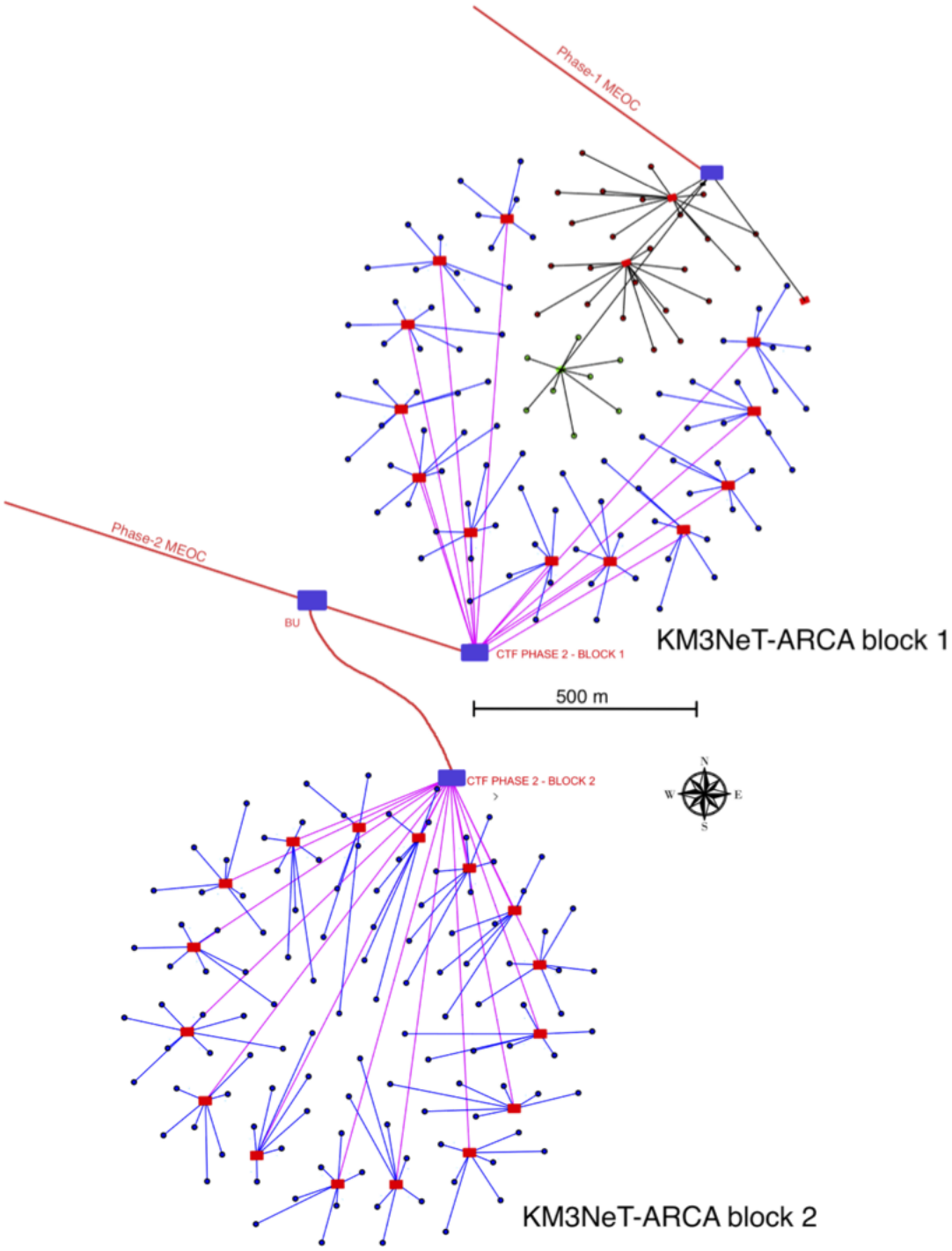

Figure 2.2 – Seafloor layout of the KM3NeT ARCA detector. The *Phase-1* represents the first construction milestone. Source: [126].

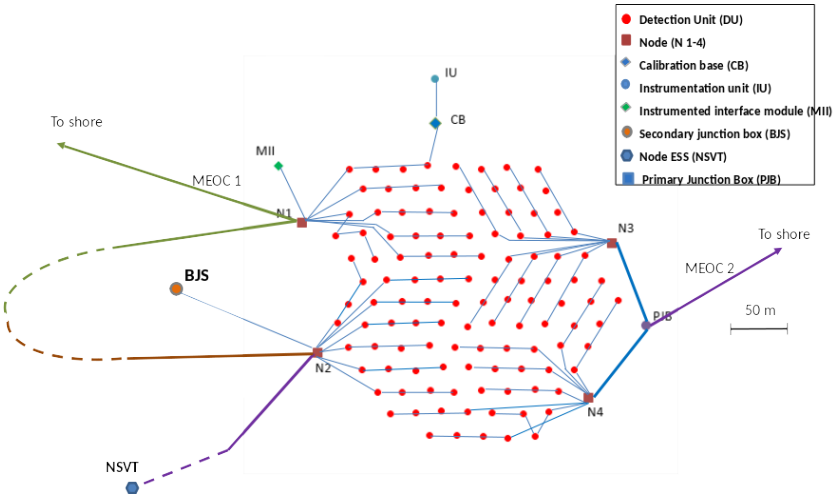

Figure 2.3 – Seafloor layout of the KM3NeT ORCA detector.

2.1.1 PMT signal digitisation and data transmission

In a PMT, photons are detected as they impinge on a photosensitive plate (*photocatode*). A single photon can result in the extraction of an electron (*photoelectron*) by photoelectric effect. The average number of emitted photoelectrons divided by the number of incident photons is referred to as *quantum efficiency* (QE) of the PMT. In general, the QE depends on the wavelength of the incident light. Inside the PMT, the photoelectrons are accelerated towards a conductive plate (*dynode*) held at a higher electric potential. Their impact on the dynode stimulates secondary electrons emission, effectively resulting in an amplification of the charge. The *collection efficiency* for the photoelectron at the first dynode is ~ 0.9. A ladder of dynodes held at stepped values of electric potential is used to repeat the acceleration process and achieve the desired charge amplification. As a result, an electric current pulse is produced at the anode in correspondence of a detected photon. The wavelength-dependent of the KM3NeT PMTs is shown in Figure 2.4. The effective detection of the Cherenkov light is granted by the fact that its spectrum has near-maximum intensity at wavelengths where the PMT is the most efficient (typical QE of ~ 0.25 at 350 nm). Also, this is well beyond the transparency limit the DOM glass (200 nm).

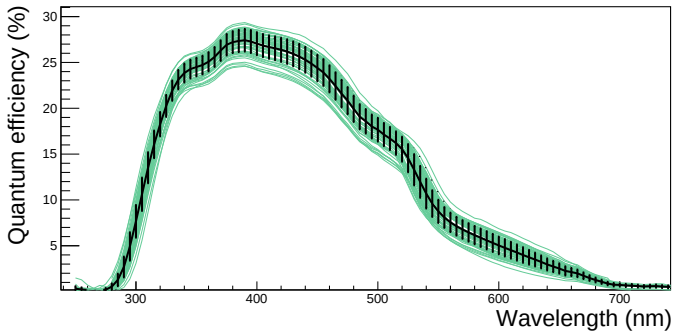

Figure 2.4 – Quantum efficiency as a function of the incident light wavelength from laboratory measurements of Hamamatsu photomultipliers employed in KM3NeT. Source: [157].

On the PMT base printed circuit board, the PMT anodic signal is preamplified and fed to a discriminator. The logic output of the latter is routed to a time-to-digital converter (TDC) implemented in the custom FPGA-based *central logic board* (CLB) of the DOM. Here, the crossing time of the leading edge and the time-over-threshold (ToT) of the pulse (see Figure 2.5) are recorded with nanosecond accuracy. The ToT is proportional to the primary charge extracted at the photocathode, which in turn depends on the number of detected photons. The PMT high-voltage level is tuned in-situ to obtain an average ToT of 26.4 ns for a single photoelectron (corresponding to a typical gain of 10^6). The discriminator threshold is set to an amplitude equivalent to 0.3 photoelectrons.

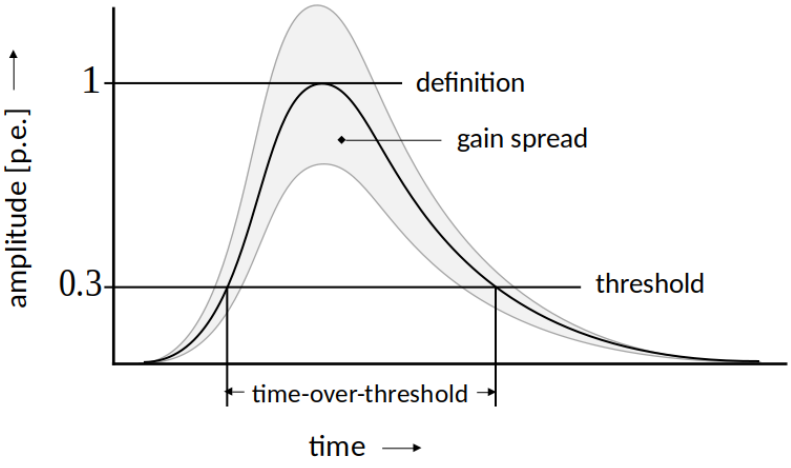

Figure 2.5 – Amplitude response of a KM3NeT PMT to a single photo electron event. Adapted from Reference [158].

Inside the CLB, the data produced by the TDC are buffered in a high-speed *first-in-first-out* (FIFO) memory and queued for the subsequent transmission through the optical network. All the hits occurring in a time interval of 100 ms are grouped in a data frame and sent to shore via the UDP network protocol. The time division is synchronised to a UTC reference distributed to the CLBs via the White Rabbit [159] protocol. As a result, the UTC timestamp of every hit is defined off-shore at nanosecond resolution. (In practice, while the relative timing of the PMTs is exploitable to nanosecond accuracy, the absolute time of the hit will carry the intrinsic uncertainty of the on-shore GPS time reference.)

The counting rate of a KM3NeT PMT in seawater is ~ 7 kHz. This is referred to as *baseline rate* and is determined by the radioactivity-induced optical background. Higher rates can occur due to bioluminescence activity, potentially reaching the MHz scale for several seconds. The *high-rate-veto* (HRV) mechanism of the CLB is programmed to disable the acquisition of a TDC channel as soon as 2000 hits are recorded in a given 100 ms time segment, effectively limiting the rate to 20 kHz. The filling status of the FIFO memory is also monitored, with the possibility to raise an additional veto (*FIFO-almost-full*) in case of saturation induced by high rates.

The hit information consists of 4 bytes for the timestamp, 1 byte for the PMT identifier and 1 byte for the time-over-threshold. In case of a ToT exceeding 255 ns, the corresponding information is split and recorded in the form of consecutive hits. Each DOMs produces on average ~ 13 Mbps of optical data. Every data frame of 100 ms generated by the CLB is assigned a header storing the UTC timestamp and the CLB status information that includes the high-rate-veto and FIFO-almost-full flags for each channel.

The acoustic signal from the piezoelectric transducer of each DOM is sampled at 24 bit / 195,3 kHz with a sigma-delta analogue-to-digital converter and encoded in the standard AES3 protocol. The corresponding data rate is 586 kbps per DOM.

2.1.2 On-shore data acquisition system

KM3NeT follows the *all-data-to-shore* data acquisition (DAQ) concept already adopted in the ANTARES experiment. After the signal digitisation, no data reduction is applied off-shore and all hit data are sent to shore to be processed in a computing farm. The corresponding throughput to an average hit rate of 450 MHz for a KM3NeT is of 27 Gbps. An overview of the KM3NeT *Trigger and Data Acquisition System* (TriDAS) is given in Figure 2.6.

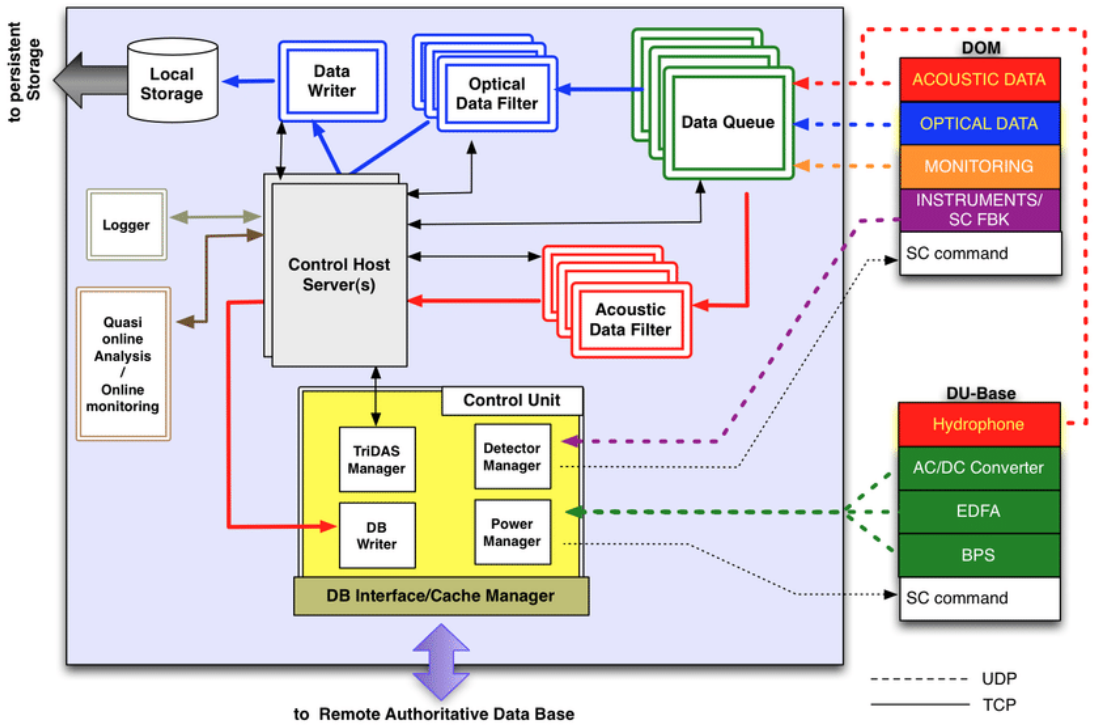

Figure 2.6 – Diagram of the Trigger and Data Acquisition System (TriDAS) of the KM3NeT neutrino detector. Source: [160].

The DOMs produce a stream of optical data, containing all the PMT hit information. DOM and DU bases also produce acoustic data used for positioning. Auxiliary communication channels allow the transmission of monitoring and slow control information. The data sent on-shore are collected by a dedicated multi-threaded software, the *data queue*. The data queue assembles the UDP packets and provides one *frame* per DOM containing the data of a 100 ms time segment. Past the data queue, the TCP protocol is adopted for the data transfer in the shore shtation. The raw data are distributed by the data queue to an array of software *data filters*. The data filters send the data to the DAQ dispatcher, known in KM3NeT jargon as *Control Host Server* or *ligier*. The data distribution by the dispatcher is regulated by a *subscription*-based mechanism. Each client application connecting to the dispatcher declares a list of *tags* identifying the required data streams. Whenever it receives a message associated to a given tag, the dispatcher cycles through all the connected clients and selectively distributes the data according to their respective subscription lists. In the same way, the dispatcher is used to distribute control messages to the different DAQ applications. The entire system operation is orchestrated by the *Control Unit*, a modular software responsible for handling the communication with the detector components, all the TriDAS applications and the interface with the database [161].

2.1.3 Optical data filtering and triggering

The most frequent physics signatures detected in KM3NeT are atmospheric muon tracks at a rate on the order of 100 Hz, against a hit rate of almost half a GHz for one building block. From this, a naive signal-to-noise ratio can be estimated at $\sim 10^{-7}$. The on-shore optical data filtering and triggering stages have to fulfill the demanding task of extracting the physics signatures from the continuous flow of hit data. As they arrive onshore, optical data are referred to as *level 0* (L0). The diagram in Figure 2.7 illustrates the flow of optical (PMT) data in the KM3NeT DAQ. In turn, each data filter processes a 100 ms segment of L0 data received from the data queue, sending the result to the DAQ dispatcher. The data filter output, which is meant for permanent storage and real-time processing, consists of the physics *triggered events* and different selections of hit data (*timeslice data*). A detailed description of its operation is given in the following.

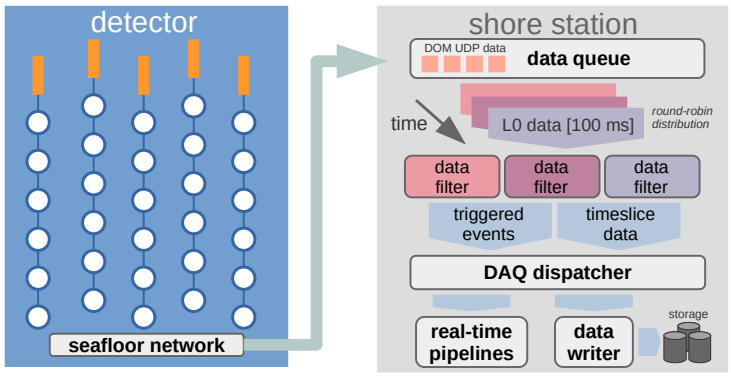

Figure 2.7 – Diagram of the optical data transmission and processing

The first stage of the hit processing is the filtering. Hits originating from PMTs in high-rate-veto or FIFO-almost-full status, recorded before the disabling of the corresponding TDC channels on the DOM FPGA, are discarded. The detector specification provided to the data filter can also require to discard the data of any PMT that needs to be software-disabled for technical reasons. After the filtering, time calibration is applied, following by clustering and selection algorithms at the DOM level. These are meant to build a selection of *local coincidences* that are fed to the trigger algorithms. The logic of the trigger input generalises the definition of *hit*, which can either correspond to a single PMT hit (L0) or to a set of hits that matches a given coincidence criterion. The hit definitions (types) used in the data filter are the following:

L0 hit single hits after time-calibration (220 kHz / DOM);

L1 hit coincidences of L0 hits occurring within 25 ns (typ.) on a single DOM (~ 1 kHz / DOM);

L2 hit L1 hits with at least 2 different hit PMTs within 10 ns (typ.) and 90° degrees (~ 1 kHz / DOM);

SN (*supernova*) L1 hits with at least 4 PMTs within 10 ns or 15 ns (typ.) and 90° degrees (5 Hz / DOM).

The coincidence time windows adopted are configurable, so the values provided refer to the typical operation of the detector at the time of writing. Starting from each 100 ms data segment, the data filter builds an intermediate data structure named *trigger timeslice* for each of the hit type definitions. In particular, L1, L2 and SN trigger timeslices are collections (arrays) of their respective hit types, which in turn are collections (arrays) of L0 hits. The L2 and SN trigger timeslices follow an identical building logic, and differ only in the parameter (minimum number of hits and maximal time difference between hit times).

The L2 and L0 trigger timeslices are the input of the KM3NeT trigger algorithms. These search independently for a minimum number of causally-connected hits across multiple DOMs that match a given event topology. The three trigger criteria are summarised in the following:

3D muon minimum number of causally connected L2 hits, on a minimum number of DOMs, in a cylinder of a given diameter and infinite length; a grid of directions is defined in order to cover the full solid angle with a given granularity;

3D shower minimum number of causally connected L2 hits, on a minimum number of DOMs, within a sphere of given radius;

MX shower minimum number of causally connected L0 hits in coincidence with a single L2 hit within a sphere of a given radius.

The minimum number of L2 hits (and DOMs) required to trigger an event is typically between 3 and 5. It is configured depending on the acceptable background rate for a given detector configuration. In the MX shower trigger, specifically developed to lower the ORCA energy threshold, the minimum number of hits is 8 (1 L2 + 7 L0). For shower triggers, the sphere radius is typically tuned to enclose the first nearest neighbour DOM along the diagonal direction, which translates to a radius of ~ 120 m for ARCA and ~ 50 m for ORCA. In the track trigger, the radius of the cylinder has a length of 125 m) for ARCA and of 38 m for ORCA. When the triggers identifies a cluster of causally-connected hits matching one of the criteria, it produces a data structure (*triggered event*) that stores the corresponding L0 hits (*triggered hits*) plus a collection (*snapshot*) of all the L0 hits occurring in a time window extending the range of the triggered hit times by a few µs (detector size divided by the speed of light in water).

The second type of data that are output by the data filter are *DAQ timeslices*. DAQ timeslices can be generated for any type of L1, L2 or SN trigger timeslice by retrieving all the original L0 hits that are in correspondence with a L1, L2 or SN hit. It should be noted that, whereas the trigger timeslices contain filtered data, the generation of DAQ timeslices is based on the original, unfiltered, L0 hits. In practice, the L1, L2 or SN hits act as *time selections* with respect to the raw L0 data of origin. Any DAQ timeslice always stores a *flat* collection of L0 hits. After the triggering and the generation of DAQ timeslices, the trigger timeslices are discarded. In addition to triggered events and timeslice data, the average rate of L0 hits for each PMT is evaluated and recorded in

a dedicated data structure named *summaryslice*, also storing the high-rate-veto and FIFO-almost-full status flags.

L1 DAQ timeslices data are used for calibration and monitoring purposes. SN DAQ timeslices data offer a low-throughput data stream that is suitable in the search for coincidences induced by low-energy supernova neutrinos. In the standard operational setup, the data filter is configured to output all summaryslices and SN DAQ timeslices. A downsampling is applied to L1 DAQ timeslices, so that only one out of n is kept at the output. The output of the original L0 data in the form of DAQ timeslices is normally foreseen only for short dedicated runs. The building of L2 hits is mainly meant for use in the trigger and, although possible, the generation of L2 DAQ timeslices has no current practical use. On the contrary, SN trigger timeslices have no use in the trigger, and are exclusively used to generate SN DAQ timeslices. From now on, the definition of *timeslice data* will refer to the content of DAQ timeslices. In Figure 2.8 the logic of the hit processing inside the data filter is illustrated.

As a general rule, all the hit data at the output of the data filter are timestamped with their raw, non-calibrated hit times, allowing the application of a best-knowledge calibration set in any later analysis.

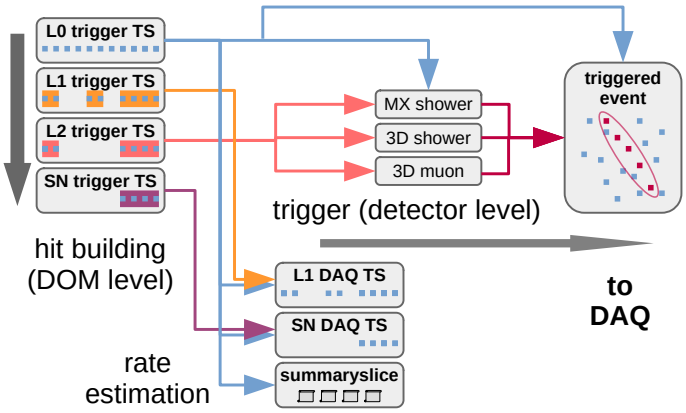

Figure 2.8 – Logic diagram of the data processing in the data filter. The bulding of the different types of trigger timeslices is illustrated, as well as their usage in the production of the different datafilter outputs (triggered events and DAQ timeslices).

The writing of the data to the shore station local storage is performed by the *data writer* software, as it receives the data from the DAQ dispatcher. The data are subsequently copied to redundant remote locations. Online analyses, as real-time event reconstruction or supernova neutrino searches, can be performed by independent applications that subscribe in parallel to the DAQ dispatcher.

2.2 Detector calibration

A rigorous set of *in-situ* calibration procedures is required to ensure the achievement of the scientific goals of KM3NeT. In particular, the angular resolution of the (track) reconstruction is critically dependent on the accuracy of the time and position calibration of the detector elements. The time calibration is required to provide accurate timing of the recorded hits across the whole instrumented volume [162]. In this, the time reference broadcasted from shore to the DU bases and the DOMs needs to be corrected taking into account the time offset of each string, DOM and individual PMT. The individual PMT photon detection efficiency is crucial to a reliable simulation of the detector. Finally, as the strings can move under the effect of sea currents, the position of the DOMs need to be accurately established as a function of time.

2.2.1 Detection Unit and inter-DOM time calibration

To ensure the consistency of the measured hit times across the whole detector, all its active elements need to be time-calibrated. This procedure consists in assigning a time offset to each string, DOM and ultimately individual PMT. The time offset is used to correct the off-shore timestamp of the data in the analysis procedures.

The DU base CLB implements a White Rabbit network interface. The WR protocol uses the measurement of the round-trip-time of the network packets transmitted from shore over the seafloor network to adjust the CLB clock for the propagation delay. Due to the different lengths of the respective optical fibres, each DOM has, in turn, a time offset with respect to the timing reference of the DU base. The White Rabbit synchronisation signal is broadcasted to the DOMs, but the asymmetric topology of the DU optical network does not allow for a WR round-trip-time measurement beyond the DU base. The propagation delay measured for the DU base is assumed as the *time offset* of the DU with respect to the on-shore master clock signal.

The time offset of each DOM with respect to the DU base clock is determined before the deployment of the line with a designated laser setup in a dark room. In this, a sequence of laser pulses is distributed to a reference PMT using optical fibres of identical length. The recorded hit times are compared to estimate the DOM time offsets. When applying the intra-DOM calibration described in section 2.2.2, the reference PMT is assigned a time offset of zero (with respect to the DOM) to establish the consistency between the intra-DOM and inter-DOM time calibrations. A backup reference PMT is usually laser-calibrated before the deployment, but only one at a time is used in the calibration procedure.

The result of the laser calibration is verified and corrected in-situ after the deployment. This procedure exploits the LED beacon (*nanobeacon*) installed on the upper hemisphere of each DOM. With a dedicated run configuration, the CLBs are programmed to flash the LED beacon at a given frequency synchronised to the detector global clock. The detection time of the corresponding light on the overlying DOMs can be used to independently check their respective time offsets.

2.2.2 Intra-DOM PMT time and efficiency calibration

The time of each recorded hit is dependent on the transit time of the individual PMT and front-end electronic channel. The transit time distribution for a population of hits on the same PMT is nearly-gaussian. Different PMT channels exhibit different mean values of the distribution. The relative *time offset* ($t0$) of each channel is defined as the difference between its mean transit time and the one of the designated reference PMT for the DOM. The standard deviation of the transit time distribution is referred to as *transit time spread* (TTS). The TTS of KM3NeT PMTs has been measured in the laboratory to be of 2.1 ns and can be considered identical for each PMT in a good approximation.

The overall *photon detection efficiency* of a DOM-mounted PMT is determined by the light collection of the reflector ring, the optical absorption in glass and optical gel, the individual QE dispersion and the collection efficiency of photoelectrons at the first dynode. The combination of these effects is estimated by *in-situ* calibration of the individual PMT.

The majority of photons detected by the DOM comes from radioactivity, dominated by the decay of the ^{40}K isotope present in sea salt. Other sub-dominant contributions come from the ^{40}K in the glass and products of the ^{238}U decay chain both in glass and water. As salinity is constant in time and across different sites, seawater natural radioactivity represents an excellent source for the in-situ calibration of the detector. The Cherenkov photons induced by radioactive decays hit the DOM almost simultaneously. The coincidence rate detected by a pair of PMTs (i, j) is proportional to the product of their respective photon detection efficiencies $\epsilon_i \cdot \epsilon_j$ and a factor $f(\theta_{i,j})$ reflecting the coincidence rate as a function of the opening angle between the PMT axes. This is estimated through `OMGSim`, a detailed DOM simulation accounting for the different radioactivity sources (see also Section 2.3.2). An example is given in Figure 2.9. The distribution of the time differences between the hits in coincidence has a nearly-gaussian shape with area $f(\theta_{i,j}) \cdot \epsilon_i \cdot \epsilon_j$, mean $t0_i - t0_j$, and variance $(TTS_i)^2 + (TTS_j)^2 = 2 \cdot (TTS)^2$. By simultaneously fitting the distributions of the 465 individual PMT pairs of a DOM, the time offsets and photon detection efficiencies of each PMT can be determined with a joint procedure referred to as *intra-DOM calibration*. By construction, the procedure allows determining only the relative time offsets, which globally sum to zero. The distribution of the time difference between hits in coincidence detected on a typical pair of nearby PMTs is shown in Figure 2.10. The data before (red) and after (blue) time calibration are shown along with the fit result (black). In order to estimate $\epsilon_i \cdot \epsilon_j$.

2.2.3 Position calibration

As the detector elements can move under the effect of sea currents, a real-time calibration of the DOM positions and orientation is implemented. To this purpose, an array of acoustic sensors is employed. An overview of the KM3NeT acoustic position-

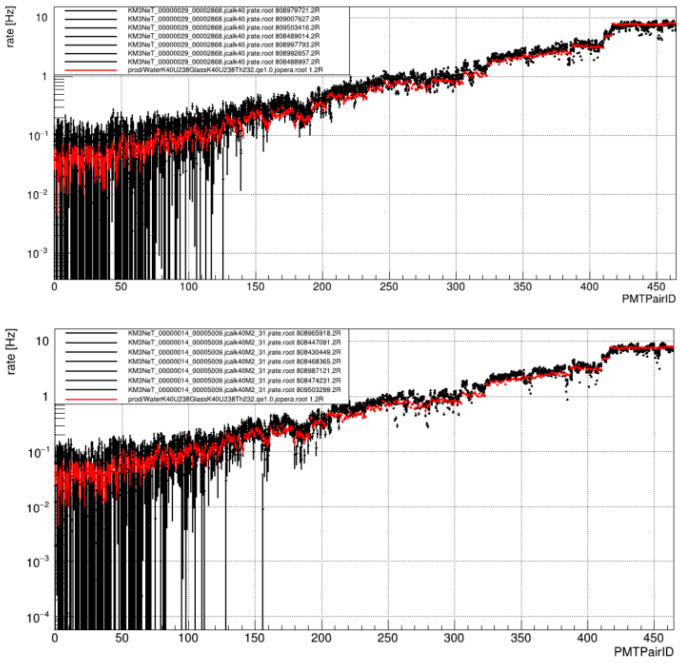

Figure 2.9 – Coincidence rate as a function of the PMT pair (ordered by opening angle) for a complete simulation of radioactivity compared with data from ARCA2 and ORCA1 detectors. Author: V. Kulikovskiy

ing system is given in Reference [164]. Each DU base is featured with a hydrophone and each DOM with a piezoelectric acoustic transducer. Autonomous beacons are installed on the seafloor at a given distance from the detector. The beacons generate acoustic signals with a constant repetition rate. The acoustic data continuously acquired by the hydrophones and the piezoelectric transducers are sent to shore and collected by the data queue.

The data queue distributes the acoustic data to an array of software acoustic data filters (ADF). In this, a continuous cross-correlation is performed between the incoming audio stream and a predefined template of the beacon signal waveform. When the value of the cross-correlation function is detected to be above a given threshold, the corresponding time is registered as *time of arrival* (ToA) of the signal. The maximum of the cross-correlation is the *quality factor* of the ToA. The ToAs produced by the ADF are distributed to the dispatcher and subsequently collected to be uploaded in the central KM3NeT database system. In the following analysis, the ToAs are processed to produce a position calibration. After a quality selection, they are fed to *multilateration* algorithm. In this, the measured times of arrival (ToA) and the known beacon positions ($\vec{B}_j$) are combined with the unknown times of emission (ToE) and receiver positions ($\vec{R}_i$) in a target function (Δ^2). The function is written as the sum of the squared differences between the experimental time of flight of the acoustic signals

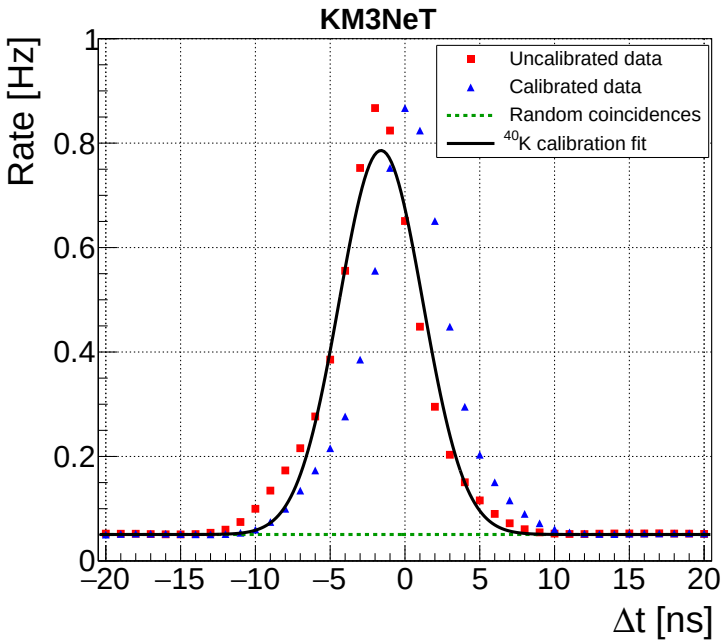

Figure 2.10 – Distribution of the time differences between the hit in coincidences for a pair of near-by PMTs for uncalibrated (red) and calibrated (blue) hit times. Superimposed are the calibration fit (black) and the background of random coincidences (green) with uniformly distributed time differences. Source: [163].

and their geometrical expectation:

$$\Delta^2(\{R_i\},\{\mathrm{ToE}_j\}) = \sum_{i,j}\left(\mathrm{ToA}_{ij} - \mathrm{ToE}_j - \frac{||\vec{R}_i - \vec{B}_j||}{c_0}\right)^2 \tag{2.1}$$

where c_0 is the speed of sound in water. A minimisation of Δ^2 yields the best fit for the set of receiver coordinates. The accuracy of the ToAs determined with the piezoelectric transducers is around 300 μs, corresponding to a position uncertainty of 50 cm. Since the movements due to sea current occur on relatively slow time scales, a median value can be estimated over a time scale of a few minutes, lowering the uncertainty to 50 μs. In Figure 2.11 the result of this median filtering is shown for the lower DOM of a deployed ARCA detection unit. The dispersion of the points represents the uncertainty on the determination of the time of arrival. The overall trend shows the movement of the detector element over a time frame of 48 hours.

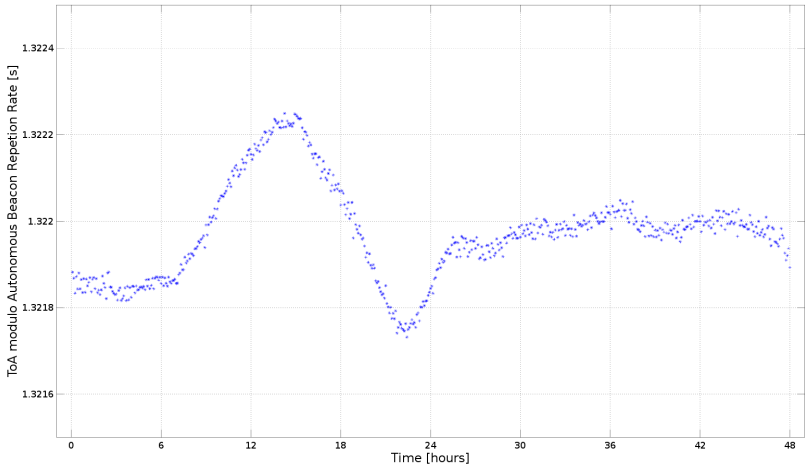

Figure 2.11 – Five-minute median values of the measured time of arrival modulo repetition rate of the autonomous beacon for the lower DOM of the first ARCA detection unit. Source: [164].

Data from the compass and accelerometer of the DOM CLBs are integrated into a *attitude and heading reference system* (AHRS). These data are used onshore to reconstruct the orientation and tilting of the DOMs. Combining with the results of the coordinates obtained from the acoustic positioning, the overall position calibration of the string is determined [165].

2.2.4 Atmospheric muons as calibration source

Atmospheric muons represent a stable source of background events that can be used as a calibration source. Given the well understood track-like topology, the reconstruction quality for this class of events is a good estimator of the overall detector

calibration [162]. In general, the time residual distributions of the reconstruction hits can be examined to find calibration errors. The quality of the reconstruction can be evaluated as a function of defined variations in the calibration parameters (DOM and DU time offset, DU position, DU length) to estimate the optimal calibration parameter set and cross-check the results of the instrumental procedures. An example is given in Figure 2.12, where the average likelihood of reconstructed muon events is evaluated as a function of an assumed time offset (w.r.t. to calibration) between the first two detection units of the ORCA detector. The maximum of the likelihood is found to be within 0.5 ns from the calibrated offset.

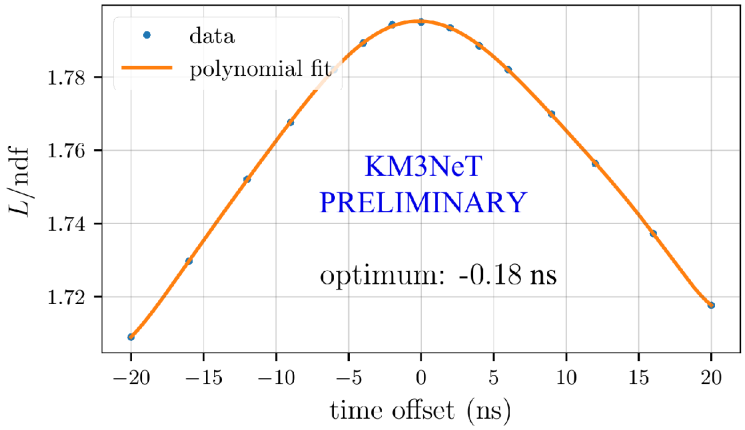

Figure 2.12 – Average likelihood divided by the number of degrees of freedom as a function of the assumed time offset between two detection units of the ORCA detector. Source: [162].

2.3 Monte Carlo simulation

The KM3NeT Monte Carlo framework is designed to simulate the detector response to the different classes of relevant physics events: atmospheric muons, atmospheric neutrinos and astrophysical neutrinos. The simulation chain is articulated on three main stages: the event generation, the charged particle propagation with the production of Cherenkov light and the simulation of detector response. At the last stage, the data taking conditions can be accounted for through a *run-by-run* simulation, based on the sampling of the *summaryslice* stream from a corresponding run file. An overview of the simulation chain is given in Figure 2.13. In the following, the different stages and the main applications are described.

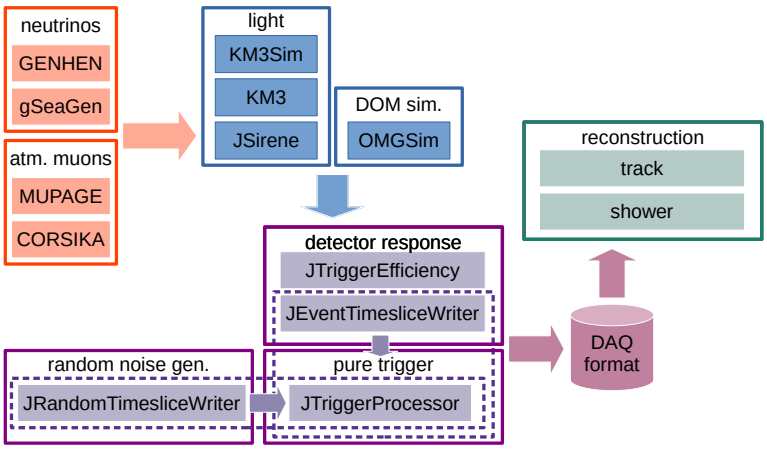

Figure 2.13 – Overview of the KM3NeT Monte Carlo chain

2.3.1 Event generation

Event generation is the first step of the simulation chain. Its purpose is to simulate neutrino interactions and atmospheric muons. The event generators produce charged particles that can be propagated in the light production stage.

To the purpose of event generation, an active volume commonly referred to as *can* is defined. The can is sized to cover the volume in which the produced light could be detected by the optical modules. The usual choice is a multiple between four and five of the light absorption length in water. Atmospheric muons are generated on the boundary surface of the can. Neutrino interactions yielding shower-like (neutral current and charged current ν_e) events are simulated with a uniform distribution within the can volume. Neutrino interactions producing muons directly (charged current ν_μ) or indirectly (charged current ν_τ) are generated in an interaction volume that encloses the can plus the muon maximum range in water and Earth crust along the three dimensions. A representation of this design is given in Figure 2.14. An accurate model of the Earth density is required to evaluate the transmission probabilities of neutrinos.

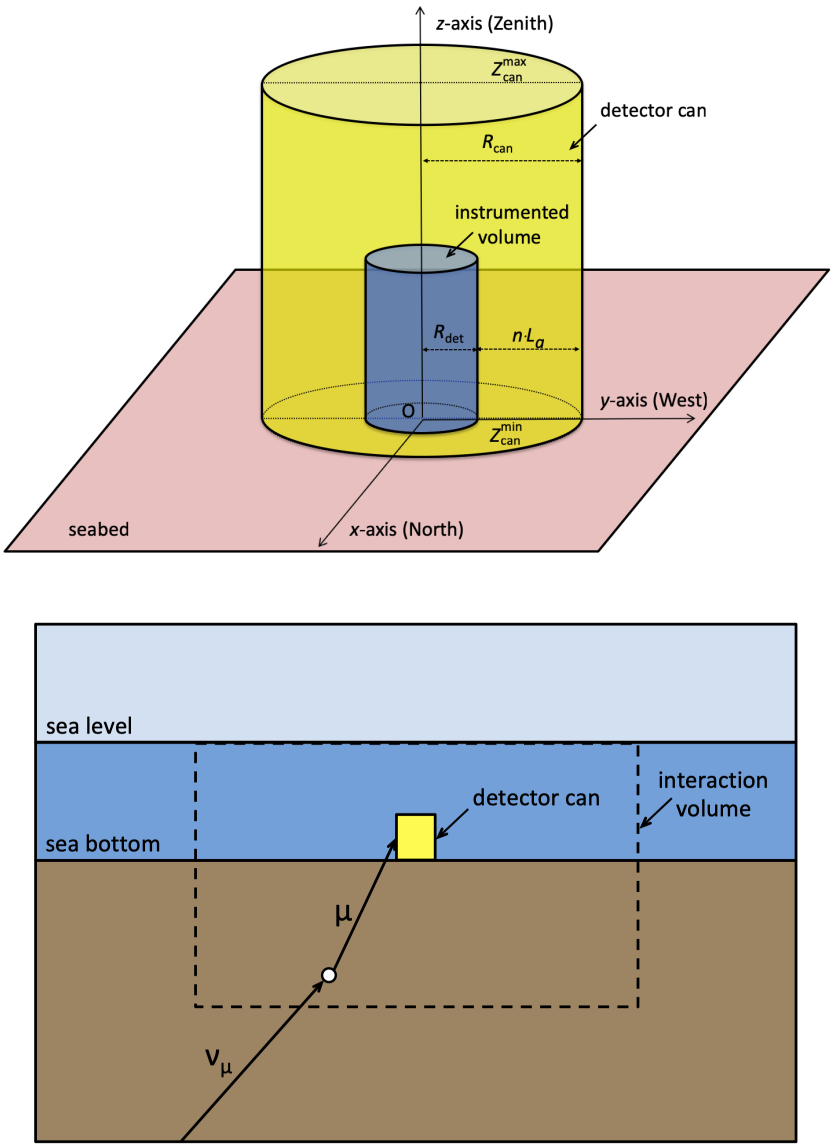

Figure 2.14 – Representation of instrumented volume, can and interaction volume in the context of event generators. Source: [166].

The normalisation of the flux of generated events is treated differently for atmospheric muons and neutrinos. The atmospheric muon flux is simulated corresponding to a given detector *live time*. Neutrinos are generated with a designated power-law spectrum which is not necessarily the one used in the final analyses. The inverse of the spectral density is carried in the *generation weight*, W_{gen}, of each neutrino event. For the purpose of the analysis procedure, events are re-weighted multiplying W_{gen} by the required neutrino spectrum $\phi(E_\nu, \theta_\nu)$ [167].

A summary of the standard event generators used in KM3NeT follows.

MUPAGE [149] is a fast and lightweight software implementing a simulation of the underwater muon flux based on a parametric formula. The parameterisation used in MUPAGE is derived from a full Monte Carlo simulation of primary cosmic ray showers based on the HEMAS code, cross-checked with data from the MACRO experiment. In MUPAGE, single muons and muon bundles are generated on the surface of a cylinder surrounding extending the instrumented volume by a distance of a few absorption lengths.

CORSIKA [168] is a complete Monte Carlo simulations for cosmic-ray air showers that can be used to simulate atmospheric muon fluxes. Given its much higher computational requirements, its dedicated to muon analyses requiring the simulation of detailed EAS physics, as in cosmic-ray composition studies. It can also be used for data - Monte Carlo comparisons and exploited to tune the MUPAGE input parameters.

gSeaGen [166] is a GENIE-based generator for neutrino-induced events oriented to underwater neutrino detectors. It simulates different types of high energy interactions for all neutrino flavours, taking into account the density and composition of the media surrounding the instrumented volume. It is suitable for simulations between 0.1 GeV and 5 TeV of energy, so it is the generator of choice for ORCA. An extension to higher energies is in preparation.

GENHEN [169] is the neutrino generator for high energy interactions up to 10^9 GeV developed for the ANTARES neutrino detector. It is used for ARCA high energy astrophysics studies.

2.3.2 Cherenkov light simulators

At this stage, the primary leptons produced at the generation stage are propagated in the detector volume, simulating the energy losses and the production of Cherenkov light. The most general approach (as in GEANT-derived simulations) is to simulate the propagation of a charged particle in a medium is decomposing its path in discrete steps with a designated resolution. At each step, the relevant physical processes are evaluated. These include energy losses by ionisation and radiative processes. Where applicable, secondary particles are also produced, like electrons and photons participating in electromagnetic showers or delta rays for muons. The simulation of Cherenkov light in the medium produces optical photons that are tracked, given a model of the water properties. In this, the optical trajectory is constructed by sampling segments according to the absorption and scattering lengths of seawater. An alternative approach, allowing for much faster computation, consists of generating the hits on a PMT according to the multidimensional probability density function of their time of arrival, previously evaluated as a function the type of the interaction and the distance (see Figure 2.15).

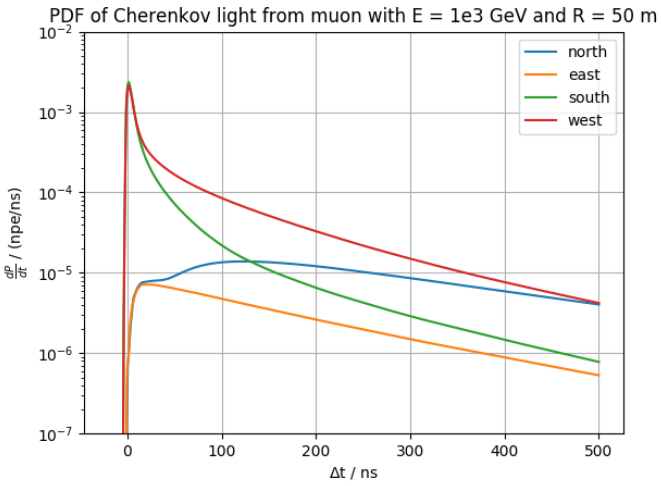

Figure 2.15 – Probability density function (PDF) of the time of arrival of Cherenkov photons from a muon interaction as a function of the PMT orientation.

A unidimensional parameterisation of the PMT angular acceptance accounts for the effects of the DOM structure, such as the absorption in the glass and optical gel, and the contribution of the reflector ring to the light collection. Finally, the wavelength-dependent quantum efficiency of the PMT is considered in the generation of the photoelectrons. In a first approximation, angular acceptance and quantum efficiency can be considered as independent multiplicative factors. A more detailed two-dimensional parameterisation of the global efficiency as a function of the photon wavelength and incidence angle can be optionally adopted. In the following, the main Cherenkov light simulation packages used in KM3NeT are described.

OMGSim [170] is a complete and detailed GEANT4 simulation of the DOM, oriented to the study of its response in seawater. It is mainly oriented to the characterisation of the radioactive backgrounds, providing a reliable model for the in-situ calibration of the detector.

KM3Sim is based on the HOURS [171] package; it implements a full GEANT4 simulation of the instrumented volume suitable for low energy neutrino interactions. Each DOM is modelled as a set of flat discs representing the PMT photocathodes.

KM3 [169] is a software package that makes use of tabulated results of GEANT3.21 simulation for segments of relativistic muon tracks and electromagnetic showers in water.

JSirene is part of the custom KM3NeT software suite Jpp; it is a fast Cherenkov light simulator exploiting tabulated probability density functions for the arrival times of photons from muons, tau particles and electromagnetic showers. In addition to the light induced by a particle in the minimum ionising regime, the simulation of delta rays and Brehmsstralung radiation is implemented in native code.

2.3.3 Detector response simulation

At the light production stage, *Monte Carlo hits* are produced from the impinging photons. From a physical perspective, a Monte Carlo hit is equivalent to a photoelectron produced at the photocathode of the PMT. Following this, the simulation of the detector response is articulated in three phases: (i) the conversion of *Monte Carlo hits* in *DAQ hits*, (ii) the simulation of the optical background and (iii) the application of data filtering and triggering algorithms to the simulated data. This part of the detector simulation is implemented via a set of classes and applications part of the ROOT-based KM3NeT software suite Jpp.

The Monte Carlo hits are processed on an event-by-event basis. The *relative* photon collection efficiency ϵ resulting from the calibration procedure is introduced as a factor to determine the effective hit probability for each PMT. If the hit survives the hit probability, a corresponding electric signal is simulated accounting for the PMT gain and gain spread. In case of one or more photoelectrons occurring within the ToT of the first hit, the hits are merged in a single pulse whose amplitude is parameterised according to the characterisation of the PMT response from laboratory measurements. If the final amplitude is above the discriminator threshold (0.3 p.e.), the corresponding hit time and ToT data are generated. Here, the hit time accounts for the transit time distribution. When atmospheric muons or neutrino interactions are simulated, the optical background is added according to fixed rates of single hits and coincidences. At this last stage, a *run-by-run* simulation can optionally be performed. In this, the summaryslice data from a run file are randomly sampled to simulate a realistic data taking condition for every triggered input event. The individual PMT counting rates are used to simulate the optical background, and channels are disabled according to the high-rate-veto flags in the sampled data. Non-functional PMTs are disabled according to the detector description file. Once all the hits in an event have been simulated, the corresponding data are processed by the same clustering and triggering algorithms applied to the real data, described in Section 2.1.2. The final data format is identical to the one produced by the detector data acquisition system and can be processed with the corresponding analysis pipelines. A summary of the Jpp application used in this stage is given in the following.

JTriggerEfficiency is the application adopted for standard muon or neutrino event simulation. For each input event, a *snapshot* of background hits is generated and the input Monte Carlo hits are added after processing. The data filtering and triggering algorithms are applied to the sequence of generated hits. A corresponding DAQ timeslice can be optionally written. Each event is simulated independently.

JRandomTimesliceWriter generates a sequence of DAQ timeslices consisting only of optical background. It is used to evaluate the contribution of random noise to triggered events.

JEventTimesliceWriter generates a sequence of DAQ timeslices in which the input events are distributed according to a designated event rate or their absolute

time defined in the Monte Carlo information. It is especially useful to study high-rate time-dependent signals as supernova neutrino bursts.

JTriggerProcessor applies the data filtering and triggering algorithms to DAQ timeslice data. It is usually run in tandem with either by `JRandomTimesliceWriter` or `JEventTimesliceWriter` to trigger the generated timeslice data. It can also be applied to DAQ file, provided that the timeslice data necessary to the trigger algorithms have been stored.

2.4 Event reconstruction

The event reconstruction in KM3NeT is based on the fit of a model to the positions and times of arrival of the hits at the PMTs. The model represents a Cherenkov cone developing along the track for a muon or at the vertex for an electromagnetic shower.

2.4.1 Track reconstruction

The track reconstruction is described in Reference [172] and [173]. The first stage of the track reconstruction is the *prefit*. The 2π hemisphere is divided into a fixed grid of N directions. For each direction, the χ^2 given by the difference between the measured and expected times of arrival of the photons on the optical modules is evaluated. Taking the z axis as parallel to the muon direction, the prefit estimates the position and the crossing time of the muon with reference to an arbitrary orthogonal plane xy: $\{x_0, y_0, t_0\}$. Causally connected hits are selected to avoid the result being biased by optical backgrounds. A designated number of prefit results, ranked by quality, is chosen as an input to the following reconstruction stage.

The core of the reconstruction is the `JGandalf` algorithm. Starting from the prefit result, two free parameters, T_x and T_y, are added to represent the direction cosines in the two coordinates. The five parameters now identifying the muon direction, $\{x_0, y_0, t_0, T_x, T_y\}$ are fitted by considering the likelihood function:

$$\mathscr{L} = \prod_{i \in \text{hits}} \mathscr{F}(E, R_i, \theta_i, |\phi_i|, \Delta t_i \mid x_0, y_0, t_0, T_x, T_y) \tag{2.2}$$

where $\mathscr{F}$ is a five-dimensional probability density function estimated semi-analitically. In this, E is the muon energy, $R_i = \sqrt{(x_i - x_0)^2 - (y_i - y_0)^2}$ the distance of closest approach of the muon to the DOM, $(\theta_i, |\phi_i|)$ the angles defining the PMT orientation and Δt_i the difference between the measured and expected time of arrival of the photon. The estimation of the maximum likelihood is a non-linear optimisation problem, solved with the Levenberg-Marquardt [174, 175] algorithm.

2.4.2 Shower reconstruction

The shower reconstruction principle is here illustrated taking as an example the case for ARCA as described in Reference [172]. In the first step, the time of the hits are used to reconstruct the shower vertex. Considering a spherical wavefront, a *M-estimator* for the vertex position is defined as:

$$\mathscr{M} = \sum_{i \in \{hits\}} \sqrt{1 + (t_i - \hat{t}_i)^2}\,;\ \hat{t}_i = t_0 + \frac{n}{c} r_i \tag{2.3}$$

where $\hat{t}_i$ is the expected time of arrival of the hit considering the distance from the vertex, r_i, the speed of light, c, and the water refraction index, n. The shower direction and energy are estimated by considering all the PMTs and their *hit* vs. *nonhit* condition. In particular, the log-likelihood estimator is defined as:

$$\log \mathscr{L} = \sum_{i \in \{\text{nonhit PMTs}\}} \log\left(p_i^{\text{nonhit}}\right) + \sum_{i \in \{\text{hit PMTs}\}} \log\left(1 - p_i^{\text{nonhit}}\right). \tag{2.4}$$

In this, the Poisson-derived probability of a *no-hit* condition, p_i^{nonhit} is given by:

$$p_i^{\text{nonhit}} = e^{-\mu_s(r_i, z_i, a_i, E_s) - R_b T} \tag{2.5}$$

where R_b is the background rate of the PMT, T is a time window $[-100, +900]$ ns centered on the expected hit time and $\mu_s(r_i, z_i, a_i, E_s)$ is the probability density function of the expected number of photons on the PMT i. This is defined as a function of the shower energy E_s and the coordinates of the PMT, (r_i, z_i, a_i) in a designated reference frame originating at the vertex (see Reference [172] for its definition). In practice, the dependence of μ_s as a function of E_s is assumed to be plainly linear, and the energy is fitted as a simple scaling factor. The shower fit is performed starting from a set of isotropic directions. In the case of ORCA, the algorithm is designed to reconstruct also the shower inelasticity (*Bjorken-y*) [176].

2.4.3 Reconstruction performance

For the ARCA detector, the resolution in direction and energy of ν_μ tracks is shown in Figure 2.16. A remarkable median error below 0,1° is achieved for energies above 100 TeV. The ARCA reconstruction performance for ν_e showers is reported in Figure 2.17. It achieves a 5% resolution on the energy and a sub-2° angular resolution on the shower direction.

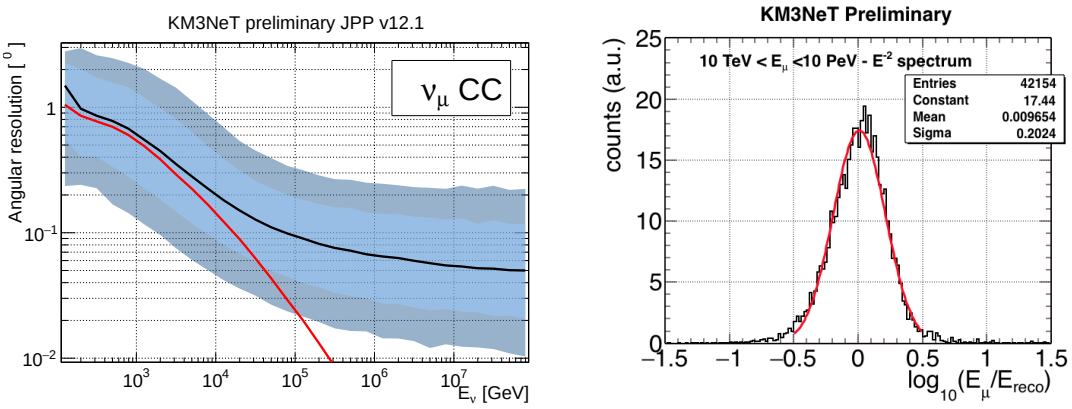

Figure 2.16 – Left: median of the angle between the neutrino and the reconstructed muon direction (black line) and between the neutrino and the true muon direction (red line), for selected ν_μ charged-current events. The dark and light blue bands represent the 90% and 68% quantiles of the distributions. Right: distribution of $\log_{10}(E_{\text{reco}}/E_\mu)$ where E_{reco} is the reconstructed and E_μ is the true muon energy for events with $E_\mu \geq 10\,\text{TeV}$ that satisfy a containment criterion. The red line represents a Gaussian fit.

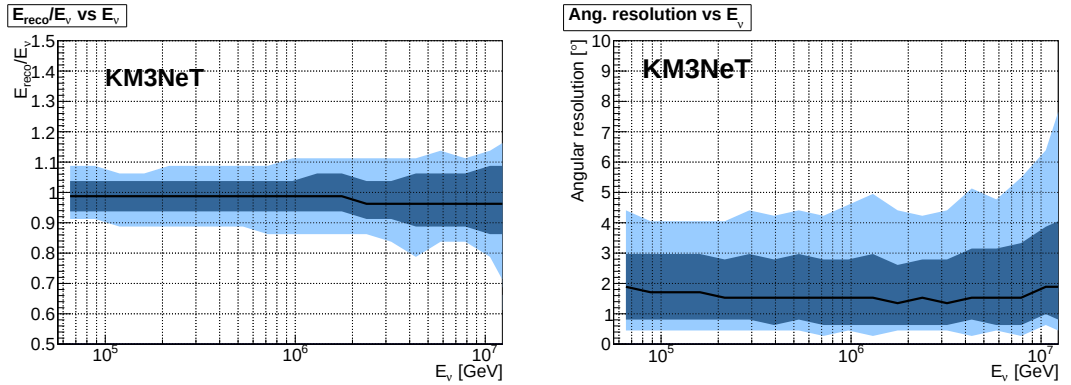

Figure 2.17 – ARCA resolutions for a selection of contained ν_e charged-current. Left: energy resolution, right: directional resolution. For both plots, the black line shows the median value; dark blue shaded regions give the 68% range, while light blue shaded regions give the 90% range. Source: [126].

For ORCA, the angular and energy resolution are reported in Figure 2.18 and Figure 2.19 for the $1-50\,\text{GeV}$ energy range considered in oscillation analyses.

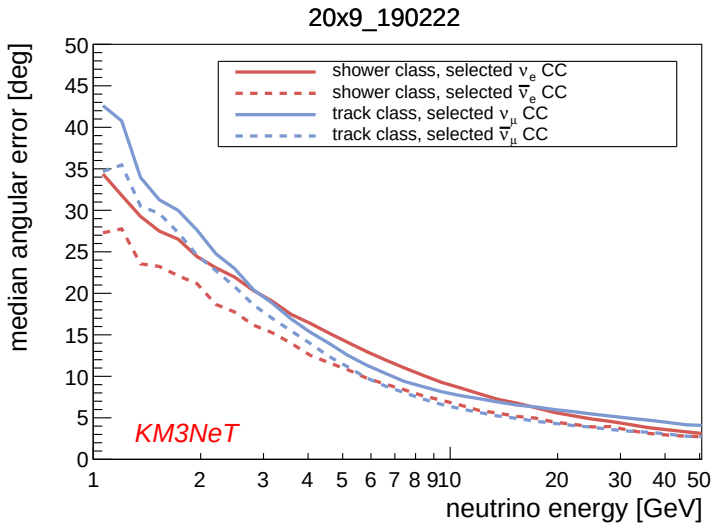

Figure 2.18 – ORCA reconstruction performance: median angular error as a function of the neutrino energy in the 1-50 GeV range for different classes of ν_e, $\overline{\nu}_e$, ν_μ and $\overline{\nu}_\mu$ events.

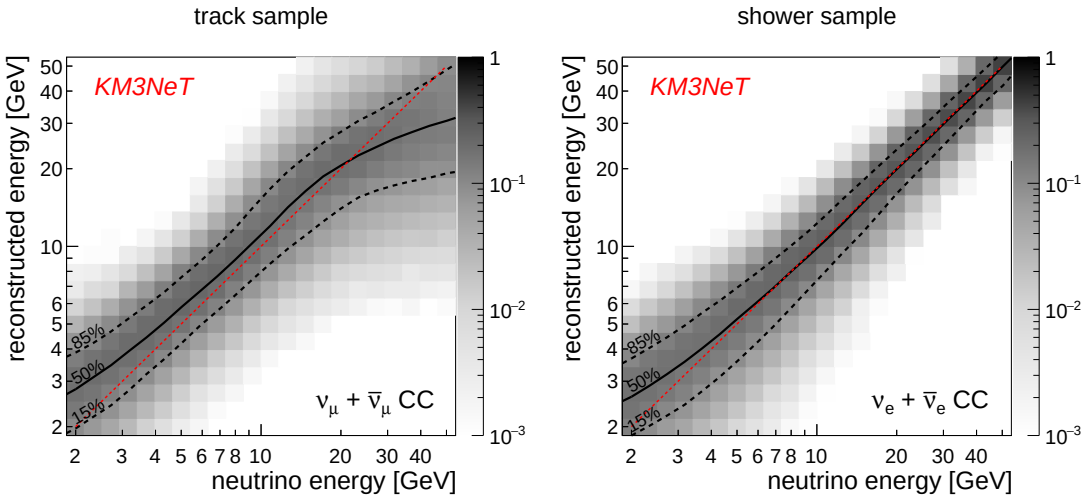

Figure 2.19 – ORCA reconstruction performance: reconstructed energy as a function of the neutrino energy for ν_μ (left) and ν_e (right) charged-current interactions. 15%, 50% and 85% contours are traced. The outgoing lepton energy is indicated with a red dashed line.

2.5 KM3NeT deployment history and current status

The pre-production model of the KM3NeT Digital Optical Module (PPM-DOM) was deployed in the sea in 2013, integrated to the ANTARES detector [177]. A pre-production detection unit (PPM-DU) consisting of three DOMs was operated between May 2014 and July 2015 at the KM3NeT-It site [178]. The PPM-DU allowed to test the DOM calibration routines and provided the first data on reconstructed atmospheric muons.

The first DU of the ARCA detector was deployed in December 2015, followed by two DUs in May 2016. The vertical alignment of the DUs was confirmed by visual inspection using the ROV. Data taking started immediately after deployment. One of the units deployed in May 2016 was recovered for inspection in July 2016. Due to electrical problems in the network infrastructure at the seabed, the operations at the KM3NeT-It site were on hold between April 2017 and January 2019, after which data taking resumed. Operations at the ARCA site stopped again in November 2019 for a renovation works at the shore station, which is still on-going at the time of writing.

The first DU of ORCA was installed in September 2017 and operated until mid-December 2017, when a failure of the main electro-optical cable occurred. The data taking was resumed in February 2019 following the replacement of a part in the main cable [163]. Four further ORCA DUs were deployed between May and July 2019, while the first DU had to been recovered due to accidental damage. In January 2020 two more ORCA DUs have been deployed, bringing the total of active strings to six. As of October 2020, ORCA detector has been continuously operating six lines for eight months.

3 Dependence of the atmospheric muon flux on seawater depth

In this chapter, the KM3NeT digital optical module is characterised as a stand-alone detector. A measurement of the total muon flux as a function of the seawater depth using data from the first KM3NeT detection units is presented. Being based on low-level data, this study is instrumental to verify the *in-situ* performance and calibration of the KM3NeT detector elements. It also provides a series of benchmarks on the accuracy of Monte Carlo simulations for the Cherenkov light from atmospheric muons.

An overview of the atmospheric muon flux is given in Section 3.1. The coincidence rates across the 31 PMTs of the DOM are illustrated in Section 3.2. The data sample used in the analysis is introduced in Section 3.3. The measured coincidence rates are shown in Section 3.4. The evaluation of the muon-induced rates of depth and their comparison with the depth dependence of a muon flux model is presented in Section 3.5. The estimation of the DOM effective area is done in Section 3.6 and the measurement of the absolute muon flux is performed in Section 3.7. The systematic uncertainties considered are discussed in Section 3.8.

This analysis has been developed by the Author, following a preliminary work by Martijn Jongen [179]. It has been peer-reviewed and published on *European Physical Journal, C* [163]. The Author is a corresponding author for the collaboration, together with S. Biagi and K. Melis. This publication represents the first measurement performed with KM3NeT data.

Sommaire

3.1 Atmospheric muon flux underwater 106
3.2 Characterisation of DOM coincidence rates 109
3.3 KM3NeT ARCA2 and ORCA1 data sample 111
3.4 Coincidence rates in ARCA2 and ORCA1 113
3.5 Depth dependence of the atmospheric muon flux 117
3.6 Estimation of the DOM effective area 120
3.7 Absolute measurement of the atmospheric muon flux 123
3.8 Evaluation of systematic uncertainties 124

3.1 Atmospheric muon flux underwater

Atmospheric muons emerge from *air showers* produced by the interaction of primary cosmic rays in the upper atmosphere. The same hadronic processes are involved in the production of atmospheric muons and atmospheric neutrinos. The main component of the muon flux is given by the decay of π and K mesons. More precise studies on the high-energy part of the spectrum have brought evidence for the existence of a so-called *prompt* muon flux from the decay of short-lived charmed hadrons [180].

The atmospheric muon flux is characterised by an intensity and energy distribution which are dependent on the zenith angle, θ. In Figure 3.1 the angular distribution at the sea level is shown for different muon energies. The overall angular distribution at the ground (sea level) is $\propto \cos^2\theta$, dominated by muons with energy $E_\mu \sim 3\,\text{GeV}$. The lower part of the energy spectrum has a steeper angular distribution. At higher energy it flattens, approaching a $1/\cos\theta$ distribution for energies much above the pions critical energy and $\theta < 60°$. At large angles low energy muons decay before reaching the surface and high-energy pions decay before they interact, yielding muons with higher average energy.

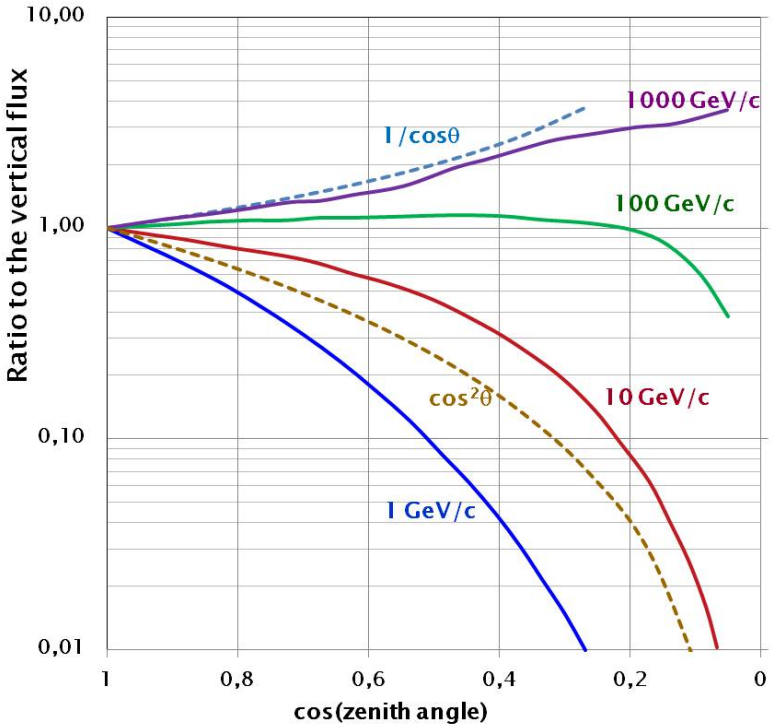

Figure 3.1 – Angular distribution of muons at the ground for different muon energies based on measurements and Monte Carlo simulations. Source: [181].

The estimation of underground or underwater fluxes is further complicated by the calculation of energy losses in the medium, yielding depth-dependent variations of

the flux intensities. The contribution of different energy loss processes of a muon in water is illustrated in Figure 3.2. Below 100 GeV, the muon can be considered a *minimum ionising particle* with a typical energy loss of $\sim 0{,}2\,\mathrm{GeV\,m^{-1}}$. Above 1 TeV, radiative processes (Bremsstrahlung, pair productions, photonuclear) dominate over ionisation. Ionisation losses are uniform along the muon trajectory, while radiative processes present stochastic fluctuations.

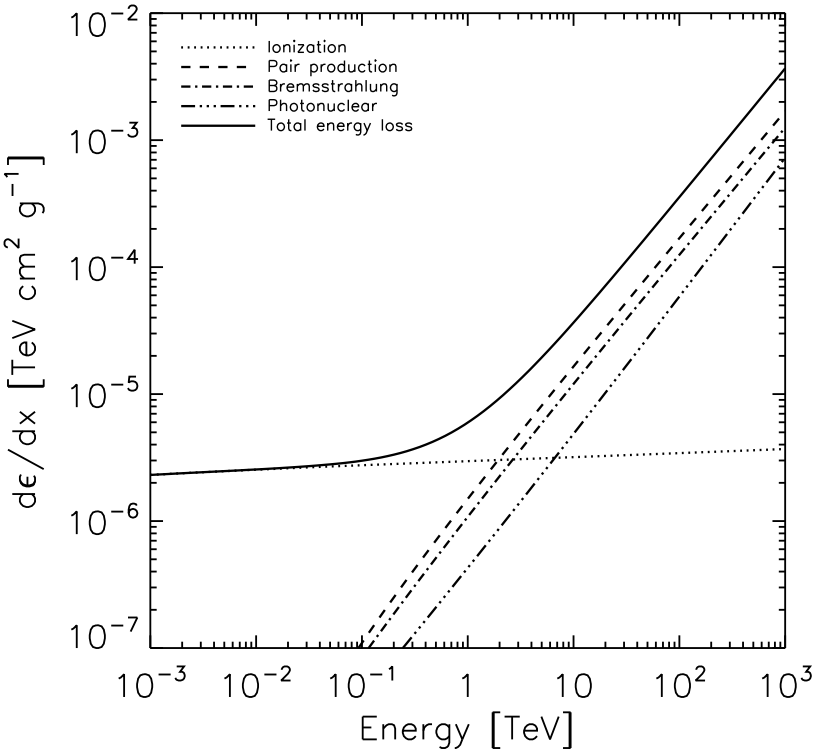

Figure 3.2 – Muon energy loss in water as a function of the energy for ionisation, pair production, bremsstrahlung and photonuclear processes. Source: [182].

A general overview of theory and experimental data on the atmospheric muon flux at sea level, underground and underwater is given in Reference [148]. In this, angle and momentum distributions for the fluxes are estimated using transport equations from an assumed composition of the primary cosmic ray spectrum. The comparison between the model and the existing measurements of the vertical *depth intensity relation* (DIR) underwater is reported in Figure 3.3. A property of the atmospheric flux often overlooked in literature is that muons can be grouped in *bundles*, where multiple muons follow parallel trajectories. A bundle is characterised by the number of component muons (*multiplicity*) and their transverse distribution in number and momentum. These features depend on the energy of the primary cosmic ray. A characterisation muon bundles is given in Reference [149], which illustrates the parameterisations used in the `MUPAGE` generator.

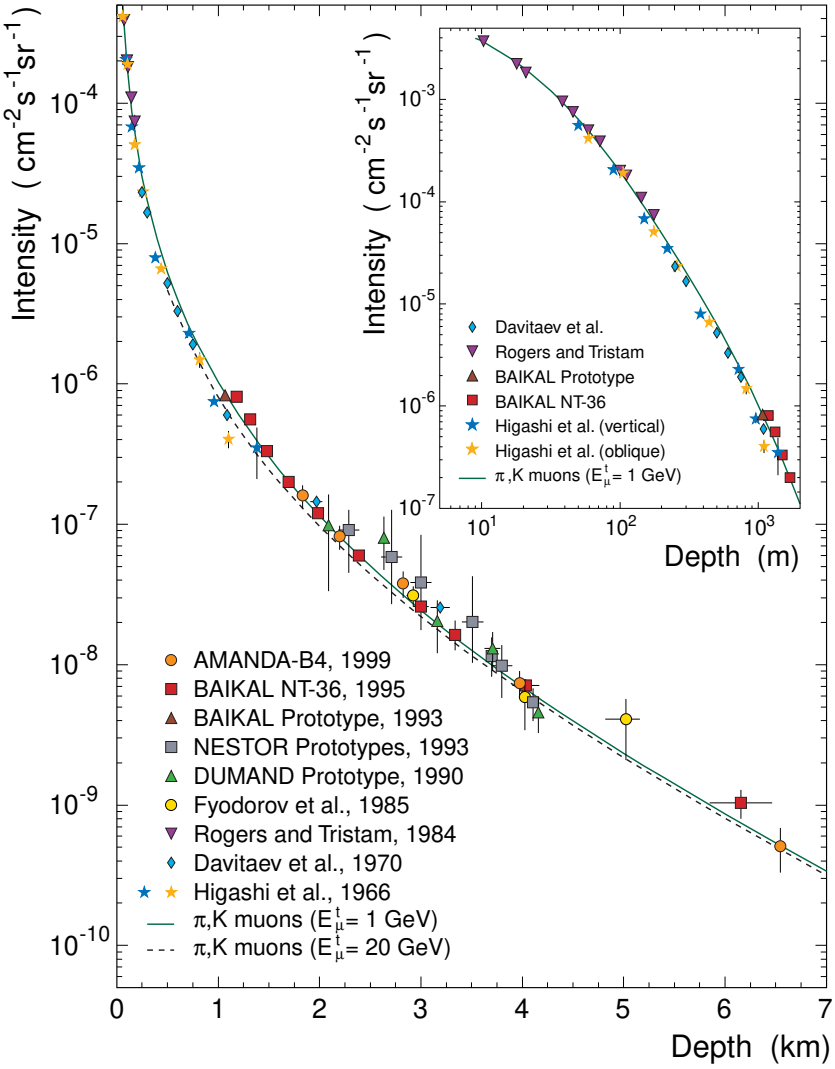

Figure 3.3 – Muon intensity as a function of depth in water. Experimental data are compared with the π, K-muon depth intensity relation. Source: [148].

Atmospheric muons are a prominent source of background for particle physics experiments. Low-background particle detectors are commonly hosted in underground laboratories, shielded by hundreds or thousands of meters of rock overburden. Auxiliary detectors surrounding the main detection volume are used to *veto* muon events. Commonly adopted technologies are tracker chambers or water buffers instrumented with PMTs. In neutrino telescopes, atmospheric muons are the most prominent source of background after the identification of physics events over the optical backgrounds. Muon tracks are also one of the signatures of charged-current neutrino interactions, so they cannot be excluded as a whole event class in the analysis samples. Identification of neutrinos relies on selecting upward going events (Earth shielding) or exploiting containment or geometrical vetos [126, 183]. Bundles are of special interest for neutrino telescopes, as they produce multiple correlated patterns

inside the instrumented volume. For ANTARES, a large fraction of events wrongly reconstructed as upgoing is induced by bundles of atmospheric muons [184]. The understanding and characterisation of the underwater atmospheric muon flux are of fundamental importance for the science goals of KM3NeT.

3.2 Characterisation of DOM coincidence rates

As described in Section 2.1.2, the trigger and reconstruction algorithms are based on the identification of correlated coincidences across multiple DOMs. Alternatively, each DOM can be exploited as a stand-alone detector for Cherenkov events. The DOM response can be characterised by the rate of coincidences detected across the 31 PMTs. The upper and lower hemispheres feature 12 and 19 PMTs, respectively. The PMTs are arranged in 5 rings of 6 PMTs plus a single PMT at the bottom pointing vertically downwards. The PMTs are spaced at 60° in azimuth and adjacent rings are staggered by 30°. Figure 3.4 provides a view of the DOM where each PMT location is designated by its ring and number.

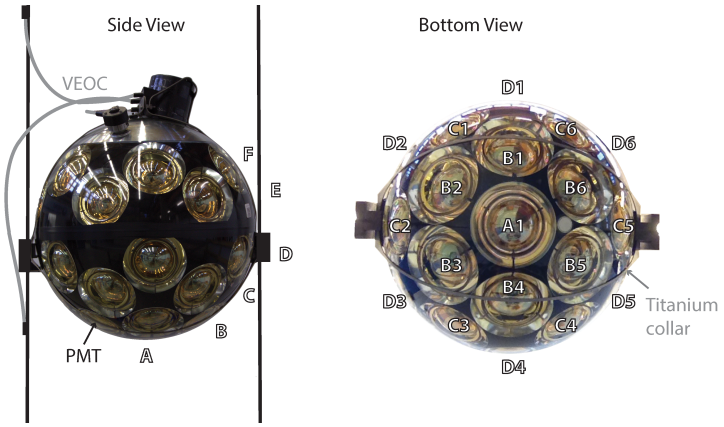

Figure 3.4 – Side view (left) and bottom view (right) of a KM3NeT DOM. See text for explanation of highlighted (mechanical) parts. The naming convention of the PMTs in terms of rings (letters) and numbers is indicated. Source: [163].

Genuine coincidences are produced by the tightly time-correlated photons of Cherenkov emissions. The typical time window for the detection of a coincidence between two or more PMTs, ΔT, is defined as a function of the hit time difference distribution illustrated in Section 2.2.2. Assuming a perfectly calibrated time offset and a Gaussian approximation for the transit time distribution, the detection efficiency for genuine coincidences, ϵ_{coinc}, is approximated as:

$$\epsilon_{\text{coinc}} \approx \text{erf}\left(\frac{1}{\sqrt{2}} \cdot \frac{\Delta T}{TTS}\right). \tag{3.1}$$

A 10 ns ΔT is typically adopted in the trigger. This value covers the full transit time distribution. It also allows for a small margin of inaccuracy on the time offset calibration used in the online data taking. Wider time windows of 15 or 25 ns are used for studies of the time difference distributions, monitoring and calibration of the detector.

Random coincidences are given by the occurrence of uncorrelated single hits within the chosen time window. For a generic PMT pair (i, j), the rate of random coincidences is:

$$R_{i,j}^{\text{random}} = 2R_i R_j \Delta T \tag{3.2}$$

where R_i and R_j are the single hit rates of the PMTs i and j respectively. For $\Delta T = 10$ ns and assuming an average rate of 7 kHz per PMT, the total rate of random coincidences for a DOM over all the 465 PMT pairs is $465 \cdot 2 \cdot (7\,\text{kHz})^2 \cdot (10\,\text{ns}) \simeq 450$ Hz. This value accounts for around half of the overall L1 rate. In this chapter, the total rate of coincidences detected by a DOM is analysed without distinction for the individual PMT pairs.

The multi-PMT design of the KM3NeT optical module provides information on the number of photons, their arrival time and incoming direction. The number of PMTs detecting (at least) one photon in coincidence is defined as *multiplicity* (M) and can be exploited as a signature to discriminate different types of Cherenkov emission. The multiplicity spectrum observed with the KM3NeT DOMs of the prototype detection unit [178] deployed in 2015 are shown Figure 3.5. The contribution from ^{40}K decays in seawater is relevant up to a multiplicity of seven. Above, atmospheric muons are dominant and can potentially illuminate all the PMTs of an optical module.

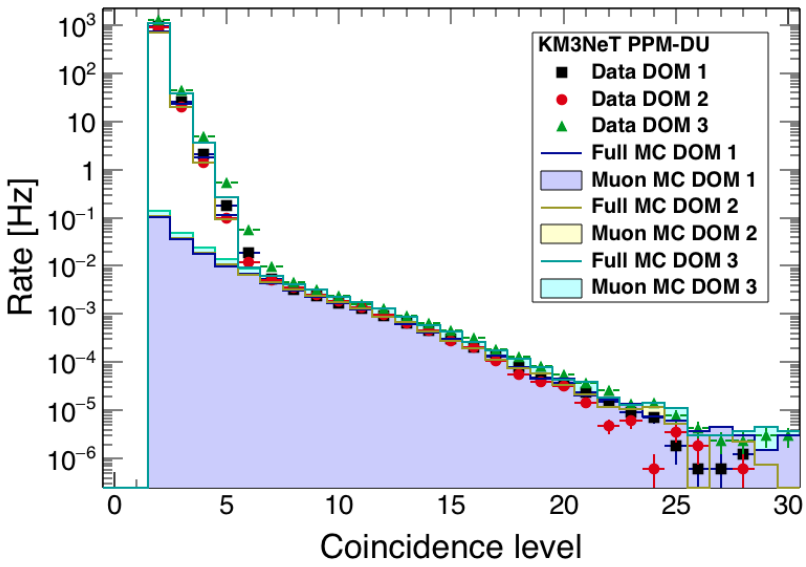

Figure 3.5 – Rates of coincidences in a time window of 25 ns as a function of the multiplicity for the 3 DOMs of the KM3NeT prototype detection unit, compared to the expected Monte Carlo rates. Symbols refer to data, histograms to Monte Carlo simulations. Source: [178].

3.3 KM3NeT ARCA2 and ORCA1 data sample

The analysis of coincidence rates presented in this chapter has been performed on a data sample from the first detection units of KM3NeT ARCA and ORCA detectors. L1 timeslice data (see Section 2.1.2) are used. In this analysis, the detector configuration *ARCA2* consists of the first two detection units of ARCA deployed between December 2015 and May 2016. Correspondingly, *ORCA1* refers to the first ORCA detection unit deployed in September 2017. The selected data taking periods for ARCA2 and ORCA1 are December 23, 2016 – March 2, 2017, and November 23, 2017 – December 13, 2017, respectively. In the considered period, four out of thirty-six DOMs of ARCA2 were not operational. ORCA1 L1 timeslice data are downscaled by a factor of 20 since November 23, 2017. Across the different data taking period periods, L1 data have been acquired with different time windows, the narrower being of 20 ns.

To ensure the unbiased estimation of the coincidence rates, the data from a DOM with at least one vetoed PMT (see Section 2.1.1) are discarded on a timeslice basis. The average fraction of vetoed PMTs is a few per mille in ARCA and a few per cent in ORCA. In a limited number of cases, a PMT is observed to be permanently in *high-rate-veto* and is ignored when applying the selection criterion.

The calibration of the PMT time offsets and the PMT photon detection efficiencies has been performed according to the procedure described in Section 2.2.2. The calibration is produced on segments of 6 hours of data to ensure sufficient statistics

for a reliable fit. In Figure 3.6, the relative deviations of each PMT efficiency compared to its all-period median are plotted. For the considered periods, the efficiencies are observed to be stable in time with deviations below 1%. However, long term monitoring of the detector performance has shown that larger variations can occur. Decreases of the PMT efficiency are observed especially on upward-looking PMTs. This is attributed to sedimentation effects, as strong sea currents seem to (partially) reverse the degradation.

ORCA1 DOMs 1 – 6 and 16 have photon detection efficiencies 15% lower than the average efficiency of the other ORCA1 and ARCA2 DOMs. The single hit rates of these PMTs reflect the same pattern. Different hypotheses have been investigated [185]. No differences in the cathode sensitivity or the angular acceptance for the PMTs in the affected DOMs are found. A correlation with the sites of PMT assembly and DOM integration is present. Anomalies in the UV cutoff of the glass, optical gel or PMT coating could be candidate explanations. No conclusive evidence has been found to date.

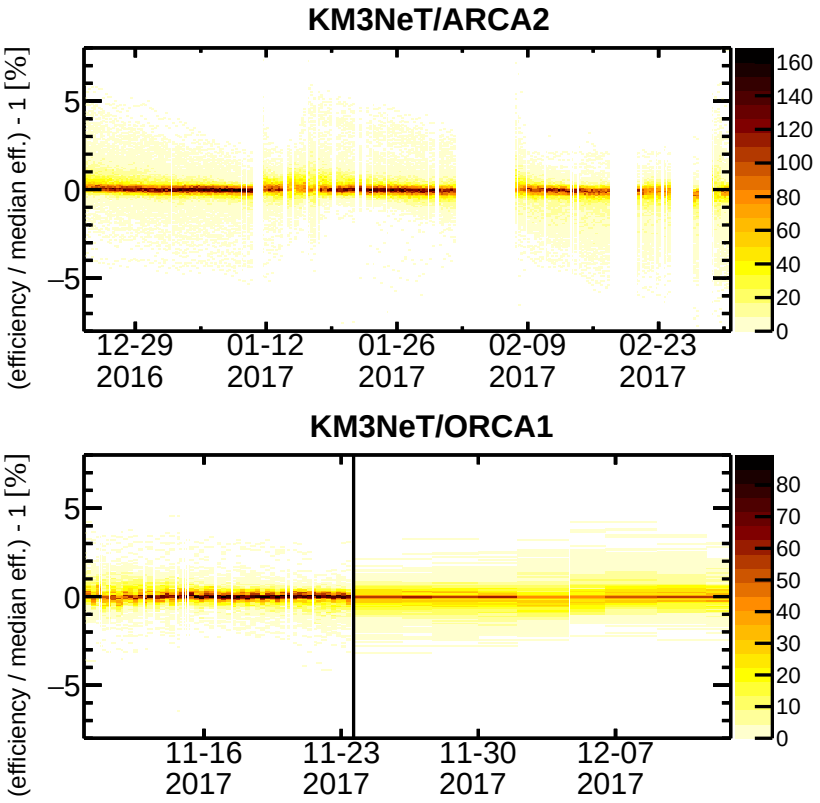

Figure 3.6 – Deviation of the estimated photon detection efficiency for each PMT with respect to its all-time median efficiency for the ARCA2 and ORCA1 detectors as a function of time. The color scale indicates the number of PMTs in each bin. Vertical white bands reflect the periods without data-taking; the vertical black line represents the time at which the L1 data stream downscaling was introduced. Source: [163].

3.4 Coincidence rates in ARCA2 and ORCA1

Using the introduced data sample, the coincidence rates as a function of the multiplicity in the ARCA2 and ORCA1 detectors have been investigated. A coincidence time window of 15 ns is adopted in this analysis. The window is large enough to allow a study of the time difference distribution, avoiding edge effects in the analysis of data acquired with a 20 ns time window and re-calibrated offline. For example, a hit in a 20 ns coincidence according to its offline-calibrated time would have been recorded if its online-calibrated time was outside of the window. In analogy with the approach described for calibration (Section 2.2.2), the analysis of the time differences between the hits is used to remove the random background from the total rate. The rate is estimated for the whole DOM. All coincidences with multiplicity $M \geq 2$ are considered

to estimate the genuine coincidence rates for multiplicity ≥ 2. For each coincidence, the $\binom{M}{2}$ time differences between the possible hit pairs are included in the distribution. The latter is finally fitted with the sum of a Gaussian function and a constant offset. To estimate the rate of genuine coincidences, the fitted offset is subtracted from the integral of the distribution. An example of the time difference distribution for a typical DOM and the corresponding fit is given in Figure 3.7.

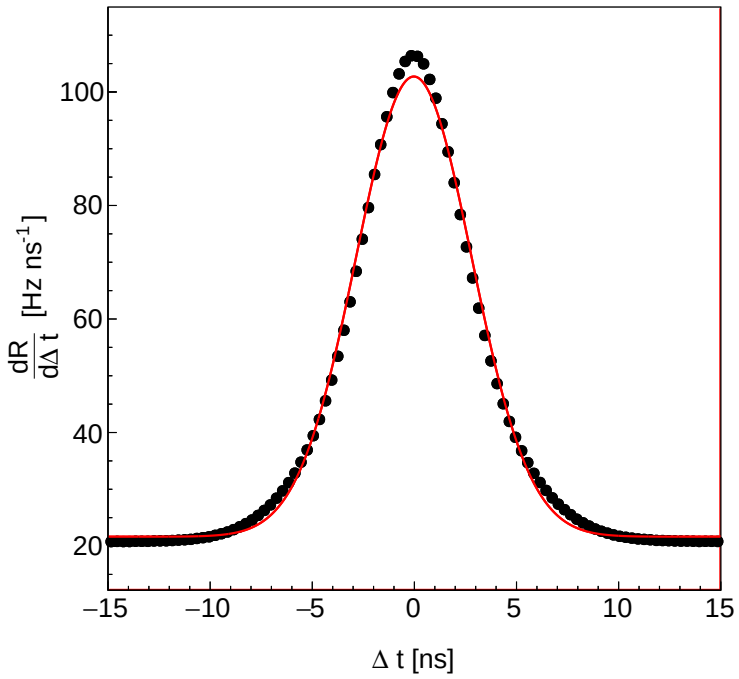

Figure 3.7 – Time difference distribution for all hit pairs in coincidences with multiplicity ≥ 2 in a typical DOM. The fit with a Gaussian function plus a constant offset is shown as a red line.

The time differences measured between all the PMT pairs follow consistently the same distribution, reflecting the correct time calibration of the optical module. A random coincidence rate of ~ 600 Hz is consistent with an average single hit of ~ 6,5 kHz per PMT according to Equation (3.2). In general, the random coincidence rate for coincidence at multiplicity M can be estimated as:

$$R^{\text{random}} \simeq \binom{31}{M} M \langle R \rangle^M (\Delta T)^{M-1} \tag{3.3}$$

where $\langle R \rangle$ is the PMT average single hit rate assumed as constant over the whole DOM.

At multiplicity three, the rate of random coincidences can be estimated to be on the order of 1 Hz. For higher multiplicities, it is heavily suppressed by the $(\Delta T)^{M-1}$ term and becomes negligible.

The coincidence rates measured with the ORCA1 and ARCA2 detectors after subtraction of the random background and averaged over all the DOMs of each detector are reported in Figure 3.8.

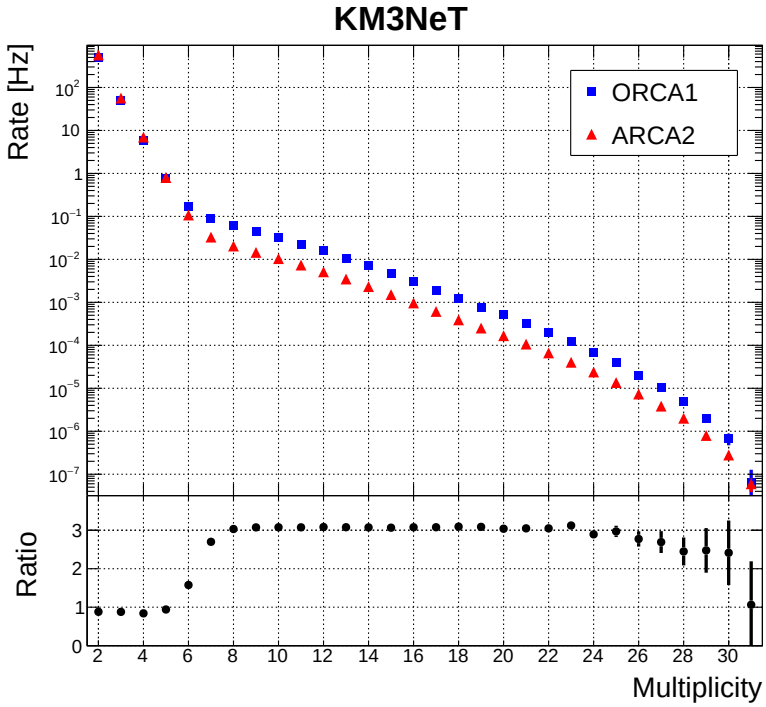

Figure 3.8 – Top: coincidence rates as a function of the multiplicity for the ORCA1 and ARCA2 detectors averaged over all the DOMs of each detector. Bottom: ratio between ORCA1 and ARCA2 coincidence rates. Up to a multiplicity of six, the coincidence rate is dominated by ^{40}K decays. Above a multiplicity of seven, atmospheric muons dominate. Only statistical errors are shown. Author's work published in [163].

The rate of ^{40}K-induced coincidences can be observed in the lower part of the spectrum. In first approximation, for multiplicity M, the rate can be approximated as follows:

$$R^{^{40}\mathrm{K}}(M) \approx (500\,\mathrm{Hz}) \cdot 10^{M-2} \tag{3.4}$$

The lower rates observed in ORCA1 compared to ARCA2 at low multiplicity is due to the difference in the average efficiency between the optical modules of the two detectors. At multiplicity two, the difference is about 12%, consistent with a quadratic dependence of the rate on the PMT efficiency (see Section 2.2.2).

The ratio between ARCA2 and ORCA1 above multiplicity seven shows a factor three difference due to the different muon intensity at different depths of the DOMs, which

is around 2310 m for ORCA and 3070 m for ARCA. This suggests the possibility of exploiting this multiplicity range to probe the intensity of the muon flux at the depth of each DOM.

In Figure 3.9, the relative contribution of each PMT to coincidences as a function of the multiplicity is shown. The higher number of close-by PMTs results in more coincidences from ^{40}K decays, reflected by a higher contribution of the lower DOM hemisphere to low-multiplicity coincidences. Shadowing effects of the rope-mounting structure can be appreciated on PMT C2 and C5. The contribution to high multiplicities comes mostly from the upper hemisphere, reflecting the downgoing direction of the light induced by atmospheric muons. The stability of the coincidence rate in the multiplicity region dominated by atmospheric muons (≥ 8) can be observed in Figure 3.10. Four ARCA2 DOMs lost one PMT each during the considered data taking, resulting in a decrease of the coincidence rates. In the following analysis, the affected data are rejected when evaluating the muon flux.

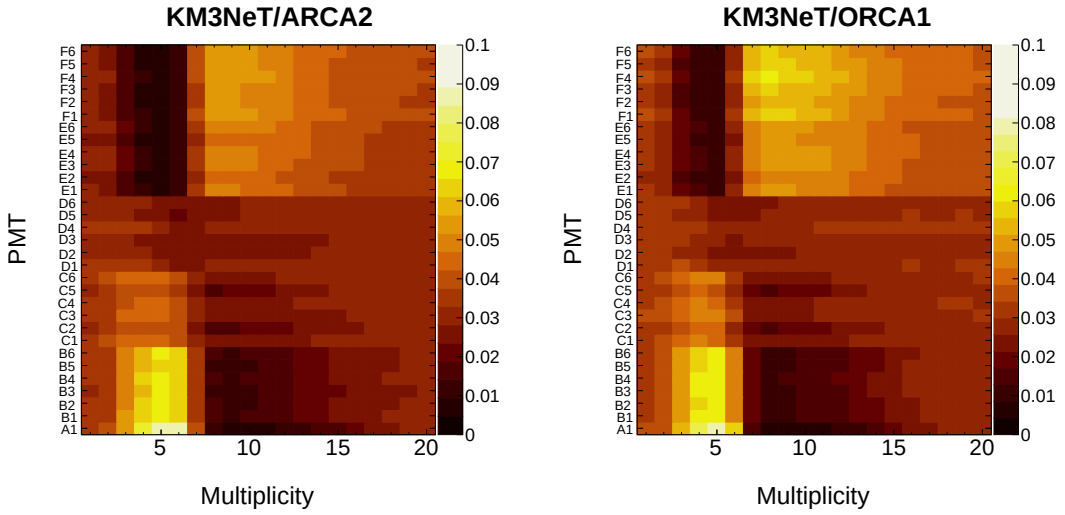

Figure 3.9 – Probability of the PMT contribution to coincidence rates as a function of the multiplicity (each abscissa bin is normalised to unity). The PMT is identified by the ring (letter) and the position of the PMT on the ring (number). The first address (A1) refers to the vertical down-facing PMT, rings from B to D belong to the lower hemisphere, while rings E and F belong to the upper hemisphere of the DOM (see Figure 3.4). Above a multiplicity of 20, statistical fluctuations dominate the pattern, and are therefore left out of the figure. Author's work published in [163].

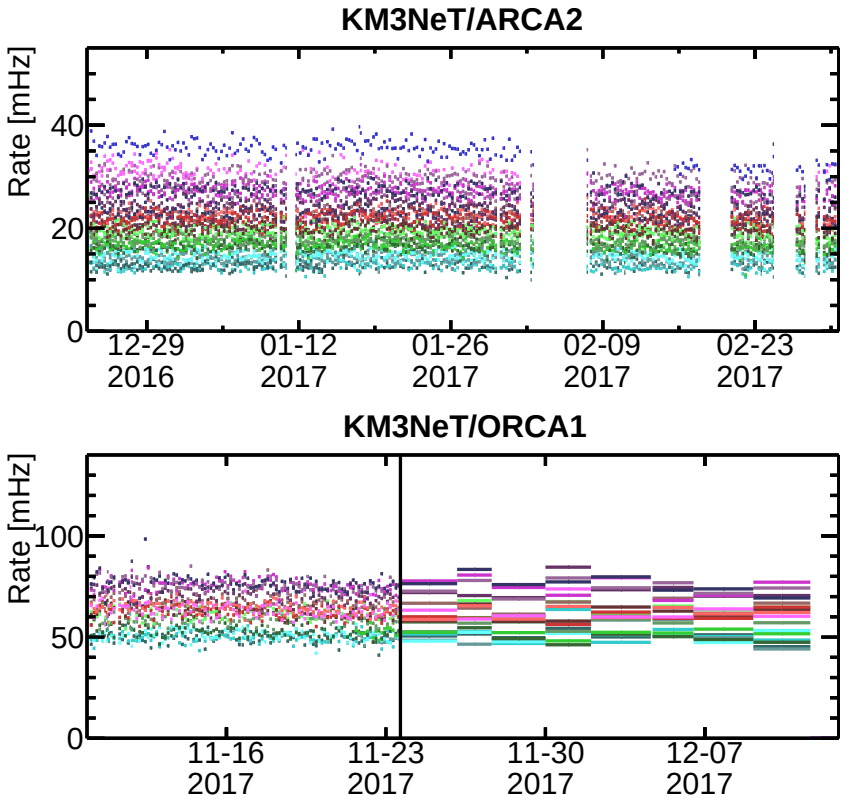

Figure 3.10 – Rate of multiplicity ≥ 8 coincidences as a function of time for the DOMs of the ARCA2 and ORCA1 detectors. Each point corresponds to one run and every colour to a single DOM. Vertical white bands are periods without data-taking. The vertical black line in the bottom plot represents the date at which the L1 data stream is downscaled (see Section 3.3). Source: [163].

3.5 Depth dependence of the atmospheric muon flux

As a result of the muon energy loss and absorption in water, a lower muon flux is expected at larger depths underwater. As already evident in Figure 3.8, the rate of coincidences with multiplicity ≥ 8 is a good proxy to probe this dependency. In Figure 3.11 such rate is shown in blue for each DOM of the ARCA2 and ORCA1 detectors.

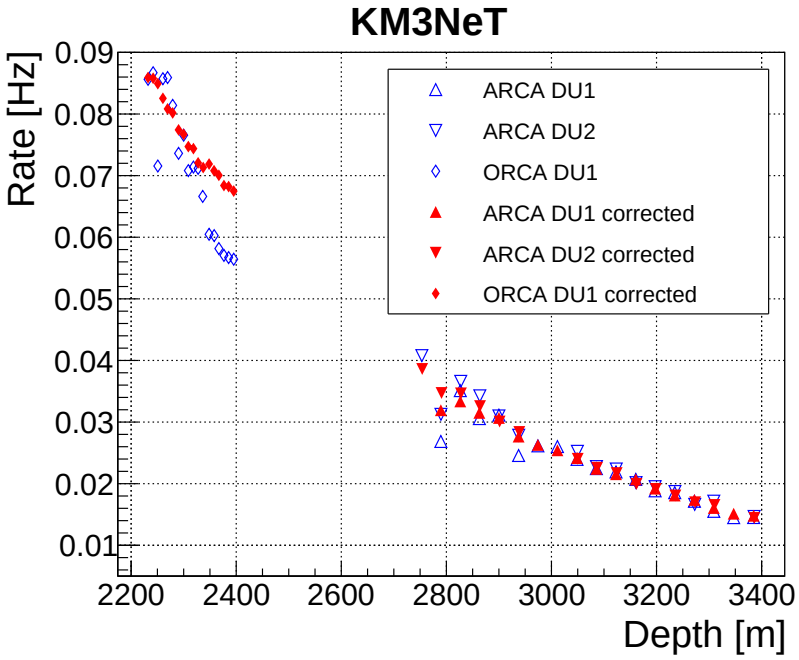

Figure 3.11 – Multiplicity ≥ 8 coincidence rate of all DOMs as function of depth below the sea level. The coincidence rates for the ARCA2 and ORCA1 detectors are reported as measured (blue hollow markers) and after the correction for the PMT photon detection efficiencies (red full markers). Statistical uncertainties are included and smaller than the marker size. Author's work published in [163].

In order to compensate for the different average efficiency of each optical module, the rate is corrected using the ratio of two simulations. In the first, referred to as 'uniform', the photon detection efficiencies are set to the average value obtained with the calibration procedure for a set of typical DOMs. In the second, referred to as 'calibrated', the photon detection efficiencies are set to their individual measured values (see Section 2.2.2). The simulations have been performed using `MUPAGE`, `KM3` and `Jpp`. The correction of the *measured* rates is obtained as follows:

$$R^{\text{data}}_{\text{corrected}} = R^{\text{data}}_{\text{measured}} \cdot \frac{R^{\text{MC}}_{\text{uniform}}}{R^{\text{MC}}_{\text{calibrated}}} \,. \tag{3.5}$$

The corrected rates are shown in red again in Figure 3.11. The subset of ORCA1 DOMs with lower efficiency introduced in Section 3.3 can be noticed. Except for DOM 17 of ARCA DU1, the correction procedure is effective in compensating the measured rates for the DOM efficiency. This DOM has later be found to have an incorrect gain due to incorrect HV tuning, making the efficiency calibration unreliable. Calibration procedures have since been improved including a fit of the gain from the time-over-threshold distribution.

The model from Bugaev et al. [148] is here considered for the estimation of the underwater vertical muon flux. Since the DOM covers the full solid angle and no angular discrimination is done in this analysis, the rate measurement is compared with the angle-integrated flux. The latter is calculated as a function of depth from the formulas provided in Reference [186]. To facilitate the comparison with the data, this flux model is here described with a simple analytic expression in the form of a vertical flux $I_\mu(d,\theta=0)$ corrected with a factor $C(d)$ that accounts for the angular integration. The vertical depth-intensity relation, $I_\mu(d,\theta=0)$, is represented with a double-exponential expression, as in historical fits of experimental data [187, 148]. The integration factor, $C(d)$, consists of the sum of a fixed offset and a depth-dependent term due to the variation of the muon angular distribution with depth. In the depth range of interest, the resulting expression reads as follows:

$$I_\mu(d) = \frac{I_\mu(d,\theta=0)}{C(d)} = \frac{A_1 \cdot e^{A_2 \cdot d} + A_3 \cdot e^{A_4 \cdot d}}{B_1 + B_2 \cdot d}\,, \tag{3.6}$$

$$A_1 = 1{,}31 \cdot 10^{-5}\,\mathrm{cm^{-2}s^{-1}sr^{-1}}\,,\ A_2 = -2{,}91 \cdot 10^{-3}\,\mathrm{m^{-1}}\,,$$
$$A_3 = 7{,}31 \cdot 10^{-7}\,\mathrm{cm^{-2}s^{-1}sr^{-1}}\,,\ A_4 = -1{,}17 \cdot 10^{-3}\,\mathrm{m^{-1}}\,,$$
$$B_1 = 4{,}16 \cdot 10^{-1}\,\mathrm{sr^{-1}}\,,\ B_2 = 1{,}07 \cdot 10^{-4}\,\mathrm{m^{-1}sr^{-1}}\,.$$

In this, the A_i parameters define the depth dependence of the vertical flux and the B_j parameters the integration factor. The water equivalent depth d is obtained by the geometrical depth multiplied for the ratio between seawater and pure water density (1.03).

This parameterisation is valid for a flux of muons with energies above 1 GeV. For a first comparison, the normalisation of the model is fitted to the data as shown in Figure 3.12. Rates at the depths probed by two DOMs (for ARCA2) are averaged to a single data point.

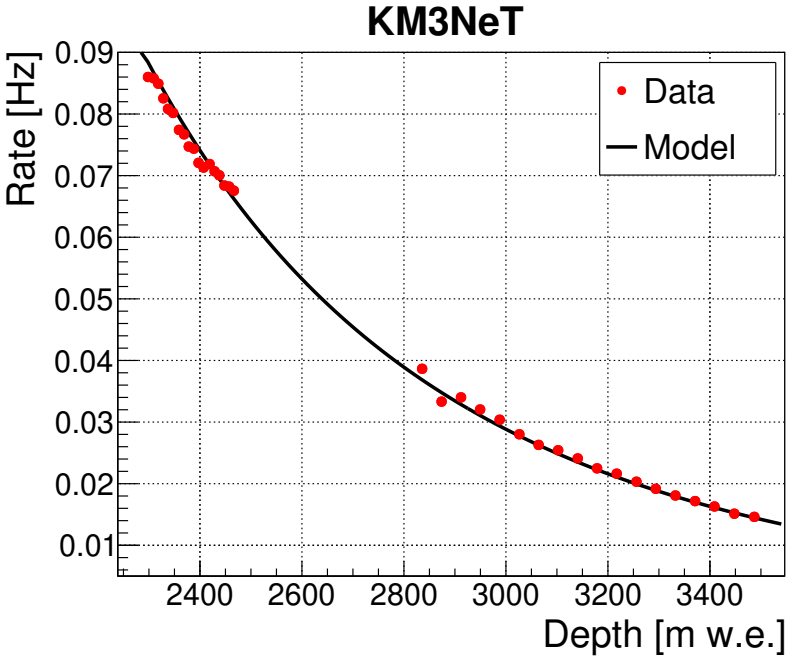

Figure 3.12 – Efficiency-corrected ≥ 8 multiplicity coincidence rates measured with the ORCA1 and ARCA2 detectors as a function of depth below the sea level (red points), fitted with the Bugaev model of the atmospheric muon flux (continuous black line). The depth is expressed in water equivalent (w.e.). Statistical uncertainties are included and smaller than markers. Author's work published in [163].

The dependence of the rates is in good agreement with the dependence of the muon flux over the considered depth interval. The RMS of the residuals is below 2%.

3.6 Estimation of the DOM effective area

To recover an absolute measurement of the muon flux at each depth, the stand-alone DOM response to atmospheric muons in terms of multiplicity ≥ 8 coincidences is quantified. The DOM *effective area* (A_{eff}) is defined as the ratio between the coincidence rate measured by the DOM and the total muon flux at its depth. The effective area is estimated through dedicated simulations based on `MUPAGE` and `KM3Sim`. Differently to the 'uniform' simulation employed in Section 3.5, here an up-to-date PMT model reflecting our best knowledge of the angular acceptance, quantum efficiency and collection efficiency is used. Using single DOM simulations, it is verified that the updated PMT model yields ~ 3% more multiplicity ≥ 8 coincidences. It is also checked that `KM3Sim` and `KM3` provide compatible results when using the same PMT model. For the evaluation of the effective area stability versus depth, the faster simulation package `KM3` is used to reduce the computational requirements of simulating a generation

volume encompassing the full height of the ARCA and ORCA detection units.

In the simulation, atmospheric muons are generated at the boundary of the generation volume (*can*) and further propagated by the Cherenkov light simulator. For the estimation of the effective area, the muon flux as a function of depth is evaluated over the surface of the can. The flat disc at the top and the side cylindrical surface are considered separately. `MUPAGE` files are analysed on an event-by-event basis. The flux as a function of depth is sampled over segments of the cylindrical surface along its vertical axis.

The flux is evaluated for the number of muon bundles (n_b) and the number of total muons (n_μ). The two are naturally connected by the relation:

$$n_\mu = n_b \langle m \rangle \tag{3.7}$$

where $\langle m \rangle$ is the average number of muons in a bundle, commonly referred to as *muon multiplicity*. In the `MUPAGE` file format (`ASCII`), information about a generated bundle is introduced by the tag `track_bundle`. A bundle is associated with a list of individual muons, each introduced by the tag `track_in`. Position and direction of the bundle are defined as the energy-weighted averages of the positions and directions of the constituting muons. Since `track_bundle` is not consistently propagated by all KM3NeT software, the generation position and direction of each bundle are here recalculated from the individual muons and designated as `alt_bundle`. For bundles generated at the can top near the edge, one or more muons could enter the can from the lateral surface. In these cases, only x and y coordinates are averaged to recalculate the generation position of the bundle (that would otherwise be wrongly attributed to the side flux).

The contribution to the flux of an event incident on a surface element depends on the projection of the surface along the muon (bundle) direction. To account for this, each event is assigned a weight of $(\cos\delta)^{-1}$ where δ is the angle between the incident direction of the muon (bundle) and the normal direction to the can at the generation point. For the flux estimated at the side, vertical muons are tangent to the surface and the weight diverges. A cut-off on the maximal weight is therefore applied, at the cost of a small bias to the estimation. Finally, since only muons entering the generation volume are generated, the flux estimated on the side of the can is multiplied by a factor two to account for the full solid angle integration. The estimation of the `MUPAGE` flux at the boundary of the generation volume for the ORCA1 and ARCA2 detector simulations are shown in Figure 3.13. As a result of the cut-off bias, a deficit of $\sim 3\%$ is observed when comparing the upper segment of the lateral surface with the flux estimated at the flat top disc (represented in the figure with a full point).

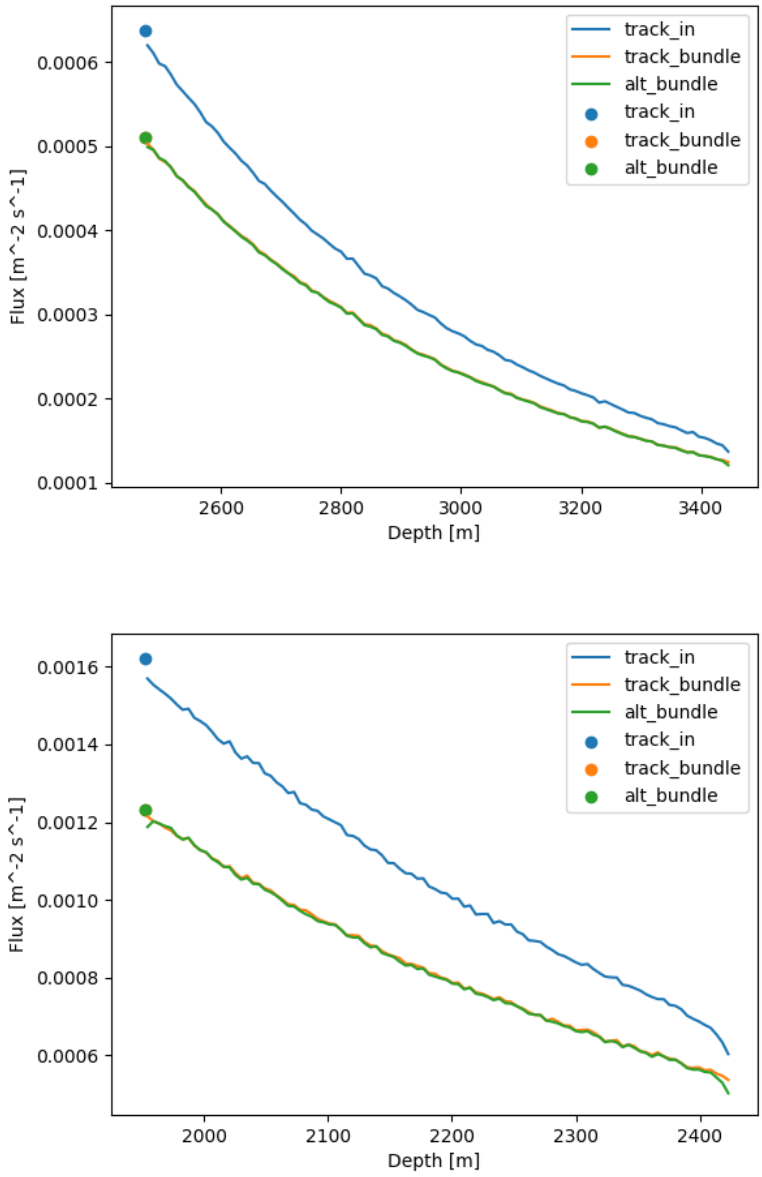

Figure 3.13 – Flux estimated at the boundary of the generation volume (can) for a `MUPAGE` simulation of atmospheric muons for ARCA2 (top) and ORCA1 (bottom) detectors. Points and lines represent the flux estimated at the flat top of the can and along the side cylindrical surface respectively. `track_in` indicates the flux of total muons, `track_bundle` the flux of bundles according to the corresponding `MUPAGE` output, `alt_bundle` the flux of recalculated bundles.

The effective area is estimated dividing the ≥ 8 multiplicity coincidence rates by the generated flux at each depth. The results are reported in figure Figure 3.14. The

effective area shows a slight variation with depth for muons but is constant for bundles. This suggests that the observed variation depends on the change of the average muon multiplicity with depth rather than other features (e.g. angular distribution). For this analysis, a constant effective area for the total number of muons is assumed as the average over the depth range. As further discussed in Section 3.8, the variation with depth is covered by the estimated systematic uncertainties. The average value of the effective area for multiplicity ≥ 8 coincidences is estimated at 96^{+5}_{-13}m^2.

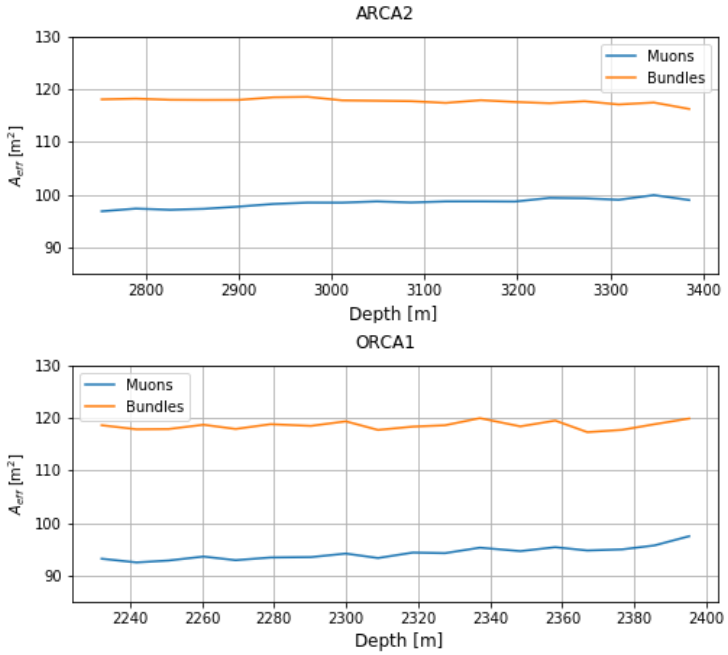

Figure 3.14 – Effective area as a function of the DOM depth for the ARCA2 and ORCA1 simulations.

3.7 Absolute measurement of the atmospheric muon flux

The muon flux at each depth is naturally calculated dividing the measured corrected rates (see Section 3.5) by the estimated DOM effective area (see Section 3.6). In Figure 3.15, the final measurement of the muon flux is given and compared with the considered Bugaev model [148, 186]. From Reference [186], a conservative systematic error of ±8% is assumed on the parameterisation of the muon flux (further discussed in Section 3.8). The previous measurement from ANTARES [147] is reported. KM3NeT ARCA2 and ORCA1 measurements are compatible with ANTARES and the Bugaev model within the systematic uncertainties. This approach is shown to provide a precise estimation of the total muon flux alongside the detector depth, complementing studies of atmospheric muons based on track reconstruction. ARCA2 and ORCA1

detection units are observed to have compatible performance, verifying the adopted calibration procedures.

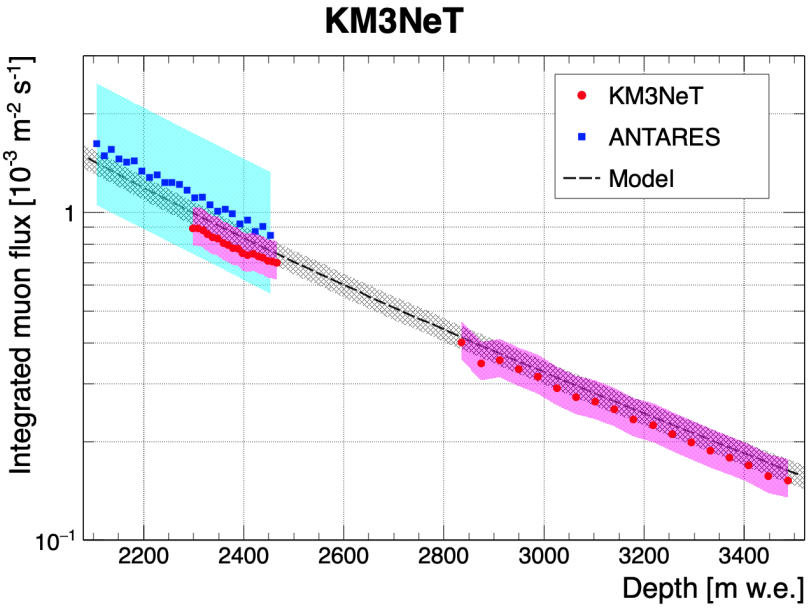

Figure 3.15 – Integrated atmospheric muon flux measured with the ORCA1 and ARCA2 detectors as a function of depth below the sea level (red points). The systematic errors are displayed as light red shadowed areas. The Bugaev model of the atmospheric muon flux is drawn with a dashed black line (quoted errors are the grey shadowed area), see text for model description. ANTARES data from [147] are included as blue points for comparison (systematic errors are the light blue shadowed area). The depth is expressed in water equivalent (w.e.). Statistical uncertainties are included and smaller than markers. Source: [163].

3.8 Evaluation of systematic uncertainties

The uncertainty on the absolute PMT efficiency has a direct impact on the rate measurement. For the parameterisation of the coincidence rates used in the calibration (see Section 2.2.2), the comparison between data and `OMGSim` for ^{40}K coincidences yields a mean difference of the rates across all PMT pairs of 5%. This covers the systematic error due to the use of a Gaussian approximation in estimating the integral of the time difference distribution used in Section 2.2.2. This value is assumed as the systematic uncertainty on the PMT efficiency normalisation. From detailed calibration studies, the uncertainty on the *relative* efficiency resulting from the accuracy of the calibration procedure has a systematic uncertainty at the 5% level as well. Conservatively, the two are added in quadrature and propagated to the DOM for a total 7% effect.

The absorption length of light in water is usually considered to be known with a 10% uncertainty. Applying this variation at the light simulation stage results in a variation of 6% on the detection rates.

Different systematic uncertainties are related to the properties of the muon flux used in the simulation to estimate the effective area. Due to the uneven distribution of the PMTs between the upper and lower hemispheres, the DOM is expected to have a larger acceptance for muons incident at larger zenith angles. Besides, the average multiplicity of the muon bundles should also be considered. A wider bundle has a higher probability of intercepting a DOM with its Cherenkov cone. At the same time, the probability for a bundle to produce more than one coincidence on the same DOM depends on its geometry. Both the angular distribution and the average multiplicity of the bundle are dependent on depth. Comparing the simulated rates with the simulated flux of bundles, instead of total muons, the effect of the varying angular distribution is found to be negligible compared to the other systematic errors. The uncertainty on the average bundle multiplicity can be considered as the dominant variable in the determination of the effective area. For this measurement, the effective area has been assumed to be constant with an uncertainty of $^{+5\%}_{-13\%}$. This interval encompasses the effect of the bundle multiplicity variation with depth as well as the uncertainty on its absolute normalisation. The latter is assigned asymmetrically, as `MUPAGE` is currently believed to overestimate the bundle multiplicity.

The total systematic uncertainty on the muon flux measurement obtained by the sum in quadrature of the evaluated factors amounts to $^{+16\%}_{-11\%}$. The sign of the asymmetry is reversed since the measured flux is inversely proportional to the effective area.

4 Core-collapse supernova neutrino detection

In this Chapter, a study of the KM3NeT detection capability for a core-collapse supernova neutrino burst is presented. This subject is the main focus of the Thesis. It represents the first astrophysical analysis based on low-level coincidence data from the KM3NeT detectors. It is also the first analysis that has become operational in the KM3NeT real-time multi-messenger framework. The development of this analysis relies on an extensive study of the timeslice data from the first two and four detection units of the ARCA and ORCA detectors, respectively. It has been instrumental to the detector development and has produced valuable feedback to the calibration, data acquisition, data quality and data analysis activities.

Sommaire

4.1 Core-collapse supernovæ . . . 127
4.1.1 Introduction . . . 127
4.1.1.1 Thermonuclear supernovæ . . . 128
4.1.1.2 Core-collapse supernovæ . . . 129
4.1.2 Core-collapse mechanism . . . 130
4.1.3 CCSN neutrino phenomenology . . . 132
4.1.4 SN 1987A . . . 133
4.1.5 Galactic and near-galactic CCSN rate and progenitors . . . 134
4.2 CCSN neutrino detection with KM3NeT . . . 136
4.2.1 Flux model . . . 137
4.2.2 Low energy neutrino interactions in water . . . 139
4.2.3 Simulation of CCSN neutrinos . . . 141
4.2.4 Effect of the photon detection efficiency . . . 142
4.3 Study of the background . . . 144
4.3.1 Data sample and Monte Carlo simulation . . . 145
4.3.2 Background coincidence rates . . . 146
4.3.3 Background filtering . . . 147
4.3.3.1 Coincidence correlation . . . 148
4.3.3.2 Triggered events . . . 150
4.4 Sensitivity estimation . . . 154
4.4.1 Statistical definitions . . . 154

4.4.2 Multiplicity selection . . . 155
4.4.3 Systematic uncertainties . . . 158
4.4.4 Detector combination . . . 158
4.4.5 Sensitivity as a function of the distance . . . 160
4.4.6 KM3NeT model in SNOwGLoBES . . . 161
4.4.7 Comparison with other experiments . . . 163
4.5 Benchmarks of the analysis algorithm . . . 163
4.5.1 Filter robustness . . . 163
4.5.2 Bioluminescence impact on detector efficiency . . . 166
4.5.3 Implications and perspective . . . 168
4.6 Online supernova trigger . . . 168
4.6.1 Multi-messenger context . . . 168
4.6.2 Statistical treatment . . . 169
4.6.2.1 Sliding window and alert dead time . . . 171
4.6.2.2 DOM counting . . . 171
4.6.3 Technical implementation . . . 172
4.6.3.1 Real-time analysis of SN timeslice data . . . 173
4.6.3.2 Trigger combination . . . 174
4.6.3.3 Alert generation and management . . . 175
4.6.4 Low-level data buffering . . . 176
4.6.5 Graphical monitoring . . . 176
4.7 Follow up of gravitational wave alerts . . . 178
4.7.1 Analysis outline . . . 178
4.7.2 S191110af (retracted) . . . 179
4.7.3 S200114f . . . 181
4.7.4 Perspective for future follow-ups . . . 183
4.7.4.1 Analysis pipeline . . . 183
4.7.4.2 Presentation of the results . . . 183
4.8 Supernova astronomy and astrophysics . . . 184
4.8.1 Flux spectral properties . . . 184
4.8.2 Standing accretion shock instability . . . 187
4.8.3 Timing and triangulation . . . 189
4.9 Conclusions and perspective . . . 191

4.1 Core-collapse supernovæ

4.1.1 Introduction

supernovæ (SNe) are powerful explosive phenomena that can mark the end of the life of massive stars. The term was coined in the 1930s in seminal works by W. Baade and F. Zwicky [76, 188]. After these, supernova events are conventionally designated with the prefix SN followed by the year and a sequential letter (e.g. SN1987A). Astronomical

observations of supernovæ have produced a conventional tree-like classification based on the optical properties of the star envelope at the maximum brightness, as illustrated in Figure 4.1.

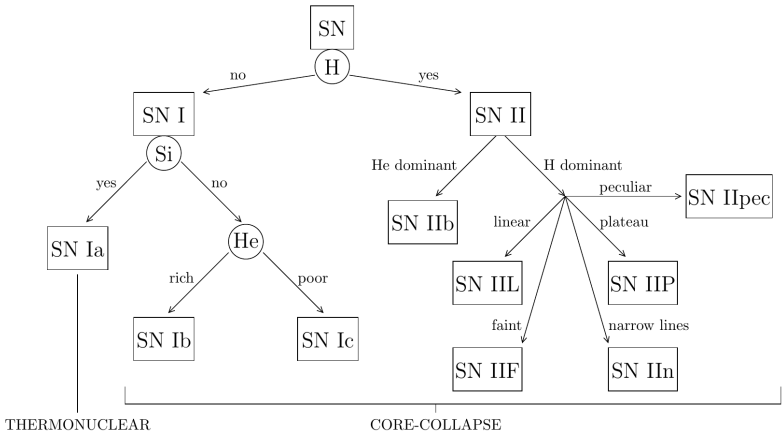

Figure 4.1 – Spectral classification of supernovæ Source: [189].

The presence or absence of hydrogen absorption lines in the spectrum divides SNe in Type I and Type II. The presence of silicon and helium lines define further ramifications. From the astrophysical point of view, the important distinction is based on the explosion mechanism. Type Ia supernovæ (H and Si-dominated spectrum) originate from *thermonuclear* explosions of white dwarfs. Type Ib,c and II supernovæ are instead the consequence of the collapse of a stellar core. A few months after the luminosity peak, the type can be distinguished as the ejecta become optically thin, exposing the SN inner regions. At this point, thermonuclear SNe exhibit a spectrum dominated by blended emission lines of iron-group elements. Spectra of core-collapse SNe, on the contrary, are characterised by intermediate-mass elements as oxygen and calcium [190]. Both supernova mechanisms are tied to a breaking of the stellar equilibrium condition. In the normal life cycle of a star, as represented in the *main sequence* of the Hertzsprung–Russell diagram, the core stands on an equilibrium between the gravitational force and the thermal pressure. When the stellar core approaches a very high density, the equilibrium is different, as the star is sustained against gravity by the pressure of degenerate electrons [191]. The equilibrium is satisfied up to the *Chandrasekar limit*, that defines the maximum mass allowed for a given electron density, which in turn is determined by the proton fraction of the star. For the typical case of white dwarfs, the proton fraction is ~ 0.5 and the corresponding *Chandrasekar mass* has the well-known value of $1{,}4\,M_\odot$.

4.1.1.1 Thermonuclear supernovæ

A white dwarf is the final stage of a star that has exhausted its thermonuclear fuel. At the equilibrium, it has a typical mass of $1M_\odot$ and a radius of ~ 5000 km corresponding

to a density of $\sim 10^6\,\mathrm{g\,cm^{-3}}$. If the white dwarf has a companion, it can accrete its mass beyond the Chandrasekar limit. Once the equilibrium is broken, the density triggers the fusion of carbon and oxygen into heavier nuclei. The resulting runaway reactions finally produce a thermonuclear explosion [192]. Typically, a thermonuclear supernova leaves behind an expanding nebula and no compact remnant. Silicon is present in its optical spectrum as it is one of the products of the C-O fusion. Iron is observable as a product of the $^{56}\mathrm{Ni} \longrightarrow {}^{56}\mathrm{Co} \longrightarrow {}^{56}\mathrm{Fe}$ nuclear decay chain. As their explosion mechanism is very well constrained, Type Ia supernovæ exhibit little variability in their observable properties. In particular, the duration of the light peak can be empirically tied to the SN total luminosity as observed by Phillips in 1993 [193]. Type Ia supernovæ are therefore excellent *standard candles* (unit of measure for luminosity) that can be used to estimate the distance of optical objects for redshifts $z \leq 1.4$.

4.1.1.2 Core-collapse supernovæ

Massive stars in the $\sim 10-50\mathrm{M}_\odot$ range can undergo a collapse of the stellar core. As the collapse forms a proto-neutron star, a shockwave is produced and propagates outwards, ionising the hydrogen envelope and expelling ejecta of matter. The compact remnant left behind may be detectable, e.g., in the form of a pulsar. The main phases of a *core-collapse supernova* (CCSN) develop at a stage in which the star is opaque to optical photons. As a consequence, $\sim 99\%$ of the progenitor gravitational energy is released as a neutrino burst of $\sim 3\cdot 10^{53}$ erg in the $\sim 10-20$ seconds following the onset of the collapse. Matter and radiation, for comparison, respectively carry 1% and 0.01% of the total energy. Neutrinos are emitted with a quasi-thermal spectrum at the 10 MeV scale, for a total in the order of 10^{58} particles.

The outcome of the supernova depends on the star initial mass and the concentration of heavy elements in the envelope (*metallicity*). The metallicity determines the optical opacity of the envelope, and therefore the radiation density in the stellar core. The latter is an important driver in the development of the CCSN process, as it fuels the disintegration of iron nuclei. The supernova type as a function of the initial mass and metallicity is shown in Figure 4.2. Stars lighter than $\sim 9\,\mathrm{M}_\odot$ end up as white dwarfs. For massive stars above $\sim 50\,\mathrm{M}_\odot$ the envelope is progressively thinned by stellar wind losses, so a higher metallicity is required to maintain the same opacity. Stars in the intermediate-mass and metallicity region can produce a supernova of type IIp (with a luminosity *plateau*) followed by a collapse into a black hole induced by the fallback of the envelope matter.

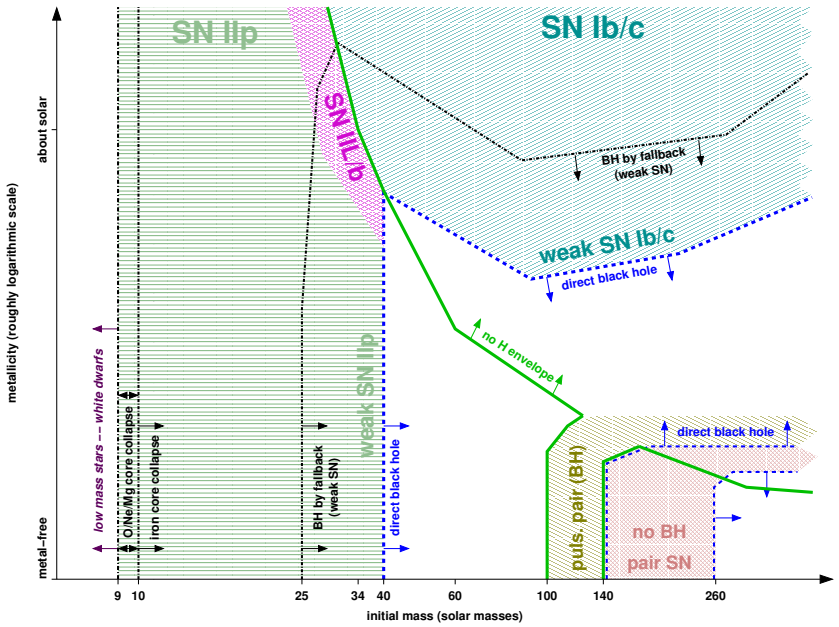

Figure 4.2 – Supernova type for non-rotating massive stars as a function of the initial mass and metallicity. Source: [194].

Due to the extreme densities reached in the stellar core, neutrino interactions play a significant role in the explosion mechanism. For this reason, neutrino intrinsic properties and the supernova mechanics are strictly related. The observation of a CCSN neutrino burst could shed light on several aspects of neutrino physics, astrophysics and nuclear physics. On the other hand, a better knowledge of neutrino properties can help in producing more accurate core-collapse models. A historical problem with the modelling of the core-collapse mechanism has been the reproduction of a successful explosion in simulations. This is especially difficult for simpler unidimensional models, that allow simpler calculations by assuming a radial symmetry for the star. Three-dimensional models have been more successful, as they allow the development of asymmetric convective motions in the mantle that can drive the explosion process. This comes at the cost of much higher computational requirements that could be satisfied only in recent years, although with standing limitations.

4.1.2 Core-collapse mechanism

A review of the core-collapse mechanism can be found in References [189, 195], on which the following description is based. Through its life cycle, a massive star in the *main sequence* goes through all the stages of nuclear fuel burning (H, He, C, O, Ne, Si). At last, the star enters the *silicon burning* phase. This is surprisingly brief (~ days) compared to the typical time scale of stellar evolution. At the end, the star presents

with an iron core surrounded by shells of lighter elements. The core radius is of a few thousands of kilometres with density in the order of $10^{10}\,\mathrm{g\,cm^{-3}}$. Iron has the lowest binding energy per nucleus and cannot participate in further fusion processes. At this point, the star is sustained by the pressure of degenerate relativistic electrons. In the so-called *capture phase* two processes take place; *iron photodissociation* and *electron capture*:

$$\gamma(124\,\mathrm{MeV}) + {}^{56}\mathrm{Fe} \rightarrow 13\,\alpha + 4\,n\,; \tag{4.1}$$

$$e^- + p \rightarrow n + \nu_e\,. \tag{4.2}$$

Electron capture can occur on free or bound protons, and is favoured by the release of iron photodissociation products. As a result, the number and kinetic energy of electrons are progressively reduced. The collapse begins as the core hits the Chandrasekar limit, which is dependent on the electron density. In lighter stars ($9-10\,\mathrm{M_\odot}$), unable to produce heavier elements on their own, a first collapse can be triggered by electron capture on magnesium and the subsequent increase in density allows for the production of the iron core.

The electron capture phase is characterised by a luminosity ramp from a non-thermal ν_e emission. In this, 10^{51} erg of energy are released over a time frame of 10 ms. The capture process endures until the inner part of the core ($\sim 0.8\mathrm{M_\odot}$) reaches a density of $\sim 3\cdot 10^{11}\,\mathrm{g\,cm^{-3}}$. Then, the inner core of the star undergoes a subsonic collapse with a velocity proportional to the radius. The outer region collapses in a supersonic free-fall regime. In approximately one second, the inner core reaches the density of nuclear matter $10^{14}\,\mathrm{g\,cm^{-3}}$. The collapse is abruptly stopped by the pressure of degenerate nucleons of the 10 km-radius *proton-neutron star* (PNS) in hydrostatic equilibrium. At the PNS surface, the collapsing matter develops a shock wave that propagates outwards with a speed of $\sim 1\cdot 10^{8}\,\mathrm{m\,s^{-1}}$. The infalling gas abruptly decelerates as it goes through the shock. In this phase, the shocked mantle presents a density gradient that goes from the nuclear matter density at the boundary of the core to $10^{9}\,\mathrm{g\,cm^{-3}}$ at the outer surface. The shock energy loss is of $\sim 1{,}5\cdot 10^{51}$ erg per 0.1 $\mathrm{M_\odot}$ of photodissociated matter. The released nucleons favour further the electron captures, producing a large number of neutrons and electron neutrinos. Neutrinos pile up behind the shock, which is opaque to them as long as its density is above $\sim 10^{11}\,\mathrm{g\,cm^{-3}}$. A few milliseconds after the bounce, as the shock crosses this density threshold, the neutrinos break free in the so-called *shock breakout pulse* or *neutronisation burst*. The pulse reaches a luminosity of $\sim 6\cdot 10^{53}\,\mathrm{erg\,s^{-1}}$ releasing $\sim 10^{51}$ erg of energy. The following stage is critical to the success of the supernova explosion. Progressively losing its energy in the propagation, the shock is bound to *stall*. Stellar matter keeps falling through the shock determining the so-called *accretion phase*. In this, the core is stirred by violent hydrodynamical motions reproducible only in complex 3D simulations. For the explosion to take place, an efficient process is required to revive the shock and power its propagation to the outer layers. One possible solution for this is *neutrino heating*, namely energy deposition by neutrinos on the shock. This corresponds to the *delayed* scenario, in which the explosion takes place after a $\sim 0{,}5$ s long accretion

phase. Under certain conditions, if the mass of the core is accreted beyond the point sustainable by the pressure of degenerate nucleons, the core can collapse into a black hole. In this case of *failed supernova*, neutrino from the accretion phase could still be detected, revealing events that would not have an optical counterpart.

4.1.3 CCSN neutrino phenomenology

CCSN neutrinos can be divided in three classes related to their interaction properties: ν_e, $\overline{\nu}_e$ and $\nu_x = \{\nu_\mu, \overline{\nu}_\mu, \nu_\tau, \overline{\nu}_\tau\}$. Muon and tau flavours cannot be distinguished as they are not allowed charged-current interactions for energies lower than the partner lepton mass (105 MeV for the muon). Electron neutrinos and antineutrinos are affected by the respective densities of neutrons and protons in the core. The largest amount of neutrinos is emitted between the accretion phase and the subsequent thermal cooldown. Inside the core, neutrinos are produced in different processes occurring at a temperature of ~ 40 MeV and confined in the stellar region where the density is above $\sim 10^{11}\,\mathrm{g\,cm^{-3}}$. The most relevant neutrino production processes are:

— electron or positron capture: $e^- + p \to n + \nu_e$, $e^+ + n \to p + \overline{\nu}_e$;
— electron pair annihilation: $e^- + e^+ \to \nu + \overline{\nu}$;
— electron-nucleon bremsstrahlung: $e^\pm + N \to e^\pm + N + \nu + \overline{\nu}$;
— nucleon-nucleon bremsstrahlung: $N + N \to N + N + \nu + \overline{\nu}$;
— plasmon decay: $\gamma \to \nu + \overline{\nu}$;
— photoannihilation: $\gamma + e^\pm \to e^\pm + \nu + \overline{\nu}$.

Neutrinos radiate from the star in correspondence of three *neutrinospheres*, namely the surfaces of last scattering for each neutrino species. The species with a lower interaction probability decouple earlier, at a smaller radius and a higher temperature. Three energy-dependent neutrinospheres for ν_x, $\overline{\nu}_e$ and ν_e emerge at radii between 50 and 100 km, with temperatures that are around 10, 15 and 20 MeV respectively. As the neutrino quasi-elastic cross section is in turn dependent on the energy, each neutrinosphere is smeared along the radial direction. The flux from a neutrinosphere can be approximated by a blackbody-like thermal spectrum subject to a pinching (i.e. suppression of the tails) that results from the cross section energy-dependence.

In the view of the shock propagation, the breakout burst occurs as the shock crosses the ν_e neutrinosphere. When the shock stalls at a radius of $100 - 300$ km, it is mostly transparent to neutrinos. Models predict that to revive the shock, 5 to 10% of the neutrinos need to be captured in it, depositing their energy. This process would be dominated by the charged-current interaction cross section of ν_e and $\overline{\nu}_e$. During the accretion phase, the infalling matter contributes to the heating of nucleons and photons in the core, enhancing the thermal neutrino emission. This creates a characteristic neutrino luminosity hump, which visible energy spectrum is partially influenced by the opacity of the shock at higher energies.

4.1.4 SN 1987A

The first and only observation of core-collapse supernova neutrinos occurred in 1987 with the explosion of the blue supergiant Sanduleak [196]. The progenitor was located in the Large Magellanic Cloud, a satellite galaxy of the Milky Way at $\sim 50\,\mathrm{kpc}$ from the Earth. The event was observed on February 24th, 1987 at a declination of $\delta = -69°$. The optical luminosity of the SN increased over the first three months afterwards. Due to the relative compactness of the progenitor (radius $\sim 10^7\,\mathrm{km}$) its emission has been relatively faint. No compact remnant has been identified despite extensive searches for pulsar signatures [197].

Four neutrino detectors were active at the time: two water Cherenkov (Kamiokande II [198], IMB [199]) and two scintillation detectors (Baksan [200], LSD [201]). Two dozen of events were detected across Kamiokande II, IMB and Baksan a few hours before the optical discovery. The event distribution as a function of time and energy is shown in Figure 4.3. Five events were detected by LSD a few hours further before, and they are usually excluded in joint analyses. Their interpretation is still debated [202, 203]. As no real-time trigger was available, the neutrino burst was discovered in the data only at a later time. A cautionary tale about Kamiokande-II observation is worth reporting: the 14 events are subject to a time uncertainty in the order of one minute, due to a drift in the clock of the detector that could not be re-calibrated as a consequence of a power fault at the facility [198].

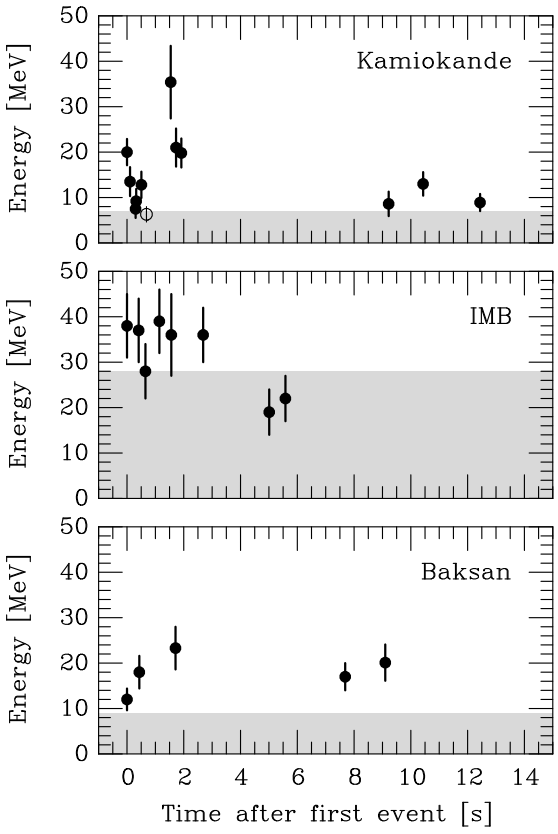

Figure 4.3 – SN 1987A neutrino observations at Kamiokande, IMB and Baksan. The energies refer to the secondary positrons from the reaction $\overline{\nu}_e + p \rightarrow n + e^+$. In the shaded area the trigger efficiency is less than 30%. The first event in each detector is assumed at the origin of the time reference. In Kamiokande, the event marked with an open circle is attributed to background. Source: [204].

The multi-messenger observation of SN1987A marks the origin of extrasolar neutrino astronomy. The number of observed neutrinos is compatible with a $\sim 3 \cdot 10^{53}$ erg scale emission of $\sim 3 \cdot 10^{57}$ neutrinos, of which 10^{28} have crossed the Earth. Although the statistical uncertainties are large, the observation is consistent with the standard model of the core-collapse outlined above, with a 0,7 s accretion phase and a typical cooling time scale of 4 s [205].

4.1.5 Galactic and near-galactic CCSN rate and progenitors

With the current generation of neutrino experiments, the horizon for CCSN detection is generally limited to the Milky Way, which edge is at 25 kpc, and its satellite galaxies, the mains being the Large and Small Magellanic Clouds at distances of $\sim 50 - 60$ kpc. The distance of the Galactic Centre, 10 kpc, is typically used as a benchmark for supernova neutrino studies. Low-background underground experiments on

the scale of few tens of kilotons are able to detect $\sim 10^3 - 10^4$ for a CCSN at 10 kpc. This is the case for the currently operating Super-Kamiokande (SK) [206] and the planned JUNO [207] detectors, based on water Cherenkov and liquid scintillator techniques, respectively. Andromeda (M31), the nearest major galaxy at a distance of 700 kpc, is beyond the sensitivity horizon for these instruments.

Galactic and near-galactic core-collapse supernovæ seem to be rare events. Written records exist for a total of nine SNe between AD 185 and 1987 [208]. Two more can be inferred by the observation of discovery remnants [209]. The last supernova observed in the Milky Way was Kepler's star in 1604 [210], and it is classified as a Type Ia. Since then, SN 1987A has been the only SN observed in the galactic and near-galactic region, aside from being the first to be seen in neutrino detectors. supernovæ may be obscured by interstellar dust if occurring in dense regions of the Galaxy. The discovery of the youngest galactic supernova remnant SNR G1.9+0.3 by the *Very Large Array* (VLA) radio observatory [209] in 1984, subsequently imaged in the X-rays by *Chandra* [211], points to an obscured supernova explosion that would otherwise have reached the Earth between 1890 and 1908. SNR G1.9+0.3, also attributed to a Type Ia supernova, is located in a dense region near the Galactic Centre at a distance of 8,5 kpc.

Different observable proxies can be combined to estimate the expected rate of Galactic core-collapse supernovæ, such as the count of massive stars (SN progenitors), the rates of extragalactic SNe, the abundance of specific stellar nucleosynthesis products, the birth rate of neutron stars, and the ages of supernova remnants. An up-to-date combined statistical evaluation [212] estimates the rate of galactic CCSNe at 1.43 ± 0.46 per century, with an expected time between events of 61^{+24}_{-14} yr. Supernova progenitor candidates are mostly red and blue supergiant stars. The distribution of the expected optically-observable SNe in the Milky Way as reported in Reference [213] is reported in Figure 4.4.

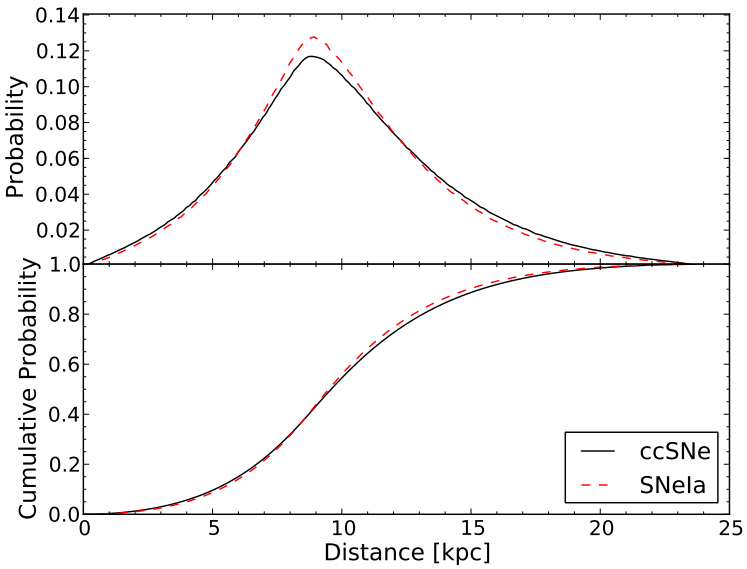

Figure 4.4 – Differential (top) and cumulative (bottom) distance distributions of expected (optical) Galactic SNe from the Sun, for core-collapse and thermonuclear (Ia) candidates. Source: [213].

.

The future Hyper-Kamiokande (HK) detector will be able to record an order of magnitude more events than SK and JUNO, covering up to 1 Mpc with reasonable sensitivity [214]. However, the two major galaxies within this horizon, Andromeda and the Triangulum, have a relatively low star formation rate and therefore an even lower expected supernova rate compared to the Milky Way [215].

The Betelgeuse red supergiant star in the Orion constellation is often examined as a promising CCSN progenitor, with a mass estimated at $15-20\,M_{\odot}$. In December 2019, a significant dimming of its luminosity has been reported. The phenomenon has been suggested as possible precursor of a supernova explosion, although different interpretation are more scientifically plausible [216]. At a distance of ~ 200 pc, large neutrino detectors could expect to observe as much as $\mathcal{O}(10^6)$ events, which would represent an unprecedented potential for the study of core-collapse supernovae. While the typical time scales of the stellar evolution make the observation of a supernova by Betelgeuse unlikely, it stands as an interesting test-case for most neutrino studies.

4.2 CCSN neutrino detection with KM3NeT

Charged-current interactions from CCSN neutrinos in water produce electrons or positrons below 100 MeV. In this energy range, the electron energy loss occurs mainly by ionisation and thermal excitation in collisions with water molecules. The typical length of a Cherenkov track for an electron or a positron is 0,5 cm per MeV of

energy [217]. Above 0,8 MeV, the particle induces production of Cherenkov light in the medium.

The instrumentation density of KM3NeT detectors is aimed at neutrinos above the GeV scale. For an event to be triggered and reconstructed, multiple photons need to be detected on different optical modules, located (tens of) metres away from each other. At CCSN energies, a relatively small number of Cherenkov photons is released in a point-like directional emission. The sparse instrumentation of the detector makes it unlikely to detect more than one photon on DOMs which are not in the proximity of the interaction.

In principle, a search for an increase of the global hit rate with single hit data (L0) would allow maximising the detector effective volume, as the majority of photons can be detected up to a distance in the order of the absorption length (80 m). This approach is adopted, for example, by IceCube [217]. For a seawater-based detector, the high optical background rate due to radioactivity and the time-variability induced by bioluminescence makes this strategy impractical. The search of CCSN neutrinos in KM3NeT relies therefore on coincidences which are for the large majority detected on a single DOM. The tight time-correlation between the hits can be exploited to reject the random contribution of uncorrelated noise. The selection of coincidences with a higher number of hit PMTs (*multiplicity*, see also Chapter 3) allows for further discrimination potential against radioactivity-induced Cherenkov emissions. Inter-DOM coincidences consisting of at least two hits on two DOMs that are nearest-neighbours could offer an additional detection channel, favouring the higher average energy emission of CCSN neutrinos over the MeV-scale radioactive background. However, they require an extended time window compared to local coincidences, making it harder to reject the random background. Preliminary evaluation of approaches based on inter-DOM coincidences has revealed a scarce potential of improving the detection sensitivity. The strategy adopted in KM3NeT relies therefore on the observation of a population of coincidences above the background, over a time scale covering the brightest part of the neutrino emission, i.e. the ~ 500 ms of the accretion phase. In this, bioluminescence and radioactive backgrounds are suppressed by the use of (high-multiplicity) coincidences, while filtering strategies are adopted to reduce the contamination from atmospheric muons.

4.2.1 Flux model

In general, the time-dependent flux of CCSN neutrinos can be described as:

$$\frac{d\Phi}{dE}(E,t) = \frac{L}{4\pi d^2} f(E, \langle E \rangle (t), \alpha(t)) \tag{4.3}$$

where $\langle E \rangle$ is the average neutrino energy, L is the neutrino luminosity, d is the distance to the source, and α is the spectral pinching parameter. At a given time, the energy

dependence of the spectrum f follows a quasi-thermal distribution:

$$f(E, \langle E \rangle, \alpha) = \frac{E^{\alpha}}{\Gamma(1+\alpha)} \left(\frac{1+\alpha}{\langle E \rangle} \right)^{1+\alpha} e^{\frac{-E(1+\alpha)}{\langle E \rangle}} . \tag{4.4}$$

The spectral pinching parameter α is defined as:

$$\alpha = \frac{\langle E_\nu^2 \rangle - 2\langle E_\nu \rangle^2}{\langle E_\nu \rangle^2 - \langle E_\nu^2 \rangle} . \tag{4.5}$$

For $\alpha = 2$ the expression reduces to a Maxwell-Boltzmann distribution, while for $\alpha > 2$ the spectrum is pinched, i.e. it has a smaller width and suppressed tails.

In this analysis, the benchmark fluxes considered come from a three-dimensional CCSN model developed by the MPA Garching group [218]. This provides the neutrino flux simulated for two different stellar progenitors of 11 $M_\odot$ and 27 $M_\odot$ that can be considered as a pessimistic and optimistic case for the detection. A third model for a40 $M_\odot$ progenitor collapsing into a black hole is taken as a benchmark for a *failed supernova* [219]. Notably, this has an higher neutrino luminosity compared to the exploding scenarios. The corresponding fluences (time-integrated flux as a function of the energy) are shown in figure Figure 4.5.

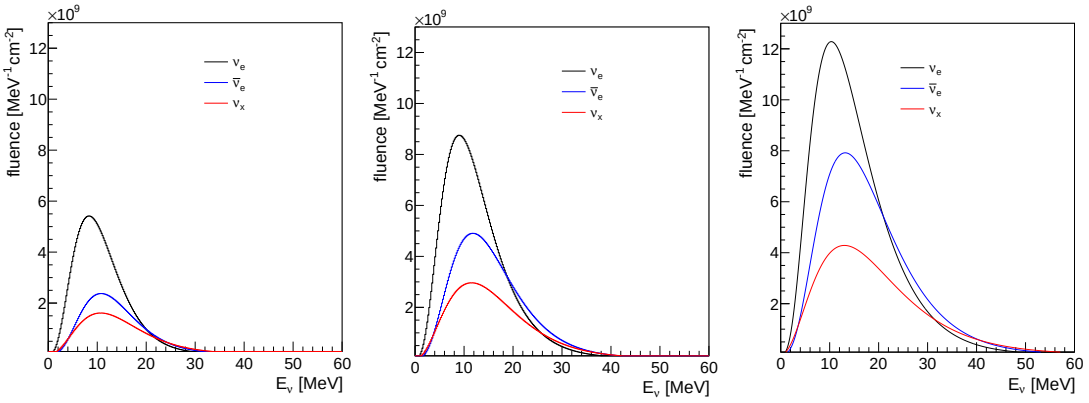

Figure 4.5 – Neutrino fluence for the accretion phase of a core-collapse supernova at 10 kpc for the Garching 3D simulation models of 40 $M_\odot$ (right), 27 $M_\odot$ (middle) and 11 $M_\odot$ (left) over a time duration of 562 ms 543 ms and 340 ms, respectively.

In general, neutrinos undergo MSW-like flavour conversion processes as they propagate in the dense stellar medium. This introduces large uncertainties in the flavour composition of flux reaching the Earth. The purpose of this analysis is to evaluate the KM3NeT performance, and this is done by assuming a designated flux hypothesis as a benchmark. The uncertainties affecting the flux are therefore excluded from the discussion.

4.2.2 Low energy neutrino interactions in water

An overview of supernova neutrino detection in different media can be found in Reference [220]. As mentioned above, the typical energies of supernova neutrinos charged-current interactions are allowed only to electronic species. It is useful to remind that charged-current interactions are subject to the following kinematic threshold [189, 220]:

$$E_\nu^{thr} = \frac{M_f^2 + m_e^2 + 2M_f m_e - M_i^2}{2M_i} \simeq M_f - M_i + m_e \tag{4.6}$$

where M_i and M_f are the masses of the initial and final nuclear states, respectively, and $m_e = 511\,\text{keV}$ the mass of the electron. In water, neutrinos in the $1 - 100\,\text{MeV}$ energy range are subject to four interaction processes:

Inverse beta decay (IBD)

$$\overline{\nu}_e + p \rightarrow n + e^+ \tag{4.7}$$

It is the charged-current interaction of electron antineutrinos with free protons (hydrogen nuclei). Given Equation (4.6), the reaction has a threshold $E_\nu^{th} \simeq 1{,}8\,\text{MeV}$. The following kinematic balance holds:

$$E_\nu = E_e + m_n + T_n - m_p \tag{4.8}$$

where E_e is the electron energy, m_n and m_p the neutron and proton masses, and $T_n \approx 0$ the (negligible) recoil kinetic energy of the neutron. From Equation (4.8) the positron energy is given by $E_e \simeq E_\nu - 1{,}3\,\text{MeV}$, reflecting the one of the incident neutrino. The γ pair produced by the positron annihilation is undetectable in a water Cherenkov detector. The combination of a relatively large cross section, low threshold and efficient energy transfer to the lepton makes inverse beta decay the favoured detection process for electron antineutrinos at low energy, in both scintillator and water Cherenkov detectors. In KM3NeT, the large majority of detected neutrino events from a CCSN burst will be IBD interactions. Since the positron emission is basically isotropic, the information on the incoming neutrino direction is lost. The recoiling neutron thermalises and is captured by a proton to form a neutron with the emission of a $\sim 2{,}2\,\text{MeV}$ γ-ray [221].

Elastic scattering on electrons (EES)

$$\nu + e \rightarrow \nu + e \tag{4.9}$$

It can occur by neutral-current interaction for all flavours, or by charged-current for electron neutrinos (cf. third and fourth diagrams of Figure 1.22). It has no threshold but a much smaller cross section than IBD, and it is most relevant in low-background detectors. The scattering is directional and some detectors may be able to point at the source through this channel.

CC interaction with oxygen (OCC)

$$\nu_e + {}^{16}\mathrm{O} \rightarrow e^- + {}^{16}\mathrm{F}\ ;\ \overline{\nu}_e + {}^{16}\mathrm{O} \rightarrow e^+ + {}^{16}\mathrm{N} \tag{4.10}$$

For these, Equation (4.6) yields a threshold of 15.4 and 11,4 MeV respectively.

NC interaction with oxygen (ONC)

$$\nu + {}^{16}\mathrm{O} \rightarrow \nu + {}^{16}\mathrm{O}^* \tag{4.11}$$

It produces de-excitation γ photons that in-turn can Compton-scatter.

The cross-sections for these interaction processes in water are shown in Figure 4.6.

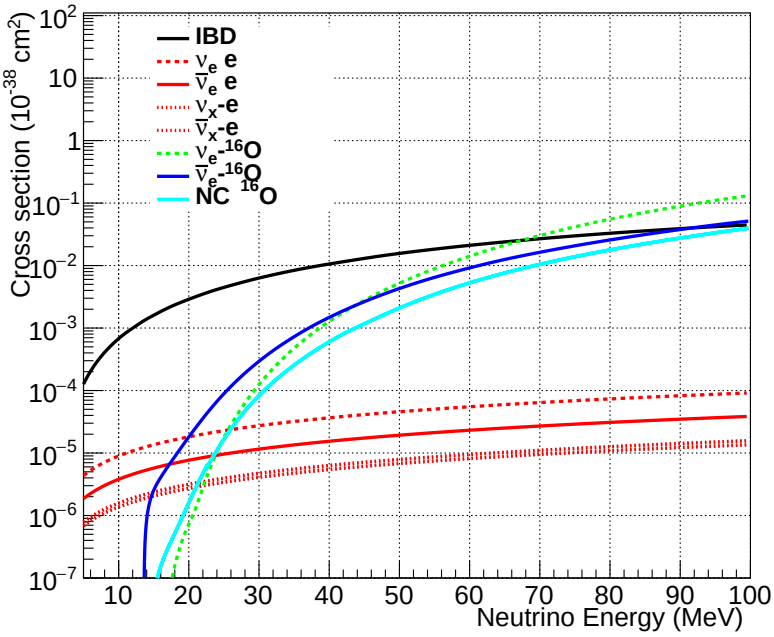

Figure 4.6 – Cross sections for CCSN neutrinos in water. Plot produced with the `SNOwGLoBES` package [222].

In this analysis, only IBD, EES and OCC interactions are considered. Cross sections for IBD and EES are taken from Reference [223] and [224] respectively. The cross sections of OCC interactions are taken as provided in the `SNOwGLoBES` software package [222]. Gamma rays from neutron capture or oxygen de-excitation can undergo Compton scattering, pushing the recoiling electron above the Cherenkov threshold [221]. This negligible contribution to the signal is ignored in this analysis. Due to the energy dependence of the cross sections, the number of interactions and detected events for each interaction channel is in general model-dependent. For the considered fluxes, the contribution of IBD, EES and OCC to the total rate is 97%, 3% and sub-percent

respectively. The CCSN detection potential of KM3NeT is mainly determined by the IBD-interacting electron antineutrino component of the flux reaching the Earth.

4.2.3 Simulation of CCSN neutrinos

Combining the neutrino flux at the Earth with the interaction cross sections for the three relevant channels, the interaction rates as a function of time are calculated. The rates normalised to a target mass of 100 kton of water are reported in Figure 4.7. A signature of hydrodynamical instabilities [225] can be observed on the different channels in the form of cyclical luminosity patterns in the time profile.

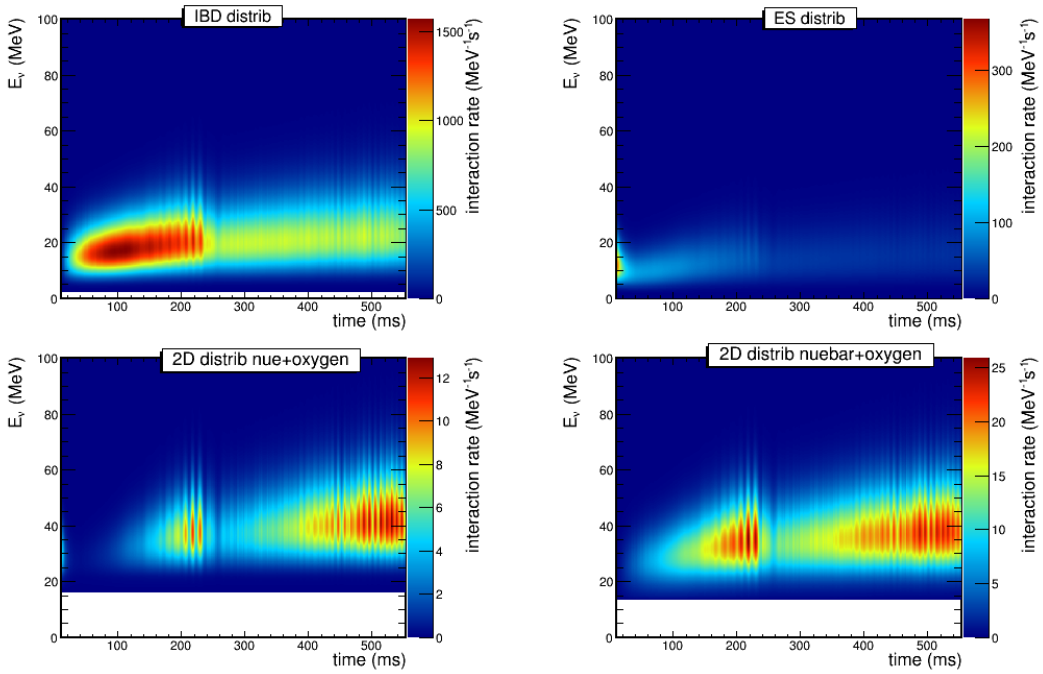

Figure 4.7 – IBD (top left), EES (top right), OCC (bottom) interaction rates for 100 kton of water.

For each simulated interaction, the energy and direction of the outgoing lepton are drawn from a probability distribution given by the differential cross section of the process. The coordinates of each interaction vertex are generated with a uniform distribution inside a sphere of 20 m radius, centred on the DOM. It is verified that an extension of 5 m of the generation radius does not increase the rate of coincidences by more than 1%. For the ORCA geometry, a portion of the generation volume is shadowed by neighbour DOMs. For the nearest neighbours at a distance of 9 m, a DOM shadows an area of $\sim 0{,}15\,\mathrm{m}^2$ on a spherical surface of $\sim 10^3\,\mathrm{m}^2$. This corresponds to a negligible ~ 0.3 per mille fraction of the solid angle. For DOMs on adjacent detection units, the effect is even smaller.

The generated leptons are processed with the `KM3Sim` software, where they are propagated accounting for the energy losses and production of the Cherenkov light. In this, the GEANT4 *cut value* is tuned for proper treatment of low energy particles. The cut value determines the minimum length of the track segment in the simulation of the particle propagation. While neutrino simulations above the GeV scale use a standard value of 500 µm, MeV particles require a cut value of 1 μm. This is verified to produce good data – Monte Carlo agreement in the absolute rates of the coincidences induced by radioactive decays, that are one order of magnitude lower in energy.

After the simulation of the Cherenkov light, the photoelectrons are processed with `JEventTimesliceWriter` and `JTriggerProcessor`. The first produces a sequence of DAQ timeslices in which the events are distributed according to their absolute time. The second applies the data filtering and triggering algorithms, and is configured to produce the L1 and SN DAQ timeslice streams used in the analysis, analogously to the real data processing (see Section 2.1.3 and 2.3). The application `JMonitorMultiplicity` is used to process timeslice data. All the hits are analysed, and coincidences are counted according to their multiplicity. For the purpose of this analysis, such coincidences are designated as *events*. Since the possibility of PMT afterpulses is not accounted for in the simulation, these interactions cannot produce more than one coincidence on a given DOM.

In the simulation, an arbitrary number N_{gen} of neutrinos is generated. This is chosen according to the desired statistical uncertainty on the result. The number of detected events as a function of the multiplicity, $N_{\text{det}}(M)$, is expressed by weighting the number of events at a given multiplicity in the simulation output, $N_{\text{MC}}(M)$, according to the relation:

$$N_{\text{det}}(M) = N_{\text{MC}}(M)\, N_{\text{gen}}^{-1}\, I_\nu\, \rho_{\text{water}}\, V_{\text{gen}}\,, \tag{4.12}$$

where I_ν is the number of neutrino interactions per unit of mass of water, $\rho_{\text{water}} = 10^3\,\text{kg}\,\text{m}^{-3}$ the water density and V_{gen} the generation volume. The presence of sea salt in water (for a 3% increment in density with respect to freshwater) is neglected. The interaction density I_ν is equal to the integral over time and energy of the rates shown in Figure 4.7, divided by 100 kton. The *effective mass* for a single DOM as a function of the multiplicity is defined as:

$$M_{\text{eff}}(M) = N_{\text{det}}(M)\, I_\nu^{-1}\,; \tag{4.13}$$

and is calculated from the simulation by substituting $N_{\text{det}}(M)$ according to Equation (4.12). For a KM3NeT building block of 115 detection units (2070 DOMs), the number of detected events and the total effective mass are reported as a function of multiplicity in Table 4.1 and 4.2.

4.2.4 Effect of the photon detection efficiency

The actual number of hits for a given number of photons reaching the DOM depends on the photon detection efficiency of all the PMTs involved. In general, the signal

Table 4.1 – Expected number of signal events as a function of the multiplicity for one instrumented block. Statistical uncertainties from the Monte Carlo simulation are reported.

Model	**Multiplicity**				
	2	**3**	**4**	**5**	**6**
11 $M_\odot$ (340 ms)	1119 ± 3	258 ± 1	$100{,}4 \pm 0{,}8$	$48{,}9 \pm 0{,}5$	$25{,}8 \pm 0{,}4$
27 $M_\odot$ (543 ms)	4806 ± 9	1120 ± 5	442 ± 3	218 ± 2	$116{,}0 \pm 1{,}5$
40 $M_\odot$ (572 ms)	$15\,240 \pm 30$	3650 ± 10	1449 ± 8	723 ± 6	399 ± 4
	7	**8**	**9**	**10**	**11**
11 $M_\odot$ (340 ms)	$13{,}3 \pm 0{,}3$	$7{,}2 \pm 0{,}2$	$3{,}4 \pm 0{,}1$	$1{,}29 \pm 0{,}08$	$0{,}50 \pm 0{,}05$
27 $M_\odot$ (543 ms)	64 ± 1	$35{,}2 \pm 0{,}8$	$19{,}4 \pm 0{,}6$	$8{,}0 \pm 0{,}4$	$1{,}9 \pm 0{,}2$
40 $M_\odot$ (572 ms)	226 ± 3	127 ± 2	$69{,}5 \pm 1{,}8$	$36{,}6 \pm 1{,}3$	$15{,}0 \pm 0{,}8$

Table 4.2 – Effective mass (in kton) as a function of the multiplicity for the 11 $M_\odot$, 27 $M_\odot$ and 40 $M_\odot$ progenitors.

Model	**Multiplicity**					
	2	**3**	**4**	**5**	**6**	**7**
11 $M_\odot$ ($\langle E_\nu \rangle = 13{,}7$ MeV)	40±4	12±3	5±1	2.5±0.6	1.3±0.4	0.6±0.2
27 $M_\odot$ ($\langle E_\nu \rangle = 15{,}7$ MeV)	53±5	16±3	7±1	4.0±0.9	2.0±0.6	1.0±0.4
40 $M_\odot$ ($\langle E_\nu \rangle = 18{,}2$ MeV)	67±7	21±4	9±2	5±1	2.7±0.8	1.5±0.5

simulation can be performed accounting for the calibrated PMT efficiencies of the operating detector. The absolute normalisation of the photon detection efficiency is affected by an uncertainty in the order of 5% [163]. To evaluate the impact of an overall scaling of the efficiency on the number of detected signal events, two additional simulations are performed to cover a ±10% variation from the nominal value (unity). This is done by tuning the corresponding parameter in input to the `JTriggerProcessor` application. The relative variation of the number of signal events for a range of minimum multiplicities is reported in Figure 4.8 as a function of the relative variation of the PMT photon detection efficiency.

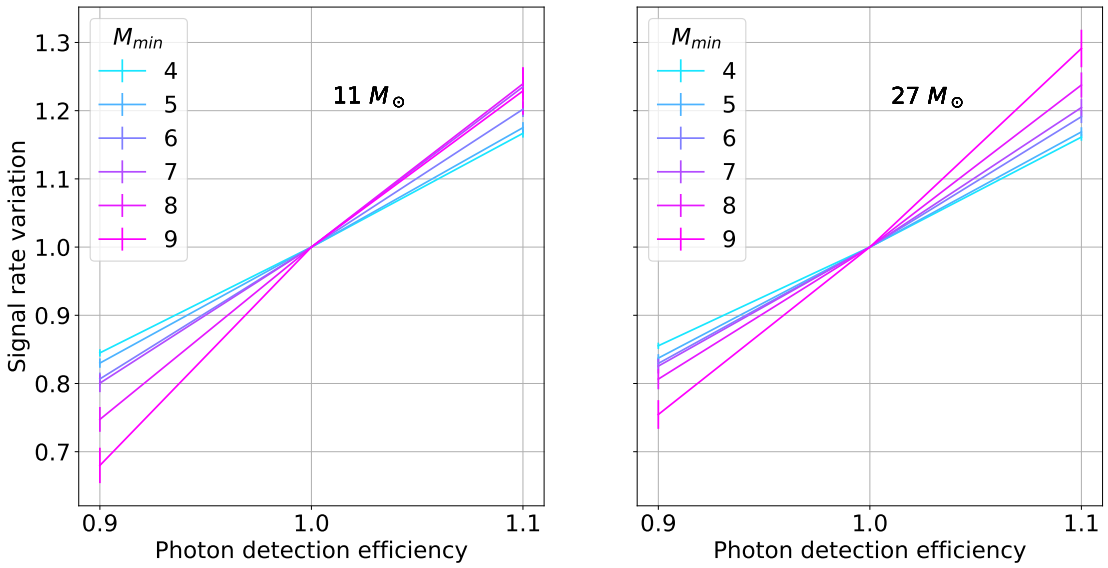

Figure 4.8 – Relative variation of the number of detected coincidences with a given minimum multiplicity as a function of the relative variation of the PMT photon detection efficiency used in the simulation. On the left for the 11 $M_\odot$ model and on the right for the 27 $M_\odot$ model.

In general, the effect is non-linear and can depend on the spectrum of the interacting neutrinos. However, for a minimum multiplicity of 6-7, the behaviour can be approximated with a linear interpolation of a ±20% variation of the number of signal events for a ±10% of the PMT efficiency.

4.3 Study of the background

The search for supernova neutrinos in KM3NeT is affected by optical backgrounds produced by bioluminescence, radioactive decays and atmospheric muons. As examined in Chapter 3, these result in typical rates of single hits and coincidences on each DOM. While searching for an overall increase in single hit rates induced by CCSN neutrinos would maximise the detector effective mass, exploiting them is problematic

due to the severe variability introduced by bioluminescence. The rate of single hits, even when integrated over all the optical modules of the detector, can undergo significant changes on the characteristic time frame of a CCSN emission. This prevents an accurate statistical modelisation of the background. For this reason, this analysis is focused on coincidences.

4.3.1 Data sample and Monte Carlo simulation

The analysis is based on SN timeslice data. These include all the L0 hits corresponding to 10 ns coincidences where at least 4 PMTs with axes within 90° are hit (see definition of DAQ timeslice in Section 2.1.3). As shown later in the Chapter, coincidences below multiplicity four do not significantly contribute to the sensitivity. The use of SN timeslice data stream provides several advantages. Being the average hit rate for SN timeslices a factor ~ 100 lower than the hit rate for L1 timeslices, the data throughput is proportionally reduced, ensuring the sustainability of its permanent storage. In addition, the generation of SN timeslice data is performed by a scalable architecture of parallel data filters that take care of the most computationally demanding task. The subsequent processing of the SN data from a full KM3NeT building block can, on the other hand, be fulfilled in real time by a single application (see Section 4.6).

The background coincidence rates are measured from the data of the first two lines of ARCA (*KM3NeT/ARCA2*) and the first four lines of ORCA (*KM3NeT/ORCA4*). These will be referred to as *sea data* in contrast to *simulated data*. The selected data taking period for ARCA2 is the same used for the analysis presented in Chapter 3, going from December 23, 2016, to March 2, 2017. The data taking period considered for ORCA4 spans from September 30, 2019, to November 4, 2019. The detectors show stable photon detection efficiencies in the considered periods, which is a prerequisite for a consistent estimation of the background rates. The average PMT efficiency for the ARCA2 and ORCA4 detector is 1.025 and 0.96, respectively. One of the aims of the analysis is to ensure that it can be applied to (almost) any data taking conditions. For this, the *reference* background rates are first measured from timeslices where at least 99% of the PMTs are active (i.e. not in *high-rate-veto* or *FIFO-almost-full* condition, from now on referred to as *active PMTs*). After the optimisation of the analysis strategy, the variation of the background distribution will be characterised as a function of the fraction of active PMTs.

A simulation of timeslice data for the case of an ARCA and an ORCA building block has been realised to evaluate the analysis on a complete detector. The simulation is based `MUPAGE` for the generation of atmospheric muons, `JSirene` for muon propagation and Cherenkov light production. `JEventTimesliceWriter` and `JTriggerProcessor` are used to produce SN timeslice data.

4.3.2 Background coincidence rates

In the analysis of SN timeslices, a time window of 10 ns is adopted to define a coincidence. For sea data, hits with a time-over-threshold below 3 ns are excluded. These short pulses do not originate from genuine photons and there is an ongoing discussion on the possibility of rejecting them in the offshore front-end electronics. For the same reason, they are not simulated.

In Figure 4.9, the average DOM coincidence rate as a function of the multiplicity is shown for the ARCA2 and ORCA4 detectors. The dominant contributions, radioactive decays and atmospheric muons, are highlighted with a shaded area over the corresponding multiplicity region. The radioactivity-induced coincidence rates are slightly higher for ARCA2 compared to ORCA4, reflecting the difference in the average efficiencies of the PMTs. The muon-induced coincidence rates show the different rates at the ORCA and ARCA depths.

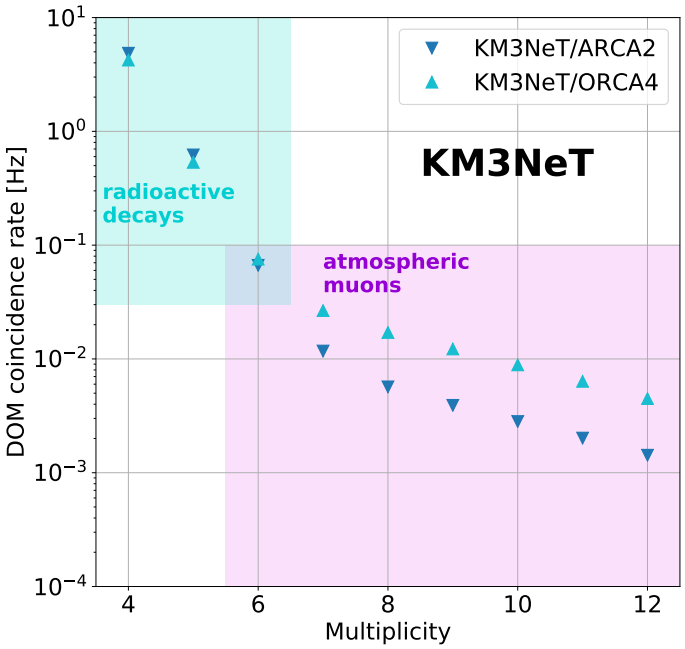

Figure 4.9 – Background coincidence rate per DOM as a function of the multiplicity for ORCA4 (light blue points) and ARCA2 (dark blue points). The dominant contribution to the low and high multiplicity regions are highlighted. Statistical errors are included and smaller than the markers. The shaded areas indicate the dominant contribution to the correspondent multiplicity region.

For a first indication of the discrimination potential, the number of background events in 500 ms for a KM3NeT ORCA and ARCA building block is reported in Figure 4.10, compared with the signal prediction for the three CCSN progenitors considered. Here, the background rates have been corrected for the PMT efficiencies,

normalising them to the nominal value used to simulate the signal.

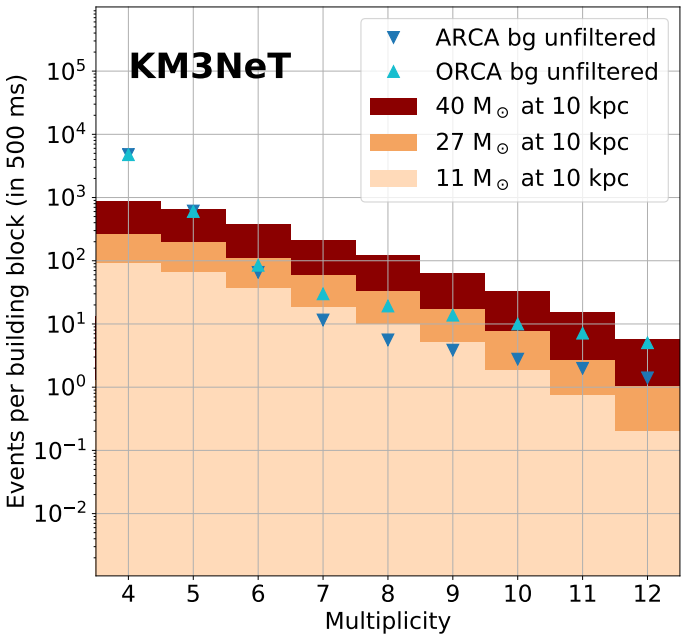

Figure 4.10 – Expected number of background events in 500 ms per KM3NeT building block as a function of the multiplicity for ORCA (light blue points) and ARCA (dark blue points) compared with the signal expectation for the 11, 27, and 40 $M_\odot$ progenitors (shades of orange filling).

At multiplicity up to four, the background dominates the signal by one order of magnitude. At multiplicity twelve and above, the expected number of signal events for a typical CCSN falls below the unit (except for the 40$M_\odot$ progenitor). The capability of reducing the background in the 4-12 multiplicity range are discussed in the following Section.

4.3.3 Background filtering

The background filtering strategy has two aims: to reduce the overall optical background rate and to suppress the detection of multiple coincidences induced by a single background event, as can be the case for PMT afterpulses and atmospheric muons. The removal of correlated spurious coincidence is also a requirement to ensure that the expected number of background events over the typical time scale of a CCSN neutrino burst is distributed according to the Poisson statistic. In particular, the distribution of the number of background events in a time window of length τ should be Poisson with an expectation value $\mu_b = \rho_b \tau$, where ρ_b is the background rate.

Radioactivity is dominated by the β decay of the ^{40}K isotope naturally present in sea salt, with the emission of ~ 1,3 MeV electrons. The induced Cherenkov photons are

for the large majority detected on an individual DOM as single hits or low multiplicity coincidences. Since the typical energy scale of CCSN neutrino interactions is an order of magnitude higher, a cut on the minimum multiplicity is the most efficient way of reducing the contribution of radioactivity to the background. On the other hand, atmospheric muons tend to produce coincidences across the different DOMs intercepting by the track Cherenkov cone. These are time-correlated on a scale of a few microseconds, that corresponds to the time a relativistic particle takes to cross the instrumented volume. Besides, afterpulses can result in the detection of spurious coincidences correlated to a genuine one, especially in presence of PMTs detecting a large number of photons. In the following, two evaluated filtering strategies are described. In the view of the background filtering, the population of coincidences detected by the DOMs across the whole detector is reduced to a population of background *events*. A background event can correspond to one or more coincidences, and can eventually be rejected by the filter logic. On the other hand, the equivalence between signal coincidences and signal events, adopted in Section 4.2.3, still holds. As the detection of supernova neutrino signatures across multiple DOMs is negligible, so it is the expected loss of signal efficiency from the application of the filters.

4.3.3.1 Coincidence correlation

The *coincidence correlation* filter is a simple approach based solely on timeslice data, exploiting time correlations between coincidences. In this, every time a coincidence at a multiplicity M_{veto} or above is recorded, the whole detector is vetoed for a duration τ_{veto} of 1 µs for ORCA and 3 µs for ARCA. The algorithm is described as follows:

1. coincidences with multiplicity below M_{veto} are discarded;
2. the remaining coincidences are clustered in *events* according to τ_{veto}, regardless of their localisation;
3. events containing coincidences on more than one DOM are discarded.

Each event surviving the filter consists of one or multiple coincidences on a single DOM within a time interval equal to τ_{veto}. In case of multiple coincidences, the time and multiplicity of the event are taken from the (first) coincidence with the highest multiplicity. An example of the filter behaviour, selecting the coincidences in the multiplicity range $7-11$, is shown in Figure 4.11 for a typical run of ARCA2 and ORCA4 respectively. The number of detections per sample (100 ms timeslice) is evaluated at each step of the algorithm. Before any filtering (*coincidences*) multiple DOMs can detect many high-multiplicity coincidences from a single muon event. After the clustering (*clusters*) the correlated coincidences are merged, and the distribution is well approximated by a Poisson. After the application of the *veto* (*events*) the expectation value of this distribution is reduced.

Table 4.3 – Rejection efficiency (reverse cumulative) of the coincidence correlation filter in ARCA2 and ORCA4 sea data.

Multiplicity	4	5	6	7	8	9	10	11	12
ARCA2	0.4%	2%	9%	21%	24%	24%	24%	24%	25%
ORCA4	4%	21%	67%	90%	95%	95%	96%	96%	96%

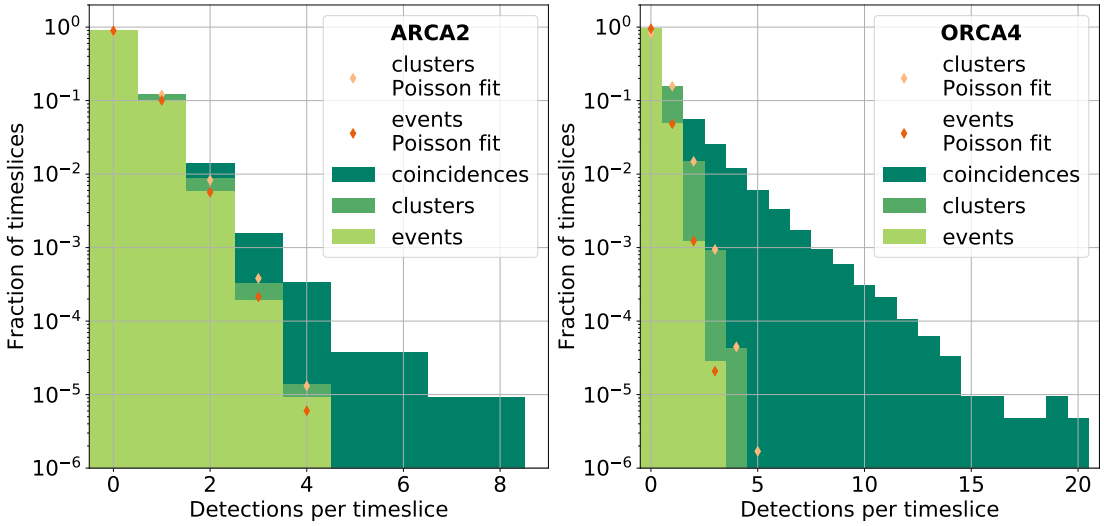

Figure 4.11 – Fraction of timeslices as a function of the number of detections in a timeslice before filtering (*coincidences*), after time-clustering (*clusters*) and after the muon veto (*events*) for a typical run of ARCA2 (left) and ORCA4 (right). A Poisson distribution with expectation value obtained from the mean of the data is superimposed for clusters and events.

The filtering introduces a dead time. A signal event is vetoed if occurring within $\pm\tau_{\text{veto}}$ with respect to the time of any coincidence having multiplicity $\geq M_{\text{veto}}$. The corresponding dead time fraction is, naturally:

$$f_{DT} = 2\,\tau_{veto}\,\rho_{M\geq M_{\text{veto}}}\,N_{DOM}\,; \tag{4.14}$$

where $\rho_{M\geq M_{\text{veto}}}$ is the DOM rate of coincidences at multiplicity M_{veto} or above and N_{DOM} the number of DOMs of the detector. A sustainable choice as $M_{\text{veto}} = 4$ corresponds to a $f_{DT} \simeq 6.5\%$ and 2% for an ARCA and ORCA building block, respectively. With this, the rejection efficiency evaluated for ARCA2 and ORCA4 data is illustrated in Table 4.3.

The ORCA background rate at multiplicity six and above is near to the residual contribution from radioactivity ($\sim 5\cdot10^{-2}$ Hz), confirming an excellent muon rejection performance. On the contrary, the rejection in ARCA is limited by the lower instrumen-

tation density. This can be explained taking into account the inverse proportionality between the distance of closest approach of a muon to the DOM and the maximum multiplicity recorded in correspondence. This relation is illustrated in Figure 4.12. As it can be observed, the majority of muons producing a maximum multiplicity of four (that would be required to veto any other coincidence by the same muon) have the closest approach below 20 m. The higher is the multiplicity of the coincidence to veto, the lower is the probability for the muon to approach a neighbour DOM near enough to produce a second one above the veto threshold. As an example, most muons producing a multiplicity of six and above have a closest approach below 10 m. As neighbouring ARCA DOMs are at a minimum of 36 (90) metres away, a significant fraction of muons are not vetoed as they will be farther than 20 m to any other DOM.

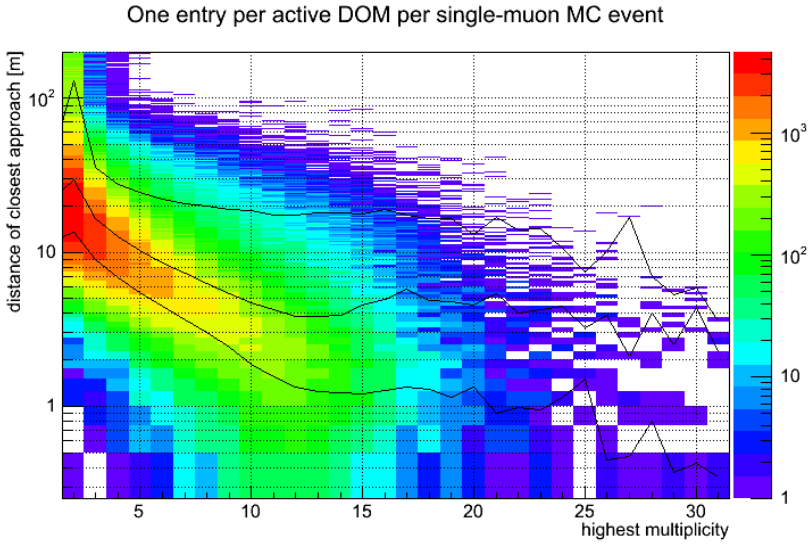

Figure 4.12 – Highest multiplicity coincidence of single-muon events versus the distance of closest approach, determined from atmospheric muon Monte Carlo. The black lines show the 10%, 50% and 90% quantiles. (Author: M. Jongen).

This filtering strategy has the advantages of simple implementation, its sole dependence on timeslice data and a dead time fraction which is negligible for a detector size up to ~ 10 detection units. In this view, it is suitable for real-time monitoring in the first commissioning stages of the KM3NeT detector. However, it is relatively inefficient as the majority of the veto-inducing coincidences come from radioactivity and not from actual muons. For this reason, a different approach using the *triggered events* is introduced in the next Section.

4.3.3.2 Triggered events

A more refined filter is developed taking advantage of the information contained in the *triggered events* produced by the KM3NeT physics triggers. As introduced in

Section 2.1.2, each triggered event contains a collection of *triggered hits* that has been identified as causally connected and matching a given event topology (spherical or cylindrical). In this analysis, for each triggered event, a *veto* is applied on the set of DOMs detecting at least one triggered hit for the duration of the time interval spanned by the triggered hits (*time range*). Coincidences are pre-selected and grouped in *SN events* following steps 1-2 of the algorithm illustrated in the previous Section. Each SN event is assigned the multiplicity and the time of the (first) coincidence with the highest multiplicity in the set. The event is then discarded if this coincidence occurs on a DOM and at a time covered by the *veto* window. The surviving SN events are considered as a function of their multiplicity.

To test the approach, sea data of ARCA2 and ORCA4 have been analysed. Each run is processed using timeslice and triggered events data. All available triggers are considered. The typical trigger criteria for the considered data-taking periods are:

— `3DMuon`: min 3 L1 hits on 3 different modules within a cylinder of 43 m diameter for ORCA; min 4 L1 hits on 4 modules, within a cylinder of 120 m for ARCA;
— `3DShower`: 3 L1 hits on 3 different DOMs within a sphere of diameter 52 m for ORCA and 250 m for ARCA;
— `MXShower`: one L1 plus at least 7 L0 hits on 3 different DOMs within a sphere of 47 m diameter for ORCA and 110 m for ARCA.

Example distribution of the time range of the triggered hits are shown for the ARCA2, ORCA4 sea data, and for the ARCA and ORCA simulated building blocks, in Figure 4.13.

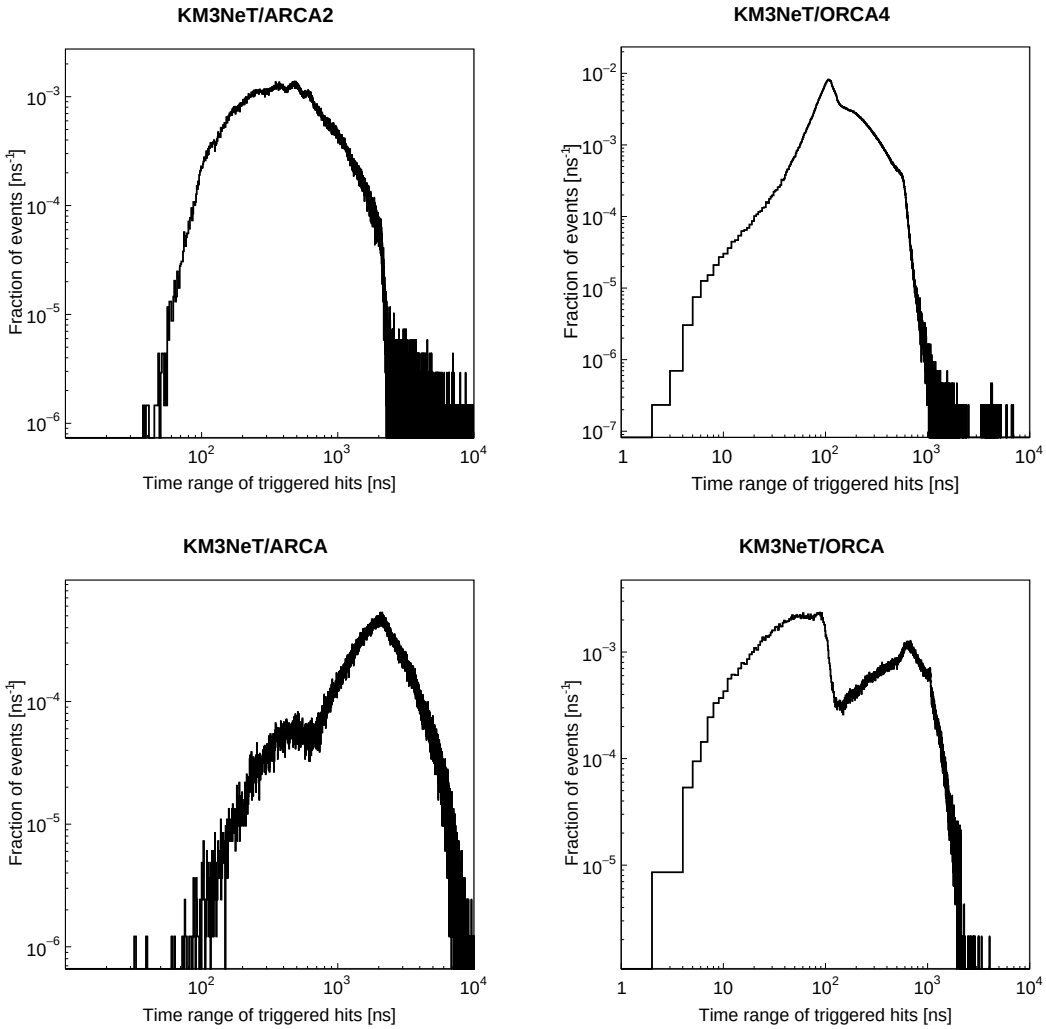

Figure 4.13 – Time range of triggered hits for sea data of ARCA2 and ORCA4 (top) and simulated data of ARCA and ORCA (one building block). The two populations visible for the 115-lines detectors come from the shower and track triggers, respectively.

The efficiency of the filter evaluated on sea data of ARCA2 and ORCA4 is reported in Table 4.4 and shows improvement compared to the coincidence correlation filter.

The dead time fraction of this approach can be estimated as the product of the total detector trigger rate for a typical time range of few microseconds on average. With conservative assumptions ($5\,\mu s \cdot 100\,Hz$) the dead time fraction is estimated at $f_{DT} \lesssim 1 \cdot 10^{-3}$.

In general, the efficiency of the veto will be dependent on the detector configuration. The higher is the number of detection units, the lower the probability for a muon to produce a coincidence on a DOM without being triggered. To evaluate the performance of the trigger for a complete detector, the simulated data for the ARCA

Table 4.4 – Rejection efficiency (reverse cumulative) as a function of the multiplicity for the triggered events based filter in ARCA2 and ORCA4.

Multiplicity	4	5	6	7	8	9	10	11	12
ARCA2	0.4%	2%	10%	22%	26%	27%	28%	29%	31%
ORCA4	4%	22%	70%	94%	98%	99%	99%	99%	99%

and ORCA building block are processed. The corresponding rejection efficiency as a function of the multiplicity is shown in Figure 4.14.

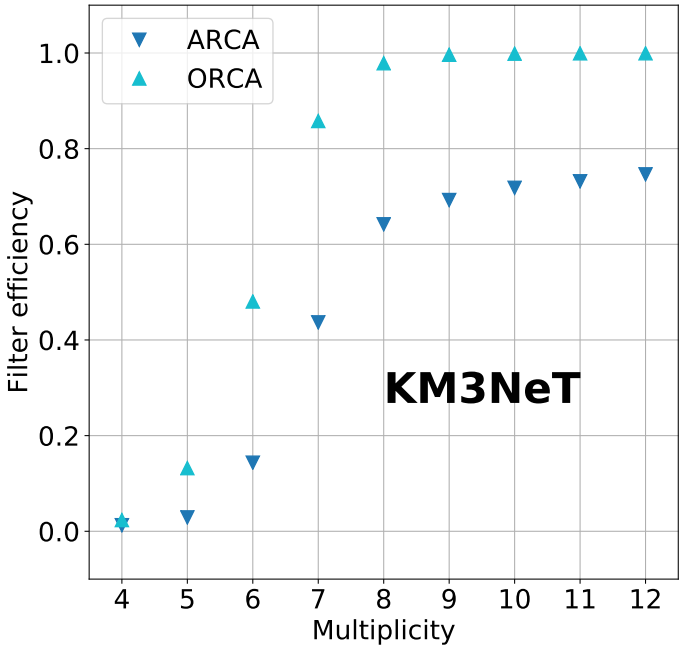

Figure 4.14 – Rejection efficiency of the *triggered events veto* as a function of the multiplicity for a KM3NeT ORCA and ARCA building block.

This estimation of the rejection efficiency through a simulation could introduce a bias if the reproduction of the atmospheric muon signatures is not sufficiently accurate. Differences in the topology of the muon bundles or approximations in the muon propagation, energy loss and Cherenkov light production, can result in a systematic uncertainty on both the absolute simulated background rates and the rejection efficiency. The `JSirene` simulation of ARCA2 has been compared with sea data and with a simulation using `KM3`. The respective rejection efficiencies as a function of the multiplicity are compared, for the reverse cumulative distribution of rates, in Figure 4.15. The larger deviation is observed when comparing `JSirene` with the data, corresponding to ~ 15% overestimation of the rejection power. As

a conservative choice, this is introduced as a +15% systematic uncertainty in the evaluation of the background.

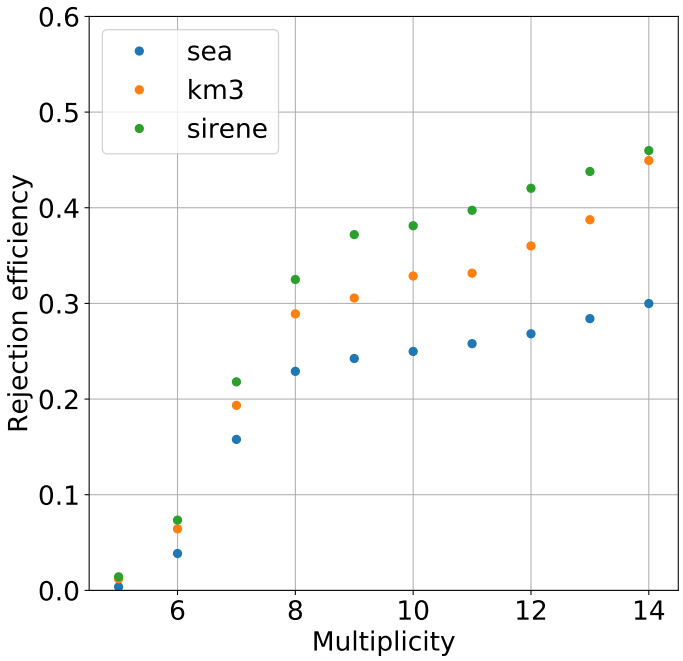

Figure 4.15 – Rejection efficiency of the *triggered events veto* as a function of the multiplicity, calculated on the reverse cumulative of the coincidence rate, for the ARCA2 detector from real data (sea) and a MUPAGE simulation using KM3 and JSirene as Cherenkov light simulators.

4.4 Sensitivity estimation

4.4.1 Statistical definitions

In a typical *Poisson counting experiment*, the number of observed events, n, is modeled with a Poisson distribution with expectation value $\mu = \mu_b + \mu_s$, where μ_s and μ_b are the expectation values for the background and the signal respectively. The *significance* of an observation of k events is then represented by the (one-tailed) *p-value*, p, namely the probability of observing a number of events $m \geq k$ from the sole background ($\mu_s = 0$, $\mu = \mu_b$), what is commonly referred to as the *null hypothesis*. For a Poisson counting experiment, the p-value for an observation of x events is calculated as:

$$p(x) = \sum_{k=x}^{+\infty} e^{-\mu} \frac{\mu^k}{k!} = 1 - \sum_{i=0}^{x-1} e^{-\mu} \frac{\mu^k}{k!} \tag{4.15}$$

A convenient representation for the p-value is the corresponding *Gaussian significance*, Z, defined as the value above which the integral of the Gaussian distribution

with mean zero and unit variance is equal to p. The significance (in units of standard deviation, σ) is therefore calculated as $Z = \Phi^{-1}(1-p)$ where Φ^{-1} is the *quantile function*, namely the inverse of the Gaussian cumulative probability function. The calculation of Z is especially straightforward when $\mu_b \gg 1$, so the Poisson distribution is well approximated by a Gaussian with standard deviation $\sigma_b = \sqrt{\mu_b}$. In this case the *significance* of an observation of s events above the background expectation μ_b is $Z \simeq s/\sigma_b$ and can be intuitively interpreted as a measure of how much the observation deviates from the background expectation, measured in standard deviations. Conventionally, in particle physics, an observation above 5σ of significance is considered sufficient to reject the null hypothesis (and possibly claim a discovery). The *sensitivity* of the experiment to a signal with a definite value of μ_s is usually defined as the *expected median significance* that the observation of the signal would produce. While the actual significance will be subject to the statistical fluctuation of the observed values, its expected median value can be usually calculated from the expectation values of background and signal, what is referred to as *Asimov data set*. The *Asimov sensitivity* for a Poisson counting experiment, Z_A, can be estimated with the formula derived in Reference [226]:

$$Z_A = \sqrt{2 \cdot \left((\mu_s + \mu_b) \cdot \ln\left(1 + \frac{\mu_s}{\mu_b}\right) - \mu_s \right)}. \tag{4.16}$$

Contrarily to the Gaussian case, the Poisson sensitivity is not reduced to a function of $\mu_s/\sqrt{\mu_b}$ (or μ_s/μ_b) only. The consequence being that the event selection with the best signal-to-noise ratio does not necessarily guarantee the best sensitivity, which is scale-dependent. Besides, it is often instructive to compare Z_A with a distribution of observations obtained through pseudo-experiments.

In this analysis, the sensitivity is estimated from the values of μ_s and μ_b calculated for a 500 ms time window following the onset of the event. The underlying assumption is that the arrival time of the neutrino burst at the detector is known from an independent observation.

4.4.2 Multiplicity selection

The background filtering strategy based on triggered events, as described in Section 4.3.3.2, is here adopted. The background event rate is calculated applying the filter efficiency estimated for the KM3NeT building block simulations to the coincidence rates measured from sea data, reported in Section 4.9. To account for the difference between the real detector (used to measure the background) and the nominal detector (used to simulate the signal), the background rates are normalised to the nominal efficiency. The three progenitors, 11, 27 and $40\,M_\odot$ are considered. The expected number of signal and background events in a 0,5 s time interval is evaluated and reported for a KM3NeT ORCA and ARCA building block in Figure 4.16.

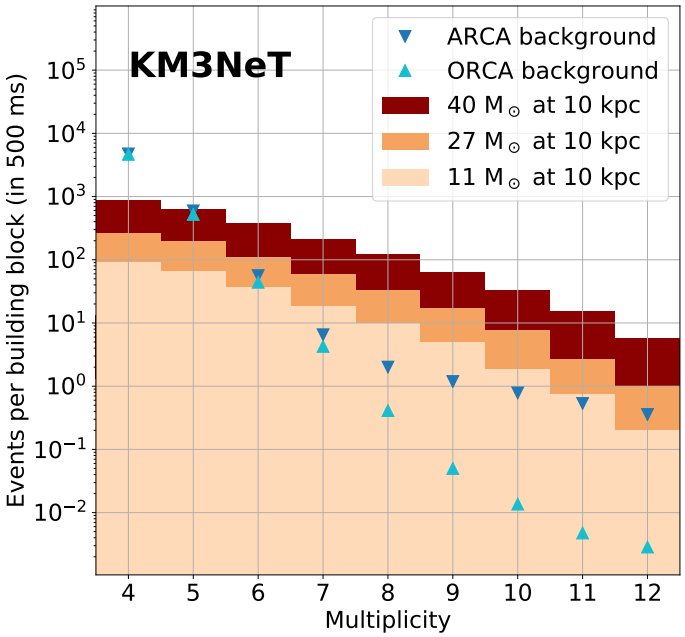

Figure 4.16 – Number of background events in 500 ms after filtering for ORCA and ARCA building blocks as a function of the multiplicity, compared with the signal expectation for the three CCSN progenitors.

Both qualitative and quantitative considerations enter the determination of the best multiplicity selection. The higher the minimum multiplicity cut, the lower the contamination from radioactive backgrounds, that are not suppressed by muon the filtering. In particular, the signal-to-noise ratio improves dramatically from multiplicity six to seven (and further from seven to eight considering ORCA). On the other hand, the detection of a neutrino spectrum with lower mean energy could be favoured by a selection that includes a lower multiplicity. At multiplicity twelve and above, the expected number of signal events drops to a maximum of a few units per building block. While in principle the signal-to-noise ratio is still favourable, this contribution is less statistically reliable. The adoption of a cut on the maximum multiplicity reduces the probability of outliers entering the final selection and excludes a region where an exhaustive characterisation of the background is affected by the lack of statistics. Finally, while the optimal selection could be different for ORCA and ARCA, adopting the same in the two detectors simplifies the statistical treatment of their combination.

Taking into account the respective sizes of the detectors (one building block for ORCA, two for ARCA), the 5σ discovery horizon as a function of the number of signal and background events in the different multiplicity selections is evaluated for the three progenitors. The results are summarised in Figure 4.17.

In light of this quantitative evaluation and the qualitative considerations expressed above, the 7 – 11 multiplicity selection is here adopted for both detectors.

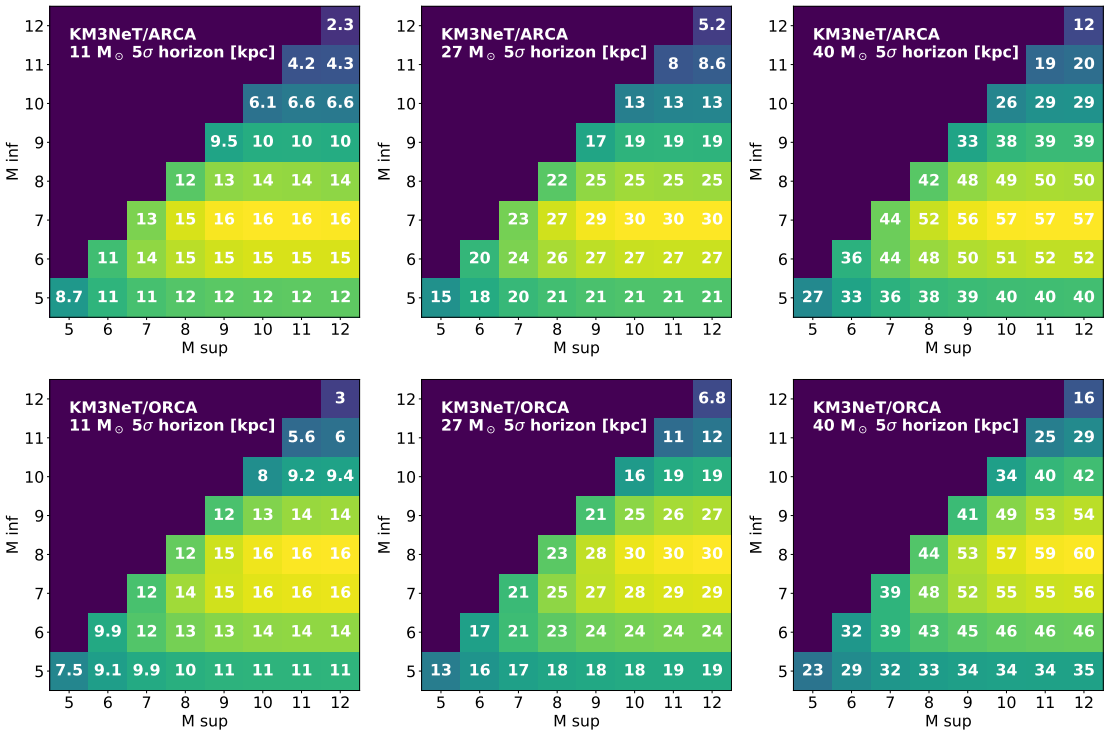

Figure 4.17 – 5σ discovery horizon for the three CCSN progenitors as function of the minimum and maximum multiplicity for the ARCA (top) and ORCA (bottom) detector.

4.4.3 Systematic uncertainties

In this section, the systematic uncertainties related to the detector performance and the determination of the sensitivity to a given flux model are reported. The uncertainties affecting the flux model are excluded from the discussion. The fluences introduced in Section 4.2.1 are taken as fixed benchmarks for the detector performance.

Generation volume The contribution of events interacting outside the simulated generation volume is estimated to be below 1% by verifying the increase in the number of events producing at least two photoelectrons for an extension of the radius from 20 to 25 metres. As higher multiplicity coincidence occurs nearer to the DOM, the effect on the event selection is negligible.

Water properties The effect of a 10% uncertainty on the water absorption length is estimated with dedicated simulations to affect the signal for less than 1%.

Cross sections IBD and ES cross-sections are precisely known with an uncertainty below 1%.

PMT efficiency A ±5% uncertainty on the absolute PMT efficiency is estimated to impact the number of signal events for ±10%, according to what has been determined in Section 4.2.4.

Instrumentation efficiency This factor is related to how reliably the expectation values for signal and background can be estimated as a function of the number of active PMTs. As it is discussed more in detail in Section 4.5.2, this accounts for a ±3% uncertainty.

Filter efficiency The data – Monte Carlo comparison for the filter efficiency evaluated in ARCA2 shows a 15% deviation between the `JSirene` simulation and sea data.

A summary of the different systematic uncertainties evaluated is shown in Table 4.5. The *(S)* and *(B)* symbols are used to indicate if the uncertainty is assigned respectively to the signal and/or the background.

4.4.4 Detector combination

Due to the different background rate in the two detectors, ARCA and ORCA are treated as individual experiments and their observations are combined to define the KM3NeT sensitivity. The combination of p-values from multiple, independent, experiment is a long-standing problem in data analysis that has no univocal solution. An annotated bibliography on the subject is available in Reference [227]. A subset of these approaches is hereby considered.

Event aggregation The sum of n Poisson variables is also distributed according to the Poisson statistic, with an expectation value given by the sum of the n individual variables. By treating the two detectors as a single experiment, where both expectation values and observations are added, a joint significance can be

Table 4.5 – Systematic uncertainties in terms or relative deviation in the number of events

Variable	Variation	Systematic error
Generation radius	+5 m	(S) <1%
IBD, ES cross sections	< 1%	(S) <1%
Absorption length	±10%	(S) ± 1%
PMT efficiency	±5%	(S) ± 10%
Instrumentation efficiency	±3%	(S, B) ±3%
Filter efficiency	data – MC	(B) +15%

evaluated. While simple and intuitive, the approach is practically limited to the case where the respective background scales are comparable. In this approach, the experiment with the higher background scale assumes a higher weight in the combination, which is not always desirable.

Fisher's method The p-values p_i observed from n independent experiments can be combined with a multiplication $p = \prod_i^n p_i$. Following an approach originally proposed by Fisher [228] a χ^2 test statistic can be derived as follows:

$$\chi^2_{2n} = -2\sum_i ln(p_i)$$

and used to determine the corresponding significance. As each experiment is treated equally, this is again not optimal in case the respective performances of the experiments are significantly different.

Stouffer's method It is based on a weighted linear combination of the individual significances:

$$Z = \frac{\sum_i w_i Z_i}{\sqrt{\sum_i w_i^2}}$$

While there is no strict rule for the attribution of the weights, they should in principle represent a figure of merit of the individual experiments.

In Figure 4.18, the Stouffer and Fisher method for the combination of ARCA and ORCA significances are compared. H0 represents the null hypothesis, namely the presence of background only. H1 represents the alternative hypothesis, chosen as an event for which the sensitivity of the individual detector is $\sim 3\sigma$. It corresponds to the number of signal events for a $27M_\odot$ progenitor at ~ 37 kpc. Poisson pseudo-experiments are used to evaluate the significance distribution for ARCA and ORCA. The combined significance is represented as a function of the individual significances

with black dash-dotted lines indicating the 1, 3, 5 and 7 σ levels. The weights used in the Stouffer's method for ARCA and ORCA are defined as by the respective sensitivities at 10 kpc for the 27$M_\odot$ progenitor.

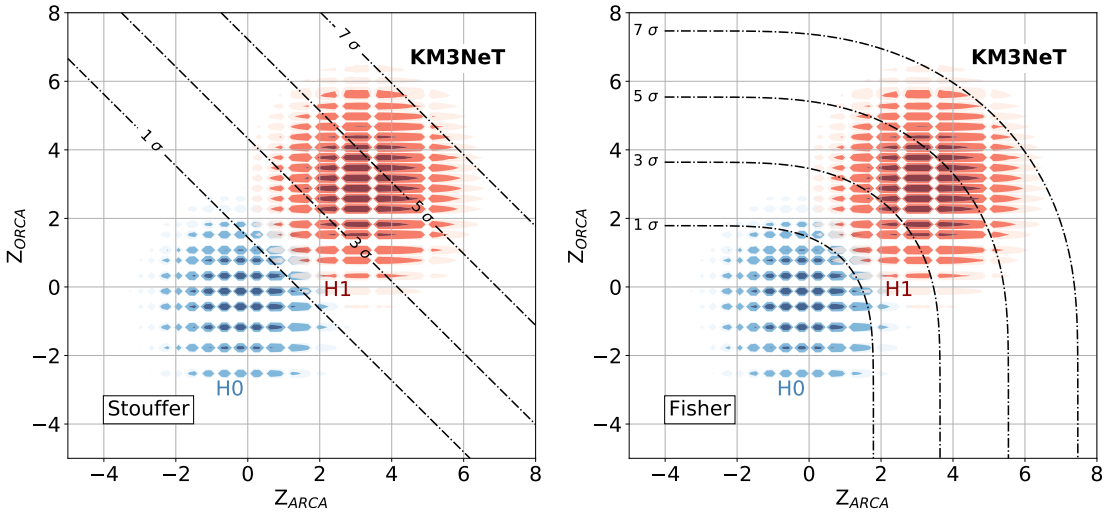

Figure 4.18 – Significance distribution for ARCA (abscissa) and ORCA (ordinate). 0.99, 0.95, 0.68 contours in blue for the null hypothesis, H0 (background only), and in red for the alternative hypothesis, H1 ($\sim 3\sigma$ individual detection). The black lines indicate the value of the combined significance as a function of the ORCA and ARCA significances according to the Stouffer (left) and Fisher (right) method.

While Fisher's method is symmetrical, in the Stouffer's method the slope of the combined sensitivity thresholds is given by the relative weights of the individual experiments. This can ensure that the thresholds are always orthogonal to the axis connecting the centres of the H0 and H1 distributions, providing optimal sensitivity to the alternative hypothesis. As ARCA and ORCA are similar in terms of sensitivity, the Fisher's and Stouffer's methods show comparable performance for the event selection here adopted. Due to its higher adaptability, the Stouffer's method is here chosen to combine the ARCA and ORCA significances.

4.4.5 Sensitivity as a function of the distance

The sensitivity for ARCA and ORCA is estimated in relation to the distance of the progenitor. The expected number of signal events, μ_s, is naturally expressed as a function of the distance as:

$$\mu_s(d) = \mu_s(10\,\mathrm{kpc}) \left(\frac{10\,\mathrm{kpc}}{d}\right)^2 \tag{4.17}$$

where $\mu_s(10\,\text{kpc})$ is estimated according to Figure 4.16. Replacing $\mu_s(d)$ for μ_s in Equation (4.16), the Asimov sensitivity Z_A to the three considered progenitors is estimated as a function of the distance for ARCA and ORCA. The KM3NeT combined sensitivity is therefore calculated as:

$$Z_{A,\text{KM3NeT}}(d) = \frac{\sum_\alpha w_\alpha Z_{A,\alpha}(d)}{\sqrt{\sum_\alpha w_\alpha^2}} \; ; \; \alpha \in \{\text{ARCA}, \text{ORCA}\} \tag{4.18}$$

where $w_\alpha = Z_{A,\alpha}(10\,\text{kpc})$. The number of signal and background events at 10 kpc for ORCA and ARCA is reported in Table 4.6. The KM3NeT sensitivity as a function of the distance is reported in Figure 4.19.

Taking into account the CCSN probability as a function of the distance (Figure 4.4), in the most conservative scenario ($11\,M_\odot$ progenitor) 95% of the galactic core-collapse supernovæ can be observed by the KM3NeT detectors at the 5σ level.

Table 4.6 – Expectation values for the number of background and signal events after the background rejection in the 7-11 multiplicity selection, for ARCA and ORCA. Signal is given for a CCSN at 10 kpc. Sensitivity is shown at 10 kpc for each detector and progenitor.

Progenitor mass	**ARCA**			**ORCA**		
	μ_b	μ_s	$\sigma_{10\,\text{kpc}}$	μ_b	μ_s	$\sigma_{10\,\text{kpc}}$
$11\,M_\odot$	22.1	72.2	11	4.9	36.1	10
$27\,M_\odot$	22.1	240	29	4.9	120	24
$40\,M_\odot$	22.1	895	71	4.9	447	57

4.4.6 KM3NeT model in `SNOwGLoBES`

`SNOwGLoBES` [222] is a GLoBES-based [229] detector simulator for core-collapse supernovæ neutrino burst. Given an input neutrino flux in the six species, it allows estimating the number of events for each considered interaction channel, as well as the reconstructed energy spectra. In `SNOwGLoBES`, a detector is described by a mass and an interaction medium. Medium target compositions are provided for lead, water, liquid argon, and liquid scintillator. A medium is defined by listing the relevant interactions for all neutrino species with the corresponding target elements. An energy-dependent cross-section is provided for each of such interactions. The definition of a detector is given by two elements. For each relevant interaction, a *smearing matrix* gives the distribution of the visible energy as a function of the energy of the interacting neutrino. A *post-smearing efficiency* vector, in turns, provides the fraction of detected events for a given visible energy.

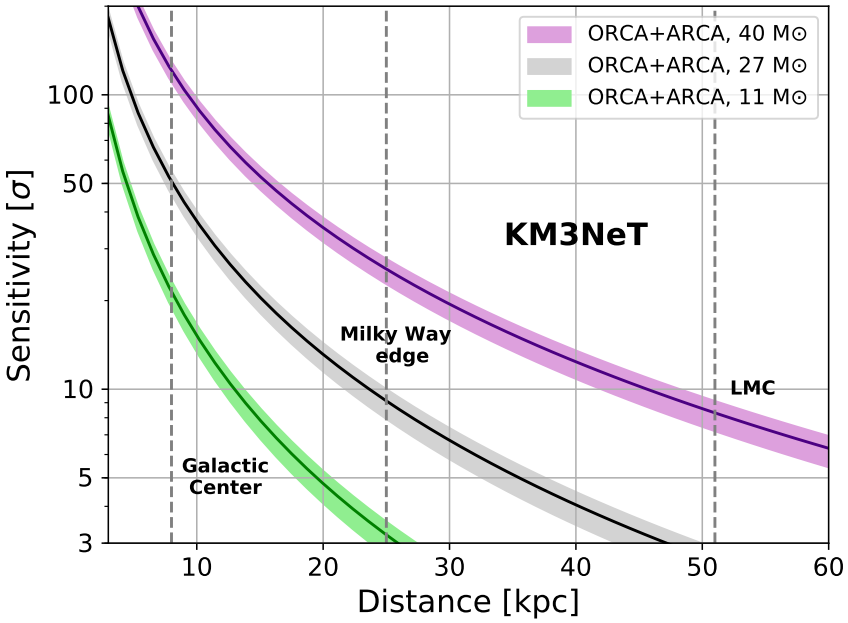

Figure 4.19 – Combined sensitivity of the KM3NeT detectors after the muon filter over the multiplicity selection range 7-11, as a function of the distance. Results are reported for the three considered progenitors, and including the systematic uncertainties. The respective distances of the Galactic Edge, Centre and Large Magellanic Clouds are indicated.

In SNOwGLoBES, events are simulated for a pre-defined number of energy bins covering the 0 – 100 MeV range. The number of interacting neutrinos is calculated from the flux and cross-section input tables. For each interaction, a value of the corresponding visible energy is drawn from the smearing matrix. Finally, the post-smearing efficiency is applied to determine the number of detected events.

In long-string Cherenkov detectors, as KM3NET and IceCube, the events are not individually reconstructed. Similarly to the IceCube implementation [230], the KM3NeT smearing matrix represents the energy of the outgoing lepton as a function of the energy of the interacting neutrino. The (post-smearing) detection efficiency represents the probability of observing at least a coincidence from a lepton at a given energy. It has been evaluated with dedicated simulations in order to cover the whole energy range with sufficiently low statistical uncertainty.

4.4.7 Comparison with other experiments

The comparison of the CCSN detection capability of different detectors is complicated by the use of different flux models and different ways of reporting the performance. For the most conservative flux here considered, the $11\,M_\odot$ progenitor, the IceCube experiment has a sensitivity consistently above 10σ up to the Galactic Edge [231]. KM3NeT is above 5σ at the same distance only starting from the $27\,M_\odot$ progenitor. The advantage of IceCube in this domain comes from the absence of optical backgrounds, as radioactivity and bioluminescence are absent in the Antarctic ice.

Low-background underground detectors are usually well sensitive up to the Magellanic Clouds, and they do not typically provide figures of merit in terms of significance versus distance. A comparison of the number of events expected in different detectors for three supernova models from Reference [232] and [233] and evaluated with SNOwGLoBES is reported in Table 4.7. In this, the number of events in KM3NeT is reported considering all coincidences, without cuts on the multiplicity. The KM3NeT and IceCube event numbers here provided are not (almost) background-free as for the ones from other experiments.

4.5 Benchmarks of the analysis algorithm

4.5.1 Filter robustness

Once determined the optimal multiplicity selection, the robustness of the background filtering requires careful evaluation. For this, the data taking periods considered for ARCA2 and ORCA4 have been entirely analysed. All timeslices have been considered regardless of the number of active PMTs. The number of events after the filter is evaluated on a per-timeslice basis, meaning data samples of 100 ms. The number of timeslices as a function of the number of events in the timeslice is reported in Figure 4.20 for the coincidence correlation strategy and in Figure 4.21 for the filter based on triggered events. A Poisson distribution with expectation value equal to the

Experiment	Type	Mass [kt]	Location	11,2 $M_\odot$	27,0 $M_\odot$	40,0 $M_\odot$
Super-K	$H_2O/\bar{\nu}_e$	32	Japan	4000/4100	7800/7600	7600/4900
Hyper-K	$H_2O/\bar{\nu}_e$	220	Japan	28K/28K	53K/52K	52K/34K
IceCube	String/$\bar{\nu}_e$	2500*	South Pole	320K/330K	660K/660K	820K/630K
KM3NeT	String/$\bar{\nu}_e$	150*	Italy/France	17K/18K	37K/38K	47K/38K
KamLAND	$C_nH_{2n}/\bar{\nu}_e$	1	Japan	190/190	360/350	340/240
Borexino	$C_nH_{2n}/\bar{\nu}_e$	0.278	Italy	52/52	100/97	96/65
JUNO	$C_nH_{2n}/\bar{\nu}_e$	20	China	3800/3800	7200/7000	6900/4700
SNO+	$C_nH_{2n}/\bar{\nu}_e$	0.7	Canada	130/130	250/240	240/160
NOνA	$C_nH_{2n}/\bar{\nu}_e$	14	USA	1900/2000	3700/3600	3600/2500
HALO	Lead/ν_e	0.079	Canada	4/3	9/8	9/9
HALO-1kT	Lead/ν_e	1	Italy	53/47	120/100	120/120
DUNE	Ar/ν_e	40	USA	2700/2500	5500/5200	5800/6000
MicroBooNe	Ar/ν_e	0.09	USA	6/5	12/11	13/13
SBND	Ar/ν_e	0.12	USA	8/7	16/15	17/18
DarkSide-20k	Ar/any ν	0.0386	Italy	-	250	-
XENONnT	Xe/any ν	0.008	Italy	75	140	-
LZ	Xe/any ν	0.007	USA	65	123	-
PandaX-4T	Xe/any ν	0.004	China	37	70	-

Table 4.7 – Estimated interaction rates for the detectors described here for three different models, s11.2c and s27.0c from [233] that form neutron stars and s40 from [232] which forms a black hole. The two numbers given are the total events over all channels using `SNOwGLoBES` assuming adiabatic MSW oscillations only for the normal mass ordering (left number) and the inverted mass order (right number). For liquid scintillator experiments, the elastic proton scattering channel is not included. For string Cherenkov detectors, the mass is given as an effective mass based on 27,0 $M_\odot$ and the normal mass ordering. Source: [234].

mean value of the data is drawn on the histogram. No significant deviation from the Poisson statistics is observed in the considered data taking periods. This confirms that the effectiveness of the background filtering and event selection is unaffected by the data taking conditions, and ensures a low-background, high-purity data sample for the CCSN neutrino search.

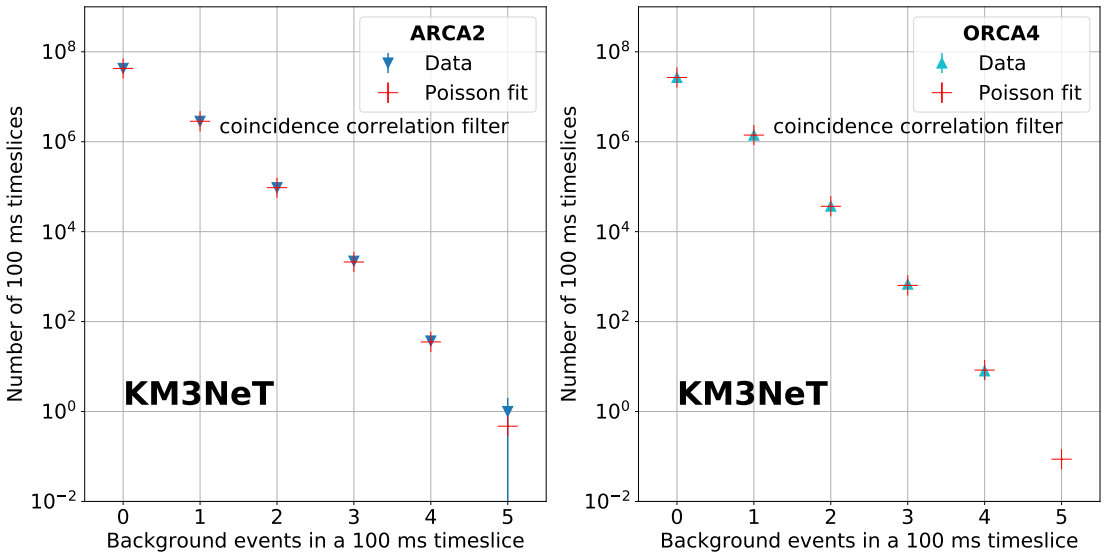

Figure 4.20 – Number of timeslices as a function of the number of the background events in the timeslice, after the coincidence-correlation filter, for the considered ARCA2 (left) and ORCA4 (right) data taking periods. Statistical errors are included. A Poisson distribution with expectation value equal to the mean value of the data is overlayed.

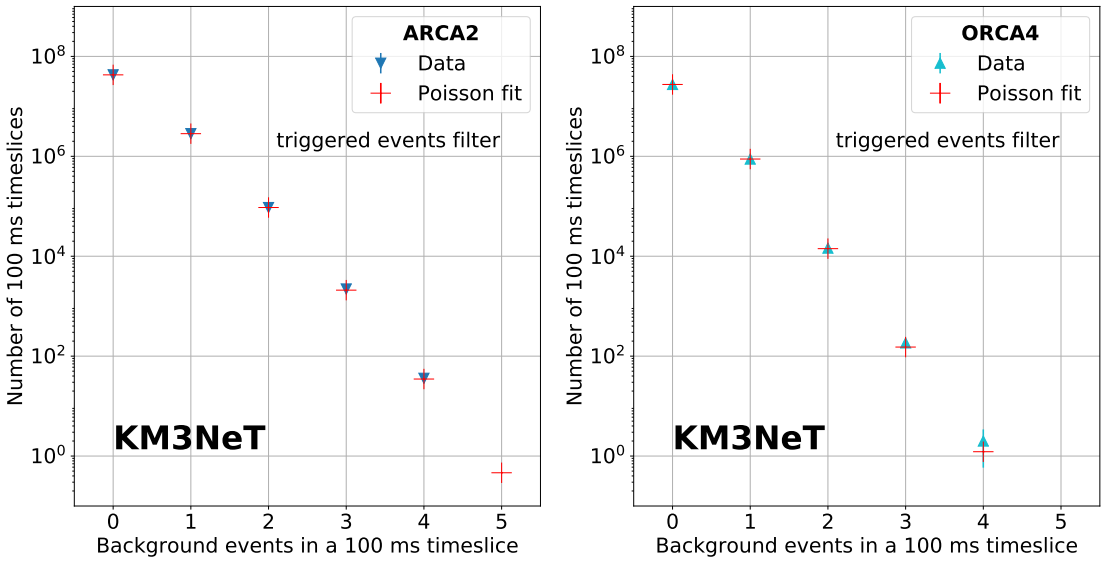

Figure 4.21 – Number of timeslices as a function of the number of the background events in the timeslice, after the triggered-events filter, for the considered ARCA2 (left) and ORCA4 (right) data taking periods. Statistical errors are included. A Poisson distribution with expectation value equal to the mean value of the data is overlayed.

4.5.2 Bioluminescence impact on detector efficiency

Atmospheric muons and water radioactivity are sources of optical background which are stable in time. While bioluminescence is effectively rejected by selecting coincidences, it can result in the suppression of a significant time-dependent fraction of the number of active PMTs. As introduced in Section 2.1.1, the *high-rate-veto* disables the data acquisition whenever a PMT exceeds a hit rate of 20 kHz evaluated on a 100 ms timeslice basis. The average fraction of PMTs in high-rate-veto is of a few per mille in ARCA and a few per cent in ORCA. The distribution of the vetoed channels may differ, with both localised and diffused effects.

The multiplicity rates, on the other hand, have a non-linear dependence on the number of active PMTs on a DOM and a general modelisation of this behaviour is out of reach. This reflects on a change in time of the expected number of background events in the supernova search time window. To evaluate this effect, ARCA2 and ORCA4 sea data are analysed to recover an empirical parameterisation of the background rate as a function of the fraction of active PMTs. In a first approximation, the spatial distribution of the vetoed channels is ignored. The *instrumentation efficiency*, ϵ, as a function of the fraction of active PMTs, f_A, is here defined as:

$$\epsilon = \frac{\rho_b(f_A)}{\rho_b(\sim 1)}. \tag{4.19}$$

where $\rho_b(f_A)$ and $\rho_b(\sim 1)$ are the background rates measured over the subset of timeslices with a fraction of active channels f_A and ~ 1 respectively. In practice, $\rho_b(\sim 1)$ is estimated accounting for the timeslices where more than 99% of PMTs are active. The average value of f_A is above 99% for ARCA and $\sim$ 95% for ORCA. The *cumulative livetime fraction* for a given value of f_A is defined as the fraction of timeslices in which the fraction of active PMTs is greater or equal to f_A. It represents the amount of time the detector has at least a fraction of f_A active channels. In Figure 4.22, the instrumentation efficiency as a function of the active channel fraction for the sea data of ARCA2 and ORCA4 is reported, together with cumulative livetime fraction. For ARCA, the detector has more than 98% active channels for 99% of the time. In ORCA, $\sim$ 15% of the time the detector has less than 90% of active channels.

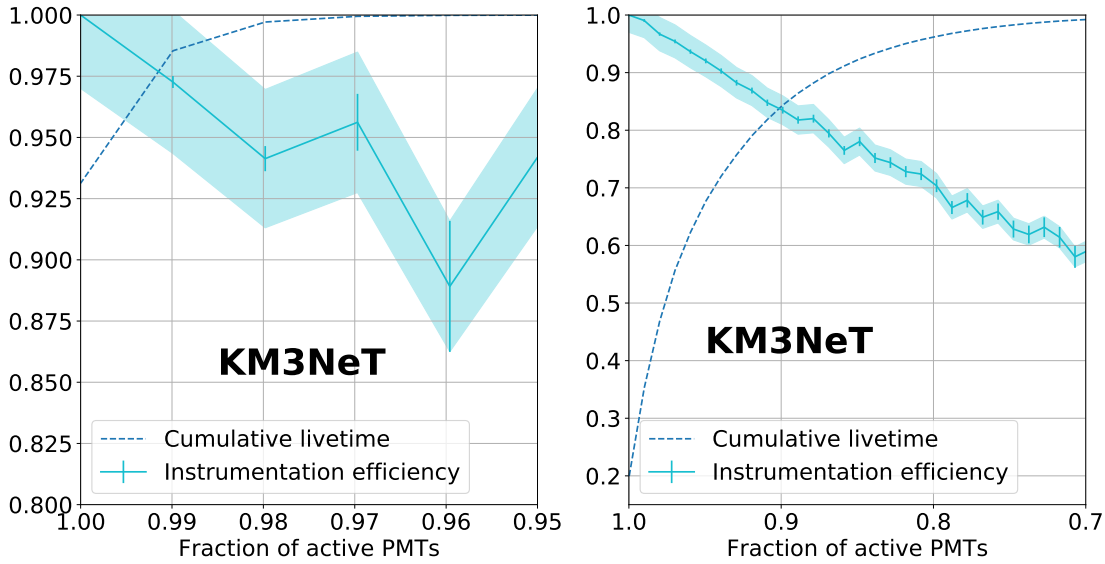

Figure 4.22 – Instrumentation efficiency for the multiplicity selection 7 – 11 and cumulative livetime fraction for the ARCA2 and ORCA4 data samples as a function of the fraction of active PMTs.

An interpolation of the instrumentation efficiency curve can be used to predict the expectation value of the background at any point in time. The stability of this parameterisation has been evaluated by taking ORCA4 monthly data samples going from October 2019 to January 2020. The month-by-month variation of $\epsilon(f_A)$ is within $\pm$3%. This value is assumed as the systematic uncertainty on the instrumentation efficiency, affecting the expectation value of the number of background events μ_b as defined in the previous section. As a conservative choice, the same uncertainty is applied to ARCA.

As for the signal, an accurate estimation of μ_s can be achieved with a simulation of the CCSN accounting for the detector status at the exact time of the event. This is in general allowed by the *run-by-run* simulation mechanism implemented in the KM3NeT framework. For this analysis, a simplified approach is adopted, applying the

same value of the instrumentation efficiency to scale both μ_s and μ_b.

4.5.3 Implications and perspective

These evaluations show that the CCSN search strategy behaves predictably under a wide range of detector conditions. The expected background rate can be inferred with reasonable uncertainty from the number of active PMTs at any point in time. It is expected that for a bigger detector the averaging of bioluminescence-induced effect over a larger volume will improve the reliability of the *instrumentation efficiency* determination. Rare anomalies due to extreme conditions, instrument malfunction or human error cannot be excluded *a priori* to present in the future, and will need to be evaluated on a case-by-case basis. While rare outliers are not much of a concern for follow-up searches, they may be problematic for the reliability of the real-time triggering system and the alert generation.

4.6 Online supernova trigger

The algorithms described in Section 4.3.3 have been implemented in the KM3NeT software suite `Jpp`. A dedicated application has been developed to process the SN timeslice data after they are distributed by the data filter to the dispatcher of the DAQ chain.

4.6.1 Multi-messenger context

The detection of `SN1987A` has been the first extrasolar multi-messenger observation of neutrinos. With the understanding that neutrinos predate the optical emission of a core-collapse supernova, the possibility of exploiting the burst to send an early warning to the astronomical community has been taken into consideration. The efforts went in the design and implementation of the *Supernova Neutrino Early Warning System* (SNEWS) [235] based on the search of a coincident observations of a supernova candidate signal in multiple neutrino detectors. SNEWS aims to the dissemination of a *prompt* and *positive* alert, with an expected false alert rate below one per century. To achieve this, the participating detectors are required to send alerts to the network with a false alarm rate of less than one per week. If a coincidence is found between at least two instruments within 10 s, an alert is disseminated through the official mailing list and dedicated machine-readable channels for the communication with LIGO, ANTARES and the Gamma-Ray Coordination Network (GCN). A SNEWS test alert is disseminated through GCN once per week, each Tuesday at 16:00 UTC. The coincidence is based on a simple `AND`-type boolean logic, and no weight or significance is attributed to an alert. The detectors participating in SNEWS are Super-Kamiokande, LVD, IceCube, Borexino, KamLAND, HALO and Daya Bay. The integration of NOvA and KM3NeT is in a commissioning phase at the time of writing.

As of today, the multi-messenger context has shifted towards a scenario where high-rate, low-significance alerts are more commonly accepted and exploited by the community. SNEWS is also transitioning to a richer multi-messenger program that will allow not only the dissemination of a wider range of alerts, but also the inclusion of real-time multimessenger analyses of the CCSN signal, such as triangulation. This is being designated in the upcoming *SNEWS 2.0 Whitepaper* [234]. This scenario dictates the requirements for the development of the KM3NeT online supernova trigger and the associated real-time infrastructure.

4.6.2 Statistical treatment

The online search is based on the same principle of the sensitivity analysis. The main difference is that, instead of being determined at a designated point in time, the significance is continuously evaluated using a sliding time window. In particular, the number of signal and background events is evaluated over a time window of length $\tau = 0{,}5\,\mathrm{s}$, sampled with a frequency of $f_s = 10\,\mathrm{Hz}$. In other words, every $\delta t = f_s^{-1} = 0{,}1\,\mathrm{s}$ the equivalent significance estimated in the previous 0,5 s is calculated. It should be noted that, while still formally defined, the *statistical significance* loses its traditional meaning in this context. In general, when multiple observations are performed, the p-value needs to be multiplied by the *trial factor*. This problem is commonly addressed as *look-elsewhere-effect* [236]. If the number of observations is not defined a priori, as it is the case when the time frame of the search is not limited, only a *trial rate* can be defined. The significance, or the corresponding p-value, is therefore translated into a *false alarm rate* (FAR):

$$\mathrm{FAR}(Z) = f_s\, p = f_s \int_Z^{+\infty} \mathcal{N}(z)\, dz \tag{4.20}$$

where $\mathcal{N}(z)$ is the normal distribution with mean zero and unit standard deviation. Equation (4.20) can be applied either to the single experiment, where p has been calculated according to Equation (4.15), or to a combination for which the overall significance, Z, has been evaluated. Substituting in Equation (4.20) the sensitivity as a function of the distance, $Z(d)$, it is possible to determine the *trigger horizon* for which an alert can be generated once a tolerated FAR is defined, as shown in Figure 4.23. The requirement to participate in the global SNEWS alert network, here set to one false alarm in 8 days, is highlighted. The steep dependence of the background rate as a function of the distance is determined by the properties of the background distribution combined with the signal quadratic scaling. The combination of the two detectors allows a triggering capability beyond the Galactic Center, up to $\sim 19\,\mathrm{kpc}$ for the $11\,\mathrm{M}_\odot$ progenitor, covering the full Galaxy for the $27\,\mathrm{M}_\odot$ progenitor.

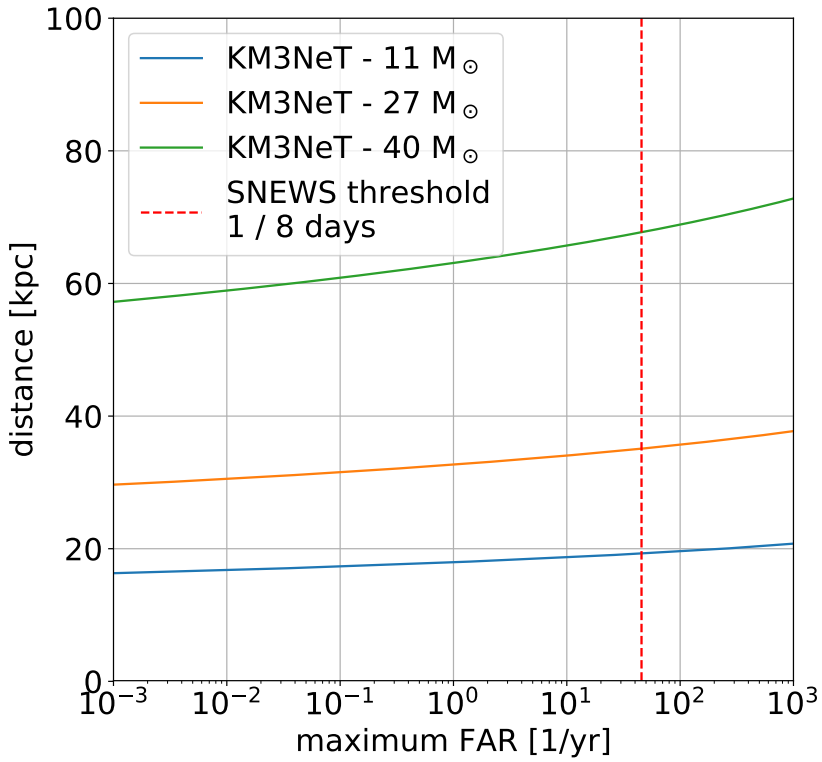

Figure 4.23 – Trigger horizon as a function of the false alarm rate (per year). This figure is a different representation of Figure 4.19, where the sensitivity is converted into its corresponding p-value and multiplied by the number of trials per year assuming a trial rate of 10 Hz. The red dashed line indicates the SNEWS limit *one in two weeks*.

4.6.2.1 Sliding window and alert dead time

The repeated sampling of the detected number of events in time defines a *stochastic process*. Here, the case of sliding window of duration τ sampled with a frequency $f_s = \delta t^{-1}$ is considered. If the ratio $\tau/\delta t$ is integer, time is divided in bins of duration δt and the sequence $\{n_i\}$ represents the number of events recorded in each bin. Each n_i is a Poisson variable with expectation value $\mu = \rho\,\delta t$ where ρ is the (background) event rate. As the samples do not overlap, they are independent and the sequence $\{n_i\}$ is a memoryless Poisson process. The operation of the *sliding window* is defined as a moving sum over the sequence $\{n_i\}$, namely a discrete convolution with a unit vector of length $k = \tau/\delta t$. The sequence $\{m_i\}$ representing the number of events in the sliding window is obtained as:

$$m_i = \sum_{j=0}^{k} h_j\, n_{i-j} \tag{4.21}$$

where $h_j = [1, ..., 1]$. This is a common operation in the domain of signal processing, where h_j takes the name of *kernel*. The convolution operation realises a *finite impulse response* (FIR) filter, which in this case is a simple *integrator* or *low-pass*.

Important to this application is the fact that each m_i is again Poisson-distributed with mean $\mu = \rho\tau = \rho\, k\,\delta t$, but the sequence $\{m_i\}$ no longer represents a *memoryless* process, as the convolution produces a correlation on a time scale of k samples. Equation (4.20), in particular, hides this aspect by incorporating in the FAR the result of the counting of the same background event in consecutive samples of the sliding window.

For the practical case of alert generation, a dead time of duration τ is implemented to prevent the sending of multiple alerts. In this case, the FAR *corrected by the dead-time* will be lower than the bare prediction of Equation (4.20). As this effect does not admit an easy analytical evaluation, a toy Monte Carlo simulation can be used to evaluate its impact. This introduces an additional problem if the desired alert is not simply boolean (above the FAR threshold or not) but needs to carry significance information. In case of a signal, the first m_i above the threshold may not correspond to the peak value and a peak detection algorithm should be applied. For the first implementation of the online trigger, Equation (4.20) is taken as a conservative estimation of the false alert rate.

4.6.2.2 DOM counting

In a few cases, a very large number of coincidences on a single DOM has been observed over a time scale of a few hundreds of milliseconds. These are not the product of a physical background but rather of a (temporary) anomaly of the instrument. Since the online supernova monitoring has been active, this type of issue has been observed once in the immediate aftermath of a detection unit deployment, in the commissioning of ORCA4. It is known that PMTs exhibit higher counting rates in the

first one or two weeks after the underwater installation of a new detection unit. Up to the end of August, 2020, with the operation of over one hundred DOMs in ORCA6 for several months, no further occurrences has been observed.

As an opt-in strategy to deal with misbehaving DOMs, the background filtering algorithm evaluates, together with the number of events, the number of unique DOMs detecting at least one event. This would reject multiple coincidences had they to occur on a single DOM, as in the case of such anomaly. This approach is here defined as *DOM counting regime*. The statistical distribution of the number of unique DOMs is binomial. It can still be approximated by a Poisson distribution if the expected number of signal and background events $\mu_s + \mu_b \ll N$, where N is the number of DOMs of the detector. In a KM3NeT building block, the condition is generally satisfied for a significance up to $\sim 10\sigma$. In a detector with a small number of DOMs, depending on the multiplicity selection, the probability that more than one genuine event is detected on single DOM is not negligible. The number of events, here re-defined with the symbol k, then follows in general a binomial distribution:

$$f(k) = \binom{N}{k} \cdot p^k (1-p)^{N-k} \; ; \; p = 1 - e^{\mu N^{-1}} \tag{4.22}$$

where p is the Poisson probability for an individual DOM to detect at least one event. For $\mu \equiv \mu_s + \mu_b$ it is possible to calculate the corresponding expected value of events in presence of signal:

$$\langle k_{s+b} \rangle = N p_{s+b} = N \left(1 - e^{\frac{\mu_s + \mu_b}{N}}\right). \tag{4.23}$$

A second single occurrence of anomalous DOM behaviour has been observed in ORCA6 at the end of August 2020. This possibly requires a re-consideration of the strategy. In particular, the number of unique modules, k, can be used to verify at any time that the number of detected events is compatible with a uniform distribution of the events across the DOMs. The implementation of this as a permanent *sanity check* is currently planned.

4.6.3 Technical implementation

In Figure 4.24, the logical structure of the KM3NeT online system is outlined. The CCSN analysis pipeline shares the infrastructure with the real-time reconstruction framework oriented to high-energy neutrino searches. The first stage is operated at the shore station of each detector. The raw data from the DAQ are analysed and different types of summary information are propagated to the central multi-messenger system. Here, messages (and data) are exchanged with a central dispatcher, analogous to the one used in the data acquisition system. The distribution works in a *many-to-many* fashion: each application can *subscribe* to the dispatcher to receive different types of messages/data and at the same time can send (processed) data back to it.

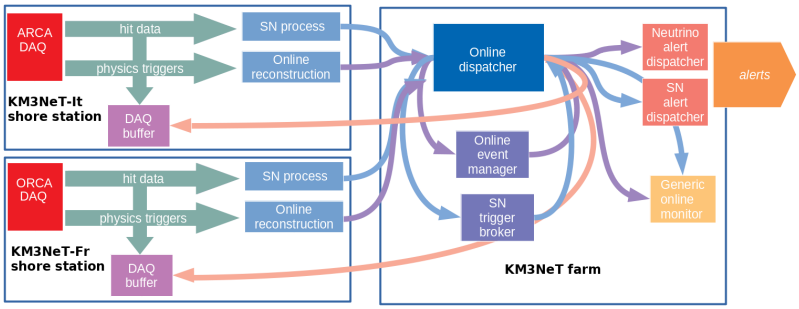

Figure 4.24 – Schematic diagram of the logical structure of the online multi-messenger system of KM3NeT.

The CCSN pipeline is articulated in three steps. In the first, raw data from the DAQ are analysed to evaluate the number of SN events with a sliding time window. The corresponding data are then propagated to the central multi-messenger system, where a trigger broker combines the significances from the two detectors. Finally, a set of applications takes care of monitoring the combined significance, generating internal alert messages and reacting to them. The type of reaction depends on the type of alert and could be the production of an external alert (SNEWS) or the generation of a control message to be distributed to the DAQ (see Section 4.6.4).

4.6.3.1 Real-time analysis of SN timeslice data

SN timeslice data consist of all coincidences at multiplicity four and above. The corresponding data throughput per DOM is estimated considering a rate of ~ 50 Hz times ~ 4 hits times 6 bytes. A building block is expected to produce ~ 2,5 MB s^{-1} of data, corresponding to an hit rate of ~ 415 kHz. The SN timeslice data are processed at the shore station of each detector.

The background filtering algorithm has been implemented in a real-time C++ application (*SN data processor*). The applications connect to the DAQ data dispatcher and subscribe to the data streams providing SN timeslices, summaryslices and triggered events. From these, it produces every 0,1 s an evaluation of the number of events in a sliding 0,5 s time window.

In the SN data processor, each received timeslice starts an iteration. The timeslice is processed applying the filter algorithms described in Section 4.3.3 and converted into a *SN data frame*. This contains a set of events defined by a DOM identifier, a time and a multiplicity. Since the data arriving on-shore are processed by parallel data filters, timeslices are not in general received in order. To deal with this, the frames are stored in the *trigger queue*. This is implemented as a *priority queue* that acts as a sorted buffer for SN data frames. The depth of the trigger queue is configured depending on the time delay that can be expected on average between two consecutive timeslices. A default depth of 100 elements (for 10 seconds) is adopted.

The set of contiguous timeslices over which the number of events is evaluated is defined as *trigger window* and is built on a `queue` container. The trigger window is fed from the front of the trigger queue, where elements appear in order of time. At each iteration, the trigger window stores an ordered sequence of the n SN data frames with the earliest timestamps that have been received up to that moment. The time of the first frame in the window, the number of events, and the number of modules detecting at least one event are stored in a dictionary-like data structure and encoded in a `JSON`-formatted [1] `ASCII` message. This *SN trigger* (`SNT`) message is propagated to the central online dispatcher. The number of active PMTs and the total hit rate of the detector, estimated from summaryslices, are also included for monitoring purposes.

4.6.3.2 Trigger combination

The online dispatcher receives the `SNT` messages from the two shore stations. Here, a dedicated dispatcher is operated. The *SN trigger* application subscribes to the dispatcher to receive all `SNT` messages. The purpose of the SN trigger is to process synchronously the data from the ARCA and ORCA detectors producing a combined significance in case of both are active. Otherwise, the application considers the significance of the sole active detector.

In general, due to the overall DAQ latency, there is a variable delay between the generation time of the data off-shore and the time at which a timeslice is received at the SN data processor. As a consequence, the `SNT` message corresponding to data generated at a time T_0 is received at the multi-messenger dispatcher at a time $T_{rec} = T_0 + \Delta T_{\text{DAQ}} + \Delta T_{\text{queue}}$. The DAQ latency, ΔT_{DAQ}, depends on a combination of factors, mainly related to the buffering of the raw data at the data queue and the data filters. It is on average fairly constant and within a few seconds, but can show occasional variations or drifts. These depend on the state of the detector and on the load of the data acquisition system, dependent on the total hit rate. The latency of the data network can be neglected.

The SN trigger is implemented in python and based on the `km3pipe` [2] framework. The application establishes whether a detector is active or not from the presence or absence of `SNT` data. In the case of two active detectors, a certain tolerance to variations of their respective latencies is required.

Each received `SNT` message starts an iteration. In an iteration, the application operates as follows:

1. the `SNT` message is pushed to a queue identified by the sender detector;
2. detectors with at least one `SNT` message in their queue are classified as *active*;
3. if at least one detector is active, the earliest timestamp available in the queue is elected as *pending time*;

1. `json.org`; [237]
2. `https://km3py.pages.km3net.de/km3pipe/`

4. all the detectors having the earliest SNT message corresponding to the *pending time* are elected as *armed detectors*;
5. the iteration proceeds either if (a) all armed detectors have more than one message in the queue *or* (b) the latest time in the queue of any detector exceeds the *pending time* by a given timeout;
6. the SNT data for the armed detectors are extracted from the respective queues, the combined trigger is evaluated and a corresponding message is generated to be sent to the dispatcher.

Step 5 is critical in defining the application behaviour. If *detector A* was an armed detector with only one element left in the queue, and the following iteration was triggered by *detector B*, *detector A* would appear as to have empty queue and considered inactive. Requiring that (a) all armed detectors have at least two elements in the queue prevents this situation. However, if *detector A* has only one element in the queue because it has stopped sending data, the condition (a) can no longer be satisfied and SNT messages from *detector B* (*C*, ...) would start queuing. When the latest queued message exceeds the designated timeout with respect to the earliest, condition (b) is triggered and the processing goes on without further waiting for *detector A*.

detector A may come back online with one or more SNT messages for which the corresponding data of *detector B* (*C*, ...) have already been processed. In this case, *detector A* will have the earliest timestamp (see step 3) and will be processed as a single *armed detector* for as long as it takes to get synchronised with the others.

As a result, the algorithm introduces a (limited) delay only when one detector that was previously synchronised stops sending data. During normal operation, data are always processed as early at possible with a mean latency of one SNT message per detector (0,1 s). The application has been verified to behave consistently across all states in which the two KM3NeT detectors are sending or not sending data. The synchronisation is always recovered after any sequence of events where one or both detectors stop and recover the transmission.

4.6.3.3 Alert generation and management

The alert generation is managed by a lightweight dedicated application. The application is configured with a set of significance thresholds and a set of corresponding *qualifiers*. The significance of every KM3NeT SN message is compared with all the thresholds and the corresponding alert messages are generated.

An alert message consists of a JSON dictionary that includes a physics type (e.g. *supernova* or *neutrino*), the qualifier and a *payload* nested dictionary containing the source message that triggered the threshold.

Applications subscribe to the dispatcher to receive all alerts and then filter them internally depending on the physics type and the qualifier. According to the qualifier, the application can trigger some action as producing an external alert or distributing a control message to the DAQ.

At firsts, three qualifiers for supernova alerts have been defined:

— `internal`: exploited internally for monitoring and testing;
— `snews-low`: FAR ~ 1 / day, propagated to the SNEWS test server;
— `snews`: FAR ~ 1 / 8 days, propagated to the SNEWS production server.

4.6.4 Low-level data buffering

During the normal KM3NeT operation, L0, L1 and L2 timeslice data are generated and used internally in the software data filter (see Section 2.1.2). After the trigger, except for dedicated calibration runs, L0 and L2 data are discarded, while L1 data are distributed to the DAQ with a downscaling factor. In case a core-collapse supernova is detected, KM3NeT has significant potential to perform astronomy- and astrophysics-oriented analyses of the detected neutrino light-curve. In general, these can be based on all available coincidence data (L1). Studies based on L0 data could also be foreseen in the future. To allow for this, the software data filter application has been augmented with the implementation of a circular buffer. The buffer can store a designated number of timeslices for any chosen type in a binary `ROOT` file, on the local memory of the machine. As a response to a specific control message distributed through the DAQ dispatcher, each data filter closes the buffer file (*dump*) and starts writing on a new one. The closed files are subsequently merged and copied to a central permanent storage location for analysis.

The choice of the size of the buffer is a trade-off between a sustainable usage of the memory resources and the acceptable worst-case delay for incoming alerts. The main requirement is to allow the effective follow-up of SNEWS alerts. According to the statistical modelling of the SNEWS network response, 90% of the alerts are produced within five minutes from the event, and 99% within eleven minutes [234]. In the setup under test at the time of writing, the buffer is configured to store 10 minutes of data. For a DAQ system with ten parallel data filters (as it is the case for the ORCA6 detector) this translates into a buffer of 60 s (600 timeslices) per data filter. Considering that the L1 data stream has a throughput of ~ 25 MB s^{-1}, the storage requirement for a KM3NeT building block will be of ~ 15 GB, that is sustainable even for a temporary storage on the machine RAM. In the current configuration, the buffer dump is triggered whenever a SNEWS GCN alert is received, or as a reaction to KM3NeT self-generated triggers with an adjustable threshold. The selection of alerts triggering the dump can be widened in the future.

4.6.5 Graphical monitoring

At each shore station, a dedicated application subscribes to receive the `SNT` messages from the dispatcher and provide visual feedback on the behaviour of the background. In Figure 4.25, sample plots as produced by the web monitoring interface are shown. A first panel is used to show the all-time histogram of the number of events evaluated with the sliding time window. As a guidance, the level of a signal with an equivalent false alarm rate of one per century is shown, together with an indication of the cor-

responding distance. A second panel shows the number of background events as a function of time, with a moving average taken over 10000 samples (1000 s).

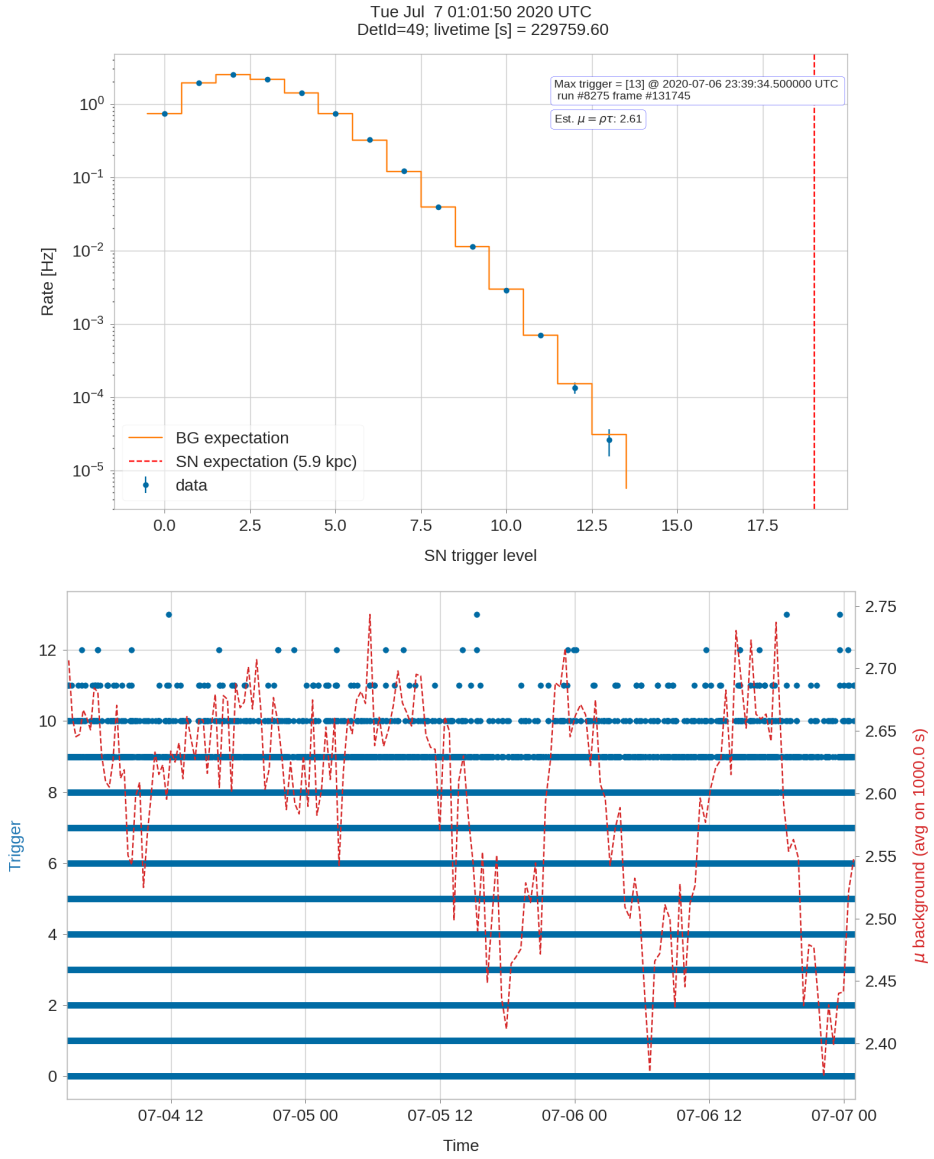

Figure 4.25 – Sample plots from the online visual monitoring of the supernova search. Top: histogram of the number of events in the sliding search window, together with a Poisson distribution based on the mean value of the data. Bottom: number of background events evaluated each 100 ms in the previous 500 ms, shown as a function of time for an interval of 48 hours. The mean over 1000 samples is drawn as a dashed red line. Cyclical, bioluminescence-induced variations due to the changing in the instrumentation efficiency can be observed.

4.7 Follow up of gravitational wave alerts

The most common scenario of gravitational wave emission is the coalescence of the two compact objects of a binary system. With a different mechanism, the asymmetric collapse of matter in a CCSN has been proposed as a possible origin for burst-like gravitational wave signatures [238, 239]. LIGO and Virgo have dedicated pipelines for the detection of *unmodeled bursts* and have performed the first surveys searching for GW emissions from CCSNe [240]. The scale on which these events would be detectable is in general model-dependent, with a typical horizon of a few megaparsecs, much smaller than the one for compact binary mergers. As such, unmodeled bursts are interesting for their possible association with Galactic or near-Galactic supernovæ.

The observation run *O3* of the LIGO-Virgo gravitational-wave observatories started on April 1, 2019. The run went through a technical break in October 2019 and subsequently continued up to March 27, 2020, when it came to an early end due to the COVID-19 pandemic. Differently from the policy adopted up to the previous *O2* run (ended in August 2017), since *O3* all alerts are public and automatically distributed to the multi-messenger community with a short latency (in the order of minutes). Event alerts can be later retracted if do not survive further scrutiny. The *O3* observation run counted 56 confirmed candidate events [3] and 24 retracted. The average rate of confirmed candidates has been slightly more than one per week. The majority of LIGO-Virgo alerts are identified as compact binary mergers, mainly merger of binary black-holes. During *O3*, two alerts for *unmodeled bursts* have been produced: `S191110af` [241] (subsequently retracted) and `S200114f` [242]. Both have been followed up with a search for an excess in KM3NeT coincidence data. The follow-up analyses have been performed examining a 400 ms time window after the time of the GW event, using the *coincidence correlation filter* as described in Section 4.3.3.1 and the 6 – 10 multiplicity selection, that at the time was considered optimal.

4.7.1 Analysis outline

The follow-up analysis of gravitational wave bursts presented here is based on *offline* data. In practice, the run file corresponding to the alert time is retrieved and *offline* analysis routines are performed. The number of signal events and the fraction of active PMTs are evaluated in the 400 ms following the start time (T0) of GW the event. As a consequence of the design of the analysis pipeline, events are binned on a 100 ms basis. The background expectation μ_b is determined from the previous analysis of long-term data or the statistics collected by the online monitoring system. The instrumentation efficiency for the average fraction of active PMTs in the considered time window is used to scale the background and signal expectation values. Using the Feldman-Cousins method [243], the 90% confidence level upper limit on the signal expectation value $\mu_{s,0.9}$ is established.

3. `gracedb.ligo.org/superevents/public/O3/`

The upper limit on the number of signal events is compared with the prediction for the $11\,M_\odot$ and $27\,M_\odot$ progenitors to set a 90% CL lower limit on the distance of the potential source:

$$d_{0.9}^{\min} = (10\,\text{kpc})\sqrt{\frac{\mu_s(10\,\text{kpc})}{\mu_{s,0.9}}}\,. \tag{4.24}$$

An upper limit on the total energy is set for a standardised quasi-thermal spectrum with $\langle E\rangle = 15\,\text{MeV}$ and $\alpha = 3$, assuming that 70% of the energy is released in the first 400 ms. Given the predicted number of signal events for this flux, the corresponding 90% upper limit on the energy is derived as:

$$E_{0.9}^{\max} = (3\cdot 10^{53}\,\text{erg})\,\frac{\mu_{s,0.9}}{0.7\,\mu_s(3\cdot 10^{53}\,\text{erg})}\,. \tag{4.25}$$

4.7.2 S191110af (retracted)

The LIGO-Virgo GW burst `S191110af` [241] has its start time (T0) at 2019-11-10 23:06:44.183 UTC and duration of 100 ms, with a false alarm rate of $\sim 12{,}7\,\text{yr}^{-1}$. Four ORCA DUs (ORCA4) and one ARCA DU (ARCA1) were operational at the time. An issue on the White Rabbit synchronisation of ARCA prevented to establish an absolute time reference for the detector with a precision sufficient for the CCSN follow-up. Therefore, only ORCA4 data are considered. In Figure 4.26, the number of events and the instrumentation efficiency as a function of time in a 3 s interval around the T0 of the event are reported. Zero events are detected in correspondence, even extending the time window by a further 0,4 s. The summary of the follow-up analysis is given in Table 4.8. The result of the follow up has been disseminated with the GCN circular #26249 [244] on the 14th of November. Later the same day, the LIGO-Virgo alert has been retracted.

Table 4.8 – Summary of the follow up of (retracted) GW candidate S191110af

Event	S191110af (retracted)
T0 date	2019-11-10
T0 time	23:06:44.183
Events [T0, T0 + 400 ms]	0
Instrumentation efficiency ϵ	0.55
$\mu_b(\epsilon)$	0.8
Feldman-Cousins $\mu_{s,0.9}$	1.7
Lower limit 27M$_\odot$ $d_{0.9}$	11,3 kpc
Lower limit 11M$_\odot$ $d_{0.9}$	5,7 kpc
Upper limit $E_{0.9}$	$2{,}75 \cdot 10^{53}$ erg

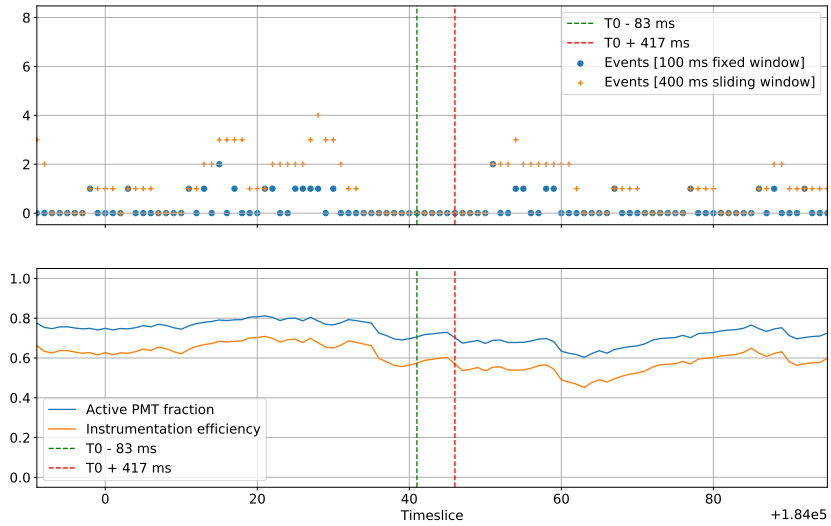

Figure 4.26 – S191110af follow up data. Top: number of events in the timeslice as a function of the timeslice index (blue dot markers) and number of events in the 400 ms ending in the same timeslice (orange cross markers.). Bottom: fraction of active PMTs and corresponding instrumentation efficiency as a function of the timeslice index. The vertical red and green dashed lines delimitate the timeslice range covering the [T0, T0 + 400ms] interval.

4.7.3 S200114f

The LIGO-Virgo GW burst S200114f [242] has been detected on Jan 14, 2020 02:13:41.239 UTC. It has a 10 ms duration and an equivalent false alert rate of one per ~ 25 yr. The event is relatively well localised with a 403 deg^2 90% area, as shown in Figure 4.27. Although Betelgeuse is located in the same region of the Sky, it falls in-between the two main contours, outside the actual confidence area.

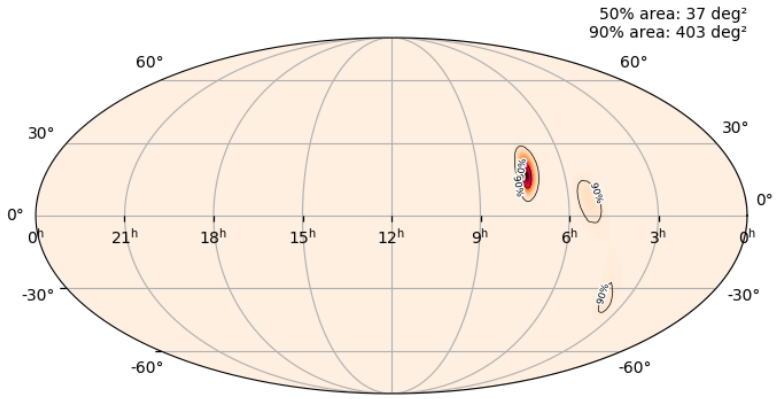

Figure 4.27 – Mollweide projection of the LIGO-Virgo localisation fit for S200114f. Source: [242].

Four ORCA DUs (ORCA4) were operational at the time with a regular physics run. The ARCA detector was powered off due to an on-going restructuring of the shore station. For ORCA4, the number of events as a function of time, evaluated on a 100 ms time basis, is shown in Figure 4.28 together with the fraction of active PMTs and the corresponding instrumentation efficiency. In the 400 ms time window following the timestamp of the GW event, *two* events are detected. An average efficiency of 0.985 is considered. The efficiency-corrected expectation value for the number of background events is $\mu_b = 1.45$. The excess over the background expectation value has a p-value of 40%, therefore not significant. Using the Feldman-Cousins method, a 90% confidence level upper limit for the signal expectation value is $\mu_{s,90\%} \simeq 4.8$. A summary of the derived limits is given in Table 4.9. The result of the follow up has been published in the GCN circular #26751 [245]. Being at a distance of 200 pc, Betelgeuse can be confidently excluded as a source. The multi-messenger follow-up campaign [246] has seen the contribution of a large number of instruments including optical and near-infrared telescopes (MASTER-Net, ZTF, DDOTI/OAN, GTC, WHT, Palomar, J-GEM, SOAR, TAROT, Gemini), neutrino telescopes (IceCube, ANTARES), ground-based Cherenkov observatories (HAWC), space-based X-ray and γ-ray detectors (MAXI/GSC, *Fermi*-GBM, INTEGRAL SPI-ACS, AGILE-GRID, *Fermi*-LAT, *Swift*-BAT, *Swift*-XRT, Konus-Wind, AstroSat CZTI) and space-based cosmic-ray detectors (CALET). No credible counterpart for the gravitational-wave event has been identified.

Table 4.9 – Summary of the follow up of GW candidate S200114f

Event	S200114f
T0 date	2020-01-14
T0 time	02:13:41.239
Events [T0, T0 + 400 ms]	2
Instrumentation efficiency ϵ	0.875
$\mu_b(\epsilon)$	1.45
Feldman-Cousins $\mu_{s,0.9}$	4.8
Lower limit $27M_\odot$ $d_{0.9}$	11,5 kpc
Lower limit $11M_\odot$ $d_{0.9}$	6,1 kpc
Upper limit $E_{0.9}$	$2{,}9 \cdot 10^{53}$ erg

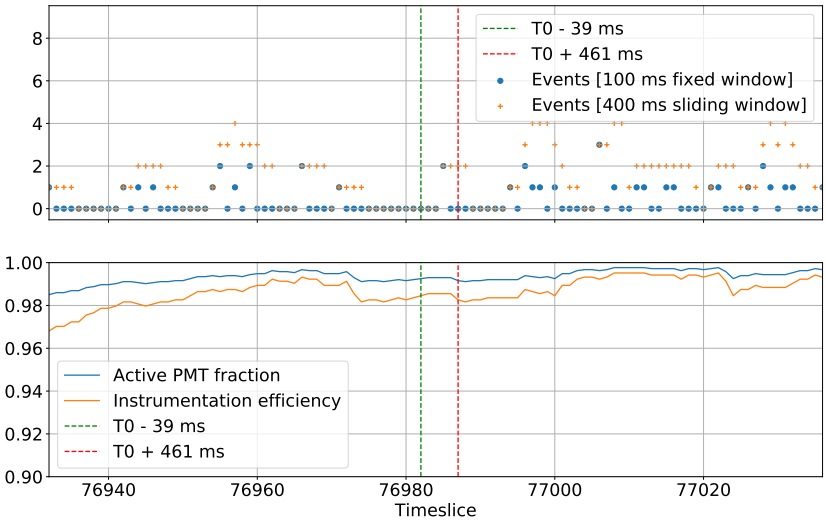

Figure 4.28 – S200114f follow up data. Top: number of events in the timeslice as a function of the timeslice index (blue dot markers) and number of events in the 400 ms ending in the same timeslice (orange cross markers.). Bottom: fraction of active PMTs and corresponding instrumentation efficiency as a function of the timeslice index. The vertical red and green dashed lines delimitate the timeslice range covering the [T0, T0 + 400ms] interval.

4.7.4 Perspective for future follow-ups

The gravitational-wave follow-ups will continue with the *O4* observation period of the Advanced LIGO, Virgo and KAGRA interferometers, foreseen in 2021-22. Some improvements foreseen for the KM3NeT follow-up strategy are here discussed.

4.7.4.1 Analysis pipeline

The analysis tools adopted in these follow-ups is the same used for the *offline* data analysis presented in this Chapter. Being originally designed for a statistical study of the background, they are subject to some limitations when used in time-dependent analyses. In particular, the events are binned in fixed time segments of 100 ms and no information on the individual event is kept. Also, despite the analysis procedure being pre-determined, they require a human intervention to produce a result. From these considerations, the pipeline could be improved by separating the analysis into two parts. The first can be implemented as part of the online trigger, where the number of events in each detector can be stored for the last 24 or 48 hours in a centralised buffer. A timestamp-based query can then be used to automatically retrieve the number of events at any point in time in the covered period. A more detailed *quasi-online* analysis can rely on the low-level data buffer. In this, the data can be accessed at an arbitrary UTC-referenced time to retrieve the number of events in a precise time window, regardless of any pre-defined time binning. These developments are part of an improvement plan for the real-time pipeline.

4.7.4.2 Presentation of the results

When a given upper limit on the number of signal events is established, the distance and energy limits are degenerate. Once fixed the spectral properties of the fluence used to estimate the signal expectation, $\mu_s(E_0, d_0)$, for a total energy E_0 and a distance d_0, the number of signal events scales naturally as:

$$\mu_s(E, d) = \mu_s(E_0, d_0)\, \frac{E}{E_0} \left(\frac{d_0}{d}\right)^2 ; \tag{4.26}$$

so the 90% upper limit, $\mu_{s,0.9}$ is translated into an upper limit on the mere quantity $E\, d^{-2}$ as follows:

$$\frac{E}{d^2} \leq \left(\frac{E}{d^2}\right)_{0.9} = \frac{E_0}{d_0^2} \frac{\mu_{s,0.9}}{\mu_s(E_0, d_0)} . \tag{4.27}$$

An upper limit on the signal expectation defines a parabola on the (E, d) plane, $E = A\, d^2$, with A a constant dependent on the spectral properties, $(\langle E \rangle, \alpha)$, of the flux. The area above the parabola represents the parameter space that can be excluded at the 90% confidence level.

As an example, if a supernova with a total energy of $3 \cdot 10^{53}$ erg at 10 kpc of distance is expected to produce $\mu_s = 10$ events, an upper limit of $\mu_{s,0.9} = 5$ results in a limit

$E\,d^{-2} \leq 0.5\,(3 \cdot 10^{53}\,\mathrm{erg})/(10\,\mathrm{kpc})^2$, as shown in Figure 4.29.

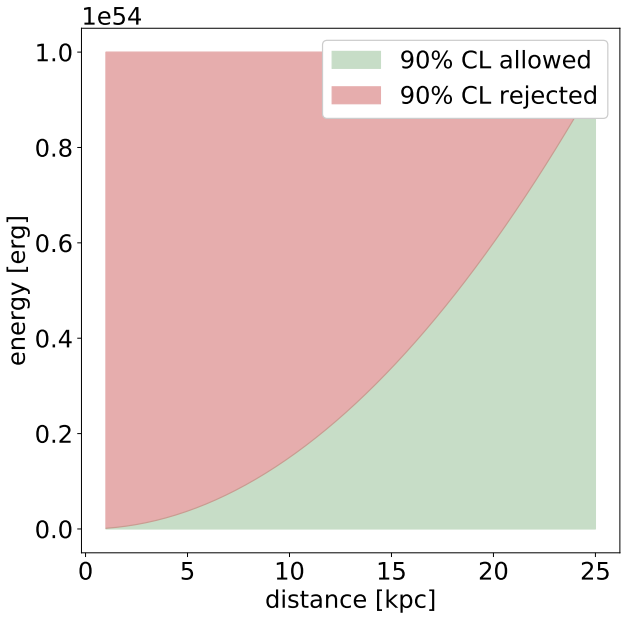

Figure 4.29 – Example of exclusion region for energy and distance determined by an upper limit of $\mu_{b,0.9} = 5$, against a signal prediction of $\mu_b = 10$ for a supernova of energy $3 \cdot 10^{53}$ erg at a distance of 10 kpc.

4.8 Supernova astronomy and astrophysics

Thanks to the large number of photosensors, KM3NeT detectors can potentially observe a supernova neutrino burst with very high statistics. By using all coincidences (starting at multiplicity two), different features of the neutrino spectrum and its time dependency can be probed. This Section illustrates the estimated capability of KM3NeT to resolve the flux spectral properties and to detect oscillations in the neutrino light-curve related to the *standing accretion shock instability* phenomenon [247]. The Author has also contributed to these analyses, that were primarily developed by M. Colomer, V. Kulikovskiy and G. Vannoye.

4.8.1 Flux spectral properties

Neutrino events at higher energies tend to produce more photons and be detected as higher-multiplicity coincidences. As a consequence, the multiplicity distribution for the population of detected events carries some information about the spectral properties of the flux. A parameterisation of the number of events at each multiplicity as a function of $\langle E \rangle$ and α, as defined in Section 4.2.1, is used to evaluate the

coincidence spectrum for different signal hypotheses. The flux spectrum is taken as described by Equation (4.3). The detector response is evaluated by considering three parameters: $\langle E \rangle$, α and Λ. The signal normalisation factor, Λ, or *signal scale* is defined as:

$$\Lambda = \frac{L_\nu}{L_\nu^0} \left(\frac{d_0^2}{d^2} \right); \tag{4.28}$$

where $L_\nu^0 = 3 \cdot 10^{53}$ erg and $d_0 = 10$ kpc are the standard reference values of the simulation. Each evaluated signal hypothesis is represented by a set of true values $(\langle E \rangle_{\text{true}}, \alpha_{\text{true}}, \Lambda_{\text{true}})$. Toy experiments are performed to construct the $\Delta\chi^2 = \chi^2(\langle \hat{E} \rangle, \hat{\alpha}, \hat{\Lambda}) - \chi^2(\langle E \rangle_{\text{true}}, \alpha_{\text{true}}, \Lambda_{\text{true}})$ probability density function, h_χ. In this notation, the values $\langle \hat{E} \rangle$, $\hat{\alpha}$, $\hat{\Lambda}$ correspond to the minimum of χ^2 while $\langle E \rangle_{\text{true}}$, α_{true}, Λ_{true} are the true values. It is verified that h_χ has a mean value below two and does not follow a χ^2 distribution with three degrees of freedom (corresponding to the case of three independent parameters). This comes from the fact that the three parameters are partially degenerate with respect to the set of observables (the number of events at each multiplicity). This distribution is used to define the $\Delta\chi^2_{\text{crit}}$ value corresponding to the 90% confidence level (C.L.) as:

$$\int_0^{\Delta\chi^2_{\text{crit}}} h_\chi(\Delta\chi^2)\, d(\Delta\chi^2) \leq 0.9\,. \tag{4.29}$$

Confidence level contours are defined as the subset of the parameter space of the $\overline{\nu}_e$ spectrum for which $\chi^2(\langle \hat{E} \rangle, \hat{\alpha}, \hat{\Lambda}) - \chi^2(\langle E \rangle, \alpha, \Lambda) \leq \Delta\chi^2_{\text{crit}}$. In this, the Asimov data set is used, starting from the true values $\alpha = 3$, $\langle E \rangle = 13$ and $\Lambda = 1$. Three different boundary conditions for α are considered: α is a free parameter in the range 2–4, α is measured with a 10% uncertainty, and α is known (fixed). The results are shown in Figure 4.30. In alternative to the confidence areas obtained from the true parameter data sets, the distribution of the fitted $\langle E_\nu \rangle$ values from simulated pseudo-experiments is built to estimate the precision of the mean neutrino energy fit. The analysis is performed for three different hypotheses on the pinching parameter and the signal scale: first assuming α and Λ are precisely known, second considering an uncertainty of 10% for both, and third without prior knowledge of these parameters. Figure 4.31 shows the distributions of $\langle E \rangle - \langle E \rangle_{true}$ and $\alpha - \alpha_{true}$ obtained for these three hypotheses, and the corresponding standard deviations (RMS). Due to the parameter degeneracy, KM3NeT as a stand-alone detector does not provide significant capability in the individual resolution of the spectral features of the neutrino flux. However, it can be expected to provide a significant contribution to joint analyses combining independent observations by different experiments.

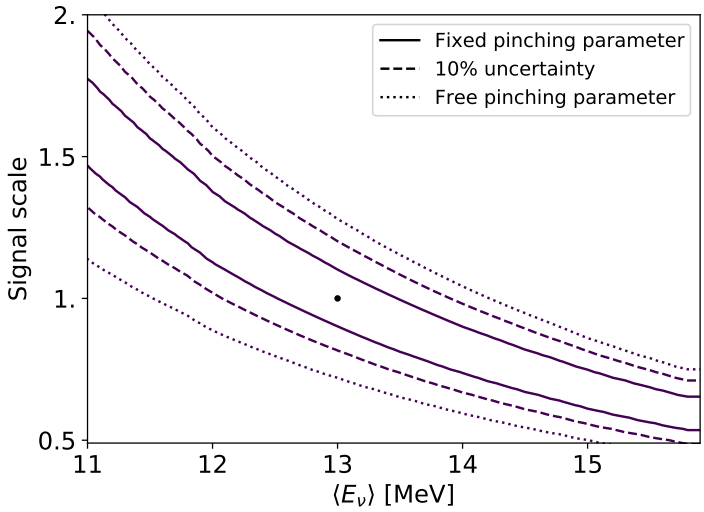

Figure 4.30 – Contours at 90% confidence level in the signal scale and $\langle E_\nu \rangle$ parameter space for the assumed combined ARCA and ORCA data sets in 500 ms window. Three options are studied for the spectral pinching shape parameter: α free in the fit in the range of 2–4 (solid line), α known with 10% uncertainty (dashed line), and α fixed (dotted line). The dot indicates the true values.

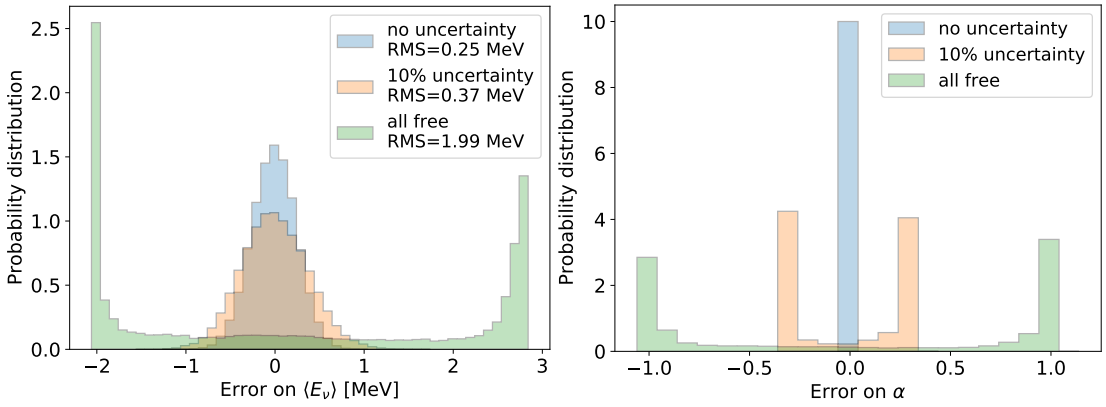

Figure 4.31 – Distributions of the error on the fitted mean energy, E_ν (left), and on the fitted pinching parameter, α (right), under three different assumptions: with α and the signal scale, Λ, known (blue), with these two parameters estimated with 10% uncertainty (red) and with all three parameters free (green). This is evaluated for the combination of ORCA and ARCA, assuming the benchmark values for the CCSN progenitor, $L_\nu^0 = 3 \cdot 10^{53}$ erg and $d_0 = 10$ kpc.

4.8.2 Standing accretion shock instability

State-of-the-art three-dimensional simulations of CCSNe predict the development of fast and asymmetric hydrodynamic motions in the core during the accretion phase. An example is the *standing accretion shock instability* (SASI) [247]. During the SASI, the stellar core develops violent hydrodynamic oscillations that can reflect on the time profile of the neutrino emission (*neutrino light-curve*) [225]. These motions are believed to favour the explosion by enhancing the neutrino energy deposition to the shock. Some models identify the SASI oscillation as a potential source of gravitational waves [248].

In KM3NET, the SASI detection is performed by searching for periodic components in the time-profile of the signal. All coincidences at multiplicity two and above are considered in the light-curve. To suppress time-correlated effects induced by bioluminescence and appearing as random coincidences, the coincidence time window is restricted to 5 ms. A fast Fourier transform (FFT) is applied to the signal over a time interval of $-150/+50$ ms centred on the peak of the light-curve. Two methods are evaluated to identify an oscillatory component: the first searches for a peak at any frequency in the power spectrum, the second searches for an energy excess around the predicted SASI frequency. In Figure 4.32 a simulation of the detected light-curve is shown together with the power spectra calculated for a small set of realisations of the simulation. The $20\,M_\odot$ from Reference [225], that exhibits enhanced oscillations, is here taken as an example.

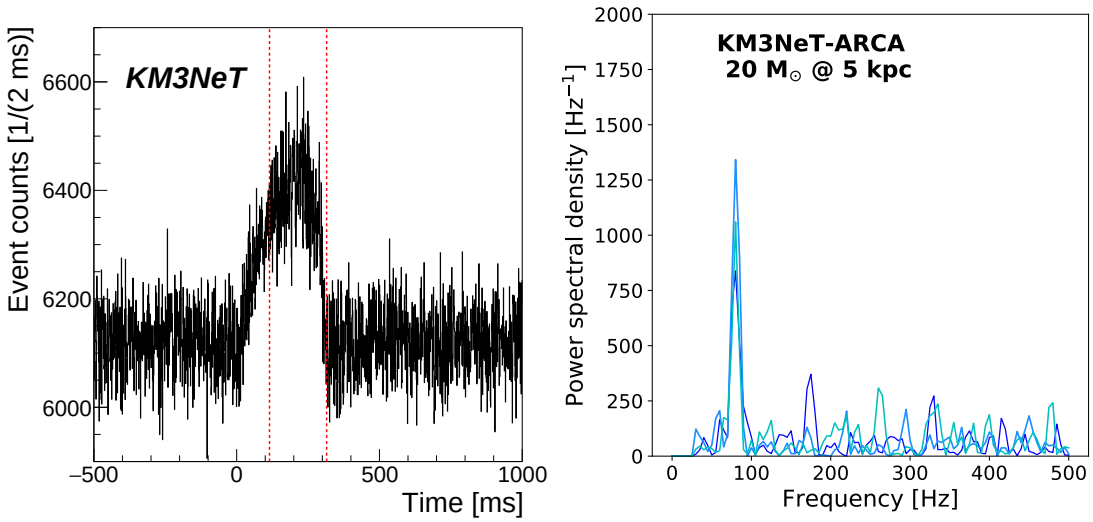

Figure 4.32 – Left: simulation of a neutrino light-curve for all coincidences at multiplicity two and above detected for a $20\,M_\odot$ progenitor in an ARCA building block. Right: power spectrum as calculated for different realisations of the signal simulation.

In addition to the $20\,M_\odot$ progenitor here introduced, the $27\,M_\odot$ and the failed SN

40 $M_\odot$ models presented in Section 4.2.1 are considered to estimate the sensitivity to the SASI. Light-curve samples for the case of pure background are simulated. The analysis is applied to each sample to estimate the corresponding peak of the power spectral density (first method) and the energy around the predicted SASI frequency (second method). Taking the ARCA detector as an example, the complementary cumulative density function (1 - CDF), built from a large set of background simulations, is shown in Figure 4.33 together with the signal expectation value for the three progenitors. The distance for each progenitor is chosen to probe the sensitivity near to the 3σ threshold.

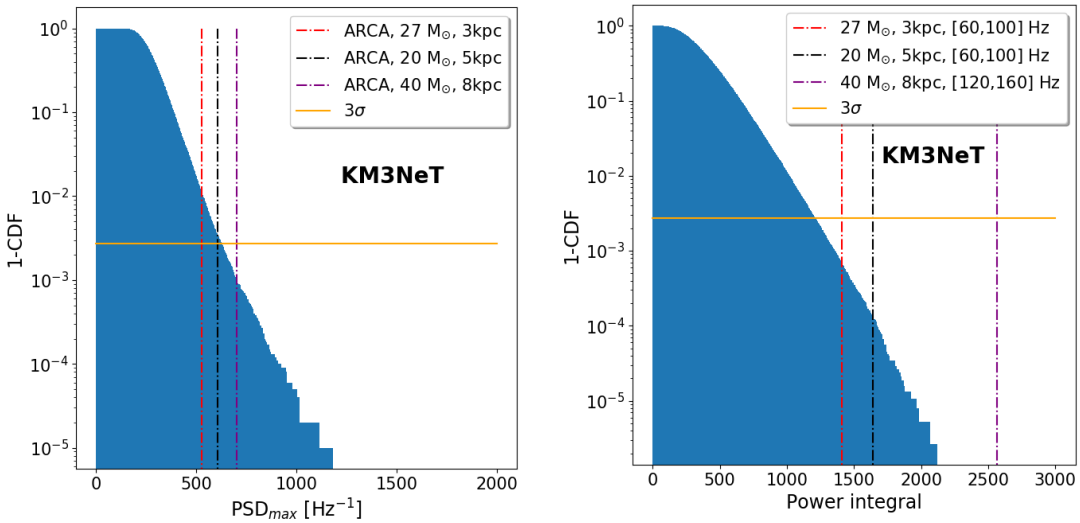

Figure 4.33 – Complementary background CDF built from an ARCA noise simulation (blue distribution). On the left as a function of the maximum power. On the right as a function of the power integral around the SASI frequency predicted by the model. The horizontal line (orange) indicates the 3σ threshold for the CDF. The vertical lines, dashed red, black and purple correspond respectively to the expectation for the signal plus background scenarios for the 27 $M_\odot$, 20 $M_\odot$, 40 $M_\odot$ progenitors at 3, 5 and 8 kpc.

The ORCA and ARCA detected neutrino signals will be delayed one to the other due to their different locations at Earth. Due to the *a priori* uncertainty on the source direction, the successful synchronisation of the light-curve data at sub-ms precision for a combined analysis is not guaranteed. Therefore, the analysis is applied to the observed light-curve independently on each site, and the significances are combined according to the Stouffer's method. The sensitivity results obtained are summarized in Table 4.10, combining ARCA and ORCA. For the two CCSN progenitors of 20 $M_\odot$ and 27 $M_\odot$, the results are provided for the distance at which the model-independent approach reaches a sensitivity close to the 3 σ level. For the failed CCSN, they are given for a source at the Galactic Center. The main systematic uncertainties are taken into

account. For the combination of ORCA and ARCA, the bioluminescence conditions add $\pm 0.3\,\sigma$ uncertainty in the SASI sensitivity results.

Table 4.10 – Sensitivity results with ORCA + ARCA for the three different stellar progenitors considered.

Progenitor	**d [kpc]**	**Method 1: Search for peak in spectrum**	**Method 2: Search for power excess around f_{SASI}**	**Coverage of Galactic CCSN**
$27\,M_\odot$	3	$2.8 \pm 0.7\,\sigma$	$4.1 \pm 0.9\,\sigma$	3%
$20\,M_\odot$	5	$3.2 \pm 0.7\,\sigma$	$4.5 \pm 0.9\,\sigma$	10%
$40\,M_\odot$	8	$3.8 \pm 0.7\,\sigma$	$> 5\,\sigma$	35%

4.8.3 Timing and triangulation

Assuming a high-significance detection has taken place, the time-domain analysis of light-curve data can be performed to estimate the time of arrival of the neutrino burst. The first motivation for this study is astronomy: not only supernova neutrinos can be an early warning for optical observations, but they can also reveal a supernova occurring in an obscured region of the Galaxy, or an optically-dark black-hole formation event. In this context, the possibility of pointing to the source through the neutrino signal assumes a fundamental role. While large, low-background, experiments as Super-Kamiokande can achieve autonomous pointing capabilities through the reconstruction of anisotropic elastic-scattering interactions [249], cross-experiment triangulation remains a valuable alternative that can be implemented in a multi-messenger philosophy. The precise arrival time of the neutrino burst can also help in the search for a correlated gravitational wave emission, assuming an emission scenario where the sensitivity of neutrino experiments is higher compared to gravitational-wave interferometers. Finally, combining data from different experiments, a precise reconstruction of the time evolution of the neutrino fluxes can provide insights on the supernova astrophysics.

Detectors that are able to collect sufficient event statistic can time the arrival of the neutrino burst by fitting a template of the signal time profile to the experimental data. For example, the leading edge of the detected light-curve can be fitted with an exponential rise [250]. The time of arrivals estimated by the individual experiments can be combined in a triangulation method [251] to reconstruct the direction of the source. An evaluation of KM3NeT performance in the determination of the absolute time of the neutrino burst is currently in progress. In general, the precision of this technique depends on the accuracy of the signal template that is used in the fit.

Whereas assuming an exponential rise is a sensible choice, this model only exploits a limited portion of light-curve, as shown in Figure 4.34. On the other hand, the complete signal shape is not known *a priori*, since the knowledge of the shape and duration of the accretion phase and the transition to the cooldown is subject to important theoretical uncertainties.

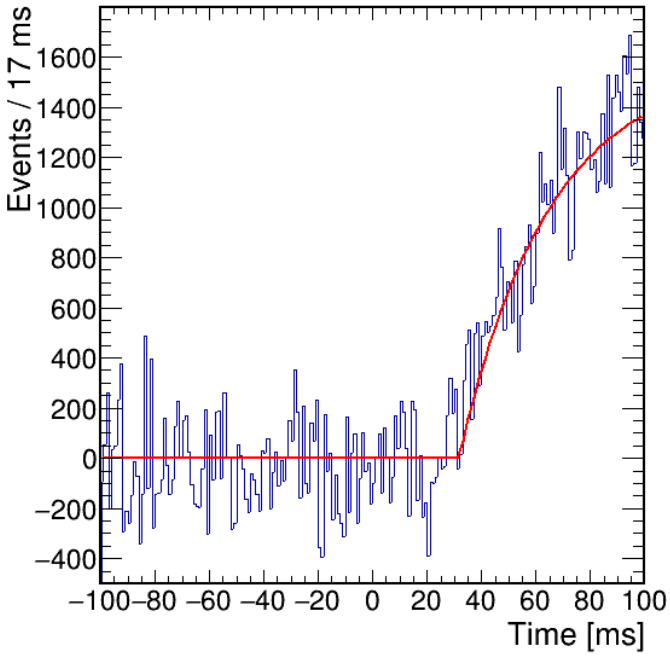

Figure 4.34 – Time distribution of the events (light-curve) for ARCA using all coincidences in a simulated light-curve detection, assuming a $20\,M_\odot$ CCSN progenitor at 5 kpc. The red line shows the fit of the simulated data with an exponential rise.

In light of this, a method exclusively based on experimental data has been proposed. In Reference [252], to which the Author has also contributed, a method to compare the experimental light-curves to reconstruct the source direction is proposed. The strategy relies on the estimation of the *relative delay* of the signal arrival time between pairs of detectors. While its performance can be different depending on the actual signal time profile, the method itself does not rely on a previous assumption of the same. Only the detected neutrino light-curves are compared. To evaluate the performance, a simple signal template and a simplified detector model are used to simulate the response of different experiments to the electron antineutrino burst, as detected through the inverse beta decay channel. KM3NeT, IceCube, Hyper- and Super-Kamiokande, and JUNO are considered. On the simulated light-curves, a χ^2 fit and a cross-correlation method are used to estimate the relative delay of the signal arrival time between two detectors. Through a set of pseudo-experiments for the detected light-curves, the uncertainty on the relative time delay is estimated for any given pair of detectors.

With the estimated uncertainties, a second set of pseudo-experiments is then realised, simulating the estimated time offsets for a given location in the Sky. The source localisation is reconstructed through triangulation, and the corresponding uncertainty is evaluated. As an example, the performance obtained for a foreseen combination of IceCube, Hyper-Kamiokande, ARCA and JUNO is reported in Figure 4.35 for a source at the Galactic Centre. The confidence areas are calculated either assuming the true delays as expectation values (*Asimov data set*, [226]) or by performing 10^5 pseudo-experiments and drawing the distribution of the best-fit positions. The 90% confidence level credible area for the considered four detectors combination has an extension of $\sim 140\,\mathrm{deg}^2$.

In KM3NeT, a quasi-online analysis of the detected neutrino light-curve is foreseen. Following a trigger, the buffered coincidence data can be analysed to count the number of coincidences as a function of time. A time binning of 1 ms provides sufficient resolution for most time-domain analyses. The obtained light-curve can be processed in real-time with a fit of the signal. At the same time, it can be shared to an external network, as it is foreseen for the `SNEWS2.0` multi-messenger plan [234].

4.9 Conclusions and perspective

The analysis conducted and illustrated in this Chapter represents the first full evaluation of the KM3NeT capability of detecting a core-collapse supernova neutrino burst. In particular, the first end-to-end simulation, from the flux description to the simulated hit data, has been realised. Data from the first deployed KM3NeT detection units have been extensively analysed to characterise the background. From this, filtering and event selection strategies have been developed. By exploiting coincidences with at least seven hit PMTs, a high-purity event selection allows achieving a 5σ sensitivity to 95% of galactic CCSN progenitors, for the most conservative flux model considered. For more optimistic flux assumptions, the KM3NeT sensitivity extends up to the Large Magellanic Cloud, the current limit for existing detectors.

The background filtering and event selection algorithms have been implemented in a real-time software, that has been operating since early 2019 at the KM3NeT ARCA and ORCA shore stations. The number of events in the supernova selection is continuously evaluated for each detector with a sliding time window. The observations of the two detectors are combined in a centralised trigger software. From this, alerts of different types and with different destinations can be generated depending on chosen false-alarm-rate thresholds. In particular, this framework enables KM3NeT to participate in the *Supernova Neutrino Early Warning System*. The first prototype of the infrastructure supporting the KM3NeT online multi-messenger activities has been commissioned as part of this work.

This analysis has been applied to the first follow-ups of external alerts, in the case of two LIGO-Virgo unmodeled gravitational-wave bursts. In a near-future perspective, the characterisation of the detector response to neutrino fluxes of different energies

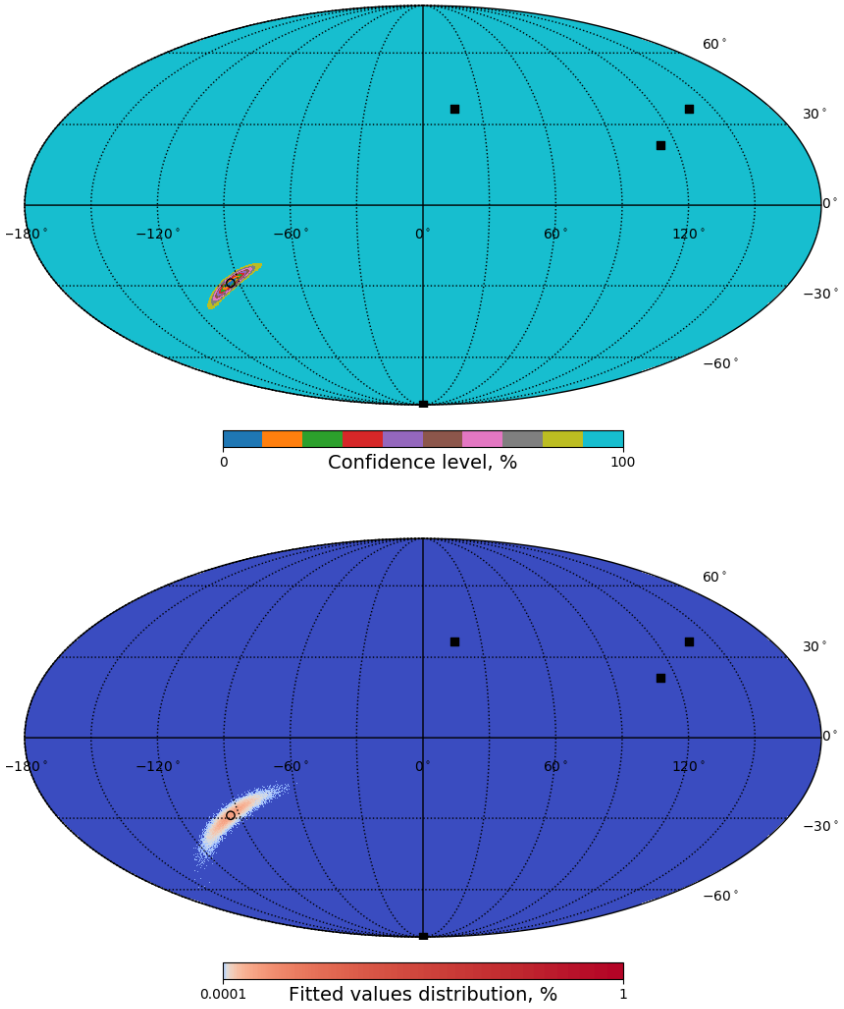

Figure 4.35 – Mollweide projection of confidence area in equatorial coordinates for a CCSN at the Galactic Centre (black dot) computed using triangulation between four detectors (black squares): IceCube, KM3NeT/ARCA, Hyper-Kamiokande and JUNO. Top: confidence area assuming true delays, bottom: fitted positions distribution for 100000 realisations of the delay sets [252]

can be applied in the search of different low-energy candidate sources (FRB, pulsars, etc.). Conversely, the first astronomy and astrophysics studies allowed by the analysis of a lower-purity data sample with a large collected statistics have been evaluated. A technical solution for the buffering of low-level data has been proposed and implemented in order to enable this kind of analysis.

The work described in this Chapter represents the first participation of the KM3NeT Collaboration in the multi-messenger astronomy community. This analysis is the subject of a paper currently at the stage of internal review by the Collaboration.

5 Absolute pointing of the detector

The event reconstruction illustrated in Section 2.4 provides spatial and directional coordinates of an event in the frame of reference of the detector. For neutrino astronomy, the reconstructed event direction needs to be translated into an absolute frame of reference, usually represented in equatorial or Galactic coordinates. The accuracy of the result depends on the knowledge of the absolute position of the detector elements. In particular, the determination of the azimuth angle in terrestrial coordinates is subject to the uncertainty on the absolute orientation of the detector footprint, here referred to as *absolute pointing*. A $\leq 0{,}1°$ degree systematic uncertainty is required to fully exploit the excellent track reconstruction accuracy of the ARCA detector.

Different approaches have been adopted in ANTARES to verify its absolute pointing. Due to their absorption of cosmic rays, the Moon and the Sun cast a *shadow* on the Earth that is detected as a decrease of the flux of atmospheric muons in correspondence of their position in the Sky. The observation in ANTARES of the shadows of the Moon [253] and Sun [254] allow to establish the detector absolute pointing with an accuracy of $0{,}73° \pm 0{,}14°$ and $0{,}45° \pm 0.12$ respectively. While in KM3NeT these approaches may reach better accuracy, their intrinsic limits cannot provide $\sim 0{,}1°$ performance. Also, this pointing verification requires several years of atmospheric muon data, whereas the KM3NeT detector will need a reliable pointing calibration much more promptly. In ANTARES, the pointing was also verified using a boat-mounted *surface array* of scintillation detectors. By searching for atmospheric muon coincidences between the surface array and the underwater detector, the latter can be calibrated cross-referencing the events with the GPS coordinates of the boat [255]. This technique produces results compatible with the Moon and Sun shadow analyses, but it is not competitive in resolution. The small size of the surface array limits the event statistic that can be collected in the typical duration of a sea campaign.

In this Chapter, an alternative technique to calibrate the positions of the KM3NeT detection unit anchors and verify the absolute pointing of the detector is evaluated. The study applies to the acoustic positioning system of ORCA, but keeps a target accuracy of $\leq 0{,}1°$. The acoustic calibration described in Section 2.2.3 establishes the *relative* position of the DOMs (and DU bases) with reference to a group of autonomous acoustic beacons deployed on the seabed. In ORCA, the absolute positions of the beacons are in turn determined with the RAMSES range meter system provided by IXBlue [1]. The beacon positions are calibrated with a horizontal plane accuracy of $\sim 1\,\text{m}$, that for a distance of 1250 m to the centre of the detector translates into a

1. ixblue.com

theoretical angular error of ~ 0,05°. The propagation of this error to the absolute calibration of the DU positions needs to be verified.

In the following, an alternative technique for the calibration of the detector pointing is proposed. An acoustic beacon on the sea surface is used to illuminate simultaneously the transducers (hydrophones) mounted on each detection unit anchor. The absolute positions of the transducers are calibrated by multilateration, with a sequence of measurements performed at different beacon positions. The position of the source is then reconstructed with a beamforming technique to verify the overall accuracy of the calibration. By correlating the beacon position as measured by the boat GPS and its position as determined in the frame of reference of the detector, the orientation of the detector footprint can be established.

5.1 Beamforming principle

The principle of *beamforming* (or *spatial filtering*) is to combine the signals of an array of isotropic transducers so that constructive interference maximally enhances the gain of the array with respect to a point in space (*scanning point*). It is a commonly adopted technique across a variety of fields, from loudspeaker systems to radio antennas. The simplest and most intuitive beamforming technique operates in the time domain and takes the name of *delay-and-sum beamforming*. As suggested by the denomination, the *scanning point* of an array of transducers is adjusted by tuning the relative delay (or phase shift) of the signal of each transducer. For a scanning point $\vec{P}$, the signal of a transducer i in position $\vec{T}_i$ is characterised by a delay:

$$\tau_i(\vec{P}) = \frac{||\vec{P} - \vec{T}_i|| - ||\vec{P} - \vec{O}||}{c_\varphi} \tag{5.1}$$

where $||\cdot||$ is the distance (norm) operator, c_φ the speed of the signal phase in the medium, and $\vec{O}$ the arbitrary origin of the frame of reference. The offset $||\vec{P} - \vec{O}||$ could be omitted, but it allows to conveniently operate in terms of *relative* delays with respect to an arbitrary point, $\vec{O}$, that can be set equal to the center of the array (or to the position of a reference transducer).

It is useful to introduce the calculation for a linear (planar) array in the far-field approximation, where the delays τ_i only depend on the angle, θ, between $\vec{P}$ and the normal to the line (plane) where the transducers are located. For two transducers at distance d, trigonometric identities yield:

$$\tau(\theta) \simeq \frac{2\,d\,\sin\theta}{c_\phi}\,. \tag{5.2}$$

This relation holds as long as the approximation error is much smaller than the wavelength, λ, used for the beamforming signal. In practice, this translates to a minimum radius $R \geq d^2\lambda^{-1}$. For an array size of 200 m and a wavelength of ~ 10 cm, the far-field

radius is ~ 400 km. In the scenario considered here, the far-field approximation clearly does not apply, but it can be taken as a useful indication in some cases.

In the beamforming operation, the signals $a_i(t)$ of an array of N transducers in positions $\{\vec{T}_i\}$ are added after compensating for their delays with respect to the propagation time between $\vec{P}$ and $\vec{T}_i$:

$$A(t,\vec{P}) = \sum_{i=0}^{N} a_i\left(t+\tau_i(\vec{P})\right) . \tag{5.3}$$

The case of an array of receivers illuminated by a source is in perfect duality with the one of an array of sources illuminating a receiver. Here, the first case is considered for a source at position $\vec{P}$. Given $s(t)$ the signal emitted by the source, the signals received at the array will be $a_i(t) = s(t-\tau_i)$. In the sum, the propagation delays are compensated and as a result $A(t,\vec{P}) = Ns(t)$. In this, the noise is a Gaussian process with mean zero and variance σ_n^2. As the sum of the noise across transducers is uncorrelated, the total noise variance is unchanged and the signal-to-noise ratio is plainly amplified by a factor N with respect to the single transducer. If the source is moved to a position $\vec{B} \neq \vec{P}$, the signals assume the values $a_i(t+\tau_i(\vec{B})) = s(t-\tau_i(\vec{B})+\tau_i(\vec{P}))$ and their sum is no longer coherent. The comparison of $s(t)$ with the result of the beamforming operation can therefore be used to reconstruct the position of $\vec{P}$.

5.2 Proof of concept

A *proof of concept* for the application of a beamforming technique to the detector pointing is here presented. Some simplifying assumptions are made. The receivers lie on a flat surface at coordinates $T_i = (x_i, y_i, 0)$. The source is a beacon at position $\vec{B} = (x_B, y_B, h_B)$ with $h_B = 2500\,\mathrm{m}$. Water is taken as a dispersionless medium with constant speed of sound $c_0 = 1500\,\mathrm{m\,s^{-1}}$. In such a case, given that the z-coordinate of the beacon is fixed, the beacon position can be identified by a zenith and azimuth angle, taking the center of the detector as the origin of a spherical coordinate system.

5.2.1 Signal template

The signal used for the beamforming is a *chirp*, namely a frequency-modulated cosine wave where the frequency is varying linearly in a range $[f_0, f_1]$ over a designated time interval $[0, t_1]$:

$$f(t) = f_0 + \alpha t\,;\ \alpha = \frac{f_0 - f_1}{t_1}. \tag{5.4}$$

In the time domain, the chirp $v(t)$, is represented by the equation:

$$v(t) = v_0 \cos\left(2\pi\left(f_0 t + \frac{\alpha}{2}t^2\right)\right) \tag{5.5}$$

where v_0 is the peak amplitude of the signal. The chirp is multiplied by a window function:

$$w(t) = e^{-\left(\frac{2t}{t_1}\right)^{100}} \tag{5.6}$$

that limits its duration in time with a steep smooth decay.

The use of a chirp is instrumental to suppress the phenomenon of *grating lobes*, i.e. multiple maximums in the gain profile of the array [256]. For a single-frequency periodic signal, and a distance between the transducers that is larger than a half-wavelength, there are naturally multiple time delays that correspond to the same phase shift [257]. In practice, this produces a *spatial aliasing* phenomenon, resulting in multiple directions (positions) for which the gain of the array is maximal. Using a broadband signal, since the spatial aliasing pattern is different at each frequency, secondary lobes can be conveniently suppressed, as exemplified in Figure 5.1.

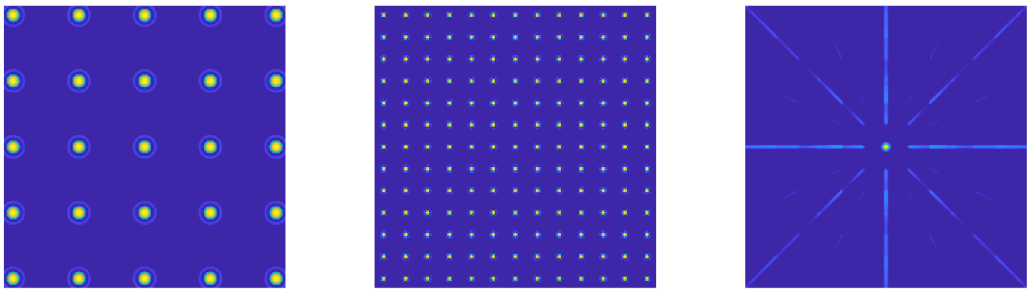

Figure 5.1 – Beamforming gain pattern as obtained with a single-frequency 5 kHz signal (left), a single-frequency 10 kHz signal, and a broadband signal (right). Spatial aliasing occurs for single-frequency signals, whereas a single focal point is found when using a broadband signal.

5.2.2 Noise and signal simulation

The real positions $\{\vec{T}_i\}$ of the receivers are assigned with a random fluctuation of the nominal values, $\{\vec{T}_i^{\star}\}$, considering an uncertainty $\sigma_x = \sigma_y = 1\,\mathrm{m}$. No further use of the nominal values is made. The beacon position $\vec{B}$ is arbitrarily located on the sea surface. Given $\vec{B}$ and $\{\vec{T}_i\}$ as inputs, the delays $\{\tau_i\}$ are calculated according to Equation (5.1). Time is discretised with a sampling frequency $f_s = 195\,\mathrm{kHz}$. A time interval $[-2T, 2T]$ is represented by a vector of $n_s = 1 + f_s 4T$ discrete time values, here referred to as *timebase*. T is chosen to cover the maximum delay plus the duration of the chirp. In correspondence, the signal received by each transducer is represented by a vector of n_s amplitude values, here referred to as *stream*. Each stream is initialised with samples of Gaussian noise according to a designated level. Accounting for the calculated delays, the windowed chirp signals are simulated as a sequence $\{v_k\}$ of amplitude samples over the interval $[-T, T]$ and summed to the (noise) stream of each transducer.

5.2.3 Footprint calibration

The estimation of the delays according to Equation (5.1) requires an accurate knowledge of the positions of the transducers. At a frequency of 10 kHz, a phase shift of π corresponds to an half-period of 50 μs, equivalent to a 7,5 cm displacement at the speed of sound. Exploiting the Taylor expansion of Equation (5.2), the expected delay variation $\delta\tau$ for a change in the angle $\delta\theta$ is:

$$\delta\tau = \tau(\theta + \delta\theta) - \tau(\theta) \simeq \frac{2\,d\,\cos\theta\,\delta\theta}{c_\phi} \tag{5.7}$$

that for $\delta\theta \sim 0{,}05°$, $d \sim 20$ m and $\cos\theta \sim 0.5$, yields a $\delta\tau \sim 10\,\mu$s.

For a beacon at a distance of $\mathcal{O}(3\,\text{km})$ and a distance between the transducers that can reach ~ 200 m, the far-field approximation does not hold. The signal from the beacon is therefore used at first to get an *absolute* calibration of the transducers positions. To this purpose, a *multilateration* technique similar to the one described in Section 2.2.3 is adopted. With respect to Equation (2.1), the time of emission is known. This information is used to offset all the received signals so that the zero of their time reference, t_0, is:

$$t_0 = \text{ToE} - \frac{||\vec{B} - \vec{O}||}{c_0}\,. \tag{5.8}$$

where ToE is the time of emission, $\vec{B}$ is the position of the beacon and $\vec{O}$ is the origin of the reference frame of the detector. The cross-correlation of the received signals with the signal template is used to calibrate the time of arrival (relative to t_0) of the signal at each transducer. The time of arrival corresponds to the maximum of the cross-correlation function. Rather than the *delay* in terms of (continuous) time, the *shift* in terms of number of samples is evaluated. With this, the time resolution on the ToA determination is $\delta t = f_s^{-1} = (195\,\text{kHz})^{-1} \simeq 5\,\mu$s, satisfying the sub-10 µs requirement evaluated above[2]. For each transducer i, the stream $\{s_k\}_i$ is cross-correlated with the signal template $\{v_k\}$ to determine the shift:

$$k_i^{\text{shf}} = \max_k\{s_k \star v_k\}_i\,. \tag{5.9}$$

By construction $k_i^{\text{shf}} = 0$ for an hypothetical transducer located at $\vec{O}$. The distance between the beacon and the transducer is therefore:

$$d(\vec{B}, \vec{T}_i) = ||\vec{B} - \vec{O}|| + c_0 k_i^{\text{shf}} f_s^{-1}\,. \tag{5.10}$$

Using at least three beacon positions, $\{B_j\}$, each transducer position T_i is determined by minimising the mean squared difference, Δ, between the expected and measured

2. It should be noted that this is not the intrinsic limit on the phase resolution of the system. The Nyquist-Shannon theorem ensures that any $f_s/2$ band-limited signal can be perfectly reconstructed in the time domain. A variety of fractional delay techniques is documented in literature [258].

distances:

$$\Delta(T_i) = \frac{1}{N}\sum_{j=0}^{N\geq 3}\left(||\vec{B}_j - \vec{T}_i|| - d(\vec{B}_j, \vec{T}_i)\right)^2 . \tag{5.11}$$

The procedures returns a set of calibrated positions for the transducers, $\{T_i^{\text{cal}}\}$.

5.2.4 Beamforming

The beamforming procedure operates as follows. The signals are simulated for a beacon at an arbitrary position $\vec{B}_0$. The simulation delays are calculated according to Equation (5.1) with the real assumed positions $\{T_i\}$. A grid of probe points $\{\vec{P_{jk}}\}$ centered at $\vec{B}_0$ is defined. The pitch of the grid is chosen to resolve an angle smaller than 0,1° at the distance of the beacon. The set of reconstruction delays to be used in the beamforming $\{\tau_i^{\text{rec}}(P_{jk})\}$ is calculated from the calibrated positions of the transducers $\{T_i^{\text{cal}}\}$. The signal of each transducer is delayed and added according to Equation (5.3). The result of the sum, here expressed in terms of samples, $\{A_n\}(P_{jk})$, is cross-correlated with the signal template $\{v_n\}$. A scalar figure of merit for the beamforming result, Q, is defined as the maximum of the cross-correlation:

$$Q(P_{jk}) = \max\{A_n(P_{jk}) \star v_n\} . \tag{5.12}$$

The profile of $Q(P_{jk})$ is evaluated in the reference frame of the detector as a function of the (x, y) or (θ, ϕ) coordinates (where θ and ϕ are the zenith and the azimuth angle, respectively). The position of the Q maximum represents the reconstructed beacon position in the reference frame of the detector. The GPS-calibrated position of the beacon then allows defining an absolute reference for the pointing of the detector. A 3 dB decrease with respect to the maximum the value of Q is defined to determine the pointing resolution.

5.2.5 Operational environment

The hydrophone connected to the DU base is a Colmar DG1330[3]. It has a bandwidth covering the 5 – 90 000 Hz range with a 700 Hz high pass filter, achieving flat response above 5 kHz. Its integrated preamplifier provides two outputs with a 20 dB gain difference. The respective sensitivities are −156 and −176 dB V µPa^{-1}. The acoustic equivalent input noise is 34 dB µPa/$\sqrt{\text{Hz}}$ at 5 kHz.

To estimate the signal-to-noise ratio (SNR) for the receivers, a simplified version of the *sonar equation*, where all the terms are expressed in decibels, is used:

$$\text{SNR} = \text{SL} - \text{TL} - \text{NL} \tag{5.13}$$

where the SL is the *source level*, TL the *transmission loss* and NL the *noise level*. The

3. https://colmaritalia.it/it/prodotti-servizi/idrofoni/idrofono-digitale-dg1330/

transmission loss as a function of the distance, d, is calculated as:

$$\mathrm{TL}(d) = 20\log_{10}(d) + \alpha(f)\,d \tag{5.14}$$

where the first term accounts for the quadratic spreading loss due to the expansion of the spherical wavefront and α represents the frequency-dependent absorption coefficient. The latter is calculated according to the Francois and Garrison model [259, 260] ,that gives a value that varies between 0.2 and 1,3 dB km^{-1} in the 5 – 15 kHz range. Finally, the noise level for a fixed bandwidth, B, is calculated as:

$$\mathrm{NL}(B) = N_{PSD}\,10\log_{10}(B) \tag{5.15}$$

where N_{PSD} is the noise power spectral density typically expressed in dB/$\sqrt{\mathrm{Hz}}$. This is determined by the combination of the equivalent input noise (EIN) of the transducer and the sea ambient noise. For calm sea conditions, the EIN figure of the transducer dominates the ambient noise.

The transducer EIN for a 20 kHz bandwidth is ~ 47 dB. The transmission loss for a 4 km distance at 15 kHz is ~ 78 dB. For a typical source sound pressure level of 190 dB µPa at 1 m the corresponding SNR is ~ 37 dB. This provides a good operational margin.

5.2.6 Simulated measurement

The procedure has been simulated considering the two cases of a set of 3 and 115 transducers respectively. Three non-collinear transducers are the minimum requirement to obtain a localisation of a point on the sea surface. The positions of the transducers are calibrated considering four beacon positions on the x and y axes, for ($x = 0$, $y = \pm 1000$ m) and ($x = \pm 1000$ m, $y = 0$). A noise level of 0.05 compared to a unit peak amplitude of the signal is considered, for an equivalent signal-to-noise ratio of ~ 26 dB. This should be a conservative assumption. In Figure 5.2, an example of the signal template (top panel), the simulated received signal (middle panel) and the result of the cross-correlation with the template (bottom panel) is reported.

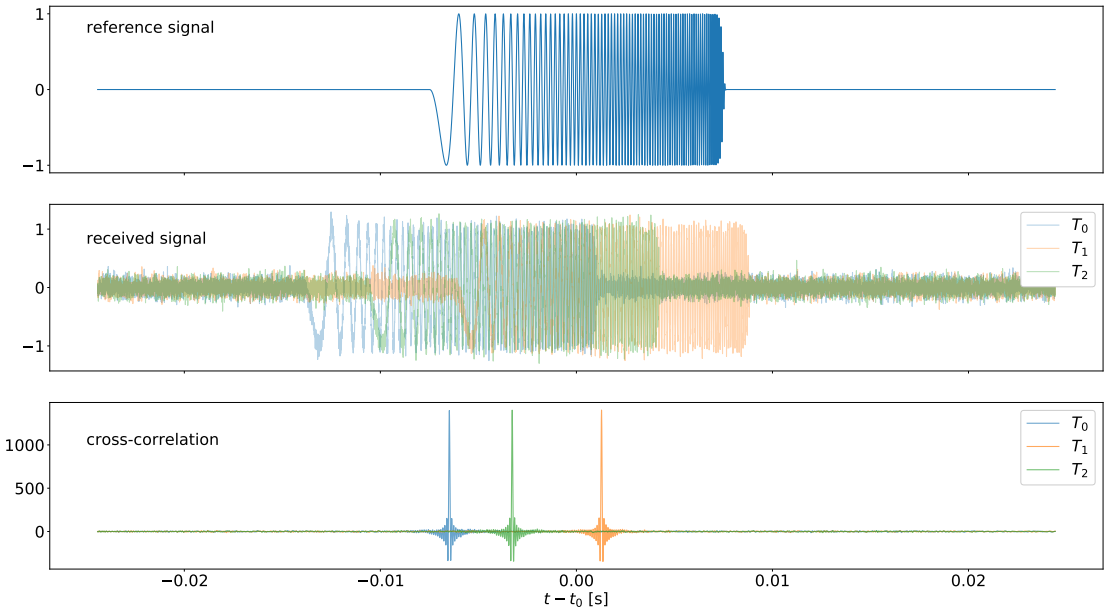

Figure 5.2 – Example of the reference signal (top) and the corresponding simulated signals (middle) for the three transducers nearest to the center of the footprint. The result of the cross-correlation between the received signals and the template is shown (bottom).

The beamforming localisation is performed for a beacon at position ($x = 1000\,\text{m}$, $y = 1000\,\text{m}$). A grid of 100×100 points covering $\pm 1°$ along the x and y axes is evaluated. In Figure 5.3, the value of Q is reported, in units of dB, as a function of the beamforming position. Considering the $-3\,\text{dB}$ contour, the position of the source is reconstructed with a precision of $\sim \pm 0{,}5°$ and $\sim \pm 0{,}1°$ for the case of 3 and 115 transducers respectively.

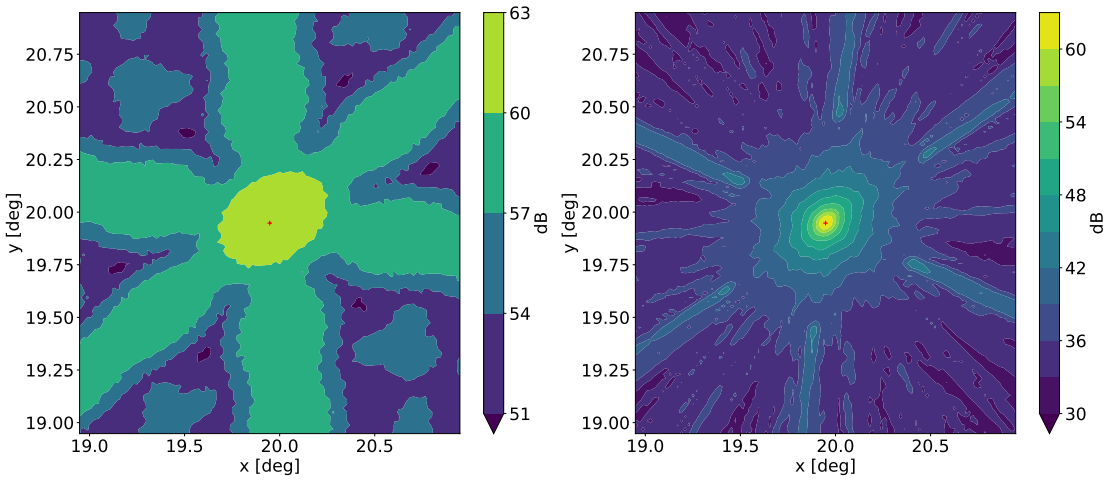

Figure 5.3 – Maximum of the cross-correlation function between the result of the delay-and-sum beamforming and the signal template, divided by the number of transducers. The case for 3 and 115 transducers are reported on the left and right panel respectively. A red cross marker indicates the true position of the beacon.

5.3 Sea survey

On September 9th, 2020, a sea acoustic survey has been conducted on board of the *GG9* vessel of IXBlue. The vessel was been equipped with a GPS-based C-NAV differential global navigation satellite system (GNSS) having real-time-kinematics (RTK) capability [1] and a IXBlue PHINS inertial navigation system [4] (fiber-optic gyroscope) for attitude and heading measurements. The employed acoustic transmission system consists of an IXBlue ECHOES 10000 transducer [5] feeded by a 2 kVA power amplifier and controlled with the IXblue DELPH [6] software platform. A survey of the depth-dependence of the sound velocity has been conducted with a Valeport sound velocity profiler [7]. Figure 5.4 shows photos of the vessel and the acoustic transducer. The data acquisition took place between 10:00 and 12:30 UTC of 09/09. In the following, absolute times will be represented in seconds since `2020-09-09T10:00:00Z`.

1. https://www.oceaneering.com/positioning-solutions/
4. https://www.ixblue.com/products/phins-surface
5. https://www.ixblue.com/sites/default/files/2020-08/Echoes-10000.pdf
6. http://delph.ixblue.com/
7. https://www.valeport.co.uk/product-types/sound-velocity/

Figure 5.4 – The GG9 vessel (left) and the ECHOES 10000 hydroacoustic transducer (right).

The clock of the control software platform was synchronised to the GPS/GNSS time reference. The transmitter has been configured to emit chirps, meant to be received by the KM3NeT acoustic instrumentation. Three hydrophones (out of six) on the bases of three ORCA detection units were functional and correctly operating. Two types of acoustic chirps have been employed, spanning the frequency range between 5 and 15 kHz with a duration of 20 and 100 ms respectively. The survey has been articulated in different segments, in which the boat was either static or moving along a designated path. Depending on the segment, the repetition time of the chirp was set to either one or four seconds.

The analysis of the acoustic data is oriented to precisely estimate the times of the acoustic chirps received by the hydrophones and use their correlation with the known times and position of the emissions, as recorded by the boat navigation system, to determine the position of the receivers. Finally, if the position estimation is sufficiently precise, the beamforming of the received signals can be performed.

5.3.1 Transmitter data

The GPS/GNSS system outputs a *pulse-per-second* (PPS) signal that is used to synchronise the transmitter emission time with high precision. Each chirp is timestamped by the control software platform. In addition to the timestamp, the vessel navigation data are associated to the chirp metadata. The navigation data consist of the ship coordinates, attitude and heading, that in turn are used to determine the transducer position in three dimensions. This information is updated once per second, although is not synchronous with respect to the acoustic emission. The data are stored with the `XTF` binary format, commonly used in sonar systems. The GPS coordinates are given in latitude and longitude, and subsequently converted to the UTM convention (northing and easting in meters, zone 32T).

The segments of the vessel path are drawn in Figure 5.5 in a latitude-longitude plane (right) as well as in UTM coordinates (left). Each arrow represents the boat trajectory and direction. The legend indicates the starting time of the segment. It can be noted that a constant longitude path does not correspond to a constant easting, as expected from the convergence of meridians. In Figure 5.6 the position of the transducer relative

to the center of the detector, and its depth, are plotted as a function of time.

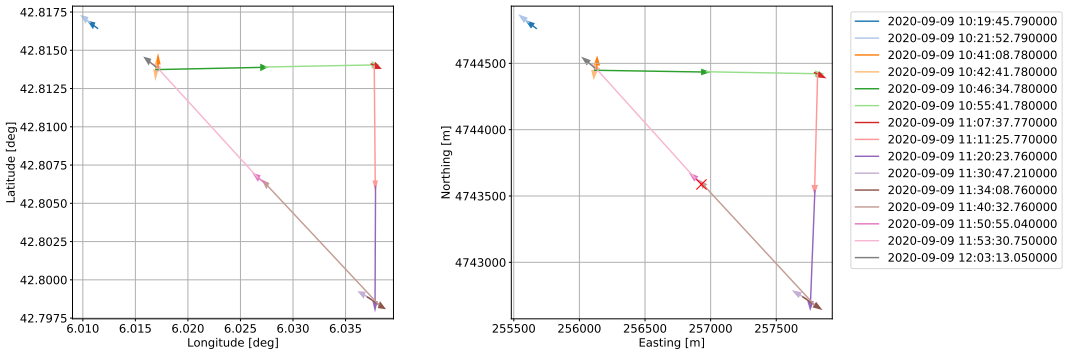

Figure 5.5 – Path of the GG9 vessel during the sea survey of 09-09-2020 in latitude and longitude (left) and northing and easting coordinates for the UTM zone 32T (right). Each arrow indicates the path and direction followed the boat along the survey segment. The legend indicates the UTC start time of the segment. The center of the ORCA detector is marked with a red cross on the right panel.

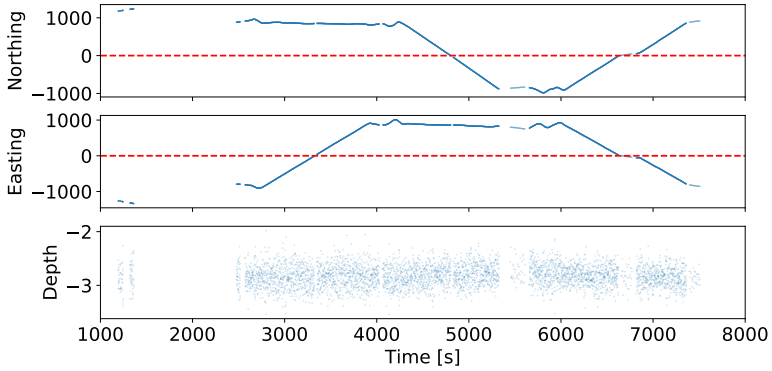

Figure 5.6 – Position of the acoustic transducer as a function of time in relative northing and easting with respect to the center of the detector, and depth from the sea surface. Each point corresponds to the navigational data associated to an acoustic chirp. Time is expressed in seconds since `2020-09-09T10:00:00Z`.

5.3.2 Hydrophone data

In the KM3NeT DAQ, raw acoustic data can be written to disk by the acoustic data filter (ADF, see Section 2.1.2) with dedicated run configurations. The ADF produces files of fixed size, containing six seconds of acoustic data for a single transducer (DU base hydrophone or DOM piezoelectric transducer). In this analysis, only the hydrophones are taken in consideration. The acoustic data are stored in a binary

format, containing UTC timestamps and sequences of acoustic samples with a 32 bit pulse code modulation (PCM) encoding. The sampling frequency is 195 312,5 Hz, corresponding to 5,12 µs per sample and a useful bandwidth of ~ 97,5 kHz. As a first step of the analysis, the data are numerically filtered with a Butterworth 4th order band-pass, with a pass band of 2.5 – 30 kHz, leaving an octave of margin around the chirp extension in frequency. To determine the time of the received acoustic chirps, the stream is cross-correlated independently with the two signal templates corresponding to the 20 ms and 100 ms chirps, respectively. For better computational efficiency, the cross-correlation is performed in the frequency domain. In order to determine the peak time, the module of the Hilbert transform of the cross-correlation is considered. This results in a strictly positive analytic function, over which the final peak search is applied. Peaks with a minimum arbitrary height of 5.0 and distant at least 0,75 s one from each other are selectet to identify a *detected chirp*. For each peak, the absolute time and the height (*quality factor*) are stored. A segment of acoustic data containing two chirps is represented in Figure 5.7, focusing on different timescales across the different processing steps. The suppression of low-frequency noise by the filtering is well visible in the top and middle panels. A detail of the cross-correlation and Hilbert transform (module) is shown on the bottom panel. The relation between the envelope of the cross-correlation and the peak of the Hilbert transform can be appreciated.

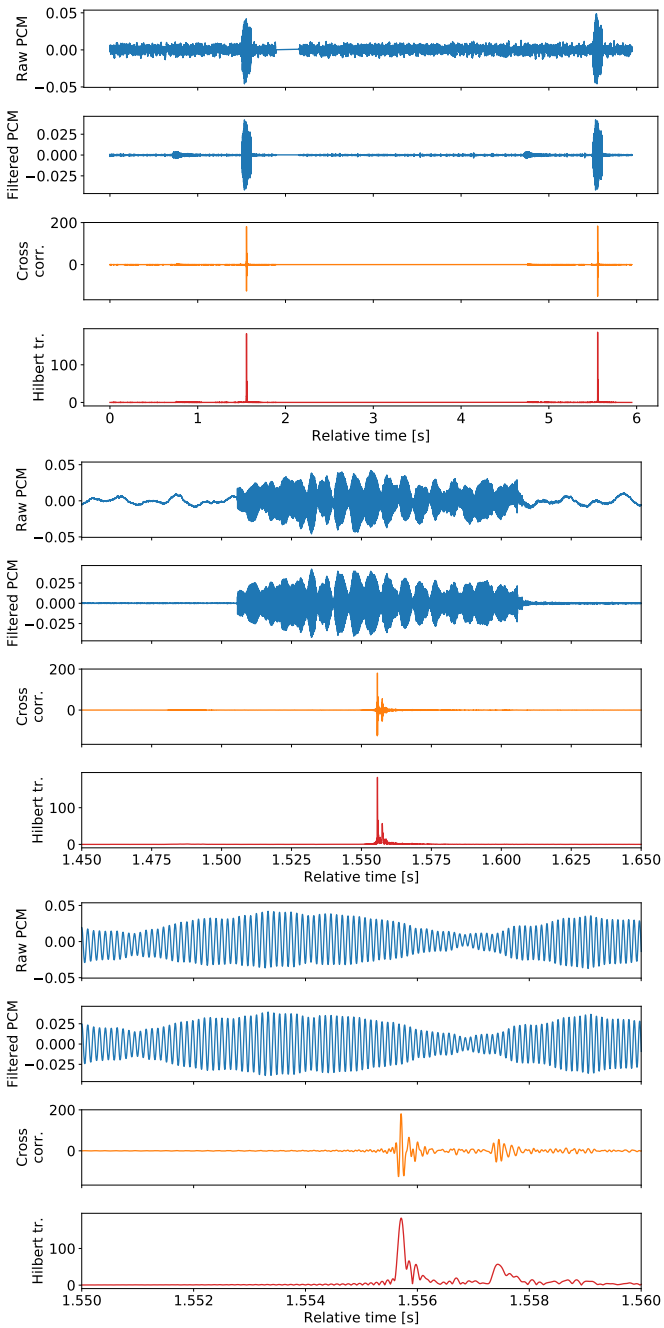

Figure 5.7 – Raw acoustic data from a KM3NeT hydrophone on the sea bottom before and after processing through a 4th-order Butterworth bandpass filter, a cross-correlation with the signal template and a Hilbert transform (module). The signal envelope is shown on three time scales: six seconds, being the entire content of a single data file (top); 200 ms centered on a 100 ms chirp (middle) and 10 ms centered on the peak of the cross correlation (bottom). The time axis is relative to the first sample in the file.

All the data acquired by the KM3NeT hydrophones during the time frame corresponding to the survey are analysed. The search for acoustic chirps is conducted with the two signal templates (20 ms and 100 ms) regardless of the configuration of the transmitter in the corresponding segment. This allows an unbiased and uniform approach in the processing of the data, largely simplifying book-keeping and reducing the possibility of errors. The quality factor of the peaks is given in arbitrary units, and it is in general proportional to the length of the chirp. The distribution of the peak qualities for the 20 ms and 100 ms detected chirps is evaluated after normalising to their duration, and is shown in Figure 5.8. For each of the two distributions, two distinct (spurious) populations can be observed near the low-end of the quality range. The first represents the background floor, while the second comes from the cross-matching between signal and a template of different durations (i.e. a 100 ms chirp and a 20 ms template, or vice-versa). A selection of detected chirps with normalised quality above 0.5 (highlighted with a vertical red line) is adopted for the next step of the analysis.

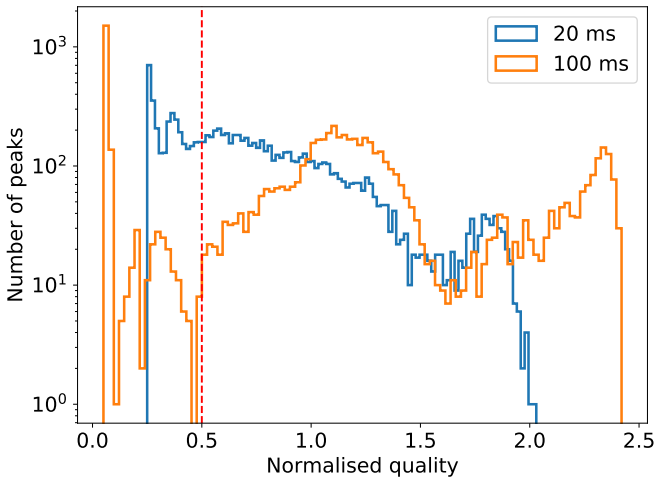

Figure 5.8 – Number of detected chirps as a function of the quality factor, normalised to the chirp duration. The quality factor has otherwise an arbitrary absolute scale. The chosen quality threshold is indicated with a vertical red line.

After the quality selection, the data on the 20 ms and 100 ms series of detected chirps are analysed separately. A search for coincident chirps on the three active hydrophones is performed. A triplet of chirps received within 0,1 s on the three hydrophones is defined as an *received event*. A deliberately large time window is adopted in order to verify the robustness of the quality selection. If more than three chirps are found in 100 ms (~ 1.2% of the occurrences) the event is discarded. A total of ~ 2000 100 ms events and ~ 1650 20 ms events is found in the data. In Figure 5.9, the progression of 20 ms and 100 ms events as a function of time is reported. The normalised quality is represented with a separate color scale for each of the two chirp types. The plot shows

no overlap between the two series of events, and a uniform progression within each segment of the survey. The slope of each sequence is inversely proportional to the repetition time. The detected chirps show naturally an increase in quality with the proximity of the vessel to the center of the detector (cf. Figure 5.6).

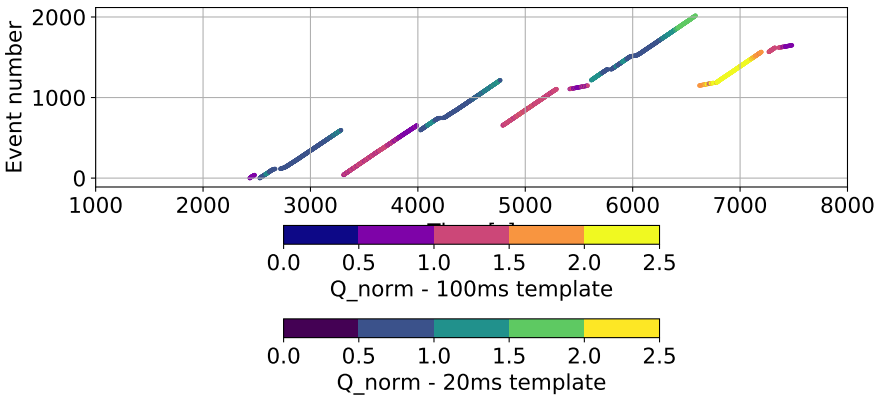

Figure 5.9 – Progressive number of the event as a function of time for 20 ms and 100 ms series, with the normalised quality represented by different color scales. Time is expressed in seconds since 2020-09-09T10:00:00Z.

5.3.3 Transmitter - hydrophones correlation

The received events are correlated with the transmitter data in order to associate an time and position of origin to each detected chirp. For this, the time of an event is determined as the average of the times of the chirp detection at the three transducers. For each chirp timestamp recorded by the transmitter control system, a corresponding event is searched in a $+1.8 \pm 0.5$s time window with respect to the transmission time. This is sufficiently ample to cover all the distances between the transmitter and the three receivers along the survey path. A total of 3377 correspondences is found, with no occurrence of more than one received event in a time window. In a first approximation, the measured average delay should be directly proportional to the distance between the transmitter and the center of the detector. In Figure 5.10 the measured delay, the distance from the center of the detector and a corresponding estimate of the sound velocity are shown as a function of the time of the event.

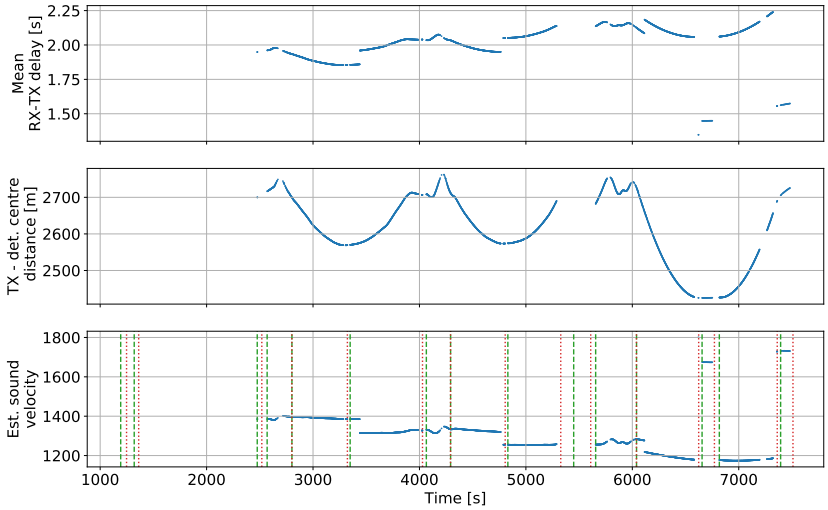

Figure 5.10 – Mean delay between reception times and emission time (top), distance between the transmitter and the center of the detector (middle) and corresponding estimated sound velocity (bottom) as a function of the emission time of the chirp. On the bottom panel, the vertical green and red lines indicate the start and end time of each segment (cf. Figure 5.5).

The estimated sound velocity should be constant, with variations below one percent as a function of the zenith angle to the detector. The values found for the delays, and therefore for the estimated sound velocity, are inconsistent with an expectation of $\sim 1500-1530\,\mathrm{ms}^{-1}$. The apparent inconsistency between the different segments of the survey suggest an issue with the reliability of the transmission timestamp, that seems to be affected by discontinuities as well as drifting behaviours. A straightforward triangulation assuming known time and position of the emission cannot be applied to these data. The study will be continued with a future sea campaign.

5.4 Preliminary conclusions

A *proof-of-concept* for the determination of the absolute pointing of the detector through acoustic multilateration and beamforming techniques has been proposed. This aims to reach an accuracy on the absolute orientation of the detector footprint at the sub-0,1° level. An acoustic survey with a transmitter on the sea surface has been conducted in order to evaluate the feasibility of the approach. The analysis of the data acquired with the KM3NeT acoustic instrumentation points to a timing issue with the transmitter control system. A new sea campaign will be planned for the development of the study.

Conclusion

The role of next-generation neutrino telescopes will be central to the near-future progress of particle physics and multi-messenger astrophysics. The KM3NeT ARCA and ORCA deep-sea detectors, currently under construction, will address fundamental questions on the sources of astrophysical neutrinos and the neutrino intrinsic properties. At the time of writing, KM3NeT has been operating with the first eight detection units deployed between 2016 and 2020 across the two sites.

An early analysis of the data from the first three KM3NeT detection units (two for ARCA and one for ORCA) has allowed for the verification of the detector performance as well as the tuning and validation of the optical module time and efficiency calibration procedures. Using KM3NeT optical modules as stand-alone muon detectors, selecting coincidences with at least eight hit PMTs, the rate of atmospheric muons has been measured on a depth range between 2200 and 3500 m underwater. The high precision reached in the probing of the flux depth dependence confirms the goodness of the PMT efficiency calibration used to correct the measured rates. Besides, the development of this study has brought several improvements to the detector simulation framework. The good agreement of the measurement with the prediction by a state-of-the-art flux model confirms that the simulation framework reflects a good understanding of the detector behaviour. This analysis has been the subject of the first publication based on KM3NeT data [163]. Due to its high sensitivity to the individual DOM behaviour, this analysis can be integrated as part of the long-term monitoring of the detector performance. With the application of a time-dependent efficiency correction, the technique could be applied to observe the seasonal modulation of the atmospheric muon flux.

The potential of KM3NeT to detect a low-energy core-collapse supernova (CCSN) neutrino burst has been evaluated. This work is the subject of a first paper, currently at the stage of internal review by the Collaboration. The detection strategy relies on the observation of a population of coincidences above the background expectation over the typical time scale of the supernova accretion phase. The contributions to the background from bioluminescence, radioactive decays in seawater and atmospheric muons have been characterised. The multi-PMT design of KM3NeT digital optical modules (DOM) is exploited to define an event selection through the distribution of coincidences as a function of the number of PMT hit in coincidence. Data from the first eight deployed detection units of KM3NeT in the ARCA and ORCA sites have been analysed to study the background features. State-of-the-art flux models have been considered in a detailed simulation of the detector response, from which the signal expectation for CCSN neutrinos in KM3NeT has been estimated. A filtering method

has been developed to reject correlated background events from atmospheric muons. The event selection achieving the best sensitivity has been determined. Combining ARCA and ORCA sensitivities, KM3NeT reaches a 5σ discovery potential for more than 95% of the galactic CCSN progenitors, under the most conservative assumption on the flux magnitude. For the most optimistic model considered, the sensitivity reaches the Large Magellanic Cloud. These analysis algorithms have been implemented in a real-time software framework. Since the first months of 2019, the data of the ARCA and ORCA detectors are processed online with a sliding time window of 500 ms, updated every 100 ms, to search for the signature of a CCSN neutrino burst. A dedicated application combines the result of the online processing of the two detectors in a single time-dependent significance figure. This acts as an input for an alert generation and management pipeline. The system has been integrated with the global *Supernova Neutrino Early Warning System* (SNEWS). In parallel, low-level data are buffered to exploit the full coincidence statistics in the follow-up of external alerts or internal triggers. The first follow-up analyses for gravitational wave events have been performed with a manual procedure, based on the retrieval of the *offline* data. As a result, the first public circulars by the KM3NeT Collaboration have been distributed through the GCN global alert network. An automatisation of the alert follow-up, to be integrated with the current pipeline, is foreseen. The buffered data also allow for the implementation of automatised *quasi-online* analyses, including the determination of the precise time of arrival of the supernova neutrino burst, and the real-time sharing of the light-curve data. These will be instrumental to the participation of KM3NeT in the SNEWS2.0 science program, aiming to combine in real-time the astronomy and astrophysics capabilities of different detectors. A triangulation method to localise the CCSN from the combination of experimental data has been proposed in a dedicated publication [252]. Besides, the approach here developed for the detection of CCSN neutrinos is applicable to any neutrino flux on the $1-100$ MeV range. The real-time and offline analyses can be extended to other types of astrophysical transients or variable sources, as fast-radio-bursts and pulsars. The gravitational-wave follow-ups will continue with the 2021-22 *O4* observation period of the Advanced LIGO, Virgo and KAGRA interferometers.

The absolute pointing accuracy of KM3NeT is crucial to the full exploitation of its angular resolution, that reaches the sub-tenth-of-degree level in the case of the ARCA track reconstruction. A *proof-of-concept* for the determination of the absolute pointing of the detector through acoustic multilateration and beamforming techniques has been proposed. Using an acoustic beacon on the sea surface, this should allow establishing the accuracy of the absolute orientation of the detector footprint at the sub-0,1° level. Some simplifying assumptions have been adopted to test the approach in a simulated setup. A measurement campaign at sea has been performed, followed by the development of the acoustic data analysis. The obtained results point to an issue with the time reference of the acoustic transmitter. A new campaign is be foreseen to further develop the study.

Bibliography

[1] Victor Hess. “On the Observations of the Penetrating Radiation during Seven Balloon Flights”. In: (2018). arXiv: 1808.02927 [physics.hist-ph] (cit. on pp. 22, 23).

[2] Per Carlson and Alessandro De Angelis. “Nationalism and internationalism in science: the case of the discovery of cosmic rays”. In: *Eur. Phys. J.* H35 (2010), pp. 309–329. DOI: 10.1140/epjh/e2011-10033-6. arXiv: 1012.5068 [physics.hist-ph] (cit. on p. 22).

[3] M. Tanabashi et al. “Review of Particle Physics”. In: *Phys. Rev.* D98.3 (2018), p. 030001. DOI: 10.1103/PhysRevD.98.030001 (cit. on pp. 23, 27, 30).

[4] Thomas K. Gaisser, Ralph Engel, and Elisa Resconi. *Cosmic Rays and Particle Physics*. 2nd ed. Cambridge University Press, 2016. DOI: 10.1017/CBO9781139192194 (cit. on pp. 23, 27).

[5] Thomas K. Gaisser. “Outstanding problems in particle astrophysics”. In: *International School of Cosmic Ray Astrophysics: 14th Course: Neutrinos and Explosive Events in the Universe: A NATO Advanced Study Institute*. Jan. 2005, pp. 3–31. arXiv: astro-ph/0501195 (cit. on pp. 23, 25, 29).

[6] Maurice M Shapiro and Rein Silberberg. “Heavy Cosmic Ray Nuclei”. In: *Annual Review of Nuclear Science* 20.1 (1970), pp. 323–392. DOI: 10.1146/annurev.ns.20.120170.001543. URL: https://doi.org/10.1146/annurev.ns.20.120170.001543 (cit. on pp. 23, 25).

[7] R. Ramaty, E. Vangioni-Flam, M. Casse, et al. “Libeb, cosmic rays and gamma-ray line astronomy”. In: *Publ. Astron. Soc. Pac.* 111 (1999), p. 651. DOI: 10.1086/316355. arXiv: astro-ph/9901073 (cit. on p. 24).

[8] Giovanni Morlino. “High Energy Cosmic Rays From Supernovae”. In: (Nov. 2016). DOI: 10.1007/978-3-319-20794-0_11-1. arXiv: 1611.10054 [astro-ph.HE] (cit. on p. 24).

[9] E.C. Stone et al. “The advanced composition explorer”. In: *AIP Conf. Proc.* 203 (1990). Ed. by W.V. Jones, J.F. Ormes, and F.J. Kerr, pp. 48–57. DOI: 10.1063/1.39173 (cit. on p. 26).

[10] A.M. Galper et al. “The PAMELA experiment: a decade of Cosmic Ray Physics in space”. In: *J. Phys. Conf. Ser.* 798.1 (2017). Ed. by Arkady Galper, Anatoly Petrukhin, Arkady Taranenko, et al., p. 012033. DOI: 10.1088/1742-6596/798/1/012033 (cit. on p. 26).

[11] R. Battiston. "The Alpha magnetic spectrometer (AMS): Search for antimatter and dark matter on the International Space Station". In: *Nucl. Phys. B Proc. Suppl.* 65 (1998), pp. 19–26. DOI: 10.1016/S0920-5632(97)00970-5. arXiv: hep-ex/9708039 (cit. on p. 26).

[12] H.S. Ahn et al. "The Cosmic Ray Energetics And Mass (CREAM) instrument". In: *Nucl. Instrum. Meth. A* 579 (2007), pp. 1034–1053. DOI: 10.1016/j.nima.2007.05.203 (cit. on p. 26).

[13] Alan Cummings, Edward Stone, Bryant C. Heikkila, et al. "Voyager 1 Observations of Galactic Cosmic Rays in the Local Interstellar Medium: Energy Density and Ionization Rates". In: *PoS* ICRC2015 (2016), p. 318. DOI: 10.22323/1.236.0318 (cit. on p. 26).

[14] Edward C. Stone, Alan C. Cummings, Bryant C. Heikkila, et al. "Cosmic ray measurements from Voyager 2 as it crossed into interstellar space". In: *Nature Astronomy* 3.11 (Nov. 2019), pp. 1013–1018. ISSN: 2397-3366. DOI: 10.1038/s41550-019-0928-3. URL: https://doi.org/10.1038/s41550-019-0928-3 (cit. on p. 26).

[15] M. Amenomori. "Northern sky Galactic Cosmic Ray anisotropy between 10-1000 TeV with the Tibet Air Shower Array". In: *Astrophys. J.* 836.2 (2017), p. 153. DOI: 10.3847/1538-4357/836/2/153. arXiv: 1701.07144 [astro-ph.HE] (cit. on p. 27).

[16] Cheng-Rui Zhu, Qiang Yuan, and Da-Ming Wei. "Studies on cosmic ray nuclei with Voyager, ACE and AMS-02: I. local interstellar spectra and solar modulation". In: *Astrophys. J.* 863.2 (2018), p. 119. DOI: 10.3847/1538-4357/aacff9. arXiv: 1807.09470 [astro-ph.HE] (cit. on p. 28).

[17] Karl-Heinz Kampert, Alan A. Watson, and Alan A. Watson. "Extensive Air Showers and Ultra High-Energy Cosmic Rays: A Historical Review". In: *Eur. Phys. J. H* 37 (2012), pp. 359–412. DOI: 10.1140/epjh/e2012-30013-x. arXiv: 1207.4827 [physics.hist-ph] (cit. on p. 28).

[18] P Sommers. "Experimental aspects of cosmic rays". In: (2006). DOI: 10.5170/CERN-2006-015.177. URL: http://cds.cern.ch/record/1017823 (cit. on pp. 28, 29).

[19] T. K. Gaisser and A. M. Hillas. "Reliability of the Method of Constant Intensity Cuts for Reconstructing the Average Development of Vertical Showers". In: *International Cosmic Ray Conference*. Vol. 8. International Cosmic Ray Conference. Jan. 1977, p. 353 (cit. on p. 28).

[20] M. Amenomori et al. "Cosmic-ray energy spectrum around the knee obtained by the Tibet experiment and future prospects". In: *Adv. Space Res.* 47 (2011), pp. 629–639. DOI: 10.1016/j.asr.2010.08.029 (cit. on p. 29).

[21] T Antoni et al. “The Cosmic ray experiment KASCADE”. In: *Nucl. Instrum. Meth. A* 513 (2003), pp. 490–510. DOI: 10.1016/S0168-9002(03)02076-X (cit. on p. 29).

[22] R.M. Baltrusaitis et al. “THE UTAH FLY’S EYE DETECTOR”. In: *Nucl. Instrum. Meth. A* 240 (1985), pp. 410–428. DOI: 10.1016/0168-9002(85)90658-8 (cit. on p. 29).

[23] R.U. Abbasi et al. “Measurement of the flux of ultrahigh energy cosmic rays from monocular observations by the High Resolution Fly’s Eye experiment”. In: *Phys. Rev. Lett.* 92 (2004), p. 151101. DOI: 10.1103/PhysRevLett.92.151101. arXiv: astro-ph/0208243 (cit. on p. 29).

[24] H. Kawai et al. “Telescope array experiment”. In: *Nucl. Phys. B Proc. Suppl.* 175-176 (2008). Ed. by Kwong Sang Cheng, Ralph Engel, Bryan Pattison, et al., pp. 221–226. DOI: 10.1016/j.nuclphysbps.2007.11.002 (cit. on p. 29).

[25] J. Abraham et al. “Properties and performance of the prototype instrument for the Pierre Auger Observatory”. In: *Nucl. Instrum. Meth. A* 523 (2004), pp. 50–95. DOI: 10.1016/j.nima.2003.12.012 (cit. on p. 29).

[26] Lyndon Evans and Philip Bryant. “LHC Machine”. In: *JINST* 3 (2008), S08001. DOI: 10.1088/1748-0221/3/08/S08001 (cit. on p. 29).

[27] B. Peters. “Primary cosmic radiation and extensive air showers”. In: *Il Nuovo Cimento* 22.4 (Nov. 1961), pp. 800–819. DOI: 10.1007/BF02783106 (cit. on p. 29).

[28] V. Berezinsky, A.Z. Gazizov, and S.I. Grigorieva. “On astrophysical solution to ultrahigh-energy cosmic rays”. In: *Phys. Rev. D* 74 (2006), p. 043005. DOI: 10.1103/PhysRevD.74.043005. arXiv: hep-ph/0204357 (cit. on p. 31).

[29] Veniamin Berezinsky, A. Gazizov, and S. Grigorieva. “Propagation and signatures of ultra high energy cosmic rays”. In: *Nucl. Phys. B Proc. Suppl.* 136 (2004). Ed. by C. Aramo, A. Insolia, and C. Tuve, pp. 147–158. DOI: 10.1016/j.nuclphysbps.2004.10.063. arXiv: astro-ph/0410650 (cit. on p. 31).

[30] D. Allard, Etienne Parizot, E. Khan, et al. “UHE nuclei propagation and the interpretation of the ankle in the cosmic-ray spectrum”. In: *Astron. Astrophys.* 443 (2005), pp. L29–L32. DOI: 10.1051/0004-6361:200500199. arXiv: astro-ph/0505566 (cit. on p. 31).

[31] Denis Allard, A.V. Olinto, and E. Parizot. “Signatures of the extragalactic cosmic-ray source composition from spectrum and shower depth measurements”. In: *Astron. Astrophys.* 473 (2007), pp. 59–66. DOI: 10.1051/0004-6361:20077478. arXiv: astro-ph/0703633 (cit. on p. 31).

[32] A A Watson. “High-energy cosmic rays and the Greisen–Zatsepin–Kuz’min effect”. In: *Rept. Prog. Phys.* 77 (2014), p. 036901. DOI: 10.1088/0034-4885/77/3/036901. arXiv: 1310.0325 [astro-ph.HE] (cit. on p. 31).

[33] Kenneth Greisen. "End to the cosmic ray spectrum?" In: *Phys. Rev. Lett.* 16 (1966), pp. 748–750. DOI: 10.1103/PhysRevLett.16.748 (cit. on p. 31).

[34] G.T. Zatsepin and V.A. Kuzmin. "Upper limit of the spectrum of cosmic rays". In: *JETP Lett.* 4 (1966), pp. 78–80 (cit. on p. 31).

[35] Antonella Castellina. "AugerPrime: the Pierre Auger Observatory Upgrade". In: *EPJ Web Conf.* 210 (2019). Ed. by I. Lhenry-Yvon, J. Biteau, O. Biteau, et al., p. 06002. DOI: 10.1051/epjconf/201921006002. arXiv: 1905.04472 [astro-ph.HE] (cit. on p. 32).

[36] Yoshiyuki Takahashi. "The JEM-EUSO mission". In: *New J. Phys.* 11 (2009), p. 065009. DOI: 10.1088/1367-2630/11/6/065009. arXiv: 0910.4187 [astro-ph.HE] (cit. on p. 32).

[37] R.J. Protheroe. "Origin and propagation of the highest energy cosmic rays". In: *International School of Cosmic Ray Astrophysics: 10th Course: Toward the Millennium in Astrophysics: Problems and Prospects*. June 1996, pp. 3–29. arXiv: astro-ph/9612212 (cit. on pp. 32–34, 37, 38).

[38] Enrico Fermi. "On the Origin of the Cosmic Radiation". In: *Phys. Rev.* 75 (1949), pp. 1169–1174. DOI: 10.1103/PhysRev.75.1169 (cit. on p. 32).

[39] E. Fermi. "Galactic Magnetic Fields and the Origin of Cosmic Radiation." In: *Astrophys. J.* 119 (1954), pp. 1–6. DOI: 10.1086/145789 (cit. on p. 32).

[40] E.M. de Gouveia Dal Pino and A. Lazarian. "Production of the large scale superluminal ejections of the microquasar GRS 1915+105 by violent magnetic reconnection". In: (July 2003). arXiv: astro-ph/0307054 (cit. on p. 35).

[41] Elisabete M. de Gouveia Dal Pino, Rafael Alves Batista, Luis S. Kadowaki, et al. "Magnetic Reconnection, Cosmic Ray Acceleration, and Gamma-Ray emission around Black Holes and Relativistic Jets". In: *PoS* BHCB2018 (2018). Ed. by Rita Cassia Anjos and Carlos Henrique Coimbra Araujo, p. 008. arXiv: 1903.08982 [astro-ph.HE] (cit. on p. 35).

[42] A.M. Hillas. "The Origin of Ultrahigh-Energy Cosmic Rays". In: *Ann. Rev. Astron. Astrophys.* 22 (1984), pp. 425–444. DOI: 10.1146/annurev.aa.22.090184.002233 (cit. on pp. 35, 36).

[43] M. Kachelriess. "Lecture notes on high energy cosmic rays". In: (2008). arXiv: 0801.4376 [astro-ph] (cit. on p. 35).

[44] M. G. Aartsen et al. "Astrophysical neutrinos and cosmic rays observed by IceCube". In: *Adv. Space Res.* 62 (2018), pp. 2902–2930. DOI: 10.1016/j.asr.2017.05.030. arXiv: 1701.03731 [astro-ph.HE] (cit. on pp. 36, 40, 70, 71, 74).

[45] U.F. Katz and Ch. Spiering. "High-Energy Neutrino Astrophysics: Status and Perspectives". In: *Prog. Part. Nucl. Phys.* 67 (2012), pp. 651–704. DOI: 10.1016/j.ppnp.2011.12.001. arXiv: 1111.0507 [astro-ph.HE] (cit. on p. 37).

[46] R.J. Protheroe and P.A. Johnson. "Propagation of ultrahigh-energy protons over cosmological distances and implications for topological defect models". In: *Astropart. Phys.* 4 (1996), p. 253. DOI: 10.1016/0927-6505(95)00039-9. arXiv: astro-ph/9506119 (cit. on p. 37).

[47] S. Hummer, M. Ruger, F. Spanier, et al. "Simplified models for photohadronic interactions in cosmic accelerators". In: *Astrophys. J.* 721 (2010), pp. 630–652. DOI: 10.1088/0004-637X/721/1/630. arXiv: 1002.1310 [astro-ph.HE] (cit. on p. 38).

[48] Imre Bartos and Marek Kowalski. *Multimessenger Astronomy*. 2399-2891. IOP Publishing, 2017. ISBN: 978-0-7503-1369-8. DOI: 10.1088/978-0-7503-1369-8. URL: http://dx.doi.org/10.1088/978-0-7503-1369-8 (cit. on pp. 39, 40).

[49] W.B. Atwood et al. "The Large Area Telescope on the Fermi Gamma-ray Space Telescope Mission". In: *Astrophys. J.* 697 (2009), pp. 1071–1102. DOI: 10.1088/0004-637X/697/2/1071. arXiv: 0902.1089 [astro-ph.IM] (cit. on p. 40).

[50] T.C. Weekes et al. "VERITAS: The Very energetic radiation imaging telescope array system". In: *Astropart. Phys.* 17 (2002), pp. 221–243. DOI: 10.1016/S0927-6505(01)00152-9. arXiv: astro-ph/0108478 (cit. on p. 40).

[51] E. Lorenz. "Status of the 17-m MAGIC telescope". In: *New Astron. Rev.* 48 (2004), pp. 339–344. DOI: 10.1016/j.newar.2003.12.059 (cit. on p. 40).

[52] G. Vasileiadis. "The HESS experimental project". In: *Nucl. Instrum. Meth. A* 553 (2005). Ed. by J. Engelfried and G. Paic, pp. 268–273. DOI: 10.1016/j.nima.2005.08.056 (cit. on p. 40).

[53] M. Actis et al. "Design concepts for the Cherenkov Telescope Array CTA: An advanced facility for ground-based high-energy gamma-ray astronomy". In: *Exper. Astron.* 32 (2011), pp. 193–316. DOI: 10.1007/s10686-011-9247-0. arXiv: 1008.3703 [astro-ph.IM] (cit. on p. 40).

[54] G. Sinnis. "MILAGRO: A low-energy threshold extensive air shower array". In: *Nucl. Phys. B Proc. Suppl.* 43 (1995). Ed. by S.J. Seestrom, pp. 141–144. DOI: 10.1016/0920-5632(95)00465-L (cit. on p. 40).

[55] A.U. Abeysekara et al. "The HAWC Gamma-Ray Observatory: Design, Calibration, and Operation". In: (Sept. 2013). arXiv: 1310.0074 [astro-ph.IM] (cit. on p. 40).

[56] Cao Zhen et al. "Introduction to Large High Altitude Air Shower Observatory (LHAASO)". In: *Chin. Astron. Astrophys.* 43 (2019), pp. 457–478. DOI: 10.1016/j.chinastron.2019.11.001 (cit. on p. 40).

[57] M. Ackermann et al. "Fermi-LAT Observations of the Diffuse Gamma-Ray Emission: Implications for Cosmic Rays and the Interstellar Medium". In: *Astrophys. J.* 750 (2012), p. 3. DOI: 10.1088/0004-637X/750/1/3. arXiv: 1202.4039 [astro-ph.HE] (cit. on p. 41).

[58] R. Atkins et al. “Evidence for TeV gamma-ray emission from the galactic plane”. In: *Phys. Rev. Lett.* 95 (2005), p. 251103. DOI: 10.1103/PhysRevLett.95.251103. arXiv: astro-ph/0502303 (cit. on p. 42).

[59] Tijana Prodanovic, Brian D. Fields, and John F. Beacom. “Diffuse gamma rays from the galactic plane: probing the GeV excess and identifying the TeV excess”. In: *Astropart. Phys.* 27 (2007), pp. 10–20. DOI: 10.1016/j.astropartphys.2006.08.007. arXiv: astro-ph/0603618 (cit. on p. 42).

[60] F. Aharonian et al. “Discovery of very-high-energy gamma-rays from the galactic centre ridge”. In: *Nature* 439 (2006), pp. 695–698. DOI: 10.1038/nature04467. arXiv: astro-ph/0603021 (cit. on p. 42).

[61] A. Abramowski et al. “Acceleration of petaelectronvolt protons in the Galactic Centre”. In: *Nature* 531 (2016), p. 476. DOI: 10.1038/nature17147. arXiv: 1603.07730 [astro-ph.HE] (cit. on p. 42).

[62] Claire Guépin, Lucia Rinchiuso, Kumiko Kotera, et al. “Pevatron at the Galactic Center: Multi-Wavelength Signatures from Millisecond Pulsars”. In: *JCAP* 07 (2018), p. 042. DOI: 10.1088/1475-7516/2018/07/042. arXiv: 1806.03307 [astro-ph.HE] (cit. on p. 42).

[63] Daniele Gaggero, Dario Grasso, Antonio Marinelli, et al. “The gamma-ray and neutrino sky: A consistent picture of Fermi-LAT, Milagro, and IceCube results”. In: *Astrophys. J. Lett.* 815.2 (2015), p. L25. DOI: 10.1088/2041-8205/815/2/L25. arXiv: 1504.00227 [astro-ph.HE] (cit. on p. 42).

[64] Meng Su, Tracy R. Slatyer, and Douglas P. Finkbeiner. “Giant Gamma-ray Bubbles from Fermi-LAT: AGN Activity or Bipolar Galactic Wind?” In: *Astrophys. J.* 724 (2010), pp. 1044–1082. DOI: 10.1088/0004-637X/724/2/1044. arXiv: 1005.5480 [astro-ph.HE] (cit. on p. 42).

[65] Gregory Dobler, Douglas P. Finkbeiner, Ilias Cholis, et al. “The Fermi Haze: A Gamma-Ray Counterpart to the Microwave Haze”. In: *Astrophys. J.* 717 (2010), pp. 825–842. DOI: 10.1088/0004-637X/717/2/825. arXiv: 0910.4583 [astro-ph.HE] (cit. on p. 42).

[66] M. Ackermann et al. “The Spectrum and Morphology of the *Fermi* Bubbles”. In: *Astrophys. J.* 793.1 (2014), p. 64. DOI: 10.1088/0004-637X/793/1/64. arXiv: 1407.7905 [astro-ph.HE] (cit. on p. 42).

[67] H.Y.K. Yang, M. Ruszkowski, and E. Zweibel. “Unveiling the Origin of the Fermi Bubbles”. In: *Galaxies* 6.1 (2018), p. 29. DOI: 10.3390/galaxies6010029. arXiv: 1802.03890 [astro-ph.HE] (cit. on p. 42).

[68] S. Abdollahi et al. “*Fermi* Large Area Telescope Fourth Source Catalog”. In: *Astrophys. J. Suppl.* 247.1 (2020), p. 33. DOI: 10.3847/1538-4365/ab6bcb. arXiv: 1902.10045 [astro-ph.HE] (cit. on p. 43).

[69] Scott P. Wakely and Deirdre Horan. "TeVCat: An online catalog for Very High Energy Gamma-Ray Astronomy". In: *30th International Cosmic Ray Conference*. Vol. 3. July 2007, pp. 1341–1344 (cit. on p. 43).

[70] A.U. Abeysekara et al. "The 2HWC HAWC Observatory Gamma Ray Catalog". In: *Astrophys. J.* 843.1 (2017), p. 40. DOI: 10.3847/1538-4357/aa7556. arXiv: 1702.02992 [astro-ph.HE] (cit. on p. 43).

[71] Kaya Mori et al. "Multiwavelength Observations of 2HWC J1928+177: Dark Accelerator or New TeV Gamma-Ray Binary?" In: *Astrophys. J.* 897.2 (2020), p. 129. DOI: 10.3847/1538-4357/ab9631. arXiv: 2005.12343 [astro-ph.HE] (cit. on p. 43).

[72] Takaaki Tanaka et al. "Study of Nonthermal Emission from SNR RX J1713.7-3946 with Suzaku". In: *Astrophys. J.* 685 (2008), p. 988. DOI: 10.1086/591020. arXiv: 0806.1490 [astro-ph] (cit. on pp. 43, 45).

[73] F. Aharonian. "Primary particle acceleration above 100 TeV in the shell-type Supernova Remnant RX J1713.7-3946 with deep H.E.S.S. observations". In: *Astron. Astrophys.* 464 (2007), pp. 235–243. DOI: 10.1051/0004-6361:20066381. arXiv: astro-ph/0611813 [astro-ph] (cit. on p. 44).

[74] H. Abdalla et al. "H.E.S.S. observations of RX J1713.7−3946 with improved angular and spectral resolution: Evidence for gamma-ray emission extending beyond the X-ray emitting shell". In: *Astron. Astrophys.* 612 (2018), A6. DOI: 10.1051/0004-6361/201629790. arXiv: 1609.08671 [astro-ph.HE] (cit. on p. 46).

[75] Adam S. Burrows. "Baade and Zwicky: "Super-novae," neutron stars, and cosmic rays". In: *Proceedings of the National Academy of Sciences* 112.5 (2015), pp. 1241–1242. ISSN: 0027-8424. DOI: 10.1073/pnas.1422666112. eprint: https://www.pnas.org/content/112/5/1241.full.pdf. URL: https://www.pnas.org/content/112/5/1241 (cit. on p. 46).

[76] W. Baade and F. Zwicky. "Remarks on Super-Novae and Cosmic Rays". In: *Phys. Rev.* 46 (1 July 1934), pp. 76–77. DOI: 10.1103/PhysRev.46.76.2. URL: https://link.aps.org/doi/10.1103/PhysRev.46.76.2 (cit. on pp. 46, 127).

[77] Pasquale Blasi. "Cosmic Ray Acceleration in Supernova Remnants". In: *ICATPP Conference on Cosmic Rays for Particle and Astroparticle Physics*. 2011, pp. 493–506. DOI: 10.1142/9789814329033_0061. arXiv: 1012.5005 [astro-ph.HE] (cit. on p. 46).

[78] Luke O'C. Drury, F A Aharonian, and H J Volk. "The Gamma-ray visibility of supernova remnants: A Test of cosmic ray origin". In: *Astron. Astrophys.* 287 (1994), pp. 959–971. arXiv: astro-ph/9305037 (cit. on p. 47).

[79] A. Fiasson. "Supernova remnants and molecular clouds". In: *48th Rencontres de Moriond on Very High Energy Phenomena in the Universe*. 2013, pp. 103–108 (cit. on p. 47).

[80] M. Tavani et al. "Direct Evidence for Hadronic Cosmic-Ray Acceleration in the Supernova Renmant IC 443". In: *Astrophys. J. Lett.* 710 (2010), pp. L151–L155. DOI: 10.1088/2041-8205/710/2/L151. arXiv: 1001.5150 [astro-ph.HE] (cit. on p. 47).

[81] Yudong Cui, Paul K.H. Yeung, P.H. Thomas Tam, et al. "Leaked GeV CRs from a Broken Shell: Explaining 9 Years of Fermi-LAT Data of SNR W28". In: *Astrophys. J.* 860.1 (2018), p. 69. DOI: 10.3847/1538-4357/aac37b. arXiv: 1805.03372 [astro-ph.HE] (cit. on p. 47).

[82] S. Gabici, D. Gaggero, and F. Zandanel. "Can supernova remnants accelerate protons up to PeV energies?" In: *28th Rencontres de Blois on Particle Physics and Cosmology*. Oct. 2016. arXiv: 1610.07638 [astro-ph.HE] (cit. on p. 47).

[83] Soebur Razzaque, Pierre Jean, and Olga Mena. "High Energy Neutrinos from Novae in Symbiotic Binaries: The Case of V407 Cygni". In: *Phys. Rev. D* 82 (2010), p. 123012. DOI: 10.1103/PhysRevD.82.123012. arXiv: 1008.5193 [astro-ph.HE] (cit. on p. 47).

[84] Julian Sitarek and Wlodek Bednarek. "GeV-TeV gamma-rays and neutrinos from the Nova V407 Cygni". In: *Phys. Rev. D* 86 (2012), p. 063011. DOI: 10.1103/PhysRevD.86.063011. arXiv: 1208.6200 [astro-ph.HE] (cit. on p. 47).

[85] Brian D. Metzger, Damiano Caprioli, Indrek Vurm, et al. "Novae as Tevatrons: Prospects for CTA and IceCube". In: *Mon. Not. Roy. Astron. Soc.* 457.2 (2016), pp. 1786–1795. DOI: 10.1093/mnras/stw123. arXiv: 1510.07639 [astro-ph.HE] (cit. on p. 47).

[86] Paul J. Morris, Garret Cotter, Anthony M. Brown, et al. "Gamma-ray Novae: Rare or Nearby?" In: *Mon. Not. Roy. Astron. Soc.* 465.1 (2017), pp. 1218–1226. DOI: 10.1093/mnras/stw2776. arXiv: 1610.09941 [astro-ph.HE] (cit. on p. 47).

[87] W. Bednarek and M. Bartosik. "Cosmic rays from galactic pulsars". In: *Astron. Astrophys.* 423 (2004), p. 405. DOI: 10.1051/0004-6361:20047005. arXiv: astro-ph/0405310 (cit. on p. 48).

[88] N.D. Kylafis, I. Contopoulos, D. Kazanas, et al. "Formation and destruction of jets in X-ray binaries". In: *Int. J. Mod. Phys. Conf. Ser.* 08 (2012). Ed. by J.M. Paredes, M. M. Ribó, F.A. Aharonian, et al., pp. 287–292. DOI: 10.1142/S2010194512004722. arXiv: 1104.1578 [astro-ph.HE] (cit. on p. 48).

[89] J. Holder. "Galactic Binary Systems". In: (Dec. 2009). arXiv: 0912.4781 [astro-ph.HE] (cit. on p. 48).

[90] Sebastian Heinz and R.A. Sunyaev. "Cosmic rays from microquasars: a narrow component to the CR spectrum?" In: *Astron. Astrophys.* 390 (2002), pp. 751–766. DOI: 10.1051/0004-6361:20020615. arXiv: astro-ph/0204183 (cit. on p. 48).

[91] M. G. Aartsen et al. "Multimessenger observations of a flaring blazar coincident with high-energy neutrino IceCube-170922A". In: *Science* 361.6398 (2018), eaat1378. DOI: 10.1126/science.aat1378. arXiv: 1807.08816 [astro-ph.HE] (cit. on p. 48).

[92] M. G. Aartsen et al. "Neutrino emission from the direction of the blazar TXS 0506+056 prior to the IceCube-170922A alert". In: *Science* 361.6398 (2018), pp. 147–151. DOI: 10.1126/science.aat2890. arXiv: 1807.08794 [astro-ph.HE] (cit. on p. 48).

[93] Xavier Rodrigues, Shan Gao, Anatoli Fedynitch, et al. "Leptohadronic Blazar Models Applied to the 2014–2015 Flare of TXS 0506+056". In: *Astrophys. J. Lett.* 874.2 (2019), p. L29. DOI: 10.3847/2041-8213/ab1267. arXiv: 1812.05939 [astro-ph.HE] (cit. on p. 48).

[94] Volker Beckmann and Chris R. Shrader. *Active Galactic Nuclei*. 2012 (cit. on p. 49).

[95] Volker Beckmann and Chris R. Shrader. "The AGN phenomenon: open issues". In: Feb. 2013. arXiv: 1302.1397 [astro-ph.HE] (cit. on p. 49).

[96] Hylke B.J. Koers and Peter Tinyakov. "Relation between the neutrino flux from Centaurus A and the associated diffuse neutrino flux". In: *Phys. Rev. D* 78 (2008), p. 083009. DOI: 10.1103/PhysRevD.78.083009. arXiv: 0802.2403 [astro-ph] (cit. on pp. 49, 50).

[97] Julia K. Becker and Peter L. Biermann. "Neutrinos from active black holes, sources of ultra high energy cosmic rays". In: *Astropart. Phys.* 31 (2009), pp. 138–148. DOI: 10.1016/j.astropartphys.2008.12.006. arXiv: 0805.1498 [astro-ph] (cit. on pp. 49, 50).

[98] Idunn B. Jacobsen, Kinwah Wu, Alvina Y. L. On, et al. "High-energy neutrino fluxes from AGN populations inferred from X-ray surveys". In: *Mon. Not. Roy. Astron. Soc.* 451.4 (2015), pp. 3649–3663. DOI: 10.1093/mnras/stv1196. arXiv: 1506.05916 [astro-ph.HE] (cit. on pp. 49, 50).

[99] A.A. Abdo et al. "Insights Into the High-Energy Gamma-ray Emission of Markarian 501 from Extensive Multifrequency Observations in the Fermi Era". In: *Astrophys. J.* 727 (2011), p. 129. DOI: 10.1088/0004-637X/727/2/129. arXiv: 1011.5260 [astro-ph.HE] (cit. on pp. 50–52).

[100] Matteo Cerruti, Catherine Boisson, and Andreas Zech. "Constraining the parameter space of the one-zone synchrotron-self-Compton model for GeV-TeV detected BL Lac objects". In: *Astron. Astrophys.* 558 (2013), A47. DOI: 10.1051/0004-6361/201220963. arXiv: 1305.4597 [astro-ph.HE] (cit. on p. 51).

[101] M.L. Ahnen et al. "Long-term multi-wavelength variability and correlation study of Markarian 421 from 2007 to 2009". In: *Astron. Astrophys.* 593 (2016), A91. DOI: 10.1051/0004-6361/201628447. arXiv: 1605.09017 [astro-ph.GA] (cit. on pp. 52, 53).

[102] Shigeo S. Kimura, Kohta Murase, and Kenji Toma. "Neutrino and Cosmic-Ray Emission and Cumulative Background from Radiatively Inefficient Accretion Flows in Low-Luminosity Active Galactic Nuclei". In: *Astrophys. J.* 806 (2015), p. 159. DOI: 10.1088/0004-637X/806/2/159. arXiv: 1411.3588 [astro-ph.HE] (cit. on p. 53).

[103] Kohta Murase, Shigeo S. Kimura, and Peter Meszaros. "Hidden Cores of Active Galactic Nuclei as the Origin of Medium-Energy Neutrinos: Critical Tests with the MeV Gamma-Ray Connection". In: *Phys. Rev. Lett.* 125.1 (2020), p. 011101. DOI: 10.1103/PhysRevLett.125.011101. arXiv: 1904.04226 [astro-ph.HE] (cit. on p. 53).

[104] Ray W. Klebesadel, Ian B. Strong, and Roy A. Olson. "Observations of Gamma-Ray Bursts of Cosmic Origin". In: *Astrophys. J.* 182 (1973), pp. L85–L88. DOI: 10.1086/181225 (cit. on p. 53).

[105] Hans A. Krimm et al. "The Swift/BAT Hard X-ray Transient Monitor". In: *Astrophys. J. Suppl.* 209 (2013), p. 14. DOI: 10.1088/0067-0049/209/1/14. arXiv: 1309.0755 [astro-ph.HE] (cit. on p. 54).

[106] Charles Meegan et al. "The Fermi Gamma-Ray Burst Monitor". In: *Astrophys. J.* 702 (2009), pp. 791–804. DOI: 10.1088/0004-637X/702/1/791. arXiv: 0908.0450 [astro-ph.IM] (cit. on p. 54).

[107] B. P. Abbott et al. "Gravitational Waves and Gamma-rays from a Binary Neutron Star Merger: GW170817 and GRB 170817A". In: *Astrophys. J.* 848.2 (2017), p. L13. DOI: 10.3847/2041-8213/aa920c. arXiv: 1710.05834 [astro-ph.HE] (cit. on p. 54).

[108] B. P. Abbott et al. "Multi-messenger Observations of a Binary Neutron Star Merger". In: *Astrophys. J.* 848.2 (2017), p. L12. DOI: 10.3847/2041-8213/aa91c9. arXiv: 1710.05833 [astro-ph.HE] (cit. on p. 54).

[109] H. Abdalla et al. "A very-high-energy component deep in the γ-ray burst afterglow". In: *Nature* 575.7783 (2019), pp. 464–467. DOI: 10.1038/s41586-019-1743-9. arXiv: 1911.08961 [astro-ph.HE] (cit. on p. 54).

[110] V.A. Acciari et al. "Teraelectronvolt emission from the γ-ray burst GRB 190114C". In: *Nature* 575.7783 (2019), pp. 455–458. DOI: 10.1038/s41586-019-1750-x. arXiv: 2006.07249 [astro-ph.HE] (cit. on p. 54).

[111] Vikas Chand et al. "Peculiar prompt emission and afterglow in H.E.S.S. detected GRB 190829A". In: *Astrophys. J.* 898.1 (2020), p. 42. DOI: 10.3847/1538-4357/ab9606. arXiv: 2001.00648 [astro-ph.HE] (cit. on p. 54).

[112] Xiang-Yu Wang, Ruo-Yu Liu, Hai-Ming Zhang, et al. "Synchrotron self-Compton emission from external shocks as the origin of the sub-TeV emission in GRB 180720B and GRB 190114C". In: (May 2019). DOI: 10.3847/1538-4357/ab426c. arXiv: 1905.11312 [astro-ph.HE] (cit. on p. 54).

[113] Enrico Peretti, Pasquale Blasi, Felix Aharonian, et al. "Cosmic ray transport and radiative processes in nuclei of starburst galaxies". In: *Mon. Not. Roy. Astron. Soc.* 487.1 (2019), pp. 168–180. DOI: 10.1093/mnras/stz1161. arXiv: 1812.01996 [astro-ph.HE] (cit. on p. 55).

[114] Gianfranco Brunetti and Thomas W. Jones. "Cosmic rays in galaxy clusters and their nonthermal emission". In: *Int. J. Mod. Phys. D* 23 (2014), p. 1430007. DOI: 10.1142/S0218271814300079. arXiv: 1401.7519 [astro-ph.CO] (cit. on p. 55).

[115] A.M. Bykov, D.C. Ellison, A. Marcowith, et al. "Cosmic ray production in supernovae". In: *Space Sci. Rev.* 214.1 (2018), p. 41. DOI: 10.1007/s11214-018-0479-4. arXiv: 1801.08890 [astro-ph.HE] (cit. on p. 55).

[116] Dafne Guetta, Roi Rahin, Imre Bartos, et al. "Constraining the fraction of core-collapse supernovae harbouring choked jets with high-energy neutrinos". In: *Mon. Not. Roy. Astron. Soc.* 492.1 (2020), pp. 843–847. DOI: 10.1093/mnras/stz3245. arXiv: 1906.07399 [astro-ph.HE] (cit. on p. 55).

[117] Kohta Murase, Anna Franckowiak, Keiichi Maeda, et al. "High-Energy Emission from Interacting Supernovae: New Constraints on Cosmic-Ray Acceleration in Dense Circumstellar Environments". In: *Astrophys. J.* 874.1 (2019), p. 80. DOI: 10.3847/1538-4357/ab0422. arXiv: 1807.01460 [astro-ph.HE] (cit. on p. 55).

[118] Claire Guépin, Kumiko Kotera, Enrico Barausse, et al. "Ultra-High Energy Cosmic Rays and Neutrinos from Tidal Disruptions by Massive Black Holes". In: *Astron. Astrophys.* 616 (2018), A179. DOI: 10.1051/0004-6361/201732392. arXiv: 1711.11274 [astro-ph.HE] (cit. on p. 55).

[119] Cecilia Lunardini and Walter Winter. "High Energy Neutrinos from the Tidal Disruption of Stars". In: *Phys. Rev. D* 95.12 (2017), p. 123001. DOI: 10.1103/PhysRevD.95.123001. arXiv: 1612.03160 [astro-ph.HE] (cit. on p. 55).

[120] Robert Stein et al. "A high-energy neutrino coincident with a tidal disruption event". In: (May 2020). arXiv: 2005.05340 [astro-ph.HE] (cit. on p. 55).

[121] Xin Qian and Jen-Chieh Peng. "Physics with Reactor Neutrinos". In: *Rept. Prog. Phys.* 82.3 (2019), p. 036201. DOI: 10.1088/1361-6633/aae881. arXiv: 1801.05386 [hep-ex] (cit. on p. 56).

[122] Ubaldo Dore, Pier Loverre, and Lucio Ludovici. "History of accelerator neutrino beams". In: *Eur. Phys. J.* H44.4-5 (2019), pp. 271–305. DOI: 10.1140/epjh/e2019-90032-x. arXiv: 1805.01373 [physics.acc-ph] (cit. on p. 56).

[123] J. A. Formaggio and G. P. Zeller. "From eV to EeV: Neutrino Cross Sections Across Energy Scales". In: *Rev. Mod. Phys.* 84 (2012), pp. 1307–1341. DOI: 10.1103/RevModPhys.84.1307. arXiv: 1305.7513 [hep-ex] (cit. on pp. 57, 58).

[124] Claudio Giganti, Stéphane Lavignac, and Marco Zito. "Neutrino oscillations: the rise of the PMNS paradigm". In: *Prog. Part. Nucl. Phys.* 98 (2018), pp. 1–54. DOI: 10.1016/j.ppnp.2017.10.001. arXiv: 1710.00715 [hep-ex] (cit. on p. 59).

[125] A. Yu. Smirnov. "The MSW effect and matter effects in neutrino oscillations". In: *Phys. Scripta* T121 (2005), pp. 57–64. DOI: 10.1088/0031-8949/2005/T121/008. arXiv: hep-ph/0412391 [hep-ph] (cit. on p. 59).

[126] S. Adrian-Martinez et al. "Letter of intent for KM3NeT 2.0". In: *J. Phys.* G43.8 (2016), p. 084001. DOI: 10.1088/0954-3899/43/8/084001. arXiv: 1601.07459 [astro-ph.IM] (cit. on pp. 60, 64, 65, 77, 81, 102, 108).

[127] Thomas K. Gaisser. "Atmospheric Neutrinos". In: (Oct. 2019). arXiv: 1910.08851 [astro-ph.HE] (cit. on p. 60).

[128] T. K. Gaisser and M. Honda. "Flux of atmospheric neutrinos". In: *Ann. Rev. Nucl. Part. Sci.* 52 (2002), pp. 153–199. DOI: 10.1146/annurev.nucl.52.050102.090645. arXiv: hep-ph/0203272 [hep-ph] (cit. on p. 60).

[129] Rikard Enberg, Mary Hall Reno, and Ina Sarcevic. "Prompt neutrino fluxes from atmospheric charm". In: *Phys. Rev.* D78 (2008), p. 043005. DOI: 10.1103/PhysRevD.78.043005. arXiv: 0806.0418 [hep-ph] (cit. on p. 60).

[130] Paolo Lipari, Maurizio Lusignoli, and Davide Meloni. "Flavor Composition and Energy Spectrum of Astrophysical Neutrinos". In: *Phys. Rev. D* 75 (2007), p. 123005. DOI: 10.1103/PhysRevD.75.123005. arXiv: 0704.0718 [astro-ph] (cit. on p. 61).

[131] Eli Waxman and John N. Bahcall. "High-energy neutrinos from astrophysical sources: An Upper bound". In: *Phys. Rev.* D59 (1999), p. 023002. DOI: 10.1103/PhysRevD.59.023002. arXiv: hep-ph/9807282 [hep-ph] (cit. on p. 61).

[132] John N. Bahcall and Eli Waxman. "High-energy astrophysical neutrinos: The Upper bound is robust". In: *Phys. Rev.* D64 (2001), p. 023002. DOI: 10.1103/PhysRevD.64.023002. arXiv: hep-ph/9902383 [hep-ph] (cit. on p. 61).

[133] Eli Waxman. "Extra Galactic sources of high energy neutrinos". In: *Phys. Scripta T* 121 (2005). Ed. by L. Bergström, O. Botner, P. Carlson, et al., pp. 147–152. DOI: 10.1088/0031-8949/2005/T121/022. arXiv: astro-ph/0502159 (cit. on p. 61).

[134] A. Achterberg et al. "First Year Performance of The IceCube Neutrino Telescope". In: *Astropart. Phys.* 26 (2006), pp. 155–173. DOI: 10.1016/j.astropartphys.2006.06.007. arXiv: astro-ph/0604450 [astro-ph] (cit. on pp. 62, 65).

[135] M. Ageron et al. “ANTARES: the first undersea neutrino telescope”. In: *Nucl. Instrum. Meth.* A656 (2011), pp. 11–38. DOI: 10.1016/j.nima.2011.06.103. arXiv: 1104.1607 [astro-ph.IM] (cit. on pp. 62, 65).

[136] Alfonso Garcia, Rhorry Gauld, Aart Heijboer, et al. “Complete predictions for high-energy neutrino propagation in matter”. In: (Apr. 2020). arXiv: 2004.04756 [hep-ph] (cit. on p. 62).

[137] Maarten de Jong. “From particle to data”. KM3NeT Bootcamp, Erlangen. 2020 (cit. on pp. 62, 63).

[138] M.G. Aartsen et al. “Measurement of South Pole ice transparency with the IceCube LED calibration system”. In: *Nucl. Instrum. Meth. A* 711 (2013), pp. 73–89. DOI: 10.1016/j.nima.2013.01.054. arXiv: 1301.5361 [astro-ph.IM] (cit. on p. 64).

[139] J.A. Aguilar et al. “Transmission of light in deep sea water at the site of the ANTARES Neutrino Telescope”. In: *Astropart. Phys.* 23 (2005), pp. 131–155. DOI: 10.1016/j.astropartphys.2004.11.006. arXiv: astro-ph/0412126 (cit. on p. 64).

[140] A. Roberts. “The Birth of high-energy neutrino astronomy: A Personal history of the DUMAND project”. In: *Rev. Mod. Phys.* 64 (1992), pp. 259–312. DOI: 10.1103/RevModPhys.64.259 (cit. on p. 64).

[141] I. A. Belolaptikov et al. “The Baikal underwater neutrino telescope: Design, performance and first results”. In: *Astropart. Phys.* 7 (1997), pp. 263–282. DOI: 10.1016/S0927-6505(97)00022-4 (cit. on p. 64).

[142] E. Andres et al. “The AMANDA neutrino telescope: Principle of operation and first results”. In: *Astropart. Phys.* 13 (2000), pp. 1–20. DOI: 10.1016/S0927-6505(99)00092-4. arXiv: astro-ph/9906203 [astro-ph] (cit. on p. 64).

[143] Paolo Piattelli. “Towards a km3 scale neutrino detector in the Mediterranean: NEMO and KM3NeT”. In: *Earth Planets Space* 62.2 (2010), pp. 201–204. DOI: 10.5047/eps.2009.09.003 (cit. on p. 65).

[144] G. Aggouras et al. “NESTOR Deep Sea Neutrino Telescope: Deployment and results”. In: *Nucl. Phys. Proc. Suppl.* 151 (2006). [,279(2006)], pp. 279–286. DOI: 10.1016/j.nuclphysbps.2005.07.060 (cit. on p. 65).

[145] A.D. Avrorin et al. “BAIKAL-GVD: The New-Generation Neutrino Telescope in Lake Baikal”. In: *Bull. Russ. Acad. Sci. Phys.* 83.8 (2019), pp. 921–922. DOI: 10.3103/S1062873819080057 (cit. on p. 65).

[146] Francis Halzen and Uli Katz. “The era of kilometer-scale neutrino detectors”. In: *Adv.High Energy Phys.* 2013 (2013), p. 680584. DOI: 10.1155/2013/680584 (cit. on p. 66).

[147] J. A. Aguilar et al. "Measurement of the atmospheric muon flux with a 4 GeV threshold in the ANTARES neutrino telescope". In: *Astropart. Phys.* 33 (2010). [Erratum: Astropart. Phys.34,185(2010)], pp. 86–90. DOI: 10.1016/j.astropartphys.2010.02.006,10.1016/j.astropartphys.2009.12.002. arXiv: 0910.4843 [astro-ph.HE] (cit. on pp. 68, 123, 124).

[148] E. V. Bugaev, A. Misaki, Vadim A. Naumov, et al. "Atmospheric muon flux at sea level, underground and underwater". In: *Phys. Rev.* D58 (1998), p. 054001. DOI: 10.1103/PhysRevD.58.054001. arXiv: hep-ph/9803488 [hep-ph] (cit. on pp. 68, 107, 108, 119, 123).

[149] Y. Becherini, A. Margiotta, M. Sioli, et al. "A Parameterisation of single and multiple muons in the deep water or ice". In: *Astropart. Phys.* 25 (2006), pp. 1–13. DOI: 10.1016/j.astropartphys.2005.10.005. arXiv: hep-ph/0507228 [hep-ph] (cit. on pp. 68, 97, 107).

[150] T. Chiarusi and M. Spurio. "High-Energy Astrophysics with Neutrino Telescopes". In: *Eur. Phys. J. C* 65 (2010), pp. 649–701. DOI: 10.1140/epjc/s10052-009-1230-9. arXiv: 0906.2634 [astro-ph.HE] (cit. on p. 69).

[151] M. G. Aartsen et al. "Observation and Characterization of a Cosmic Muon Neutrino Flux from the Northern Hemisphere using six years of IceCube data". In: *Astrophys. J.* 833.1 (2016), p. 3. DOI: 10.3847/0004-637X/833/1/3. arXiv: 1607.08006 [astro-ph.HE] (cit. on p. 72).

[152] A. Albert et al. "All-flavor Search for a Diffuse Flux of Cosmic Neutrinos with Nine Years of ANTARES Data". In: *Astrophys. J.* 853.1 (2018), p. L7. DOI: 10.3847/2041-8213/aaa4f6. arXiv: 1711.07212 [astro-ph.HE] (cit. on pp. 72, 73).

[153] S. Hummer, M. Maltoni, W. Winter, et al. "Energy dependent neutrino flavor ratios from cosmic accelerators on the Hillas plot". In: *Astropart. Phys.* 34 (2010), pp. 205–224. DOI: 10.1016/j.astropartphys.2010.07.003. arXiv: 1007.0006 [astro-ph.HE] (cit. on p. 73).

[154] Kohta Murase and Eli Waxman. "Constraining High-Energy Cosmic Neutrino Sources: Implications and Prospects". In: *Phys. Rev.* D94.10 (2016), p. 103006. DOI: 10.1103/PhysRevD.94.103006. arXiv: 1607.01601 [astro-ph.HE] (cit. on pp. 74, 75).

[155] M.G. Aartsen et al. "The contribution of Fermi-2LAC blazars to the diffuse TeV-PeV neutrino flux". In: *Astrophys. J.* 835.1 (2017), p. 45. DOI: 10.3847/1538-4357/835/1/45. arXiv: 1611.03874 [astro-ph.HE] (cit. on p. 74).

[156] M. G. Aartsen et al. "All-sky Search for Time-integrated Neutrino Emission from Astrophysical Sources with 7 yr of IceCube Data". In: *Astrophys. J.* 835.2 (2017), p. 151. DOI: 10.3847/1538-4357/835/2/151. arXiv: 1609.04981 [astro-ph.HE] (cit. on pp. 75, 76).

[157] S. Aiello et al. “Characterisation of the Hamamatsu photomultipliers for the KM3NeT Neutrino Telescope”. In: *JINST* 13.05 (2018), P05035. DOI: 10.1088/1748-0221/13/05/P05035 (cit. on p. 83).

[158] Maarten De Jong et al. *Jpp - Documentation*. Version 12.0.0. URL: https://common.pages.km3net.de/jpp (cit. on p. 83).

[159] P. P. M. Jansweijer, H. Z. Peek, and E. De Wolf. “White Rabbit: Sub-nanosecond timing over Ethernet”. In: *Nucl. Instrum. Meth.* A725 (2013), pp. 187–190. DOI: 10.1016/j.nima.2012.12.096 (cit. on p. 84).

[160] Simone Biagi, Tommaso Chiarusi, Paolo Piattelli, et al. “The data acquisition system of the KM3NeT detector”. In: *PoS* ICRC2015 (2016), p. 1172. DOI: 10.22323/1.236.1172 (cit. on p. 85).

[161] S. Aiello et al. “The Control Unit of the KM3NeT Data Acquisition System”. In: *Comput. Phys. Commun.* 256 (2020), p. 107433. DOI: 10.1016/j.cpc.2020.107433. arXiv: 1910.00112 [astro-ph.IM] (cit. on p. 85).

[162] Irene Di Palma. “KM3NeT Time Calibration”. In: *EPJ Web Conf.* 207 (2019). Ed. by C. Spiering, p. 07001. DOI: 10.1051/epjconf/201920707001 (cit. on pp. 89, 94).

[163] M. Ageron et al. “Dependence of atmospheric muon flux on seawater depth measured with the first KM3NeT detection units”. In: (2019). DOI: 10.1140/epjc/s10052-020-7629-z. arXiv: 1906.02704 [physics.ins-det] (cit. on pp. 92, 104, 105, 109, 113, 115–118, 120, 124, 144, 210).

[164] Salvatore Viola and Rosa Coniglione. “The KM3NeT acoustic positioning system”. In: *PoS* ICRC2017 (2018), p. 1031. DOI: 10.22323/1.301.1031 (cit. on pp. 91, 93).

[165] Giorgio Riccobene. “The Positioning system for KM3NeT”. In: *EPJ Web Conf.* 207 (2019). Ed. by C. Spiering, p. 07005. DOI: 10.1051/epjconf/201920707005 (cit. on p. 93).

[166] Sebastiano Aiello et al. “gSeaGen: the KM3NeT GENIE-based code for neutrino telescopes”. In: (Mar. 2020). arXiv: 2003.14040 [astro-ph.IM] (cit. on pp. 96, 97).

[167] Carla Distefano. “gSeaGen: a GENIE-based code for neutrino telescopes”. In: *EPJ Web Conf.* 116 (2016), p. 08001. DOI: 10.1051/epjconf/201611608001. arXiv: 1602.00501 [astro-ph.IM] (cit. on p. 96).

[168] D. Heck, J. Knapp, J.N. Capdevielle, et al. “CORSIKA: A Monte Carlo code to simulate extensive air showers”. In: (Feb. 1998) (cit. on p. 97).

[169] A. Margiotta. “Common simulation tools for large volume neutrino detectors”. In: *Nucl. Instrum. Meth.* A725 (2013), pp. 98–101. DOI: 10.1016/j.nima.2012.11.172 (cit. on pp. 97, 98).

[170] Marta Colomer, Damien Dornic, and Vladimir Kulikovskiy. "Detailed KM3NeT optical module simulation with Geant4 and supernova neutrino detection study". In: *PoS* ICRC2017 (2018), p. 983. DOI: 10.22323/1.301.0983 (cit. on p. 98).

[171] A. G. Tsirigotis, A. Leisos, and S. E. Tzamarias. "HOU Reconstruction & Simulation (HOURS): A complete simulation and reconstruction package for very large volume underwater neutrino telescopes". In: *Nucl. Instrum. Meth.* A626-627 (2011), S185–S187. DOI: 10.1016/j.nima.2010.06.258 (cit. on p. 98).

[172] Karel Melis, Aart Heijboer, and Maarten de Jong. "KM3NeT/ARCA Event Reconstruction Algorithms". In: *PoS* ICRC2017 (2018), p. 950. DOI: 10.22323/1.301.0950 (cit. on pp. 100, 101).

[173] Brian O Fearraigh. *Track Reconstruction in KM3NeT*. Jpp - Documentation. URL: https://common.pages.km3net.de/jpp (cit. on p. 100).

[174] KENNETH LEVENBERG. "A METHOD FOR THE SOLUTION OF CERTAIN NON-LINEAR PROBLEMS IN LEAST SQUARES". In: *Quarterly of Applied Mathematics* 2.2 (1944), pp. 164–168. ISSN: 0033569X, 15524485. URL: http://www.jstor.org/stable/43633451 (cit. on p. 100).

[175] Donald W Marquardt. "An Algorithm for Least-Squares Estimation of Nonlinear Parameters". In: *Journal of the Society for Industrial and Applied Mathematics* 11.2 (1963), pp. 431–441. DOI: 10.1137/0111030. URL: https://doi.org/10.1137/0111030 (cit. on p. 100).

[176] Jannik Hofestädt. "Event reconstruction in the KM3NeT/ORCA detector". In: *PoS* NEUTEL2017 (2018), p. 076. DOI: 10.22323/1.307.0076 (cit. on p. 101).

[177] S. Adrián-Martínez et al. "Deep sea tests of a prototype of the KM3NeT digital optical module". In: *Eur. Phys. J. C* 74.9 (2014), p. 3056. DOI: 10.1140/epjc/s10052-014-3056-3. arXiv: 1405.0839 [astro-ph.IM] (cit. on p. 104).

[178] S. Adrián-Martínez et al. "The prototype detection unit of the KM3NeT detector". In: *Eur. Phys. J.* C76.2 (2016), p. 54. DOI: 10.1140/epjc/s10052-015-3868-9. arXiv: 1510.01561 [astro-ph.IM] (cit. on pp. 104, 110, 111).

[179] Martijn Jongen. "Measurement of the depth dependence of coincidence rates induced by atmospheric muons with the first two KM3NeT Detection Units". In: *PoS* ICRC2017 (2018), p. 1018. DOI: 10.22323/1.301.1018 (cit. on p. 105).

[180] T. S. Sinegovskaya and S. I. Sinegovsky. "Prompt muon contribution to the flux underwater". In: *Phys. Rev.* D63 (2001), p. 096004. DOI: 10.1103/PhysRevD.63.096004. arXiv: hep-ph/0007234 [hep-ph] (cit. on p. 106).

[181] Stefano Cecchini and Maurizio Spurio. "Atmospheric muons: experimental aspects". In: (2012). arXiv: 1208.1171 [astro-ph.EP] (cit. on p. 106).

[182] Tri L. Astraatmadja. "On the detection of TeV gamma-rays from GRB with km-cube neutrino telescopes — I. Muon event rate from single GRBs". In: *Mon. Not. Roy. Astron. Soc.* 418 (2011), pp. 1774–1786. DOI: 10.1111/j.1365-2966.2011.19598.x. arXiv: 1108.1720 [astro-ph.HE] (cit. on p. 107).

[183] Konstantinos Pikounis, Ekaterini Tzamariudaki, and Christos Markou. "Analysis of High Energy Starting Events with the KM3NeT/ARCA detector". In: *EPJ Web Conf.* 207 (2019), p. 02006. DOI: 10.1051/epjconf/201920702006 (cit. on p. 108).

[184] S. Cecchini, E. Korolkova, Annarita Margiotta, et al. "Atmospheric muon background in the antares detector". In: *Proceedings, 29th International Cosmic Ray Conference (ICRC 2005) - by Forschungszentrum Karlsruhe, Institute for Nuclear Physics, and University Karlsruhe, Institute for Experimental Nuclear Physics: Pune, India, August 3-11, 2005*. Vol. 5. 2005, pp. 51–54. arXiv: astro-ph/0510799 [astro-ph] (cit. on p. 109).

[185] Jannik Hofestädt and Dorothea Samtleben. *Report on problems with data from ORCA-DU 2*. KM3NeT Internal Note. 2019 (cit. on p. 112).

[186] S. I. Klimushin, E. V. Bugaev, and Igor A. Sokalski. "On the parametrization of atmospheric muon angular flux underwater". In: *Phys. Rev.* D64 (2001), p. 014016. DOI: 10.1103/PhysRevD.64.014016. arXiv: hep-ph/0012032 [hep-ph] (cit. on pp. 119, 123).

[187] M. Crouch. "An Improved World Survey Expression for Cosmic Ray Vertical Intensity VS. Depth in Standard Rock". In: *International Cosmic Ray Conference*. Vol. 6. International Cosmic Ray Conference. Jan. 1987, p. 165 (cit. on p. 119).

[188] W. Baade and F. Zwicky. "On Super-Novae". In: *Proceedings of the National Academy of Sciences* 20.5 (1934), pp. 254–259. ISSN: 0027-8424. DOI: 10.1073/pnas.20.5.254. eprint: https://www.pnas.org/content/20/5/254.full.pdf. URL: https://www.pnas.org/content/20/5/254 (cit. on p. 127).

[189] Carlo Giunti and Chung W. Kim. *Fundamentals of Neutrino Physics and Astrophysics*. Apr. 2007. ISBN: 978-0-19-850871-7 (cit. on pp. 128, 130, 139).

[190] Alexei V. Filippenko. "Optical spectra of supernovae". In: *Ann. Rev. Astron. Astrophys.* 35 (1997), pp. 309–355. DOI: 10.1146/annurev.astro.35.1.309 (cit. on p. 128).

[191] B. Herbst. *The Chandrasekhar Limit, Iron-56 and Core Collapse Supernovae*. Wesleyan University – ASTRONOMY 155: Introductory Astronomy, URL: https://wesfiles.wesleyan.edu/courses/astr155/Home.html. (cit. on p. 128).

[192] S.E. Woosley and T.A. Weaver. "The Physics of supernova explosions". In: *Ann. Rev. Astron. Astrophys.* 24 (1986), pp. 205–253. DOI: 10.1146/annurev.aa.24.090186.001225 (cit. on p. 129).

[193] M.M. Phillips. "The absolute magnitudes of Type IA supernovae". In: *Astrophys. J. Lett.* 413 (1993), pp. L105–L108. DOI: 10.1086/186970 (cit. on p. 129).

[194] Alexander Heger, C.L. Fryer, S.E. Woosley, et al. "How massive single stars end their life". In: *Astrophys. J.* 591 (2003), pp. 288–300. DOI: 10.1086/375341. arXiv: astro-ph/0212469 (cit. on p. 130).

[195] H.-Thomas Janka, Florian Hanke, Lorenz Huedepohl, et al. "Core-Collapse Supernovae: Reflections and Directions". In: *PTEP* 2012 (2012), 01A309. DOI: 10.1093/ptep/pts067. arXiv: 1211.1378 [astro-ph.SR] (cit. on p. 130).

[196] Nolan R. Walborn, Barry M. Lasker, Victoria G. Laidler, et al. "The composite image of Sanduleak -69 deg 202, candidate precursor to Supernova 1987A in the Large Magellanic Cloud". In: *Astrophys. J. Lett.* 321 (1987), pp. L41–L44. DOI: 10.1086/185002 (cit. on p. 133).

[197] R.N. Manchester. "Searching for a Pulsar in SN 1987A". In: *AIP Conf. Proc.* 937.1 (2007). Ed. by Stefan Immler, Kurt Weiler, and Richard McCray, pp. 134–143. DOI: 10.1063/1.2803553. arXiv: 0708.2372 [astro-ph] (cit. on p. 133).

[198] K.S. Hirata et al. "Observation in the Kamiokande-II Detector of the Neutrino Burst from Supernova SN 1987a". In: *Phys. Rev. D* 38 (1988), pp. 448–458. DOI: 10.1103/PhysRevD.38.448 (cit. on p. 133).

[199] Todd Haines et al. "Neutrinos From SN1987A in the Imb Detector". In: *Nucl. Instrum. Meth. A* 264 (1988). Ed. by K.C. Wali, pp. 28–31. DOI: 10.1016/0168-9002(88)91097-2 (cit. on p. 133).

[200] E.N. Alekseev, L.N. Alekseeva, I.V. Krivosheina, et al. "DETECTION OF THE NEUTRINO SIGNAL FROM SN1987A USING THE INR BAKSAN UNDERGROUND SCINTILLATION TELESCOPE". In: *20th International Cosmic Ray Conference*. 1987, pp. 59–67 (cit. on p. 133).

[201] M. Aglietta et al. "On the event observed in the Mont Blanc Underground Neutrino observatory during the occurrence of Supernova 1987a". In: *Europhys. Lett.* 3 (1987), pp. 1315–1320. DOI: 10.1209/0295-5075/3/12/011 (cit. on p. 133).

[202] Natalia Agafonova, Walter Fulgione, Alexey Malgin, et al. "Possible explanation of the neutrino signal from SN1987A detected with the LSD". In: *EPJ Web Conf.* 191 (2018). Ed. by V.E. Volkova, Y.V. Zhezher, D.G. Levkov, et al., p. 03004. DOI: 10.1051/epjconf/201819103004 (cit. on p. 133).

[203] Rodolfo Valentim, Jorge E. Horvath, and Eraldo M. Rangel. "Evidence for Two Neutrino Bursts from SN1987A". In: *Int. J. Mod. Phys. Conf. Ser.* 45 (2017). Ed. by Alexander Lunkes dos Santos, César Augusto Zen Vasconcellos, Daniel Tavares da Silva, et al., p. 1760040. DOI: 10.1142/S2010194517600400. arXiv: 1706.07824 [astro-ph.HE] (cit. on p. 133).

[204] Georg G. Raffelt. "Particle physics from stars". In: *Ann. Rev. Nucl. Part. Sci.* 49 (1999), pp. 163–216. DOI: 10.1146/annurev.nucl.49.1.163. arXiv: hep-ph/9903472 (cit. on p. 134).

[205] Thomas J. Loredo and Don Q. Lamb. "Bayesian analysis of neutrinos observed from supernova SN-1987A". In: *Phys. Rev. D* 65 (2002), p. 063002. DOI: 10.1103/PhysRevD.65.063002. arXiv: astro-ph/0107260 (cit. on p. 134).

[206] M. Ikeda et al. "Search for Supernova Neutrino Bursts at Super-Kamiokande". In: *Astrophys. J.* 669 (2007), pp. 519–524. DOI: 10.1086/521547. arXiv: 0706.2283 [astro-ph] (cit. on p. 135).

[207] Fengpeng An et al. "Neutrino Physics with JUNO". In: *J. Phys. G* 43.3 (2016), p. 030401. DOI: 10.1088/0954-3899/43/3/030401. arXiv: 1507.05613 [physics.ins-det] (cit. on p. 135).

[208] David A. Green and F. Richard Stephenson. "The Historical supernovae". In: *Lect. Notes Phys.* 598 (2003), p. 7. DOI: 10.1007/3-540-45863-8_2. arXiv: astro-ph/0301603 [astro-ph] (cit. on p. 135).

[209] D. A. Green and S. F. Gull. "Two new young galactic supernova remnants". In: *Nature* 312.5994 (Dec. 1984), pp. 527–529. DOI: 10.1038/312527a0 (cit. on p. 135).

[210] Jacco Vink. "Supernova 1604, Kepler's supernova, and its remnant". In: (Dec. 2016). DOI: 10.1007/978-3-319-20794-0_49-1. arXiv: 1612.06905 [astro-ph.HE] (cit. on p. 135).

[211] Stephen P. Reynolds, K.J. Borkowski, D.A. Green, et al. "The Youngest Galactic Supernova Remnant: G1.9+0.3". In: *Astrophys. J. Lett.* 680 (2008), p. L41. DOI: 10.1086/589570. arXiv: 0803.1487 [astro-ph] (cit. on p. 135).

[212] Karolina Rozwadowska, Francesco Vissani, and Enrico Cappellaro. "On the rate of core collapse supernovae in the milky way". In: *New Astron.* 83 (2021), p. 101498. DOI: 10.1016/j.newast.2020.101498. arXiv: 2009.03438 [astro-ph.HE] (cit. on p. 135).

[213] Scott M. Adams, C. S. Kochanek, John F. Beacom, et al. "Observing the Next Galactic Supernova". In: *Astrophys. J.* 778 (2013), p. 164. DOI: 10.1088/0004-637X/778/2/164. arXiv: 1306.0559 [astro-ph.HE] (cit. on pp. 135, 136).

[214] Jost Migenda. "Astroparticle Physics in Hyper-Kamiokande". In: *PoS* EPS-HEP2017 (2017). Ed. by Paolo Checchia et al., p. 020. DOI: 10.22323/1.314.0020. arXiv: 1710.08345 [physics.ins-det] (cit. on p. 136).

[215] S.V. Bergh and G.A. Tammann. "Galactic and extragalactic supernova rates". In: *Ann. Rev. Astron. Astrophys.* 29 (1991), pp. 363–407. DOI: 10.1146/annurev.aa.29.090191.002051 (cit. on p. 136).

[216] Emily M. Levesque and Philip Massey. "Betelgeuse Just Is Not That Cool: Effective Temperature Alone Cannot Explain the Recent Dimming of Betelgeuse". In: *The Astrophysical Journal* 891.2 (Mar. 2020), p. L37. ISSN: 2041-8213. DOI: 10.3847/2041-8213/ab7935. URL: http://dx.doi.org/10.3847/2041-8213/ab7935 (cit. on p. 136).

[217] R. Abbasi et al. "IceCube Sensitivity for Low-Energy Neutrinos from Nearby Supernovae". In: *Astron. Astrophys.* 535 (2011). [Erratum: Astron.Astrophys. 563, C1 (2014)], A109. DOI: 10.1051/0004-6361/201117810e. arXiv: 1108.0171 [astro-ph.HE] (cit. on p. 137).

[218] Irene Tamborra, Georg Raffelt, Florian Hanke, et al. "Neutrino emission characteristics and detection opportunities based on three-dimensional supernova simulations". In: *Phys. Rev. D* 90.4 (2014), p. 045032. DOI: 10.1103/PhysRevD.90.045032. arXiv: 1406.0006 [astro-ph.SR] (cit. on p. 138).

[219] Laurie Walk, Irene Tamborra, Hans-Thomas Janka, et al. "Neutrino emission characteristics of black hole formation in three-dimensional simulations of stellar collapse". In: (2019). arXiv: 1910.12971 [astro-ph.HE] (cit. on p. 138).

[220] Kate Scholberg. "Supernova Neutrino Detection". In: *Ann. Rev. Nucl. Part. Sci.* 62 (2012), pp. 81–103. DOI: 10.1146/annurev-nucl-102711-095006. arXiv: 1205.6003 [astro-ph.IM] (cit. on p. 139).

[221] Thomas Kowarik. "Supernova Neutrinos in AMANDA and IceCube-Monte Carlo Development and Data Analysis". PhD thesis. Mainz U., Inst. Phys., 2010 (cit. on pp. 139, 140).

[222] Kate Scholberg. "SNOwGLoBES: SuperNova Observatories with GLoBES". In: *APS April Meeting Abstracts*. Vol. 2011. APS Meeting Abstracts. Apr. 2011, p. L11.006 (cit. on pp. 140, 161).

[223] Alessandro Strumia and Francesco Vissani. "Precise quasielastic neutrino/nucleon cross-section". In: *Phys. Lett. B* 564 (2003), pp. 42–54. DOI: 10.1016/S0370-2693(03)00616-6. arXiv: astro-ph/0302055 (cit. on p. 140).

[224] Gaby Radel and Rolf Beyer. "Neutrino electron scattering". In: *Mod. Phys. Lett. A* 8 (1993), pp. 1067–1088. DOI: 10.1142/S0217732393002567 (cit. on p. 140).

[225] Irene Tamborra, Florian Hanke, Bernhard Müller, et al. "Neutrino signature of supernova hydrodynamical instabilities in three dimensions". In: *Phys. Rev. Lett.* 111.12 (2013), p. 121104. DOI: 10.1103/PhysRevLett.111.121104. arXiv: 1307.7936 [astro-ph.SR] (cit. on pp. 141, 187).

[226] Glen Cowan, Kyle Cranmer, Eilam Gross, et al. "Asymptotic formulae for likelihood-based tests of new physics". In: *Eur. Phys. J. C* 71 (2011). [Erratum: Eur.Phys.J.C 73, 2501 (2013)], p. 1554. DOI: 10.1140/epjc/s10052-011-1554-0. arXiv: 1007.1727 [physics.data-an] (cit. on pp. 155, 191).

[227] Robert D. Cousins. "Annotated Bibliography of Some Papers on Combining Significances or p-values". In: (May 2007). arXiv: 0705.2209 [physics.data-an] (cit. on p. 158).

[228] R.A. Fisher. *Statistical methods for research workers*. Edinburgh Oliver & Boyd, 1925 (cit. on p. 159).

[229] Patrick Huber, Joachim Kopp, Manfred Lindner, et al. "GLoBES: General Long Baseline Experiment Simulator". In: *Comput. Phys. Commun.* 177 (2007), pp. 439–440. DOI: 10.1016/j.cpc.2007.05.007 (cit. on p. 161).

[230] Felix Malmenbeck and Erin O'Sullivan. "Implementing IceCube in SNOwGLoBES". In: *36th International Cosmic Ray Conference*. Sept. 2019. arXiv: 1909.00886 [astro-ph.HE] (cit. on p. 163).

[231] Robert Cross, Alexander Fritz, and Spencer Griswold. "Eleven Year Search for Supernovae with the IceCube Neutrino Observatory". In: *PoS* ICRC2019 (2020), p. 889. DOI: 10.22323/1.358.0889. arXiv: 1908.07249 [astro-ph.HE] (cit. on p. 163).

[232] Evan O'Connor. "An Open-Source Neutrino Radiation Hydrodynamics Code for Core-Collapse Supernovae". In: *Astrophys. J. Suppl.* 219.2 (2015), p. 24. DOI: 10.1088/0067-0049/219/2/24. arXiv: 1411.7058 [astro-ph.HE] (cit. on pp. 163, 164).

[233] Alessandro Mirizzi et al. "Supernova Neutrinos: Production, Oscillations and Detection". In: *Riv. Nuovo Cim.* 39.1-2 (2016), p. 1. DOI: 10.1393/ncr/i2016-10120-8. arXiv: 1508.00785 [astro-ph.HE] (cit. on pp. 163, 164).

[234] S. Al Kharusi et al. "SNEWS 2.0: A Next-Generation SuperNova EarlyWarning System for Multi-messenger Astronomy". working draft. 2020 (cit. on pp. 164, 169, 176, 191).

[235] Pietro Antonioli et al. "SNEWS: The Supernova Early Warning System". In: *New J. Phys.* 6 (2004), p. 114. DOI: 10.1088/1367-2630/6/1/114. arXiv: astro-ph/0406214 (cit. on p. 168).

[236] Eilam Gross and Ofer Vitells. "Trial factors for the look elsewhere effect in high energy physics". In: *Eur. Phys. J. C* 70 (2010), pp. 525–530. DOI: 10.1140/epjc/s10052-010-1470-8. arXiv: 1005.1891 [physics.data-an] (cit. on p. 169).

[237] Pierre Bourhis, Juan L. Reutter, Fernando Suárez, et al. "JSON: data model, query languages and schema specification". In: *CoRR* abs/1701.02221 (2017). arXiv: 1701.02221. URL: http://arxiv.org/abs/1701.02221 (cit. on p. 174).

[238] G.S. Bisnovatyi-Kogan and S.G. Moiseenko. "Gravitational waves and core-collapse supernovae". In: *Phys. Usp.* 60.8 (2017), pp. 843–850. DOI: 10.3367/UFNe.2016.11.038112. arXiv: 1810.12198 [astro-ph.HE] (cit. on p. 178).

[239] David Radice, Viktoriya Morozova, Adam Burrows, et al. "Characterizing the Gravitational Wave Signal from Core-Collapse Supernovae". In: *Astrophys. J. Lett.* 876.1 (2019), p. L9. DOI: 10.3847/2041-8213/ab191a. arXiv: 1812.07703 [astro-ph.HE] (cit. on p. 178).

[240] B.P. Abbott et al. "A First Targeted Search for Gravitational-Wave Bursts from Core-Collapse Supernovae in Data of First-Generation Laser Interferometer Detectors". In: *Phys. Rev. D* 94.10 (2016), p. 102001. DOI: 10.1103/PhysRevD.94.102001. arXiv: 1605.01785 [gr-qc] (cit. on p. 178).

[241] LIGO Scientific Collaboration and Virgo Collaboration. "LIGO/Virgo S191110af: Identification of a GW unmodeled transient candidate". In: *GRB Coordinates Network* 26222 (Nov. 2019). https://gracedb.ligo.org/superevents/S191110af, p. 1. URL: https://gcn.gsfc.nasa.gov/gcn3/26222.gcn3 (cit. on pp. 178, 179).

[242] LIGO Scientific Collaboration and Virgo Collaboration. "LIGO/Virgo S200114f: Identification of a GW unmodeled transient candidate". In: *GRB Coordinates Network* 26734 (Jan. 2020). https://gracedb.ligo.org/superevents/S200114f, p. 1. URL: https://gcn.gsfc.nasa.gov/gcn3/26734.gcn3 (cit. on pp. 178, 181).

[243] Gary J. Feldman and Robert D. Cousins. "A Unified approach to the classical statistical analysis of small signals". In: *Phys. Rev. D* 57 (1998), pp. 3873–3889. DOI: 10.1103/PhysRevD.57.3873. arXiv: physics/9711021 (cit. on p. 178).

[244] Marta Colomer, Massimiliano Lincetto, Alexis Coleiro, et al. *GCN CIRCULAR 26249, LIGO/Virgo S191110af: Upper limits from KM3NeT MeV neutrino search.* Nov. 2019 (cit. on p. 179).

[245] Marta Colomer, Massimiliano Lincetto, Alexis Coleiro, et al. *GCN CIRCULAR 26751, LIGO/Virgo S200114f: Constraints on a CCSN origin from KM3NeT MeV neutrino search.* Jan. 2020 (cit. on p. 181).

[246] *GCN Circ archive: MASTER-Net, IceCube, HAWC, MAXI/GSC, Fermi-GBM, ZTF, ANTARES, INTEGRAL SPI-ACS, AGILE, Fermi-LAT, Swift/BAT, AGILE-GRID, DDOTI/OAN, CALET, GTC, WHT, Swift-XRT, Palomar, J-GEM, SOAR, Konus-Wind, AstroSat CZTI, TAROT, Gemini.* https://gcn.gsfc.nasa.gov/other/S200114f.gcn3 (cit. on p. 181).

[247] Tina Lund, Andreas Marek, Cecilia Lunardini, et al. "Fast time variations of supernova neutrino fluxes and their detectability". In: *Phys. Rev. D* 82 (2010), p. 063007. DOI: 10.1103/PhysRevD.82.063007. arXiv: 1006.1889 [astro-ph.HE] (cit. on pp. 184, 187).

[248] Vincent Roma, Jade Powell, Ik Siong Heng, et al. "Astrophysics with core-collapse supernova gravitational wave signals in the next generation of gravitational wave detectors". In: *Phys. Rev.* D99.6 (2019), p. 063018. DOI: 10.1103/PhysRevD.99.063018. arXiv: 1901.08692 [astro-ph.IM] (cit. on p. 187).

[249] R. Tomas, D. Semikoz, G.G. Raffelt, et al. "Supernova pointing with low-energy and high-energy neutrino detectors". In: *Phys. Rev. D* 68 (2003), p. 093013. DOI: 10.1103/PhysRevD.68.093013. arXiv: hep-ph/0307050 (cit. on p. 189).

[250] Rasmus S.L. Hansen, Manfred Lindner, and Oliver Scholer. "Timing the neutrino signal of a Galactic supernova". In: *Phys. Rev. D* 101.12 (2020), p. 123018. DOI: 10.1103/PhysRevD.101.123018. arXiv: 1904.11461 [hep-ph] (cit. on p. 189).

[251] Vedran Brdar, Manfred Lindner, and Xun-Jie Xu. "Neutrino astronomy with supernova neutrinos". In: *JCAP* 04 (2018), p. 025. DOI: 10.1088/1475-7516/2018/04/025. arXiv: 1802.02577 [hep-ph] (cit. on p. 189).

[252] A. Coleiro, M. Colomer Molla, D. Dornic, et al. "Combining neutrino experimental light-curves for pointing to the next Galactic Core-Collapse Supernova". In: *Eur. Phys. J. C* 80.9 (2020), p. 856. DOI: 10.1140/epjc/s10052-020-8407-7. arXiv: 2003.04864 [astro-ph.HE] (cit. on pp. 190, 192, 211).

[253] A. Albert et al. "The cosmic ray shadow of the Moon observed with the ANTARES neutrino telescope". In: *Eur. Phys. J. C* 78.12 (2018), p. 1006. DOI: 10.1140/epjc/s10052-018-6451-3. arXiv: 1807.11815 [astro-ph.HE] (cit. on p. 194).

[254] A. Albert et al. "Observation of the cosmic ray shadow of the Sun with the ANTARES neutrino telescope". In: (July 2020). arXiv: 2007.00931 [astro-ph.HE] (cit. on p. 194).

[255] Matteo Sanguineti. "Pointing accuracy of the ANTARES detector: Moon shadow and surface array analysis". In: *PoS* ICRC2017 (2018), p. 1053. DOI: 10.22323/1.301.1053 (cit. on p. 194).

[256] Thomas L. Szabo. "Chapter 7 - Array Beamforming". In: *Diagnostic Ultrasound Imaging: Inside Out (Second Edition)*. Ed. by Thomas L. Szabo. Second Edition. Boston: Academic Press, 2014, pp. 209–255. ISBN: 978-0-12-396487-8. DOI: https://doi.org/10.1016/B978-0-12-396487-8.00007-0. URL: http://www.sciencedirect.com/science/article/pii/B9780123964878000070 (cit. on p. 197).

[257] Peter Delos, Bon Broughton, and Jon Kraft. *Phased Array Antenna Patterns—Part 2: Grating Lobes and Beam Squint*. Ed. by Analog Devices. June 2020. URL: https://www.analog.com/en/analog-dialogue/articles/phased-array-antenna-patterns-part2.html (cit. on p. 197).

[258] T. I. Laakso, V. Valimaki, M. Karjalainen, et al. "Splitting the unit delay [FIR/all pass filters design]". In: *IEEE Signal Processing Magazine* 13.1 (1996), pp. 30–60 (cit. on p. 198).

[259] R. E. Francois and G. R. Garrison. "Sound absorption based on ocean measurements: Part I: Pure water and magnesium sulfate contributions". In: *The Journal of the Acoustical Society of America* 72.3 (1982), pp. 896–907. DOI: 10.1121/1.388170. eprint: https://doi.org/10.1121/1.388170. URL: https://doi.org/10.1121/1.388170 (cit. on p. 200).

[260] R. E. Francois and G. R. Garrison. “Sound absorption based on ocean measurements. Part II: Boric acid contribution and equation for total absorption”. In: *The Journal of the Acoustical Society of America* 72.6 (1982), pp. 1879–1890. DOI: 10.1121/1.388673. eprint: https://doi.org/10.1121/1.388673. URL: https://doi.org/10.1121/1.388673 (cit. on p. 200).